SINGLET MOLECULAR OXYGEN:

A SHOCK TUBE STUDY OF THE EXCITED STATES

by

M.D. PEDLEY, M.A.

A thesis submitted to the University of Keele in partial fulfilment of the requirements for the Degree of Doctor of Philosophy.

DEPARTMENT OF CHEMISTRY

UNIVERSITY OF KEELE

AUGUST 1978

ORIGINAL COPY IS TIGHTLY BOUND AND TEXT IS CLOSE TO THE EDGE OF THE PAGE

To Mum, Dad and Rokhy,

without whose encouragement

this would never have been written.

The work reported in this thesis was carried out by the author and Mrs. Patricia M. Borrell under the supervision of Dr. Peter Borrell. The construction of the apparatus described in Chapter 2 and the room temperature studies of the deactivation of $O_2(^1\Delta_g)$ and of $O_2(^1\Sigma_g^+)$ in pure oxygen, discussed in Chapter 3, were performed jointly. Some of the high temperature experiments, in particular those in which mixed driver gases were used to obtain temperatures between 700 and 1100 K, were also performed by Mrs. Borrell, and a few by Mr. Kevin Grant; the worker responsible for each run is indicated in Tables 7.1-7.6 of the results in Chapter 7.

ACKNOWLEDGEMENTS

In presenting this thesis I would like to acknowledge the contributions of the following people:

Dr. Peter Borrell for his guidance and encouragement throughout the work, and for his considerable help with the computing.

Professor Ian T. Millar for persuading me to return to university.

Mrs. Patricia M. Borrell, my coworker in many of the experiments described here.

The technical staff of the Chemistry Department, especially Mr. Peter Holbrook and Mr. Bob Dix in the Electronics Workshop, and Mr. Chris Cork, the departmental glass blower.

The computer operators for their patient assistance through the many hours spent on analysis of the results.

Mrs. Iris Jones for typing the thesis.

Mr. Kevin Grant for reading the drafts of each chapter; his comments were at once helpful, constructive and encouraging.

The Science Research Council for financial support from 1.10.75 to 31.12.77, and the Department of Chemistry for providing financial assistance in subsequent months.

ABSTRACT

A discharge flow shock tube has been built and used to study reactions of the singlet excited states of molecular oxygen, $O_2(^1\Delta_g)$ and $O_2(^1\Sigma_g^+)$, at temperatures of up to 1650 K.

The reactions of $O_2(^1\Delta_g)$ were the dimol emission, the energy pooling reaction, and collisional quenching in oxygen. The dimol emission was found to vary with $T^{\frac{1}{2}}$, within experimental error, confirming that the reaction is collision controlled and that a stable O_4 molecule is not an intermediate. The rates of the other reactions showed no simple temperature dependence; the rate constant for energy pooling rises from the room temperature value of 1.22×10^4 dm^3 mole^{-1} s^{-1} to 5.3×10^4 dm^3 mole^{-1} s^{-1} at 600 K and 8.14×10^5 dm^3 mole^{-1} s^{-1} at 1500 K, and that for quenching of $O_2(^1\Delta_g)$ is less than 5×10^4 dm^3 mole^{-1} s^{-1} at 1500 K. A precise value of 0.94×10^3 dm^3 mole^{-1} s^{-1} was obtained for the quenching rate constant at room temperature.

The quenching of $O_2(^1\Sigma_g^+)$ proved more suitable for study. The rate constant for deactivation by oxygen increases with temperature more rapidly than was observed for quenching by nitrogen or has been reported for quenching by other species. Thus quenching by oxygen is slower than by nitrogen at room temperature, but is more rapid at temperatures above $\sim$ 1150 K; the respective rate constants at 600 and 1500 K are 0.92×10^6 and 7.32×10^6 dm^3 mole^{-1} s^{-1} for quenching by oxygen and 1.93×10^6 and 6.17×10^6 dm^3 mole^{-1} s^{-1} for nitrogen. No simple temperature dependence was observed for quenching by nitrogen, but the oxygen results gave a reasonable fit to the empirical equation

$$k = 2.33 \times 10^9 \, e^{-67.2 \, T^{-1/3}}$$

The discharge flow shock tube was shown to be suitable for further high temperature studies of the reactions of singlet molecular oxygen and of other short-lived species. It may also be used for room temperature measurements of the rate constants; the long observation section allows exceptionally precise measurements to be made.

CONTENTS

1. INTRODUCTION

1.1. The study of chemical reactions at high temperatures

The nature of chemical reactions has been of considerable interest for many years now. The principal source of basic information about such processes is the reaction kinetics: by following the time dependence of the removal of the reactants or the formation of the products, it is possible to determine the rate of a reaction, its order, and the nature of the all important rate-determining step.

The temperature dependence of the rate of a chemical reaction provides quite a lot of information about its nature. The rate of nearly all chemical reactions increases with temperature; the vast majority are activation controlled, and the rate constant, k, varies with the temperature, T, according to the Arrhenius expression

$$k = ze^{-Eact/RT} \qquad (1.1)$$

(where Eact is the activation energy for a particular reaction, R the gas constant, and z a proportionality factor).

The reactions of short-lived, unstable intermediates in the gaseous phase frequently require no activation energy. Such reactions are collision controlled and their rates should vary with the collision frequency; the rate constant will then have a temperature dependence of the form

$$k = CT^{\frac{1}{2}} \qquad (1.2)$$

Reactions which are activation controlled have been interpreted by collision theory and by activated complex theory. Neither model is entirely satisfactory; the collision model usually gives an incorrect estimate of the preexponential constant, z, and exact interpretation of the activated complex model requires unobtainable information about the

collision complex. In recent years many workers have obtained information on interactions on the molecular scale by studies of the reaction dynamics. Such experiments include the use of crossed molecular beams[1] to give information about the nature of the interactions between the reactants and the lifetime of any collision complex that is formed. Similarly, studies of the chemiluminescence of the products formed in energy transfer processes[2] tell us about the distribution of energy amongst the products of chemical reactions.

Such information has improved our understanding of reactions which take place at a rate significantly different from that predicted by collision theory. The reactions of some metastable species are much slower than the collision frequency, despite the absence of any activation energy; the temperature dependence of such processes may be quite different from those in (1.1) and (1.2). Studies of these reactions at high temperatures have been restricted by the cost and difficulty of constructing a furnace capable of maintaining a constant, high temperature throughout the apparatus; the advantages of a shock tube for such work are well known.

A promising tool for such measurements is the discharge flow shock tube,[3] in which a discharge flow system (as is frequently used to study the reactions of short-lived species at room temperature) is coupled to a shock tube. In this work we aimed to construct a discharge flow shock tube suitable for such measurements and to use this system to further elucidate the nature of the mechanisms of quenching of singlet molecular oxygen, a metastable species with an unusually long lifetime. Singlet molecular oxygen is a species of unusual interest because of its presence both in the upper atmosphere and in polluted lower atmospheres,[4] the ease with which it takes part in organic reactions,[5] and because of its implication in a number of important biochemical processes[6] (possibly including blood disease and some forms of cancer).

The structure and properties of singlet molecular oxygen, and the shock tube and its use in chemistry, are discussed separately in the next two sections.

1.2. Singlet Molecular Oxygen

1.2.1. Structure and Spectroscopy

An early and critical test of the Heitler-London and molecular orbital theories of bonding between atoms was the structure of molecular oxygen (O_2). The valence bond approach assumes that the four 2p electrons which are unpaired in the two atoms of oxygen will combine to form two bonds; O_2 is thus predicted to be diamagnetic, with no unpaired electrons and a double bond between the atoms. On the other hand, the molecular orbital treatment of all the electrons around the oxygen nuclei gives rise to the electronic configuration (figure 1.1[7]):

$$O_2: \quad (1s\sigma)^2(1s\sigma^*)^2(2s\sigma)^2(2s\sigma^*)^2(2p\sigma)^2(2p\pi)^4(2p\pi^*)^2$$

The two degenerate $2p\pi^*$ antibonding orbitals are not complete, as they contain only two electrons. These electrons may be arranged in a number of ways, but the configuration of lowest energy is that in which they are unpaired and have parallel spins. Thus the molecular orbital model predicts that O_2 is paramagnetic in the ground state, and in fact this is found to be the case.[8] Although the Heitler-London model was able to predict the paramagnetic ground state by "re-examination", this was at the time a great triumph for the molecular orbital theory.

The two electrons in the $2p\pi^*$ molecular orbitals can give rise to three states:[9] if the two electrons are paired in the same orbital (with opposed spins), their total angular momentum is $2h/2\pi$, giving rise to a $^1\Delta g$ state; if the two electrons remain in different orbitals, their total angular momentum is zero, giving rise to a $^1\Sigma_g^+$ state in which the electron spins are opposed and a $^3\Sigma_g^-$ state in which the spins are parallel. Hunds rules state that the triplet will lie lowest in energy, as was observed above, and that, of the two singlet states, $O_2(^1\Delta_g)$ lies lower in energy than $O_2(^1\Sigma_g^+)$, because its electrons have the higher orbital angular momentum.

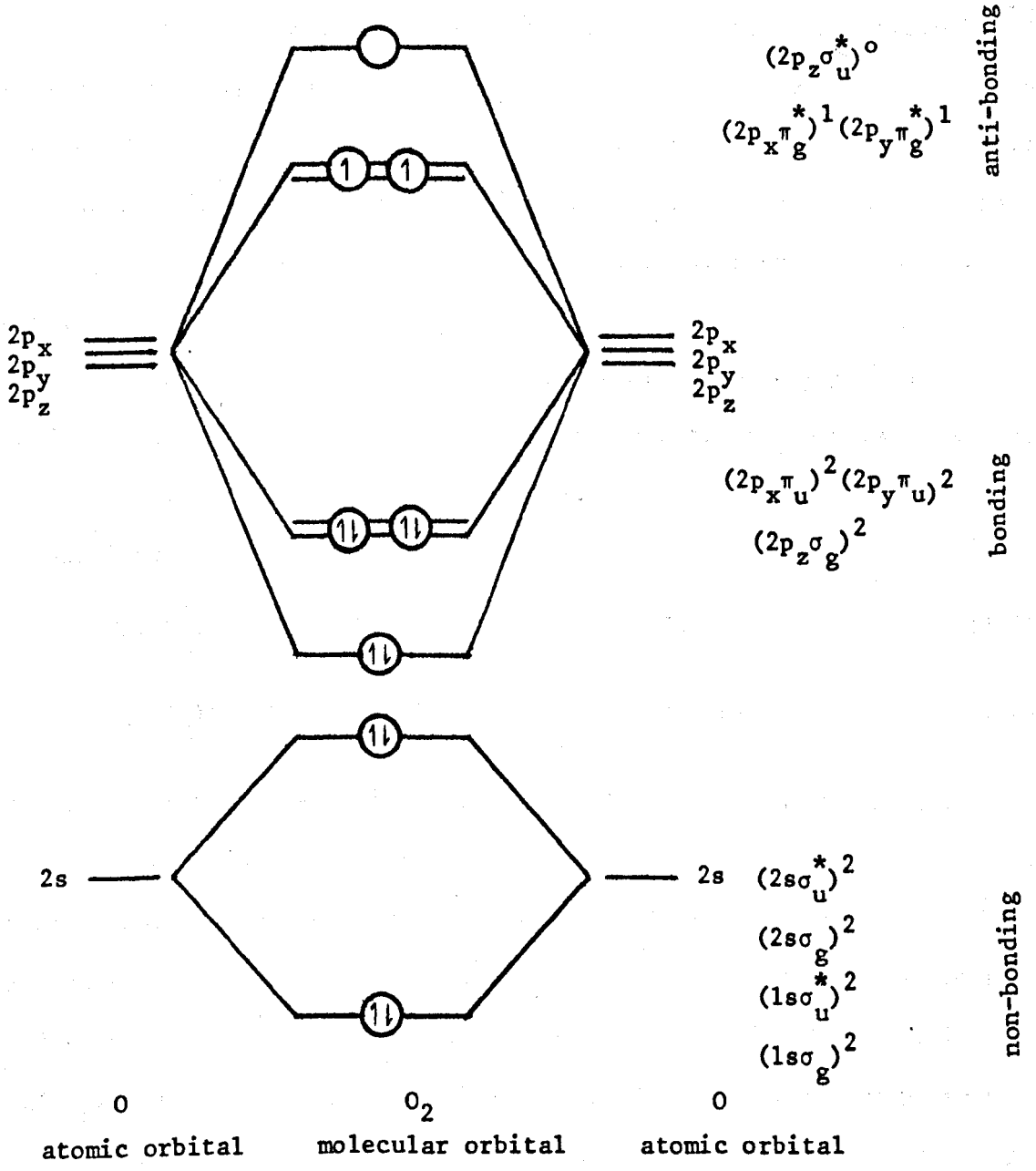

FIGURE 1.1

ELECTRONIC CONFIGURATION OF OXYGEN MOLECULE

KK. $(2s\sigma_g)^2(2s\sigma_u^*)^2(2p\sigma_g)^2(2p\pi_u)^4(2p\pi_g^*)^1(2p\pi_g^*)^1$

The two singlet states have been given the collective name "singlet molecular oxygen". As might be expected, they do not lie far above the ground state in energy; this is demonstrated by the potential energy curves for several states of the oxygen molecule in figure 1.2[10]. (The higher energy curves in this diagram correspond to states in which electrons have been promoted to the $(2p\sigma^*)$, $(3p\pi^*)$ and $(4p\pi)$ orbitals.) Considering the early theoretical interest in molecular oxygen, it is surprising how little interest in singlet molecular oxygen was shown until around 1963-64.

The energies of the three low-lying states of oxygen[8] are shown in figure 1.3. Electric dipole transitions between the singlet states and the ground state are spin forbidden, but weak magnetic dipole transitions are allowed.[11]

$$O_2(^1\Sigma_g^+)(v=o) \rightarrow O_2(^3\Sigma_g^-)(v=o) + h\nu(\ 762nm) \qquad (1.3)$$

$$O_2(^1\Delta_g)(v=o) \rightarrow O_2(^3\Sigma_g^-)(v=o) + h\nu(1270nm) \qquad (1.4)$$

The low energy of the excited states is illustrated by these emissions, which are both in the near infrared whereas the vast majority of electronic transitions are in the ultraviolet and visible part of the spectrum. The radiative lifetimes of $O_2(^1\Sigma_g^+)$ and $O_2(^1\Delta_g)$ have been calculated to be 12s[12] and 45 minutes[13,14] respectively; the extraordinarily high stability of $O_2(^1\Delta_g)$ has been confirmed by observations in the upper atmosphere where, at the low pressure, only a little collision enhancement of the decay occurs and a half life of over 30 minutes has been recorded.[15]

A number of weak, spin forbidden transitions between the singlet states and the ground state have been observed in the visible and near infrared regions of the spectrum, both in absorption[16] and emission.[7,11,17] These transitions are generally enhanced by collisions which mix states, thus introducing some allowed character into a previously forbidden

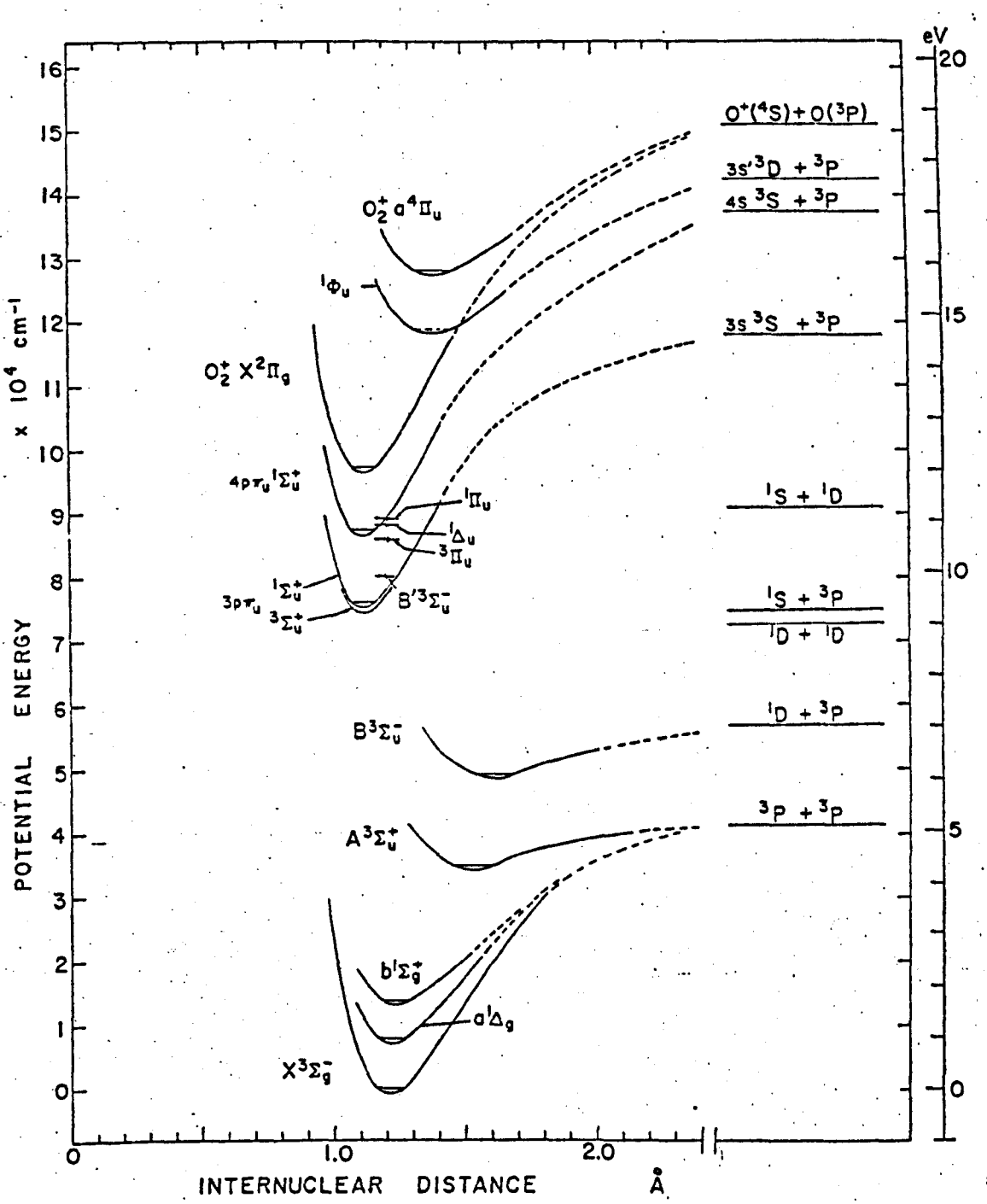

Figure I.2 Potential Energy Curves for Oxygen (Reproduced From Reference IO).

States, Energies and Transitions of Oxygen

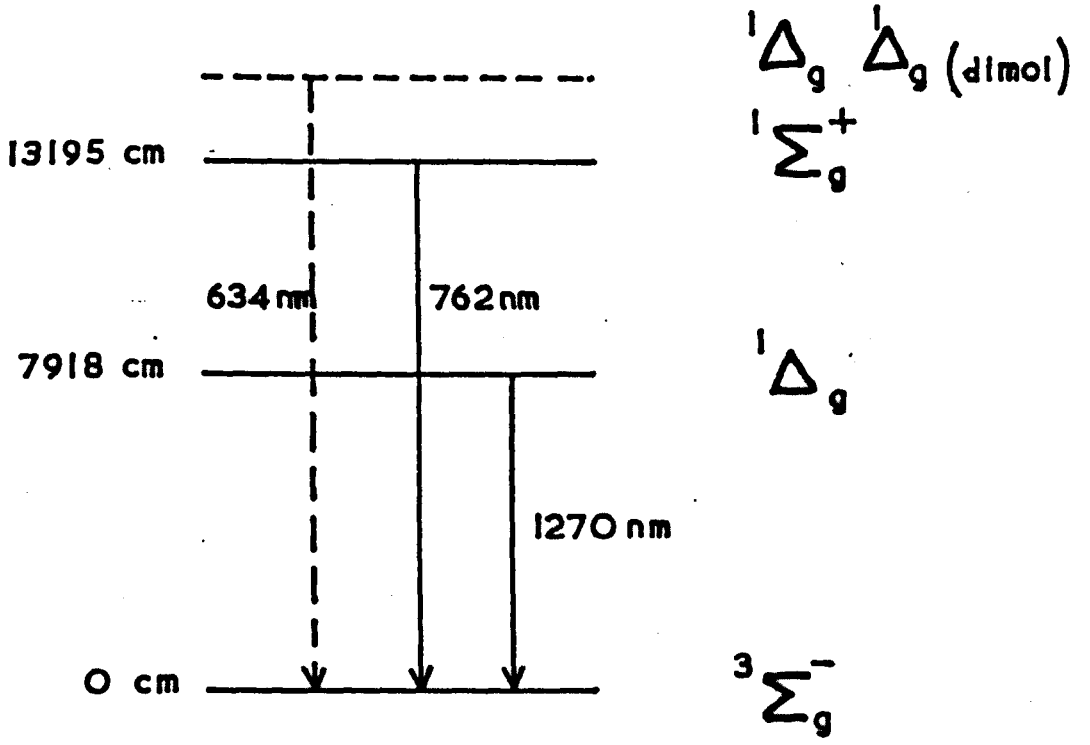

FIGURE I.3 Low Lying Excited States of Oxygen

transition. Thus of the following transitions observed in absorption

1270nm: $O_2(^1\Delta_g)(v=o) + O_2(^3\Sigma_g^-)(v=o) \leftarrow O_2(^3\Sigma_g^-)(v=o) + O_2(^3\Sigma_g^-)(v=o)$ (1.5)

1070nm: $O_2(^1\Delta_g)(v=1) + O_2(^3\Sigma_g^-)(v=o) \leftarrow O_2(^3\Sigma_g^-)(v=o) + O_2(^3\Sigma_g^-)(v=o)$ (1.6)

762nm: $O_2(^1\Sigma_g^+)(v=o) \leftarrow O_2(^3\Sigma_g^-)(v=o)$ (1.7)

634nm: $O_2(^1\Delta_g)(v=o) + O_2(^1\Delta_g)(v=o) \leftarrow O_2(^3\Sigma_g^-)(v=o) + O_2(^3\Sigma_g^-)(v=o)$ (1.8)

580nm: $O_2(^1\Delta_g)(v=o) + O_2(^1\Delta_g)(v=1) \leftarrow O_2(^3\Sigma_g^-)(v=o) + O_2(^3\Sigma_g^-)(v=o)$ (1.9)

(1.5) and (1.6) are collision enhanced (their intensity varying with the square of the oxygen pressure). (1.7) is very nearly a pure magnetic dipole transition, showing collision enhancement only at high oxygen pressures. (1.8) and (1.9) are perhaps the most interesting as they are collision induced simultaneous transitions in which two oxygen molecules are excited by a single photon.

As these absorptions are all very weak, the emission spectra of $O_2(^1\Sigma_g^+)$ and $O_2(^1\Delta_g)$ have been studied in rather greater detail. Transitions to vibrationally excited states of $O_2(^3\Sigma_g^-)$ and further collision induced simultaneous transitions

477nm: $O_2(^1\Delta_g)(v=o) + O_2(^1\Sigma_g^+)(v=o) \rightarrow O_2(^3\Sigma_g^-)(v=o) + O_2(^3\Sigma_g^-)(v=o)$ (1.10)

380nm: $O_2(^1\Sigma_g^+)(v=o) + O_2(^1\Sigma_g^+)(v=o) \rightarrow o_2(^3\Sigma_g^-)(v=o) + O_2(^3\Sigma_g^-)(v=o)$ (1.11)

have been observed.[17,18]

The emission spectra of singlet oxygen obtained by Khan and by Vohra et.al. are shown in figures 1.4 and 1.5; the peaks observed by Vohra at 738 and 835nm have not been identified. The most intense transition in the visible part of the spectrum is the red band at 634nm. This red emission was observed in the decomposition of hydrogen peroxide by alkaline hypochlorite by several workers over the years,[19-23] but the first serious study was by Khan and Kasha[24] who initially interpreted it as being the $O_2(^1\Sigma_g^+) \rightarrow O_2(^3\Sigma_g^-)$ system shifted to higher energy by

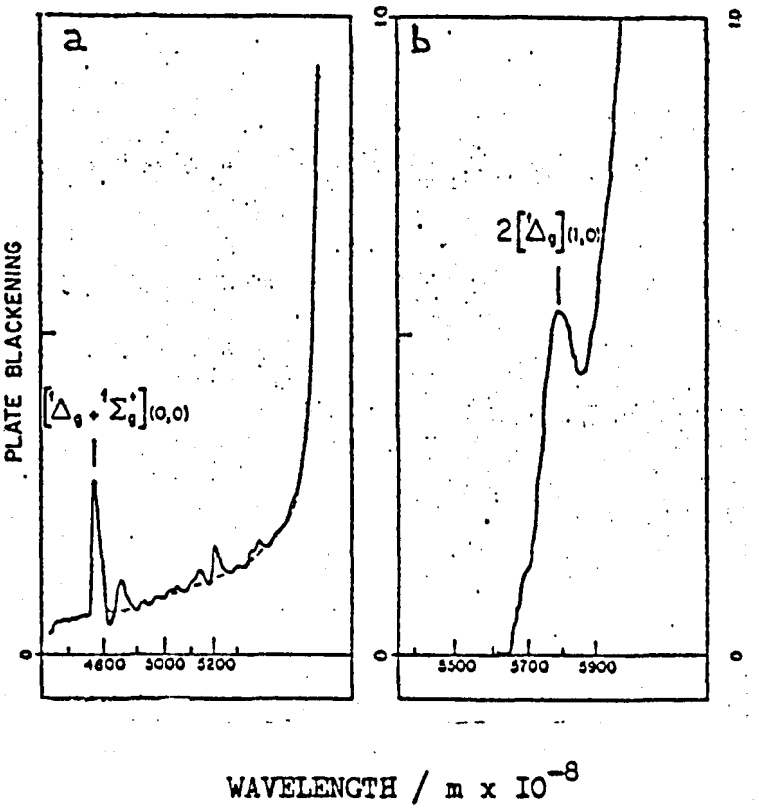

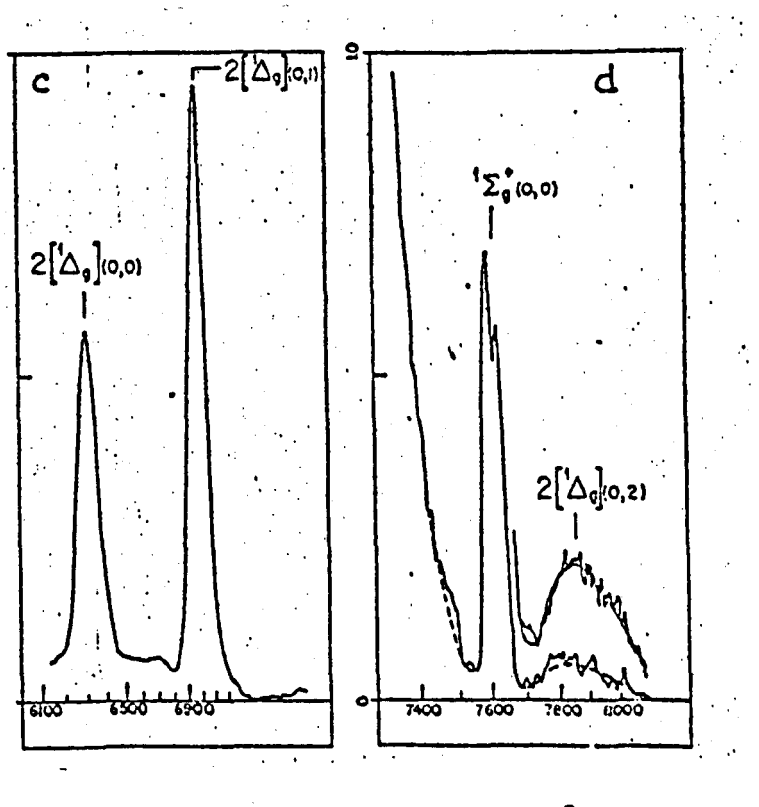

FIGURE I.4 Chemiluminescence Bands for the Aqueous Reaction at 293 K of Hydrogen Peroxide with Hypochlorite. (Reference I8).

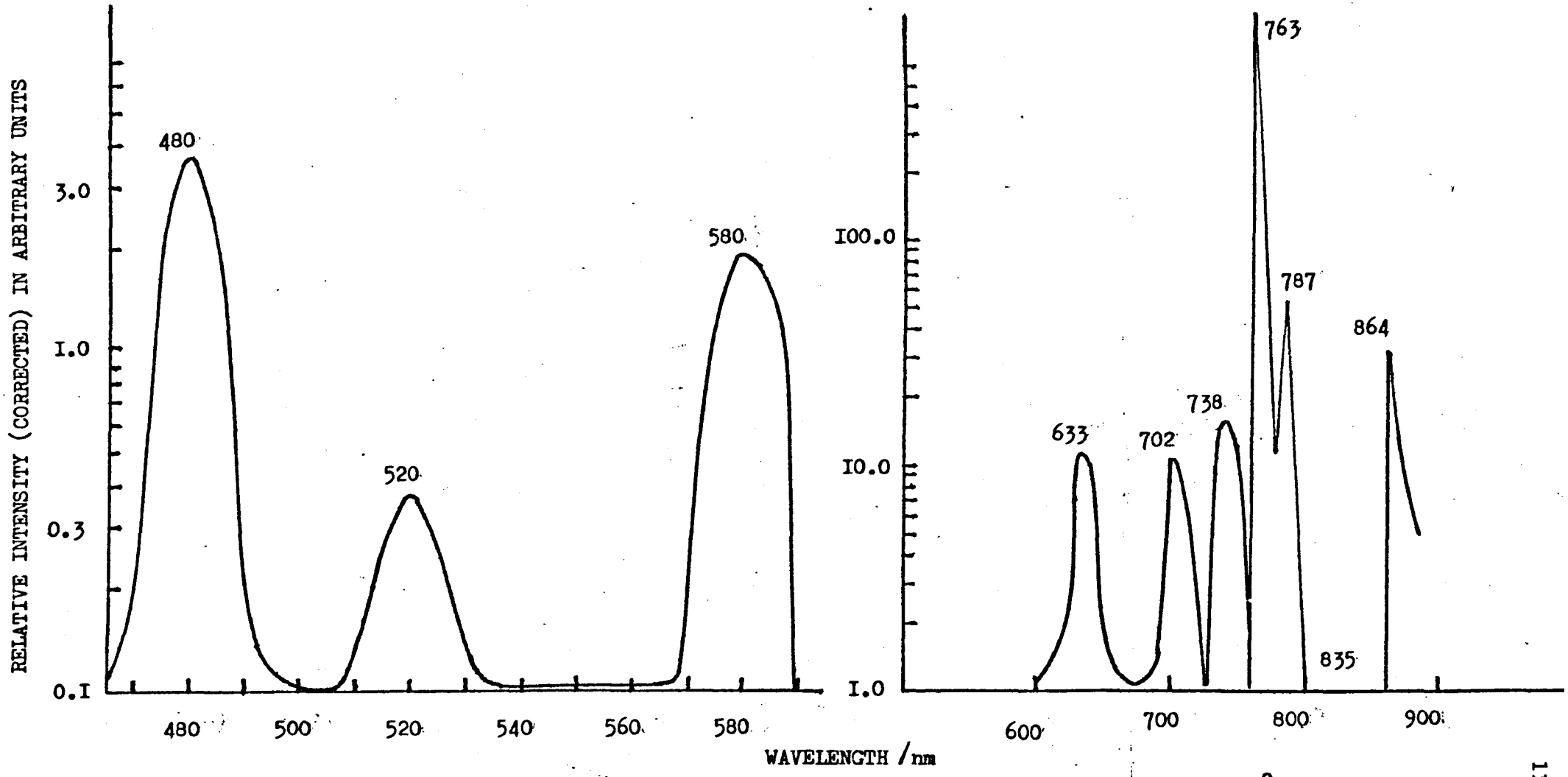

FIGURE 1.5 Emission Spectrum of Singlet Molecular Oxygen at 0.75 KN m^{-2}

hydration of the oxygen. Arnold et.al.[25] established the true nature of this emission which has been christened the "dimol" emission. It has frequently been suggested that the emission is from the O_4 molecule,[26,27] rather than a collision induced simultaneous transition:

$$O_2(^1\Delta_g) + O_2(^1\Delta_g) \rightarrow O_4 \rightarrow O_2(^3\Sigma_g^-) + O_2(^3\Sigma_g^-) + h\nu(634nm) \qquad (1.12)$$

This intermediate has considerable appeal as it could also be invoked to account for the unusual "energy pooling" reactions[28] of $O_2(^1\Delta_g)$ such as

$$O_2(^1\Delta_g) + O_2(^1\Delta_g) \rightarrow O_2(^1\Sigma_g^+) + O_2(^3\Sigma_g^-) \qquad (1.13)$$

However, Arnold[29] has measured the temperature dependence of reaction (1.12) and does not obtain an activation energy consistent with the formation of a bound complex. As equivalent transitions are observed in reactions (1.10) and (1.11) and also in absorption (1.8), interpretation in terms of a bound O_4 molecule is rather less desirable than at first sight. It seems far more likely that the long lifetime of $O_2(^1\Delta_g)$ and, to a lesser extent, $O_2(^1\Sigma_g^+)$ is sufficient to allow collisional reactions between these excited states to be observed.

Nevertheless, several studies of liquid and solid oxygen have been made in the hope of isolating this molecule,[30,31] and Goodman and Brus[32] have studied the structure of and energy transfer processes within isolated $(O_2)_2$ dimers in a solid neon host at 4.2 K. They suggest that the lifetime of a simple collision complex in the gas phase is sufficient for the energy transfer reactions they observe at 4.2 K. Most other workers in this field tend to assume the existence of the O_4 molecule in all three phases as their starting point, despite the conclusions of Krupenie[30] that this is far from proven even in liquid and solid oxygen.

1.2.2. Formation

Nearly all molecules have singlet ground states; the Wigner spin conservation rules also restrict the electronic states of the products

of reactions between such states to singlets. Consequently, reactions in which molecular oxygen is formed often produce detectable concentrations of singlet molecular oxygen in the gas evolved

e.g. $K_3CrO_8 + H_2O$ (or H_2O_2) $\rightarrow O_2(^1\Delta_g)$ (1.14)[33]

$2H_2O_2 \rightarrow 2H_2O + O_2(^1\Delta_g)$ (1.15)[19-23]

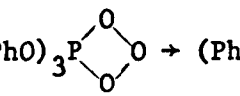

(1.16)[34]

$2O_2^- \rightarrow O_2(^1\Delta_g) + O_2(^3\Sigma_g^-) + 2e^-$ (1.17)[35]

The singlet molecular oxygen formed is rapidly quenched to the ground state, but the oxygen evolved may contain as much as 6% in the singlet states.[33] Such reactions are a useful source of singlet molecular oxygen in situ, but suffer from the disadvantages of side reactions and the formation of unwanted by-products in the system.

$O_2(^1\Sigma_g^+)$ may be formed directly in these reactions, but it is quenched very rapidly to $O_2(^1\Delta_g)$. An appreciable concentration is always produced in the presence of $O_2(^1\Delta_g)$ by the energy pooling reaction

$$O_2(^1\Delta_g) + O_2(^1\Delta_g) \rightarrow O_2(^1\Sigma_g^+) + O_2(^3\Sigma_g^-) \quad (1.13)$$

Young and Black[28,36] have observed the direct formation of $O_2(^1\Sigma_g^+)$ from atomic oxygen formed by the nitrogen titration

$$N + NO \rightarrow N_2 + O \quad (1.18)$$

$$O + O \rightarrow O_2(^1\Sigma_g^+) \quad (1.19)$$

in which no emission from $O_2(^1\Delta_g)$ is observed, and recently a number of workers have prepared $O_2(^1\Sigma_g^+)$ free of $O_2(^1\Delta_g)$ by excitation of the ground state using a tunable dye laser at approximately atmospheric pressure,[37,38] $O_2(^1\Delta_g)$ has also been prepared in this way[39,40] using a neodymium:glass laser or a neodyomium:yttrium aluminium garnet laser which both give an intense pulsed output at ≈1060nm and excite oxygen to $O_2(^1\Delta_g)(v=1)$.

This reaction requires a pressure of about 35 atmospheres, which places considerable limitations on the reactions which may be performed.

Singlet molecular oxygen is also formed by the photolysis of ozone[11] at wavelengths of 240-310nm. The reaction is of importance as the principal mechanism of loss of ozone in the upper atmosphere. Once again, spin conservation gives rise to $O_2(^1\Delta_g)$ in preference to the ground state.

$$O_3 \xrightarrow{h\nu} O(^1D) + O_2(^1\Delta_g) \qquad (1.20)$$

Collins et. al.[41] have used this reaction to prepare $O_2(^1\Delta_g)$ uncontaminated by the ground state; it allowed them to observe many absorption systems of $O_2(^1\Delta_g)$ and identify several Rydberg series leading to the first ionisation potential of $O_2(^1\Delta_g)$, all of which are normally masked by absorptions from $O_2(^3\Sigma_g^-)$.

In the presence of $O_2(^3\Sigma_g^-)$, $O_2(^1\Sigma_g^+)$ is formed by the energy exchange reaction

$$O(^1D) + O_2(^3\Sigma_g^-) \rightarrow O(^3P) + O_2(^1\Sigma_g^+) \qquad (1.21)$$

Snelling[42] has measured the efficiency of reaction (1.21) to be as high as 0.85 (he suggests that earlier measurements giving efficiencies of 10^{-2}-1.0 were the result of imprecise experimentation).

Energy transfer from excited triplet state, and possibly excited singlet state, sensitizer molecules to $O_2(^3\Sigma_g^-)$ also gives rise to the singlet states

$$^1(^3M_1 + O_2(^3\Sigma_g^-)) \rightarrow {}^1M_o + O_2(^1\Sigma_g^+) \qquad (1.22)$$

$$^1M_1 + O_2(^3\Sigma_g^-) \rightarrow {}^3M_1 + O_2(^1\Delta_g) \qquad (1.23)$$

Kearns[43,44] has studied these processes in some detail; he confirms that high energy triplet state sensitizers give rise principally to $O_2(^1\Sigma_g^+)$ and low energy triplet sensitizers mainly to $O_2(^1\Delta_g)$, but considers it to be unlikely that singlet molecular oxygen is formed in the quenching of excited

singlet states, as this process takes place primarily by relaxation to the charge-transfer state

$$^1M_1 + O_2(^3\Sigma_g^-) \rightarrow (M^+ + O_2^-) \qquad (1.24)$$

This technique has frequently been used to prepare singlet molecular oxygen in solution. In a typical experiment, the triplet state of methylene blue[45] is formed by laser excitation to an excited singlet state, followed by intersystem crossing; singlet oxygen is then produced by energy transfer. It is rather less suitable for gas phase work, although Snelling[46] has successfully used benzene to sensitize formation of $O_2(^1\Delta_g)$ and Abrahamson[47-49] SO_2 and other sensitizers for formation of $O_2(^1\Sigma_g^+)$. Frankiewicz and Berry[50] have studied the formation of $O_2(^1\Delta_g)$ photosensitized by electronically excited NO_2 (which is a doublet, as is the ground state). $O_2(^1\Sigma_g^+)$ is formed by

$$^2NO_2 + h\nu \ (700 > \lambda > 405nm) \rightarrow {}^2NO_2^* \qquad (1.25)$$

$$^2NO_2^* + O_2(^3\Sigma_g^-) \rightarrow {}^2NO_2 + O_2(^1\Delta_g) \qquad (1.26)$$

the reaction[51]

$$^2NO_2^* + O_2(^1\Delta_g) \rightarrow {}^2NO_2 + O_2(^1\Sigma_g^+) \qquad (1.27)$$

The most common technique used for the experimental production of singlet molecular oxygen is to pass a microwave discharge through oxygen[11]. The exact processes taking place in the discharge are not well established, but large quantities of singlet molecular oxygen, together with atomic oxygen and a little ozone, are formed. Atomic oxygen may be removed by distilling mercury through the discharge[52]; this reacts to form a layer of mercuric oxide on the far side of the discharge. The mercuric oxide layer also appears to remove atomic oxygen and to enhance the concentration of singlet molecular oxygen, possibly by the process[11]

$$Hg + O \xrightarrow{wall} HgO \qquad (1.28)$$

$$HgO + O \longrightarrow Hg + O_2(^1\Delta_g) \qquad (1.29)$$

Singlet oxygen does not appear to be formed directly in the discharge; Wayne[53] and Von Engel[54] have shown that the concentrations of $O_2(^1\Delta_g)$ and ozone build up just downstream of the discharge, suggesting that some atom recombination process is taking place. There is no evidence to suggest that $O_2(^1\Sigma_g^+)$ is formed other than by the energy pooling reaction, but it is present in significant quantities because of the high concentration of $O_2(^1\Delta_g)$ (as much as 10% of the bulk gas[43]). The preparation of $^1O_2$ using a microwave discharge is easily controlled and produces no chemical byproducts. However, Ogryzlo[55] has suggested that many measurements using this source of singlet oxygen have produced erroneous values as a result of the presence of atomic oxygen in the system and that even the "best" mercuric oxide surface does not reduce the atom concentration to the point where it has no effect on kinetic measurements.

1.2.3. Reactions

Many reactions of singlet molecular oxygen have been reported over the last fifteen years. In this section we shall consider the three principal groups: organic oxidations, non-reactive quenching, and electronic energy transfer.

(i) Organic Oxidations

$O_2(^1\Delta_g)$ readily undergoes concerted cycloaddition to unsaturated hydrocarbons by the Diels-Alder and structurally related "ene" reactions

Diels-Alder 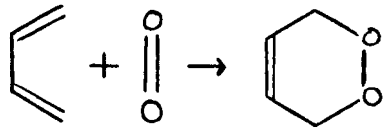 (1.30)

Ene: 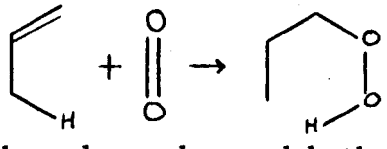 (1.31)

Reactions of this type have been observed both in the gas phase and in solution[5,43]. Ogryzlo[55] has suggested that (in the gas phase at least) (1.30) is not a typical Diels Alder reaction and that a charge-transfer

mechanism is the principal driving force; the simple "ene" mechanism is probably an adequate description of reaction (1.31)[57].

Foote (1964) has demonstrated that dye-sensitized photooxidation reactions have such a mechanism[58]; the intermediate $O_2(^1\Delta_g)$ is formed by the energy transfer reaction (1.22). This mechanism had in fact been proposed by Kautsky in the thirties.[59]

In polluted atmospheres singlet oxygen is formed by several of the reactions described in section 1.2.2.[60]; the principal source is energy transfer from electronically excited NO_2[4,60]. Olefins present in the atmosphere will react with any singlet molecular oxygen, and in the presence of nitric oxide, free radicals of the general type $RC\overset{O}{\underset{O.}{=}}$ are formed[60]. Such radicals are important in the photochemical chain reaction; they are also formed in the reactions of atomic oxygen and ozone, and it has been shown[4] that the contribution of singlet oxygen to the formation of these radicals is insignificantly small in comparison with the other sources.

Although singlet molecular oxygen is not of importance in the photochemical chain reaction, the products of its organic reactions are unusual and not very pleasant. A recent review of the role of singlet molecular oxygen in biochemical processes[6] suggests that singlet molecular oxygen may be responsible for blood disease, some forms of cancer, ageing processes and other forms of ill-health.

(ii) Non-reactive Quenching

The rates of deactivation of $O_2(^1\Sigma_g^+)$ and $O_2(^1\Delta_g)$ in the gaseous phase have been measured for a large number of inert quenchers. Table 1.1 (after Davidson and Ogryzlo[61]) shows that $O_2(^1\Sigma_g^+)$ is deactivated far more rapidly than $O_2(^1\Delta_g)$, because the quenching reaction

$$O_2(^1\Sigma_g^+) + M \rightarrow O_2(^1\Delta_g) + M \qquad (1.32)$$

is spin-allowed, while the reaction

$$O_2(^1\Delta_g) + M \rightarrow O_2(^3\Sigma_g^-) + M \qquad (1.33)$$

is nominally forbidden. Nevertheless, reaction (1.32) is still quite slow, taking place at a rate 10^2-10^7 lower than the collision frequency. The efficiency of quenching of $O_2(^1\Sigma_g^+)$ increases with increasing value of the fundamental vibration frequency of the quencher[61,68], and consequently molecules containing hydrogen tend to be the best quenchers, and oxygen, which has a low vibration frequency is a poor quenching agent. As a result, a number of inaccurate quenching measurements have been made in systems where the presence of a few ppm of water significantly increases the rate of deactivation. This has been demonstrated by Thrush[71] for quenching of $O_2(^1\Sigma_g^+)$ by oxygen, and the reported rates of quenching by the inert gases are probably also significantly overestimated.

Highly substituted amines are particularly effective at quenching $O_2(^1\Delta_g)$; the rate constants increase with increasing substitution of the amine[84], in direct contrast with the rate of quenching of $O_2(^1\Sigma_g^+)$ which shows a slight decrease. Wilson[86] has suggested that a charge-transfer interaction can account for these results, and a correlation between quenching efficiencies and ionization energies of the quencher has been noted[84]. The quenching efficiencies of some sulphides[85] may be seen to follow a similar trend.

The rates of quenching of $O_2(^1\Delta_g)$ by olefins have been measured by Ogryzlo[87] and by Ackerman[88]. They are not included in Table 1.1 as Ogryzlo, himself, has suggested[55] that the presence of atomic oxygen in these systems has resulted in serious errors in the measured rate constants.

Several mechanisms have been proposed for the collisional quenching reactions of $O_2(^1\Sigma_g^+)$. Kear and Abrahamson[68] assumed the process to take place by transfer of the electronic energy of $O_2(^1\Sigma_g^+)$ to vibrational energy of the quencher and that this energy transfer is controlled by short range,

TABLE 1.1

Rate Constants for the Quenching of $O_2(^1\Sigma_g^+)$ and $O_2(^1\Delta_g)$

QUENCHER AND ν OF HIGHEST FUNDAMENTAL	$Kq(^1\Sigma)$ dm^3 $mole^{-1}$ s^{-1} BEST VALUE	REPORTED VALUE	$Kq(^1\Delta)$ dm^3 $mole^{-1}$ s^{-1} BEST VALUE	REPORTED VALUE
He	6×10^3	$\sim 6 \times 10^3$ (62) $< 6 \times 10^4$ (63) $\sim 6 \times 10^4$ (64) $< 7 \times 10^5$ (65)	4.8	$\leqslant 6$ (62) < 5 (66) 4.8 (41)
Ar	9×10^3	9×10^3 (62) $< 6 \times 10^4$ (63) 3.5×10^3 (64) 1.5×10^6 (65)	5.3	$\leqslant 6$ (62) < 120 (67) < 5 (66) 5.4 (41)
Kr			5	5 (41)
Xe			20	20 (41)
$H_2(4405cm^{-1})$	2.4×10^8	6.6×10^8 (68) 2.4×10^8 (62) 2.4×10^8 (63) 6.6×10^8 (64) 6×10^8 (69) 3.9×10^8 (70) 2.4×10^8 (71) 4.9×10^8 (72)	2.7×10^3	2.2×10^3 (62) 2.7×10^3 (66) 3.2×10^3 (41)

QUENCHER AND ν OF HIGHEST FUNDAMENTAL	$Kq(^1\Sigma)$ dm^3 $mole^{-1}$ s^{-1} BEST VALUE	REPORTED VALUE		$Kq(^1\Delta)$ dm^3 $mole^{-1}$ s^{-1} BEST VALUE	REPORTED VALUE	
HD($3817cm^{-1}$)	1.5×10^8	1.1×10^8	(63)			
		1.9×10^8	(69)			
D_2 ($3118\ cm^{-1}$)	1.0×10^7	1.2×10^7	(63)			
		1.2×10^7	(64)			
		1.1×10^7	(69)			
		1.0×10^7	(68)			
N_2 ($2359cm^{-1}$)	1.3×10^6	1.3×10^6	(62)			
		1.2×10^6	(73)			
		1.8×10^6	(63)		≤ 6	(62)
		1.1×10^6	(64)		≤ 42	(67)
		1.3×10^6	(70)	50	< 1.3	(66)
		1.4×10^6	(74)		< 84	(75)
		1.5×10^6	(65)		83	(41)
		1.3×10^6	(68)			
		1.3×10^6	(37)			
CO ($2168cm^{-1}$)	2.3×10^6	1.8×10^6	(73)			
		2.6×10^6	(64)		$< 4 \times 10^4$	(41)
		2.0×10^6	(70)	5.0×10^3	5.0×10^3	(79)
		1.5×10^6	(65)			
		3.4×10^6	(68)			

QUENCHER AND ν OF HIGHEST FUNDAMENTAL	$Kq(^1\Sigma)$ dm^3 $mole^{-1}$ s^{-1} BEST VALUE	REPORTED VALUE		$Kq(^1\Delta)$ dm^3 $mole^{-1}$ s^{-1} BEST VALUE	REPORTED VALUE	
O_2 ($1580cm^{-1}$)	2.6×10^4	9.0×10^4	(62)	9.1×10^2	1.0×10^3	(62)
		9.0×10^4	(73)		1.4×10^3	(67)
		$\sim 6.0 \times 10^5$	(63)		1.3×10^3	(66)
		2.7×10^5	(64)		1.2×10^3	(75)
		6.6×10^4	(70)		1×10^3	(76)
		$< 6.0 \times 10^4$	(74)		9.4×10^2	(77)
		2.8×10^4	(68)		9×10^2	(40)
		2.8×10^4	(71)		8.9×10^2	(78)
		2.4×10^4	(37)			
		2.4×10^4	(38)			
NO ($1904cm^{-1}$)	2.6×10^7	3.3×10^7	(62)	2.3×10^4	2.7×10^4	(62)
		2.4×10^7	(63)		2.7×10^4	(51)
		2.5×10^7	(64)		1.5×10^4	(80)
H_2O ($3756cm^{-1}$)	2.4×10^9	3.0×10^9	(62)	3.1×10^3	2.4×10^3	(62)
		2.4×10^9	(63)		8.3×10^3	(67)
		2.0×10^9	(64)		3.4×10^3	(66)
		3.3×10^9	(69)			
		$\sim 1.2 \times 10^{10}$	(70)			
		6×10^8	(65)			
		1.2×10^9	(68)			
		2.8×10^9	(71)			

QUENCHER AND ν OF HIGHEST FUNDAMENTAL	$Kq(^1\Sigma)$ dm^3 $mole^{-1}$ s^{-1} BEST VALUE	REPORTED VALUE		$Kq(^1\Delta)$ dm^3 $mole^{-1}$ s^{-1} BEST VALUE	REPORTED VALUE	
D_2O ($2789cm^{-1}$)	5.0×10^8	2.4×10^8	(63)			
		2.3×10^9	(69)			
		4.9×10^8	(65)			
		5.0×10^8	(79)			
N_2O ($2224cm^{-1}$)	4.5×10^7	1.1×10^8	(62)			
		4.2×10^7	(69)	< 45	$\leq$ 60	(62)
		8.1×10^7	(68)		< 45	(66)
		4.5×10^7	(79)			
CO_2 ($2344cm^{-1}$)	2.0×10^8	2.5×10^8	(68)			
		1.8×10^8	(62)			
		1.8×10^8	(73)			
		9.0×10^7	(63)	1.5×10^3	< 50	(62)
		2.6×10^8	(64)		2.5×10^3	(67)
		1.2×10^8	(70)		< 9	(66)
		2.8×10^7	(65)		1.5×10^3	(80)
CS_2 ($1532cm^{-1}$)	1.7×10^6	1.7×10^6	(68)			
H_2S ($2627cm^{-1}$)	2×10^8	3.8×10^8	(68)			
		1.5×10^7	(65)			

QUENCHER AND ν OF HIGHEST FUNDAMENTAL	$Kq(^1\Sigma)$ dm^3 $mole^{-1}$ s^{-1} BEST VALUE	REPORTED VALUE		$Kq(^1\Delta)$ dm^3 $mole^{-1}$ s^{-1} BEST VALUE	REPORTED VALUE	
HCl ($2885cm^{-1}$)	4.2×10^7	4.0×10^7	(81)			
		4.4×10^7	(79)			
DCl	3.5×10^6	3.5×10^6	(79)			
HBr ($2564cm^{-1}$)	2.3×10^8	2.3×10^8	(82)			
NO_2 ($1618cm^{-1}$)	1.7×10^7	1.5×10^7	(63)	3×10^3	3×10^3	(62)
		1.9×10^7	(69)			
SO_2 ($1362cm^{-1}$)	1×10^5	4.0×10^5	(68)			
		1.8×10^6	(63(			
CH_4 ($3020cm^{-1}$)	4.6×10^7	4.4×10^7	(61)	8.4×10^3	8.4×10^3	(62)
		4.5×10^7	(62)			
		6.6×10^7	(69)			
		8×10^6	(65)			
		5.0×10^7	(68)			
C_2H_6 ($2995cm^{-1}$)	2.0×10^8	1.9×10^8	(61)			
		2.8×10^8	(68)			
		2.2×10^8	(69)			
C_3H_8 ($2980cm^{-1}$)	2.3×10^8	2.7×10^8	(61)			
		2.2×10^8	(62)			
		2.0×10^8	(79)			

QUENCHER AND ν OF HIGHEST FUNDAMENTAL	$Kq(^1\Sigma)$ dm^3 $mole^{-1}$ s^{-1} BEST VALUE	REPORTED VALUE		$Kq(^1\Delta)$ dm^3 $mole^{-1}$ s^{-1} BEST VALUE	REPORTED VALUE	
$n\text{-}C_4H_{10}$	3.8×10^8	3.8×10^8	(61)			
$iso\text{-}C_4H_{10}$	2.9×10^8	2.9×10^8	(61)			
$n\text{-}C_5H_{12}$	4.5×10^8	4.5×10^8	(61)			
$n\text{-}C_6H_{14}$	5.5×10^8	5.5×10^8	(61)			
$n\text{-}C_7H_{16}$	6.0×10^8	6.0×10^8	(61)			
$cyclo\text{-}C_3H_6$	3.7×10^8	3.7×10^8	(61)			
$cyclo\text{-}C_6H_{12}$	5.8×10^8	5.8×10^8	(61)			
$CH_3\text{-}cyclo\text{-}C_5H_9$	5.2×10^8	5.2×10^8	(61)			
$CH_3\text{-}cyclo\text{-}C_6H_{11}$	5.8×10^8	5.8×10^8	(61)			
CH_3I	1.8×10^8	1.8×10^8	(63)			
$CHCl_3$	8.8×10^7	8.8×10^7	(65)			
CF_4 ($1265 cm^{-1}$)	1.6×10^6	1.6×10^6	(68)			
CF_2Cl_2	1.8×10^6	1.8×10^6	(62)	2.4×10^2	2.4×10^2	(62)
CCl_4 ($791\ cm^{-1}$)	7.5×10^5	2.7×10^5	(68)			
		1.8×10^6	(63)			
C_2H_2 ($3374 cm^{-1}$)	2.5×10^8	2.7×10^8	(83)			
		2.3×10^8	(79)			

QUENCHER AND ν OF HIGHEST FUNDAMENTAL	$Kq(^1\Sigma)$ dm^3 $mole^{-1}$ s^{-1} BEST VALUE	REPORTED VALUE		$Kq(^1\Delta)$ dm^3 $mole^{-1}$ s^{-1} BEST VALUE	REPORTED VALUE	
C_2D_2 ($2700cm^{-1}$)	4.9×10^7	4.9×10^7	(69)			
C_2H_4 ($3272cm^{-1}$)	2.1×10^8	1.2×10^8	(62)	1.2×10^3	1.2×10^3	(62)
		1.9×10^8	(64)			
		2.7×10^8	(83)			
		2.6×10^8	(69)			
		2.3×10^8	(68)			
C_2D_4 ($2304cm^{-1}$)	8.4×10^7	8.4×10^7	(69)			
C_2D_6 ($2225cm^{-1}$)	1.0×10^8	1.0×10^8	(68)			
C_2F_6	1.9×10^6	1.9×10^6	(68)			
SF_6 ($965cm^{-1}$)	3.4×10^5	3.4×10^5	(64)	≤ 6	≤ 6	(62)
					≤ 7	(66)
NH_3 ($3414cm^{-1}$)	1.2×10^9	1.3×10^9	(61)	4.2×10^3	4.2×10^3	(62)
		1.1×10^9	(62)			
		1.8×10^9	(63)			
		5.2×10^7	(64)			
		1.6×10^8	(65)			
		1.2×10^9	(79)			

QUENCHER AND ν OF HIGHEST FUNDAMENTAL	$Kq(^1\Sigma)$ dm^3 $mole^{-1}$ s^{-1} BEST VALUE	REPORTED VALUE		$Kq(^1\Delta)$ dm^3 $mole^{-1}$ s^{-1} BEST VALUE	REPORTED VALUE	
CH_3NH_2	1.1×10^9	1.1×10^9	(61)	8.0×10^3	8.0×10^3	(84)
$C_2H_5NH_2$	8.9×10^8	8.9×10^8	(61)	7.0×10^3	7.0×10^3	(84)
$(CH_3)_2NH$	5.6×10^8	5.6×10^8	(61)	5.6×10^4	5.6×10^4	(84)
$(C_2H_5)_2NH$				7.3×10^4	7.3×10^4	(84)
$(CH_3)_3N$	3.6×10^8	3.6×10^8	(61)	1.9×10^6	1.9×10^6	(84)
$(C_2H_5)_3N$	5.8×10^8	5.8×10^8	(61)	2.0×10^6	2.0×10^6	(84)
CH_3SH				2.3×10^3	2.3×10^3	(85)
$(CH_3)_2S$				1.6×10^5	1.6×10^5	(85)
$(C_2H_5)_2S$				4.1×10^5	4.1×10^5	(85)
$(CH_3)_2S_2$				1.0×10^4	1.0×10^4	(85)
CH_3OH ($3682cm^{-1}$)	2.4×10^9	2.4×10^9	(63)			
		2.6×10^8	(65)			
CH_3CH_2OH	1.9×10^9	1.9×10^9	(56)			

repulsive interactions. Braithwaite, Davidson and Ogryzlo[89,72,82] have calculated the contribution of specific long range interactions and conclude that both long and short range interactions contribute significantly to the quenching process. Both models stress the importance of processes in which there is near resonance between the electronic energy lost by $O_2(^1\Sigma_g^+)$ and the vibrational energy gained by the quencher and the oxygen molecule. The rate constants for quenching by simple diatomic molecules, calculated using these models are qualitatively correct, but tend to be slightly lower than observed experimentally; both models quite spectacularly fail to predict the rate of quenching by oxygen itself.

In contrast with these workers, Thomas and Thrush[90] have studied the distribution of energy among the vibrational modes of the products. They find a much broader distribution of energy than expected by Abrahamson and by Ogryzlo; analysis of their results by statistical theory gives a common linear surprisal plot for the quenching of both $O_2(^1\Sigma_g^+)$ and $O_2(^1\Delta_g)$ by H_2O, D_2O, C_2H_2, NH_3, N_2O, CO_2, NO, CO, HCl and DCl. Although the surprisal analysis shows that the energy released on quenching is much more likely to appear as vibrational energy of the products than would be expected on a purely statistical basis, their results show that resonant energy transfer is not important. On the basis of these results, Thomas and Thrush suggest that $O_2(^1\Sigma_g^+)$ and $O_2(^1\Delta_g)$ are quenched by a common, non-specific mechanism, probably on the repulsive part of the intermolecular potential. They postulate that, in a few cases such as the energy pooling reaction, specific, near resonant long range interactions may sometimes occur. Such issues will be clarified only by further measurements of the temperature dependence of reaction rates and of the distribution of energy amongst the product molecules.

It is interesting to note that the collisional quenching of singlet molecular oxygen in solution has been successfully interpreted[45] by the simplest of models assuming resonant energy transfer. The rate of deactivation (Table 1.2) depends solely on the intensity of absorption by the solvent at the wavelengths corresponding to the transitions

1270nm : $O_2(^1\Delta_g) \rightarrow O_2(^3\Sigma_g^-)(v=0)$ (1.4)

1590nm : $O_2(^1\Delta_g) \rightarrow O_2(^3\Sigma_g^-)(v=1)$ (1.34)

2120nm : $O_2(^1\Delta_g) \rightarrow O_2(^3\Sigma_g^-)(v=2)$ (1.35)

and

1920nm : $O_2(^1\Sigma_g^+) \rightarrow O_2(^1\Delta_g)(v=0)$ (1.36)

Little or no dependence on solvent polarity is observed, and the lifetime of $O_2(^1\Delta_g)$ is only about an order of magnitude below that observed in the gaseous phase.

(iii) Electronic Energy Transfer

The energy pooling reaction has been mentioned earlier;

$$O_2(^1\Delta_g) + O_2(^1\Delta_g) \rightarrow O_2(^3\Sigma_g^-) + O_2(^1\Sigma_g^+) \quad (1.13)$$

it is one of a number of unusual reactions between $O_2(^1\Delta_g)$ and other low lying excited species. The most satisfactory estimate of the rate of this reaction[92] is $1.22 \pm 0.3 \times 10^4$ dm^3 mole^{-1} s^{-1}. Schurath[93] has shown that it produces $O_2(^1\Sigma_g^+)$ preferentially with two quanta of vibrational energy, and that the relative probabilities of formation of $O_2(^1\Sigma_g^+)(v=0)$ and $O_2(^1\Sigma_g^+)(v=1)$ are roughly 0.5 and 0.02. This has led to the suggestion of Thrush mentioned earlier that specific long range interactions may be significant in this reaction. The rate of vibrational relaxation of $O_2(^1\Sigma_g^+)(v=2)$ to $O_2(^1\Sigma_g^+)(v=0)$ is very large (5×10^8 dm^3 mole^{-1} s^{-1}) and consequently the observed band intensities for the transition

$$O_2(^1\Sigma_g^+) \rightarrow O_2(^3\Sigma_g^-) + h\nu(762nm) \quad (1.3)$$

TABLE 1.2.

Absolute Rate Constants for the Deactivation of $O_2(^1\Delta_g)$ in Various Solvents

Solvent	K_q ($dm^3\ mole^{-1} s^{-1}$)	$\tau = {}^1/K_q$ (μs)	Solvent absorption in 1cm cell O.D. 1270nm	O.D. 1590nm
H_2O	5.0×10^5	2	0.47	3.4
D_2O	5.0×10^4	20	0.06	0.27
CH_3COCH_3	3.9×10^4	26	0.015	0.08
CD_3COCD_3	3.9×10^4	26	0.002	0.13
CH_3OH	1.4×10^5	7	0.18	3.9
C_2H_5OH	8.3×10^4	12	0.14	2.0
C_6H_{12}	6.1×10^4	17	0.09	0.08
C_6H_6	4.2×10^4	24	0.009	0.11
CH_3CN	3.3×10^4	30	0.016	0.14
$CHCl_3$	1.7×10^4	60	0.002	0.01
CS_2	5.0×10^3	200	< 0.0005	0.00
CCl_4	1.4×10^3	700	< 0.0005	0.00
D_2O:CH_3OH, 1:1	9.1×10^4	11	0.10	1.0
D_2O:CD_3OD, 1:1	2.9×10^4	35	0.03	0.30

are very nearly that expected for thermal equilibrium except in the presence of high concentrations of strong electronic quenchers.

Jones and Bayes[94] have shown that the spin allowed electronic energy exchange reaction

$$^{32}O_2(^1\Delta_g) + {}^{36}O_2(^3\Sigma_g^-) \rightleftharpoons {}^{32}O_2(^3\Sigma_g^-) + {}^{36}O_2(^1\Delta_g) \qquad (1.37)$$

is extremely fast, occurring in at least one in ten hard sphere collisions. Schurath has proposed that the very rapid vibrational relaxation of $O_2(^1\Sigma_g^+)(v=2)$ takes place by the similar exchange process

$$O_2(^1\Sigma_g^+)(v=2) + O_2(^3\Sigma_g^-) \rightleftharpoons O_2(^3\Sigma_g^-) + O_2(^1\Sigma_g^+)(v=0) \qquad (1.38)$$

In support of this he has shown that $O_2(^1\Sigma_g^+)(v=2)$ is deactivated to $O_2(^1\Sigma_g^+)(v=0)$ far more rapidly than to $O_2(^1\Sigma_g^+)(v=1)$. However, Parker and Ritke[39] have measured the rate of vibrational relaxation of $O_2(^1\Delta_g)(v=1)$ and find that this process is very slow with a rate of $\sim 7 \times 10^2$ ℓ mole^{-1} s^{-1} at 300 K (c.f. the rate of vibrational deactivation of $O_2(^3\Sigma_g^-)(v=1)$ at 300 K is 1.2×10^3 ℓ mole^{-1} s^{-1}). Thus it does not appear that reaction (1.37) contributes significantly to the vibrational relaxation of $O_2(^1\Delta_g)$, and the validity of reaction (1.38) must be open to doubt.

Other electronic energy transfer reactions of this type are rare because few species exist with electronically excited states of energy as low as that of $O_2(^1\Delta_g)$ and $O_2(^1\Sigma_g^+)$. The reactions of singlet molecular oxygen with iodine, initially reported by Ogryzlo[95], have been studied by Thrush[96] and the following steps identified:

$$I_2(^1\Sigma_g^+) + O_2(^1\Sigma_g^+) \rightarrow I_2(^3\pi_u) + O_2(^3\Sigma_g^-) \qquad (1.39)$$

$$I_2(^3\pi_u) + O_2(^1\Delta_g) \rightarrow I_2(^3\pi_{ou}^+) + O_2(^3\Sigma_g^-) \qquad (1.40)$$

Intense yellow chemiluminescence results from the radiative decay of $I_2(^3\pi_{ou}^+)$. Atomic iodine is also formed in the system[97] and undergoes further reactions

$$I + O_2(^1\Delta_g) \rightarrow I(^2P_{\frac{1}{2}}) + O_2(^3\Sigma_g^-) \quad (1.41)$$

$$I(^2P_{\frac{1}{2}}) + O_2(^1\Delta_g) \rightarrow I + O_2(^1\Sigma_g^+) \quad (1.42)$$

$$I(^2P_{\frac{1}{2}}) \rightarrow I + h\nu \quad . \quad (1.43)$$

$$I(^2P_{\frac{1}{2}}) + O_2(^3\Sigma_g^-) \rightarrow I + O_2(^1\Delta_g) \quad (1.44)$$

Ogryzlo also reported the reaction[95]

$$O_2(^1\Delta_g) + O_2(^1\Sigma_g^+) + {}^2NO_2 \rightarrow 2O_2(^3\Sigma_g^-) + {}^2NO_2^* \quad (1.45)$$

but only the reverse reaction[50]

$${}^2NO_2^* + O_2(^3\Sigma_g^-) \rightarrow {}^2NO_2 + O_2(^1\Delta_g) \quad (1.26)$$

and the reaction[51]

$${}^2NO_2^* + O_2(^1\Delta_g) \qquad {}^2NO_2 + O_2(^1\Sigma_g^+) \quad (1.27)$$

have been studied in depth. The reaction with ${}^2NO_2^*$ is very much faster than any quenching reaction of $O_2(^1\Delta_g)$ (rate 2-6 x 10^{10} dm^3 $mole^{-1}$ s^{-1}).

The formation of $O_2(^1\Delta_g)$ and $O_2(^1\Sigma_g^+)$ by energy transfer from triplet excited states has been mentioned in section 1.2.2. In systems where high concentrations of $O_2(^1\Delta_g)$ and excited triplets are present, $O_2(^1\Delta_g)$ is quenched very rapidly by the spin allowed process[43]

$$^3(^3M + {}^1\Delta_g) \rightarrow {}^3(M^+ + O_2^-) \quad (1.46)$$

Experiments using naphthalene and quinoxaline as triplet sensitizers[98] have shown that this reaction is very nearly diffusion controlled.

1.3. The Shock Tube

1.3.1. Basic Principles

The shock tube is a heater. Its usefulness to the chemist comes from its ability to produce very high temperatures in a gas almost instantaneously (rise time typically $\sim 10^{7}$-10^{-9}s [3,99]). Hence it is possible to study the temperature dependence of chemical reactions and molecular relaxation processes by taking a system initially at equilibrium, disturbing this equilibrium by raising the temperature and observing the relaxation of the system to the equilibrium at the new temperature. The principal disadvantages of the shock tube in this respect are the very limited time for which measurements can be made (10^{-3}-10^{-4}s), and the inherently poor precision of all measurements. For this reason, a well designed furnace, although more costly, is probably more suitable for the study of chemical equilibria at elevated temperatures; such measurements, however, give us little or no information about the mechanisms of the processes involved.

A simple shock tube is shown in figure (1.6). The driver section contains gas at a high pressure and the test section the gas under study, usually at a pressure[100] of 0.1-1.5 KN m^{-2}. When the diaphragm separating the two sections bursts, a shock wave is propagated through the test gas. The formation of a plane shock wave has been described by Becker[101] in terms of a piston (i.e. the driver gas) accelerating into a gas in small increments until a constant velocity is reached. The first increment causes a weak compression wave that travels through the test gas at the velocity of sound. The gas is heated by the adiabatic compression and consequently the next compression wave travels through the gas at a slightly greater velocity (the velocity of sound in the heated gas). Eventually a situation is reached where a series of compression waves are moving through the test gas, each at a slightly greater velocity than its

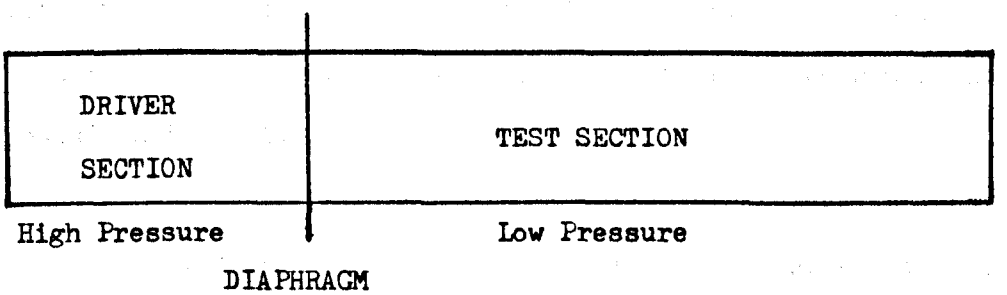

FIGURE 1.6 A Simple Shock Tube

predecessor. Naturally these compression waves cannot overtake each other; instead they coalesce into a steep shock front moving at a velocity greater than the velocity of sound in and thus propagating into the gas before the shock front. The temperature and density gradients across this shock front are considerable. The heated gas behind the shock front moves at the velocity of the piston (in reality the contact surface between the driver and test gases). The shock wave travels more rapidly than the contact surface so that the column of heated gas increases continuously in length.

At the same time as the formation of compression waves in front of the contact surface, expansion waves are propagated backwards into the driver gas. As the adiabatic expansion cools the gas, each successive wave will move at a slightly lower velocity than its predecessor, and consequently, rather than coalescing to a single wave front, they will spread out. This region is known as the rarefaction fan. The rarefaction fan is reflected at the end of the driver section and then moves in the direction of the expanding gas at a velocity greater than that of the shock front; the shock wave ends when the rarefaction fan meets the shock front[102]. In an ideal shock the maximum time for which observations may be made at an observation station is the time it takes the column of heated gas to pass by; this column is longest, and hence the flow duration is at a maximum at the point immediately before the expansion fan meets the contact surface (figure 1.7).

Although the formation of a shock wave has been described as a series of adiabatic compressions, the process is not reversible and there is an increase in entropy[103-105]. The shock compression produces a much greater temperature and a lower density than an isentropic compression of the same strength (of course, this is exactly what is desired.).

The conditions behind the shock front are described in a number of

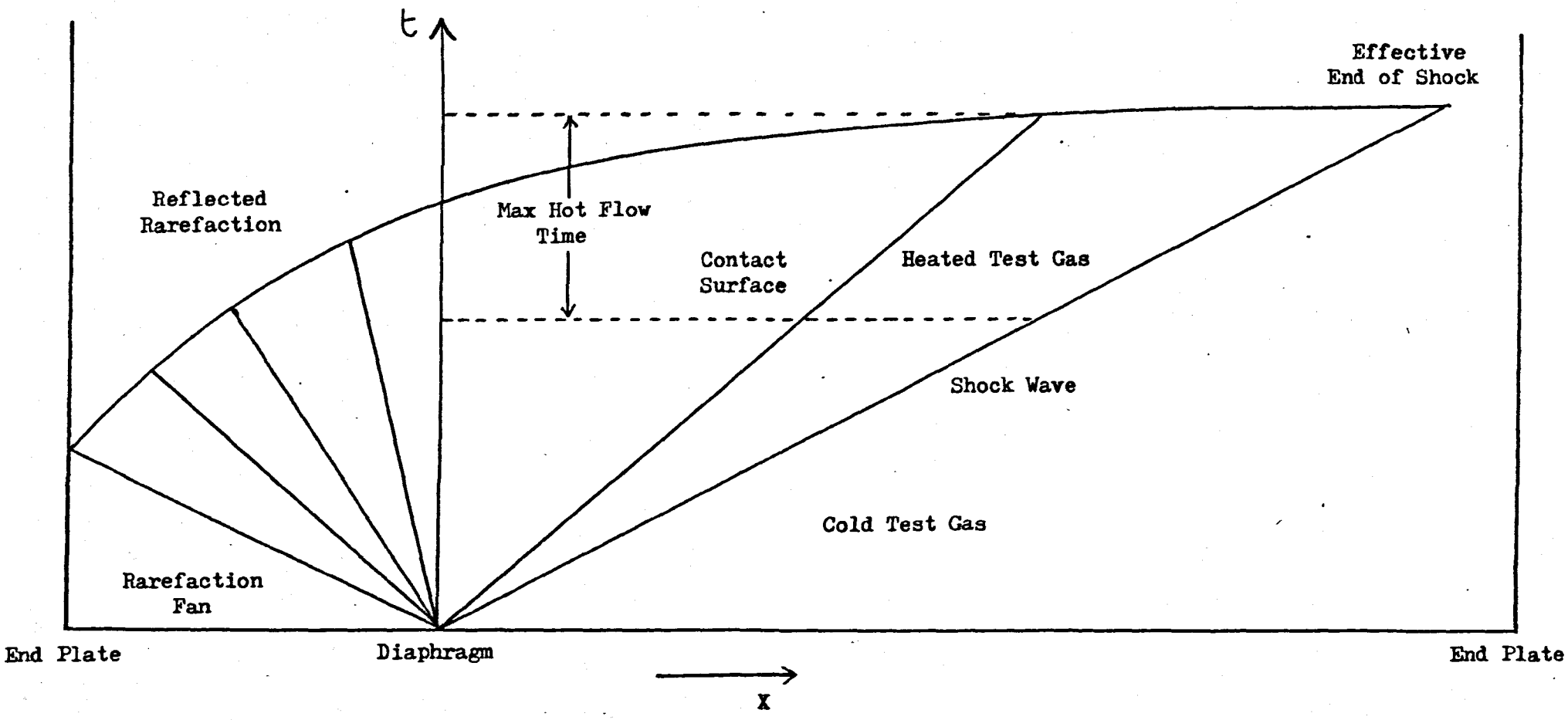

FIGURE 1.7 X-t Diagram of Gas Flows in the Shock Tube

standard texts[100,102,106-109]. The shock parameters are conveniently obtained using shock-fixed coordinates in which the shock front is considered to be at rest (figure 1.8). The basic equations relating the conditions of density, ρ, temperature, T, and pressure, P, before and behind the shock front, are derived assuming that the mass, momentum and energy of the gas are conserved as it passes through the shock front. The conservation equations, arranged in a relevant form, are:

Mass: $$\rho_1 U_1 = \rho_2 U_2 \tag{1.47}$$

Momentum: $$P_1 + \rho_1 U_1^2 = P_2 + \rho_2 U_2^2 \tag{1.48}$$

Energy: $$H_1 + \tfrac{1}{2}U_1^2 = H_2 + \tfrac{1}{2}U_2^2 \tag{1.49}$$

(the suffixes 1 and 2 refer to conditions in the gas before and behind the shock front respectively; U is the velocity of the gas in shock-fixed coordinates, and H the enthalpy.)

Equations (1.47) - (1.49) contain eight unknowns: the enthalpy, H, may be expressed as a function of temperature, f(T), and thus by measuring the initial conditions, P_1, ρ_1 and T_1, only five unknowns are left. Three of these are related by the equation of state for the gas; at the low pressures used in shock tube experiments, the ideal gas relation is usually sufficient

$$P = \rho r T \tag{1.50}$$

($r = R/M$, where R is the gas constant and M the molecular weight of the gas). The equations allow three of the remaining four independent variables to be expressed in terms of any one other; it is the usual practice to relate them to the shock velocity, U_1, which is reasonably easily measured.

When estimating the enthalpy of a real gas under the conditions behind the shock front, it is necessary to take into account the large change in population of its vibrational energy levels with temperature. Immediately after the shock front has passed, the population is unchanged from that at room temperature, and the gas is said to be "frozen"; the

(a) Laboratory Coordinates

Shock Front at Velocity U

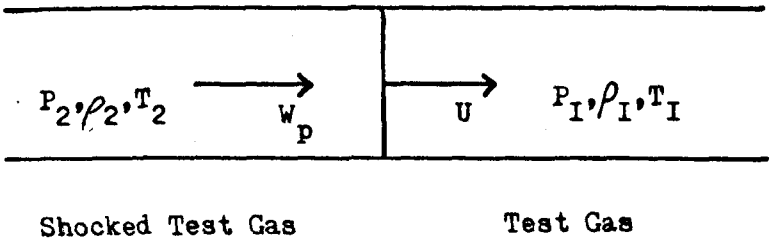

(b) Shock Coordinates

Shock Front at Rest

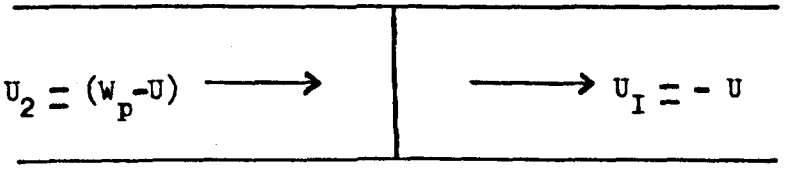

FIGURE 1.8 Coordinate Systems Used for the Shock Equations

enthalpy change is then given by:

$$H_2 - H_1 = Cp(T_2 - T_1) \qquad (1.51)$$

where Cp is the specific heat at constant pressure, and is independent of temperature. When the population of the vibrational levels of the shock-heated gas reaches equilibrium, the gas is "relaxed", and its enthalpy is no longer a simple function of the temperature. It is then necessary to know the function, H = f(T), for the individual gas.

For some years now, a simple computer program, written by Millikan[110,111], has been used in this department to calculate the shock parameters in gases where vibrational relaxation is complete. Initially, the ideal relations are used to calculate the conditions behind the shock front in the frozen gas. The function, H = f(T), which is obtained by polynomical curve fitting to the enthalpy data in the J.A.N.A.F. tables[112], is then used to calculate the enthalpy of the relaxed gas at that temperature. The difference in these values is used to make new estimates of the temperature, density and pressure behind the shock front. The enthalpy of the gas at this new temperature is then calculated as part of an iterative loop which ends when the calculated conditions behind the shock front are sufficiently self-consistent.

1.3.2. General Applications

The applications of the shock tube are many and varied. Apart from the study of high temperature chemical reactions, it has been used widely in physics to study gas flows and boundary layer formation at surfaces, and plasma flows[113] (generated by very strong shocks). In gas dynamic lasers (which are at present the most powerful type of continuous wave laser), the population inversion necessary for laser action is created by the non-equilibrium collision processes which occur in the rapid supersonic expansion of a hot gas; a shock tube is often used

to produce the heated gas under controlled conditions[114].

Chemists have used the shock tube to study reactions in which species stable at room temperature are decomposed by heat (both the kinetics of the processes and the nature of the products are of interest) and to study the metastable species generated in the heated gas[113]. The shock tube has also been used widely to study the temperature dependence of the vibrational relaxation of a large number of small molecules[109]; it produces the high temperature required sufficiently rapidly for the vibrational relaxation to be observed, usually by monitoring the changes in density behind the shock front. The experimental results are analysed, assuming the Landau-Teller model for a harmonic oscillator[115]; the rates of vibrational relaxation of simple molecules are found to vary with the absolute temperature as

$$\log \tau = AT^{-1/3} + B \qquad (1.52)$$

where τ is the relaxation time of the gas. A number of workers have derived this relation theoretically, the most widely used model being that of Swartz, Slawsky and Herzfeld[116] (SSH theory). Borrell[109] has listed the rates of vibrational relaxation of many molecules measured over the temperature range 300-5000 K.

The reactions of metastable species formed in the shock heated gas are less amenable to study for a number of reasons: the rate of formation of the metastable species has to be considerably greater than the rates of its reactions at that temperature; the concentration is frequently uncertain if the formation reaction is not complete; other unwanted species formed along with those of interest may well affect the kinetics of the system. Nevertheless, several systems have been studied; an example of some relevance to the present work is the study of the vibrational relaxation of small molecules in the presence of atomic oxygen generated by the thermal decomposition of ozone

$$O_3 + M \rightarrow O\cdot + O_2 + M \qquad (1.53)$$

The rates of relaxation of O_2[117], and CO and CO_2[118] have been shown by such experiments to be 2-3 orders of magnitude greater when dilute in oxygen atoms than the rate of self relaxation.

The problems associated with such measurements are largely avoided if the metastable species are generated prior to the shock. Several techniques could be suitable for such experiments: laser excitation of the ground state, flash photolysis, the electric discharge and chemical reactions. Flash photolysis experiments suffer from the serious drawback that the temperature of the gas, immediately prior to the shock, but after the flash, is most uncertain; such measurements must of necessity include a measurement of the temperature behind the shock front. Presumably, laser excitation will have similar disadvantages, although there should be fewer problems with side reactions. The electric discharge and most chemical reactions do heat the test gas, but the effects should be far less severe. The lifetime of the metastable species is an important factor in all such experiments; a system in which it is formed continuously by chemical reaction in a gas flow has obvious advantages over the other techniques for the study of molecules with a very short lifetime.

1.3.3. Discharge flow shock tube experiments

Surprisingly few experiments have been described in which the metastable species are formed prior to the shock; apart from a few unsatisfactory flash photolysis measurements, in all cases reported the excited states have been generated by an electrical discharge. Hartunian[119] used a "glow discharge shock tube" as far back as 1966 to study the chemiluminescent reactions

$$NO + O\cdot \rightarrow NO_2 + h\nu \qquad (1.54)$$

$$CO + O\cdot \rightarrow CO_2 + h\nu \qquad (1.55)$$

A radio frequency discharge was used to generate atomic oxygen inside the shock tube close to the diaphragm. A flowing gas system was used; the NO or CO was admitted a short distance downstream from the discharge and the flowing gases were pumped out of the shock tube at the far end from the diaphragm.

Gross[120-122] used the apparatus built by Hartunian to study other chemiluminescent "afterglow" reactions:

$$N\bullet + N\bullet \rightarrow N_2 + h\nu \qquad (1.56)$$

$$N\bullet + O\bullet \rightarrow NO + h\nu \text{ (several bands)} \qquad (1.57)$$

$$SO\bullet + O\bullet \rightarrow SO_2 + h\nu \qquad (1.58)$$

However, experiments using this apparently promising technique have since been reported only by Glass[3] (1973) and as preliminary studies by A. Brittain and P.M. Borrell on an atomic nitrogen discharge[123] (1970). Using a tube very similar to that described above, Glass showed, primarily for his own satisfaction, that the structure of the shock wave in the flowing discharge tube is no different from that in a static system. He observed a shock attenuation of less than 1% and measured the thickness of the shock front to be 0.2-0.25mm in both flowing and static systems. He then repeated the measurements of the vibrational relaxation of O_2 in the presence of atomic oxygen described earlier, using atomic oxygen formed in the rf discharge and following the relaxation by a conventional laser schlieren technique. His measurements agreed quite well with those obtained by Kiefer and Lutz over the temperature range 1000-3500 K using more conventional techniques. Although Glass is still using discharge flow systems at room temperature to study vibrational relaxation in the presence of atomic species[124], he has reported no further high temperature studies.

A discharge flow shock tube should be very suitable for the study of the reactions of singlet molecular oxygen at high temperatures.

Because of its high stability towards deactivation, $O_2(^1\Delta_g)$ need not be generated inside the tube itself; this reduces the possibility of heating effects and shock irregularities caused by the discharge and by the admission of reactants midway down the shock tube still further. $O_2(^1\Sigma_g^+)$ is formed continuously inside the shock tube by the energy pooling reaction. This is an example of a system in which the intermediate is formed by chemical reaction; because the lifetime of $O_2(^1\Sigma_g^+)$ is shorter than that of $O_2(^1\Delta_g)$ by a factor of 10^2-10^5, any other preparative technique would require it to be generated inside the shock tube and studied within a very short time of formation.

1.4. Aims of the present work

This thesis describes the construction and testing of the discharge flow shock tube designed to study the kinetics of quenching of singlet molecular oxygen. The flexibility of this system has been tested by measuring the rates of collisonal deactivation of $O_2(^1\Sigma_g^+)$ both in pure O_2 and in O_2/N_2 mixtures, and by studying the dimol emission and the energy pooling reaction, over a wide range of temperature. In principle, such a system should be suitable for the study of other excited species; the results of these experiments should allow evaluation of the conditions in which the discharge flow shock tube can successfully be used.

2. EXPERIMENTAL

2.1. Introduction

This chapter describes the apparatus and experimental techniques used in these experiments to study the collisional reactions of singlet molecular oxygen, both in pure oxygen and in oxygen/nitrogen mixtures.

In the discharge flow shock tube, the test section of the shock tube is also the observation section of the discharge flow system, and the apparatus may be used for discharge flow experiments at room temperature. However, as a matter of convenience, the designs of the shock tube and the discharge flow apparatus are discussed separately in sections 2.2. and 2.3.

2.2. The Shock Tube

The shock tube used in these experiments comprises a pyrex glass test section of length approximately 5m and a stainless steel driver section of length 1.25m, as shown in figure 2.1. The tube is of cylindrical cross section (diameter 51mm). The diaphragm separating the two sections is burst simply by raising the pressure of the driver gas.

The shock tube (overall length 6m) is built on a framework of Handyangle sections and is about 1½m above floor level. The observation station, at which photomultiplier detectors are positioned, is approximately 4m from the diaphragm.

2.2.1. Shock Tube Design

Equations for calculation of the optimum lengths of test and driver sections in an ideal shock tube have been available for many years,[100] but workers in the sixties have suggested that the non idealities of shock flows place a significant limit on their usefulness.[125]

The hot flow duration of a shock is the time during which observations may be made. It is the period between the arrival of the shock front at the observation station and the subsequent arrival of the contact surface. This time increases as the observation station moves away from the diaphragm, but for real shocks eventually reaches a limit dependent on the tube cross section. The tube should be designed so that this time during which the high temperature system may be studied is as long as possible, while bearing in mind the facts that the hot flow time cannot be increased indefinitely by increasing the distance from diaphragm to observation station, and that there is always a physical limit to the tube dimensions.

The rarefaction fan (chapter 1) will overtake the contact surface before the shock wave comes to an end. This will give rise to serious

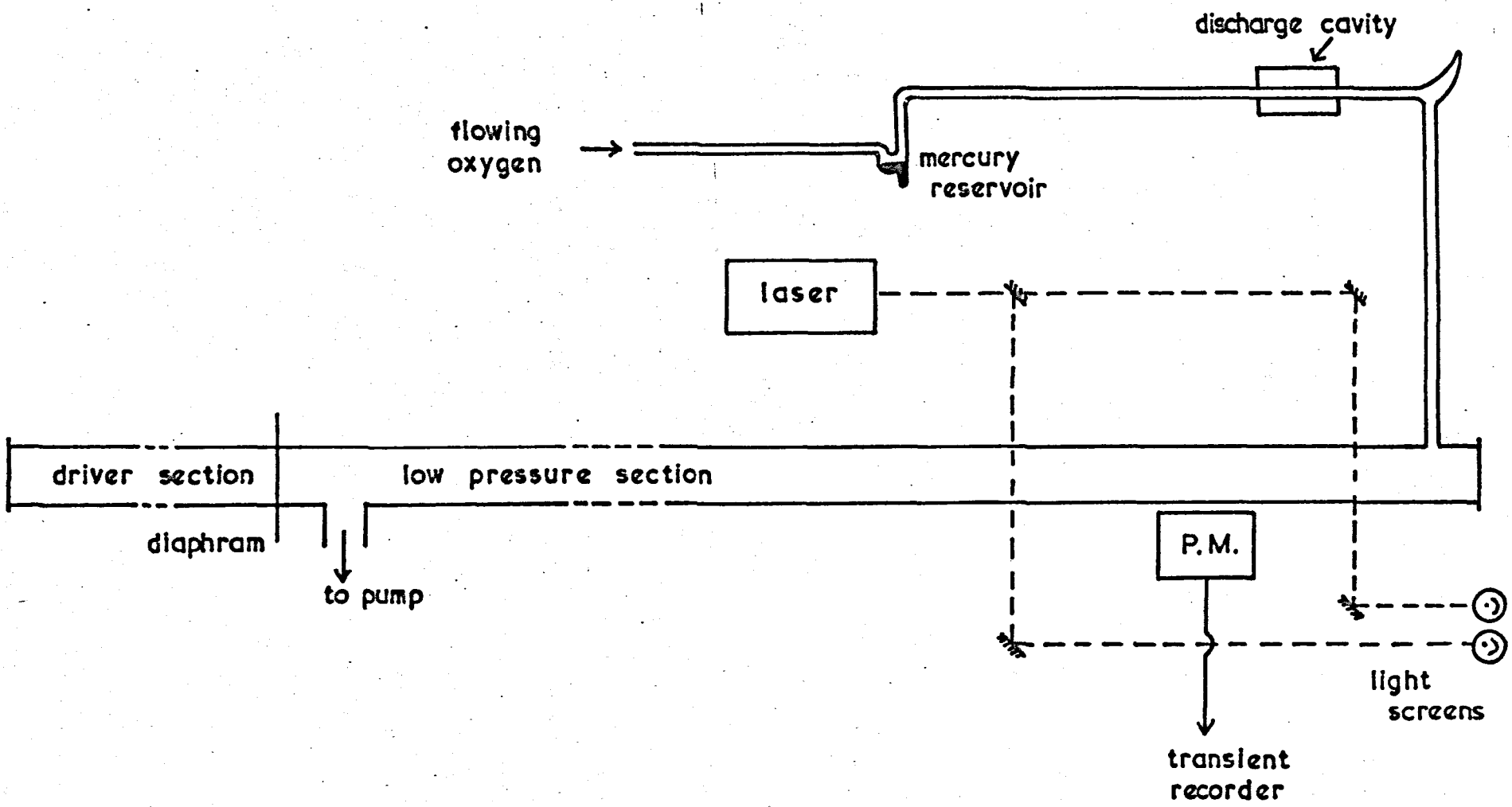

Figure 2.1 Discharge Flow Shock Tube Apparatus

changes in the conditions in the heated test gas and should not occur until after the contact surface has passed the observation station. The shock duration may be increased by lengthening the driver section.

The observation station should not be too close to the end of the shock tube, because the reflected shock will reduce the period of hot flow for which useful measurements can be made.

The equations relating the duration of the shock wave to the shock velocity, the length of the driver section and the nature of the test gas are outlined in Appendix A.1. Our apparatus has a driver section of length 1.25m; a nitrogen driver is used to produce slow shocks into oxygen of velocity 0.85-0.95 kms^{-1} and helium is used for faster shocks (velocity 1.4-1.7 kms^{-1}). The equations predict that slow shocks will effectively end 6.9-8.4m from the diaphragm; fast shocks have a much shorter duration and should end after travelling only 3.0-3.75m.

These calculations would seem to suggest that for satisfactory measurements over the entire range of shock velocities, the observation station should be placed no more than 3m from the diaphragm. However, in reality the shock wave has certainly not come to an end even at a distance of 4m from the diaphragm, and in consequence, the observation station is placed at this position along the shock tube test section. The ideal flow calculations often give a poor estimate of the minimum tube dimensions and should not be taken too literally.

2.2.2. The Test Section

The test section is constructed from QVF piping. This tubing is very convenient for shock tube systems as sections are easily connected together using standard couplings and PTFE gaskets (figure 2.2[126]). Although a metal test section has structural advantages over a glass tube and allows faster shocks to be studied, it would not be suitable for the study of the excited molecules as their rate of removal at a metal surface is very high. The glass tube has the added advantage of allowing

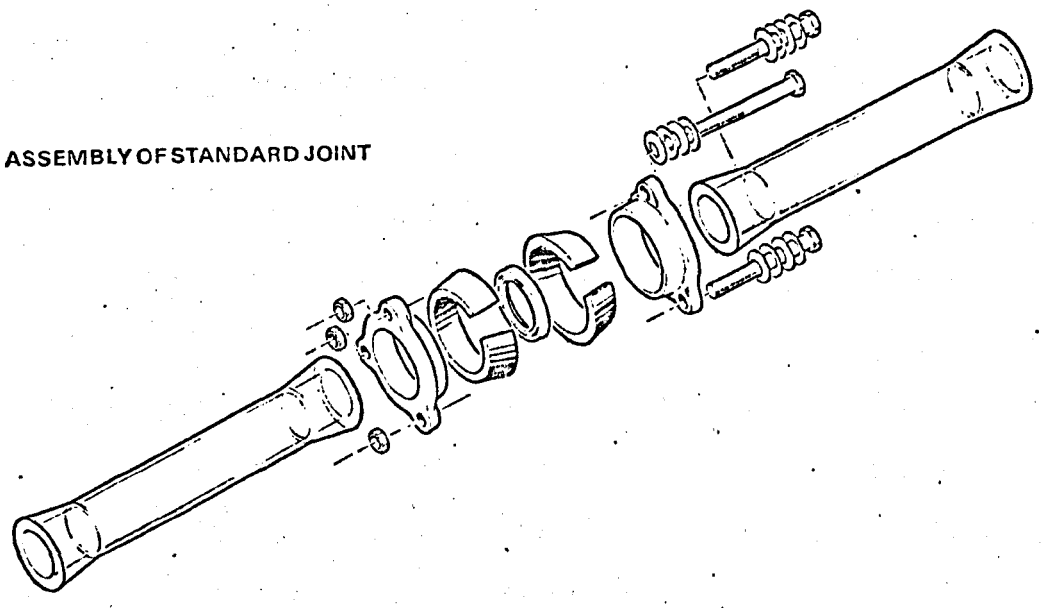

FIGURE 2.2 Standard Q.V.F. Coupling (Taken from Corning Handbook)

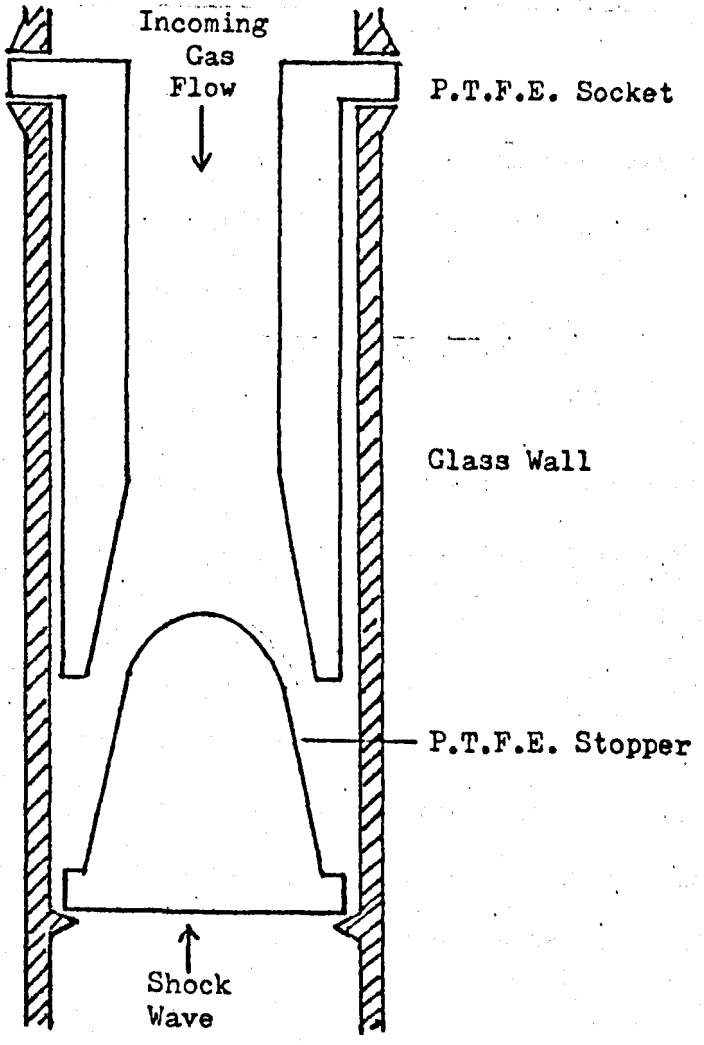

FIGURE 2.3 Gas Inlet Valve

observations to be made at any point along the tube (as in a standard discharge flow or flowing afterglow system at room temperature).

Irregularities in the wall of a shock tube, such as will occur at a join between two sections unless they are perfectly aligned, may give rise to a Mach line or standing shock in the main gas flow.[100] To minimise the number of joins, the main part of the test section (length 4.5m) was specially manufactured from a single length of piping. Short QVF sections with sidearms are joined at each end and allow the gases under study to enter and leave the test section.

The test section is mounted securely on QVF rubber supports attached to the framework. These supports absorb the considerable forces produced along the axis of a shock tube when the diaphragm is burst. The end of the test section is sealed by a brass plate connected using a QVF coupling; QVF glass tube closures are not used as they are scored and increasingly weakened in each shock by fragments of the diaphragm material.

The test gases may enter the shock tube test section at either end and early experiments were performed using both arrangements. The present configuration with the gases entering at the end farthest from the diaphragm was chosen because it gave a significantly greater concentration of excited species at the observation station. A simple but effective valve (figure 2.3) in the gas inlet closes when reached by the shock (probably the contact surface), preventing fragments of diaphragm from being blown into the discharge section. The valve was constructed from parts of a broken QVF flow control valve.

The flowing gas is pumped out of the test section at the diaphragm end at a rate controlled by a QVF flow control valve. The pump is an Edwards Model 1SC 3000 capable of producing a high rate of flow. It is situated in the basement of the department and connected by about 30m of 25mm glass and copper tubing.

The test section is left under vacuum when not in use; overnight leakage of air may be as much as 15mm Hg (2KN m^{-2}). This corresponds to a leakage flow rate of $\sim 5 \times 10^{-3}$ $m\ell s^{-1}$ at atmospheric pressure, and, with the test gas flow rate between 15-30 $m\ell s^{-1}$, only about 0.02% of the gas in the test section will result from this leakage. This figure is certainly not significant when the test gases are oxygen and nitrogen.

2.2.3. The Driver Section

The driver section of the shock tube is mounted on rollers, both to absorb the recoil when the shock is fired, and to facilitate the changing of the diaphragm. A bank of Edwards Speedivalve high pressure taps allows admission of a selection of driver gases from cylinders equipped with Edwards high pressure heads (type OR14), venting of the driver section to the atmosphere, or evacuation using a small Edwards rotary pump. Nylon tubing (6mm or 16mm O.D.) together with the appropriate Simplifix couplings is used for all high pressure connections.

Gases entering the driver section pass through a copper tube (length 1m, diameter 5cm) filled with a mixture of molecular sieves 4a and 13X. These molecular sieves absorb water, small organic molecules, and straight and branched chain hydrocarbons up to about C14 [127]; the latter are important as oil in the driver gas is a major source of contamination in the test section.

The driver section is closed at one end by a stainless steel plate and 'O' ring seal, and at the other end it is separated from the test section by the diaphragm.

2.2.4. The Diaphragm

The diaphragm is sandwiched between two O rings attached to the driver and test section (figure 2.4). It is secured in position by hand-tightening the butterfly nuts.

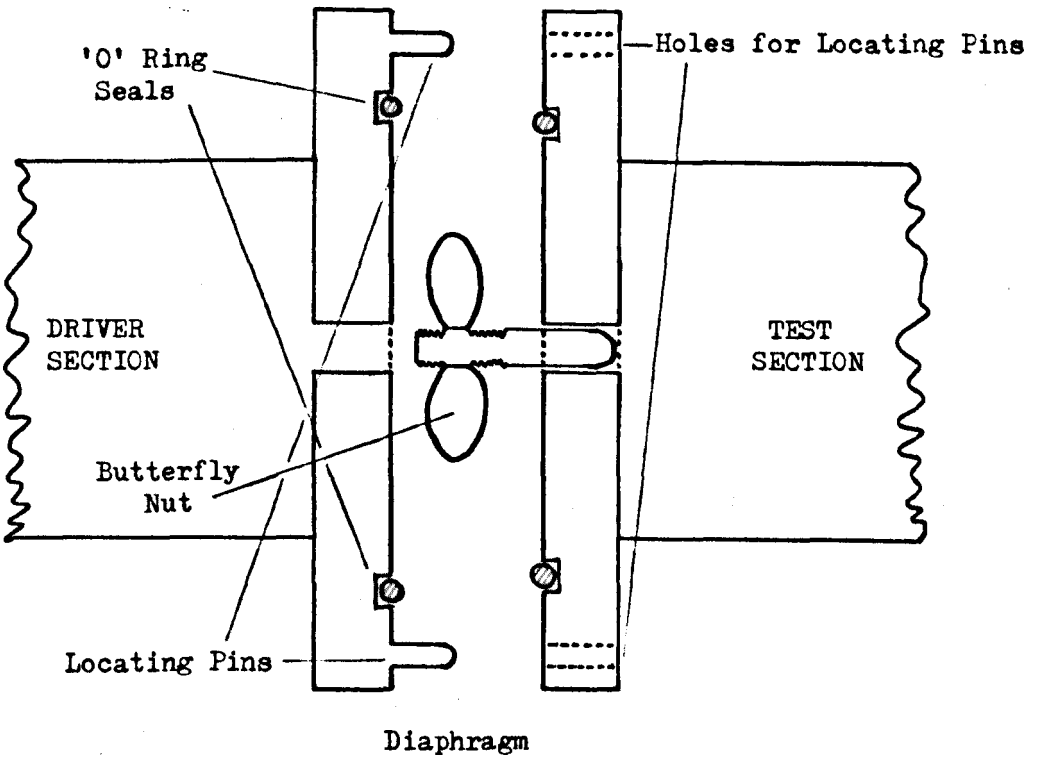

FIGURE 2.4 Construction of Diaphragm Mounting

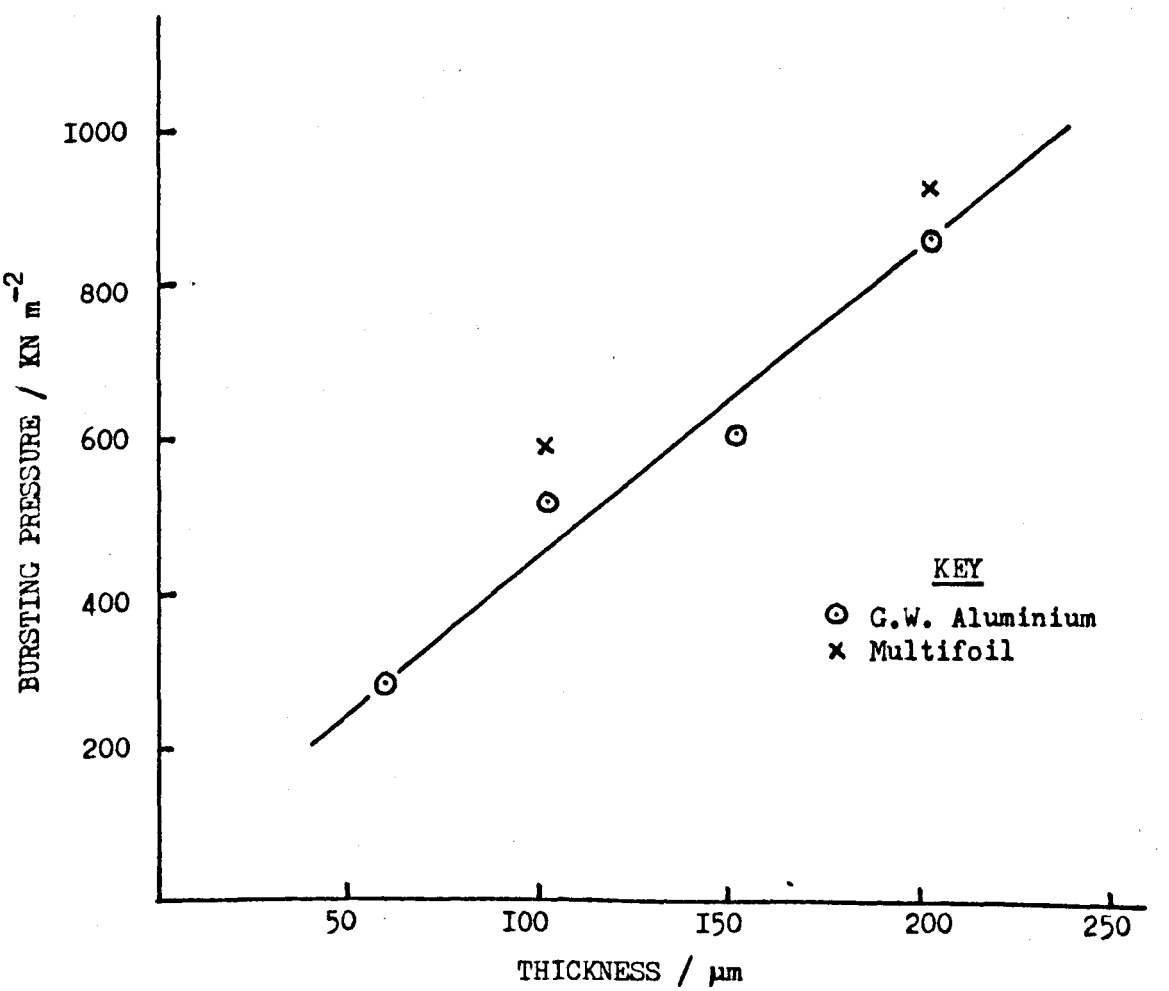

FIGURE 2.5 Diaphragm Bursting Pressures

The diaphragm mounting is of a type used in this laboratory for some years,[99,128] but, although simple and convenient, a number of problems were experienced with it. At pressures in the driver section above 400 KNm^{-2}, gas leaks from the driver section to the atmosphere (fortunately the test section does not leak). This problem was partially solved by changing the 'O' ring on the low pressure side to one of a slightly smaller diameter than that on the driver side, so the diaphragm was squashed between the two, but the system still leaks frequently when using multiple thicknesses of diaphragm material.

The many diaphragm materials available have been reviewed by a number of authors[100,102]; it appears that the ideal diaphragm should burst cleanly without tearing and fold or petal back as much as possible to allow the driver gas to flow out freely. Some authors suggest scribing the diaphragm along two diameters at right angles to promote clean bursting, but Gaydon and Hurle[100] say this is ineffective for metals softer than steel. For a slow, non-ideal burst the shock front will take an appreciable time to build up and this may result in a reduced hot flow time. However, this is not of particular importance in these experiments.

Both aluminium foil and Melinex diaphragms have been used in this laboratory in the past; most workers[99,128] have preferred aluminium foil because Gaydon and Hurle suggest that non-metallic diaphragms are unsuitable for spectroscopic work as they tend to burn and produce impurity spectra. Melinex also tends to split rather than burst cleanly and the flow of driver gas is probably severely restricted. Although there was no evidence of Melinex burning in our system where the transient temperatures rarely exceed 1600 K, aluminium foil was chosen for these experiments. The author believes that the choice of diaphragm material is not of great importance for this work.

Two thicknesses of aluminium foil (50 μm and 150 μm) were available. Using combinations of these it was possible to perform shocks using diaphragm bursting pressures of 275-850 KNm^{-2}. The pressure required to burst the diaphragm is roughly proportional to the diaphragm thickness (figure 2.5) but may vary with the source of the material. Recently several other thicknesses of aluminium have been obtained and tested; diaphragm leakage was not significant even at 950 KNm^{-2} when a suitable single thickness of aluminium was used.

2.2.5. Driver Gases

The shock velocity obtained for a particular diaphragm pressure ratio, P_4/P_1 (where P_4 is the bursting pressure in the driver section and P_1 the pressure in the test section prior to the shock), are calculated from the ideal shock relations outlined in chapter 1, in Appendix A.2.

Figure 2.6 shows the range of shock velocities produced by bursting several driver gases into oxygen. Safety and practical considerations limit the diaphragm bursting pressures; for a typical pressure (P_1) of 6.5mm Hg (0.87 KNm^{-2}) and a diaphragm bursting pressure (P_4) of 275-850 KNm^{-2}, $\log_{10}(P_4/P_1)$ varies between 2.5 and 3.0.

Although the fastest shocks for a given diaphragm pressure ratio are produced using hydrogen as the driver gas, this was ruled out as there is some danger of explosion when driving into oxygen, especially in the presence of an electrical discharge. Consequently the best alternative, helium, is used to produce fast shocks. To extend our range of measurement to low temperatures a nitrogen driver is used to produce shocks of low velocity. The overall temperature range available for study is 600-1600 K. A gap occurs between the temperatures produced by the fastest nitrogen and the slowest helium shock (850-1050 K). Shocks using mixed helium and nitrogen as the driver gas produce

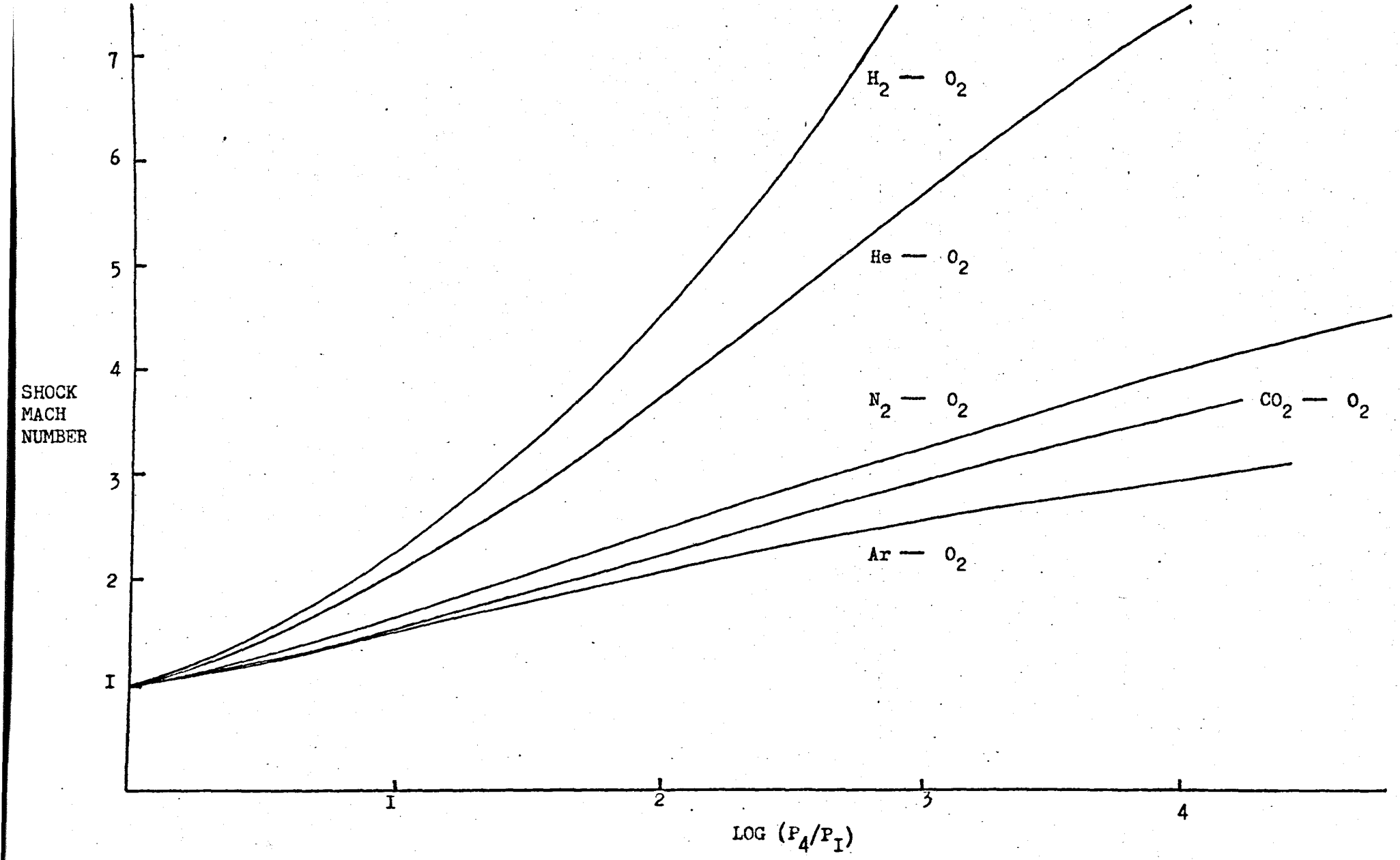

FIGURE 2.6 Shock Velocities from Diaphragm Pressure Ratios

temperatures in this region, but the inevitably imperfect mixing of the driver gases produces some unusual flow nonuniformities (chapter 5).

The observed shock velocities are only about 10% lower than predicted from the diaphragm pressure ratios; the two are compared in Table 2.1. The predictions of the ideal shock relations are in this case, extremely good; this is in contrast with the observations made in section 2.2.1.

Table 2.1

BURSTING PRESSURE (KN m^{-2})	$LOG_{10}(P_4/P_1)$	SHOCK VELOCITY (Km s^{-1})			
		He DRIVER		N_2 DRIVER	
		CALC	OBS	CALC	OBS
275	2.50	1.56	1.35	0.94	0.87
450	2.71	1.70	1.47	1.00	0.92
655	2.88	1.80	1.55		
850	3.00	1.89	1.65		

2.2.6. Pressure Measurement

Early experiments used Edwards "Speedivac" model CG3 vacuum dial gauges (calibrated for 0-2.7 KNm^{-2}) situated at each end of the test section to measure the pressure of the test gas. These confirmed that there is no significant pressure gradient along the tube, but, after some months use, their accuracy was shown to be remarkably poor and they were replaced by a simple manometer at the diaphragm end of the test section. One arm of this manometer is connected to the test section of the shock

tube and the other is evacuated; diethyl phthalate (density measured by the author to be 1.136×10^3 kgm^3 at 24 ^oC), which has an extremely low vapour pressure at room temperature, is the manometer fluid. The manometer is shut off from the test section immediately before each shock as the fluid is otherwise driven out into the vacuum system.

The pressure in the driver section of the shock tube is measured by a Budenberg dial gauge (0-1400 KNm^{-2} including pressures of less than one atmosphere); a pointer records the pressure at which the diaphragm bursts.

2.2.7. Measurement of the shock velocity

In this work the parameters of density, pressure and temperature behind the shock front are calculated from the measured shock velocity and not measured directly. Direct measurement of density and pressure is practical only in a metal shock tube as the pressure sensitive devices must be embedded in the tube wall;[100] glass tubes have been known to shatter when weakened in this way.[129] The temperature behind the shock front can be measured by a spectroscopic technique, but this is not practical in our system. For an ideal shock this would not matter, but in a real system one is reduced to estimating the changes in these parameters behind the shock front due to non-uniform flow and the finite vibrational relaxation rate of the shocked gas; this is a significant limitation on the precision of any results. Nevertheless, several workers have shown that estimates of the shock conditions from the velocity do agree well with the experimentally measured conditions.[130]

The shock velocity in the observation region is measured by a laser schlieren technique developed in this laboratory some years earlier.[128] A beam of light from a 1.0 mW helium/neon laser (Ferranti GP2) passes through the shock tube at an angle of 87-89^o to the tube and travels along a path of length approximately 5m (being reflected one or

more times in the course of this path) to an EMI 9660B photomultiplier light screen. The photomultiplier light screen operates at 800 V, using a Brandenberg Model 470 EHT supply; the output circuit contains an emitter follower (Venner Electronics). The system is adjusted so that the photomultiplier (the output of which is displayed on an oscilloscope screen) is initially very close to saturation; when the shock is fired the laser beam is deflected by the shock front and the photomultiplier saturates. The pulse in the emission is used to trigger a timing device.

In the present system, three light screens are used; the output from light screen 1 triggers the "start" on two Hewlett Packard Time Interval Units (Model 5263A) and light screens 2 and 3 each trigger a "stop". The time interval meters control digital counters (Venner Electronics Type TSA5536) which record the times for the shock front to travel from light screen 1 to light screen 2 and light screen 3. The accuracy of such measurements, determined by an oven-controlled 2MHz high stability crystal oscillator inside the digital counter, is ± 1μs. As the distance between the light screens is known, two estimates of the shock velocity may be made.

In principle, all three light screens can be operated using one laser and dividing the beam in three by a series of face silvered partially transmitting mirrors (the beam is broadened by refraction if the rear surface of the mirror is used), but this arrangement is not very reliable in practice and two lasers are used (the beam from one of these is divided in two). Presumably a single laser is not suitable because of the reduced intensity and also because of the extent to which the beams are broadened by the many refractions and reflections they undergo on their way to the detector.

It is not entirely certain whether the deflection of the laser beam by the shock front is caused by reflection, refraction, or both.

The calculations of Gutteridge[99] suggested that refraction across the shock front where the density of the test gas changes by a factor of ~ 5 is sufficient to explain the effect, but they have been found to contain large arithmetic errors. When oxygen, initially at 0.87 KNm^{-2}, is present in the test section, the refractive index across the shock front is only about 1.0000087; calculations using Gutteridge's equations show that the deflection of the laser beam, even for a path length of 5m, is only $\sim 3x10^{-2}$mm, and it is most unlikely that this would be detected by the photomultipliers.

Reflection of the laser beam will certainly cause an appreciable deflection - about 17.5cm for an angle of 89° and 52.5cm for an angle of 87° to the shock tube, assuming a path length of 5m. However, the critical angle for total reflection at the shock front is about 89° 45' and only a small proportion of the laser light will be reflected. It may well be that this is enough to trigger the time interval units, or it may be that both refraction and reflection contribute.

What is certain is that the light screens do work, and that even in the worse cases the estimates of shock velocity so obtained agree to ± 0.5%. The lasers are situated too close together for any apparent deceleration or aceleration of the shock to have significance, but some measurements of shock deceleration were made using an extra laser considerably nearer to the diaphragm; the results are discussed in chapter 5.

It is most important for the successful operation of the laser light screens that the optical equipment is mounted as securely and as independently from the main frame of the shock tube as is possible. In the initial configuration the lasers and mirrors were mounted on tables close to, but not connected directly to the main frame of the tube; the light screens frequently misfired as a result of stray vibrations in the main frame or even the vibration resulting from bursting the diaphragm.

Isolation of all lasers and mirrors at a distance of at least 1m from the shock tube system increased the reliability of the light screen system dramatically. The sensitivity was also improved, allowing the study of slow shocks at temperatures below 700 K.

Despite these improvements it was common for at least one light screen to misfire and many measurements relied on a single estimate of the shock velocity. For a few very slow shocks where only the first light screen fired (and there was thus no time measurement) the shock velocity has been estimated from the appearance of the shock front on the photographic record; the accuracy of these measurements is quite good, but the precision is much lower (± 2%).

2.2.8. Cleaning the Shock Tube

The walls of the shock tube inevitably require cleaning after a few shocks as a result of contamination both from oil in the driver gas and mercuric oxide dust from the discharge system (section 2.3). Fragments of aluminium foil which break from the diaphragm when it bursts are normally driven to the end of the test section and these must be removed at the same time.

The tube is cleaned by pushing a wad of cotton wool soaked in ether along the test section from the diaphragm to the far end, which is opened to the atmosphere. The driver section is cleaned in similar fashion. Ether was chosen as the solvent because of its high volatility; it was felt that other solvents would be more difficult to remove from the surface of the tube wall. After cleaning, the diaphragm is replaced and the system pumped for at least 2-3 hours.

This very simple cleaning technique is all that is possible for a vessel of such length and volume ($\sim$ 10 dm^3), but its efficacity is confirmed by the low rate constant measured for the room temperature deactivation of $O_2(^1\Delta_g)$ at the wall in this system (chapter 3).

2.3. The Discharge Flow System

The discharge flow apparatus is shown in figures 2.1 and 2.7. Pyrex tubing and glassware is used throughout except in the region of the discharge; the diameter of the tubing is not critical (6-12mm). Nearly all taps are of the Quickfit "Rotaflo" type (large or small), but a few of the older Springham taps using viton A rubber diaphragms remain.

Of the test gases used, oxygen alone is discharged and the nitrogen flow is mixed in after the discharge. The treatment of the gases as far as the discharge section is identical.

2.3.1. General Description

Cylinder gas at about 35 KNm^{-2} above atmosphere passes into an Edwards VPC 1 vacuum and pressure controller. The pressure of gas on the outlet side of the controller may be varied between 20 and 450 KNm^{-2} and is normally set using the mercury manometer at 90 KNm^{-2}, a little below atmospheric pressure.

The gas flow is controlled by the needle valve and measured by the capillary flowmeter (figure 2.8) described below. The gas is dried by passage through a column (60cm x 1cm diameter) of molecular sieve type 3A. The tap immediately after the molecular sieve is used to switch on the gas flow; the entire section of line before this tap is maintained permanently at working pressure. The pressure on the discharge side of the needle valve is of the same magnitude as that in the observation section ($\sim$ 1 KNm^{-2}).

The low pressure gas is passed through a trap at 77 K packed with molecular sieve (type 4a) to remove any remaining moisture, carbon dioxide and hydrocarbons.[41] The presence of water in our system presents a considerable problem as it deactivates $O_2(^1\Sigma_g^+)$ with an efficiency 10^3-10^5 that of oxygen and nitrogen at room temperature and can give rise to appreciable errors in the observed rate constants; most of the

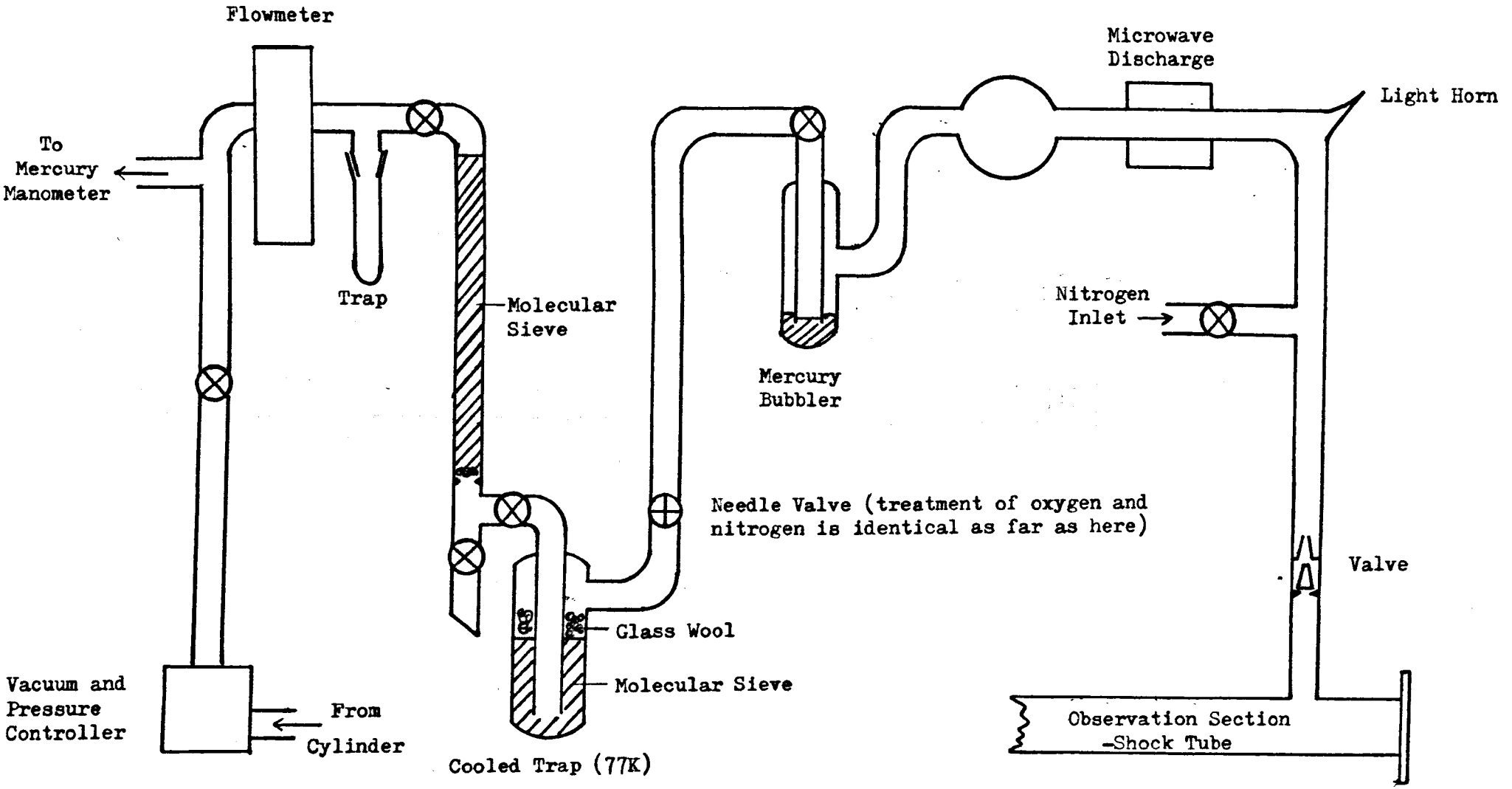

FIGURE 2.7 Discharge-Flow Apparatus (Oxygen Flow Only)

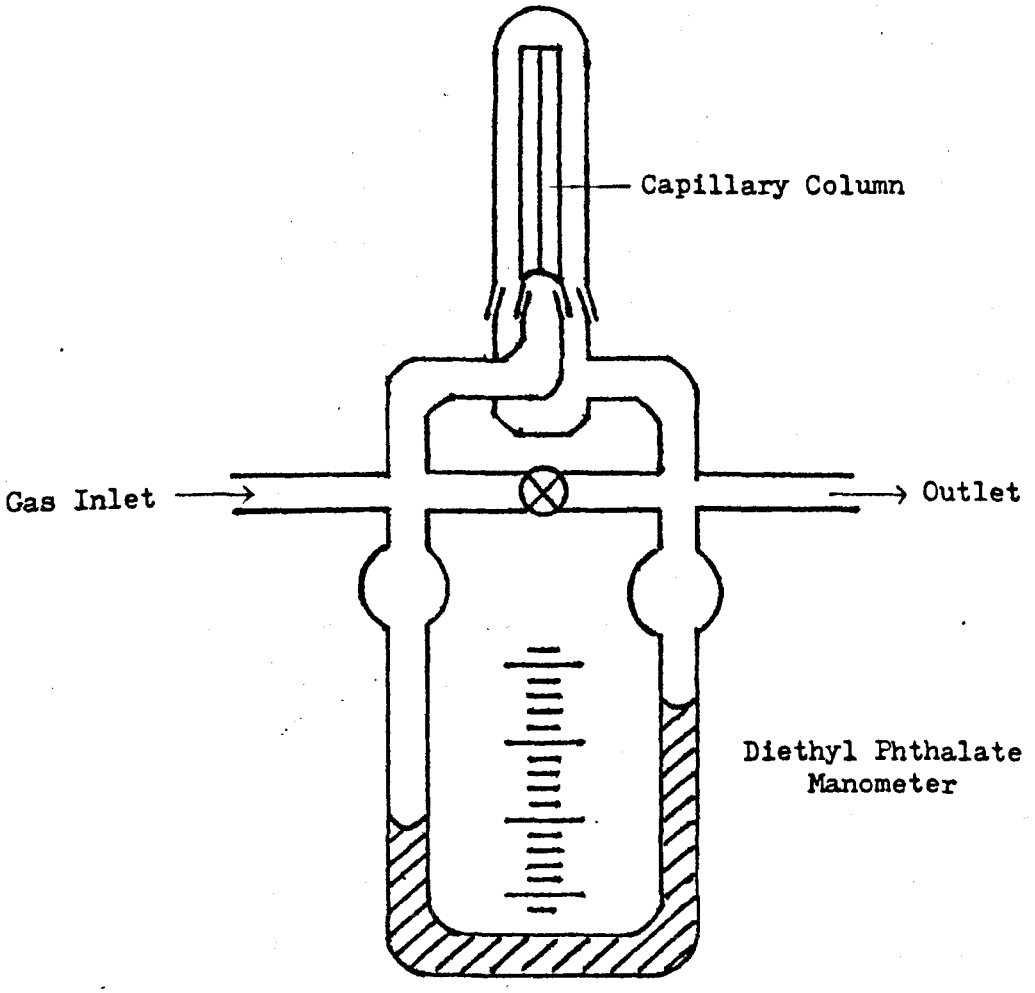

FIGURE 2.8 Capillary Flowmeter

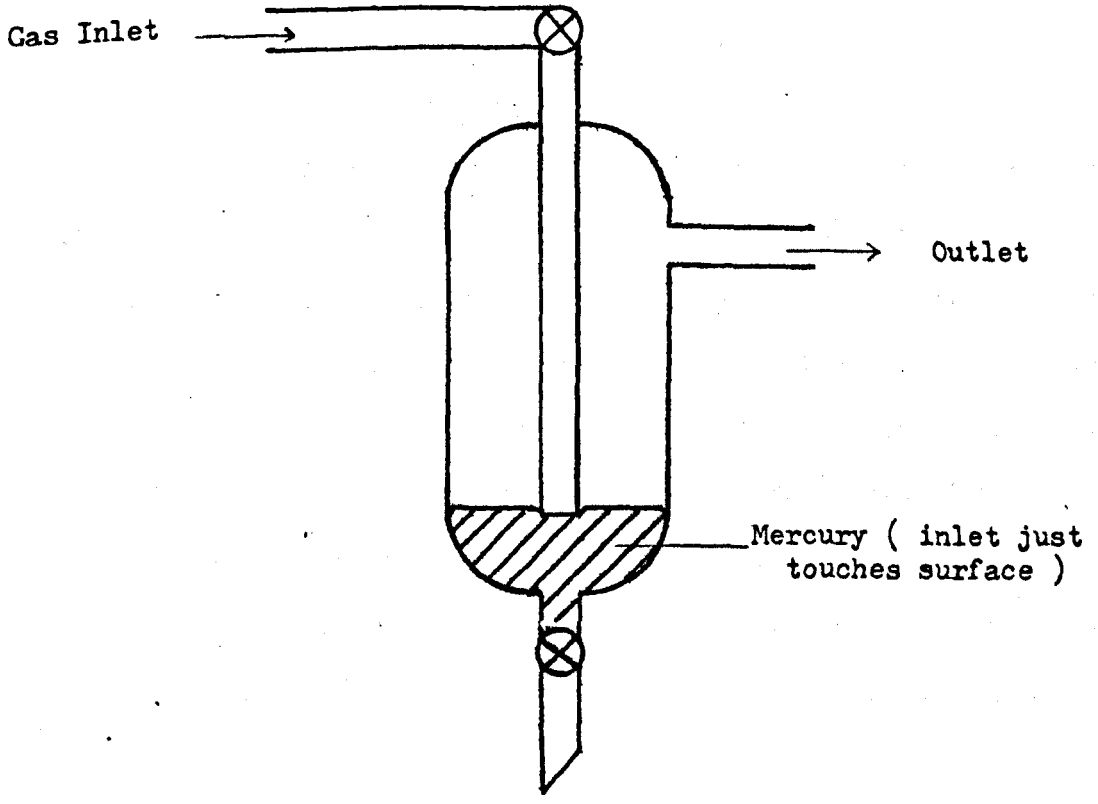

FIGURE 2.9 Mercury Bubbler

water vapour in the observation region of this apparatus is admitted when changing the diaphragm.

The dry oxygen is saturated with mercury vapour by passage through a simple bubbler (figure 2.9). This produces small fluctuations in the flow, and a 1ℓ bulb is placed between the bubbler and the discharge to damp them out.

The discharge section is of 10mm quartz tubing joined by graded seals; quartz is used as the high temperature in the discharge tends to soften pyrex, giving rise to pinholes and indentations. A Microtron Mark III microwave generator is used to power the discharge; it has an output of 0-200 W. A reflected power meter facilitates tuning of the microwave cavity for optimum performance. The discharge is cooled by a gentle flow of compressed air and the hottest part of the system is in fact 2-3cm beyond the discharge, where atom recombination is presumably at a maximum.[53,54] It is almost always necessary to light the discharge using a Tesla EHT coil. A 90 degree bend equiped with a black-painted light horn minimises transmission of light from the discharge down the tube to the observation section.

The tube after the discharge has a thick coating of mercuric oxide formed by reaction of mercury vapour with the atomic oxygen generated by the discharge. The concentration of singlet molecular oxygen in the observation section is enhanced dramatically by the introduction of mercury vapour into the system, and the growth of a mercuric oxide layer is believed to be significant[11] in this process. In our few tests with a system completely free of mercury and mercuric oxide, a considerable enhancement of the emission from $O_2(^1\Sigma_g^+)$ and $O_2(^1\Delta_g)$ was observed on addition of mercury before the discharge, but little further increase was recorded as the oxide layer built up.

The observation section is approximately 150cm from the discharge;

for almost all of this length wide (25mm) tubing is used to minimise the surface deactivation of the excited states. The nitrogen additive, if required, joins the oxygen flow midway along this section.

2.3.2. Capillary Flowmeters

The theoretical rate of flow of a gas of viscosity η through a cylindrical tube of length ℓ and radius r, having a pressure different (P_1-P_2) across its end is given by Meyers equation[131]

$$nRT = \frac{\pi r^4}{16\eta\ell} (P_1^2-P_2^2) \left(1 + \frac{4\lambda}{r}\right) \qquad (2.1)$$

where n is the number of moles of gas, R the universal gas constant, and λ the mean free path of the gas. If the mean pressure of the gas is assumed to be $(P_1 + P_2)/2$ and the small correction for λ ignored, this reduces to a form of Poiseuille's equation, which normally applies to the viscous flow of liquids:

$$V = \frac{\pi r^4 (P_1-P_2)}{8\eta\ell} \qquad (2.2)$$

(where V is the volume of gas flowing through the tube in unit time).

The flowmeters used in this apparatus measure the pressure drop across a capillary tube as the difference in levels, L, of the two arms of a simple diethyl phthalate manometer. It follows from equation (2.2) that

$$V \propto L \qquad (2.3)$$

In reality it is always found that the relation between V and L is gently curved over a wide range of flows.[132] Hence it is necessary to calibrate each flowmeter for use under experimental conditions.

Equation (2.1) shows that for a constant pressure drop across a single flowmeter

$$V \propto 1/\eta \qquad (2.4)$$

Although this relation is probably inaccurate over a wide range of viscosities, it was considered to be sufficiently accurate for this work; all flowmeters were calibrated using oxygen (at 295 K) and the calibrations converted for use with nitrogen by the relation

$$VN_2 = \frac{Vo_2 \, no_2}{\eta N_2} \qquad (2.5)$$

Using the following values for the viscosities of oxygen and nitrogen[133]

O_2 : 290 K 2.012×10^{-5} $kgm^{-1} s^{-1}$

300 K 2.068×10^{-5} $kgm^{-1} s^{-1}$

N_2 : 10.9 °C 1.707×10^{-5} $kgm^{-1} s^{-1}$

27.4 °C 1.781×10^{-5} $kgm^{-1} s^{-1}$

from which the following viscosities at 295 K have been extrapolated,

O_2 : 295 K 2.040×10^{-5} $kgm^{-1} s^{-1}$

N_2 : 295 K 1.756×10^{-5} $kgm^{-1} s^{-1}$

equation (2.5) becomes

$$VN_2 = 1.162 \, Vo_2 \qquad (2.6)$$

The temperature dependence of this relation is small over the operating temperature range of 290–300 K.

To calibrate a flowmeter, the system was set running as for a standard flow experiment and the difference in levels of the diethyl phthalate manometer and the pressure in the observation section recorded. The flow control valve to the main pump was then closed and gas allowed to flow into the system for approximately two minutes (timed with a stopwatch). The oxygen flow was then shut off at the tap above the pressure controller, the needle valve fully opened, and the closed system allowed to come to equilibrium. The pressure rise (12–35 KNm^{-2}) was read using the mercury manometer. It was noted that neither the flow rate nor the

pressure in the system before the needle valve changed significantly with increasing pressure in the discharge and observation sections. A "zero" value for the pressure rise was obtained when the valve at the main pump and tap at the oxygen inlet were shut off simultaneously; the rise in pressure of $\sim$ 12 KNm^{-2} was of course due to the oxygen at 90 KNm^{-2} already in the section of the flow system before the needle valve.

The volume of the shock tube-discharge flow system from the tap at the oxygen inlet to the diaphragm was measured by allowing air at atmospheric pressure to expand from a litre bulb into the evacuated system and measuring the pressure rise on the mercury barometer. The volume of the system estimated in this way was 14.7 ± 0.2 ℓ.

From these measurements the rate of flow of oxygen at room temperature (295 K) and atmospheric pressure was readily estimated. The flow rate in these experiments varied from 17.5-28.0 ml s^{-1} at one atmosphere or 2.0-3.3 ℓ s^{-1} at the test pressure; this corresponds to a flow velocity along the shock tube test section of 1.0-1.65 m s^{-1}.

2.3.3. The Vacuum System

A comprehensive vacuum system (figure 2.10) is attached to the shock tube frame. The system is equipped with two rotary pumps and an oil diffusion pump, which allow the gas inlet part of the discharge flow section to be evacuated while shut off from the shock tube. Facilities are also available for the storage of small quantities of test gases in bulbs equipped with a cold finger and attached to the line. A needle valve admits such gases to the main flow immediately after the discharge at a controlled rate measured by a capillary flowmeter.

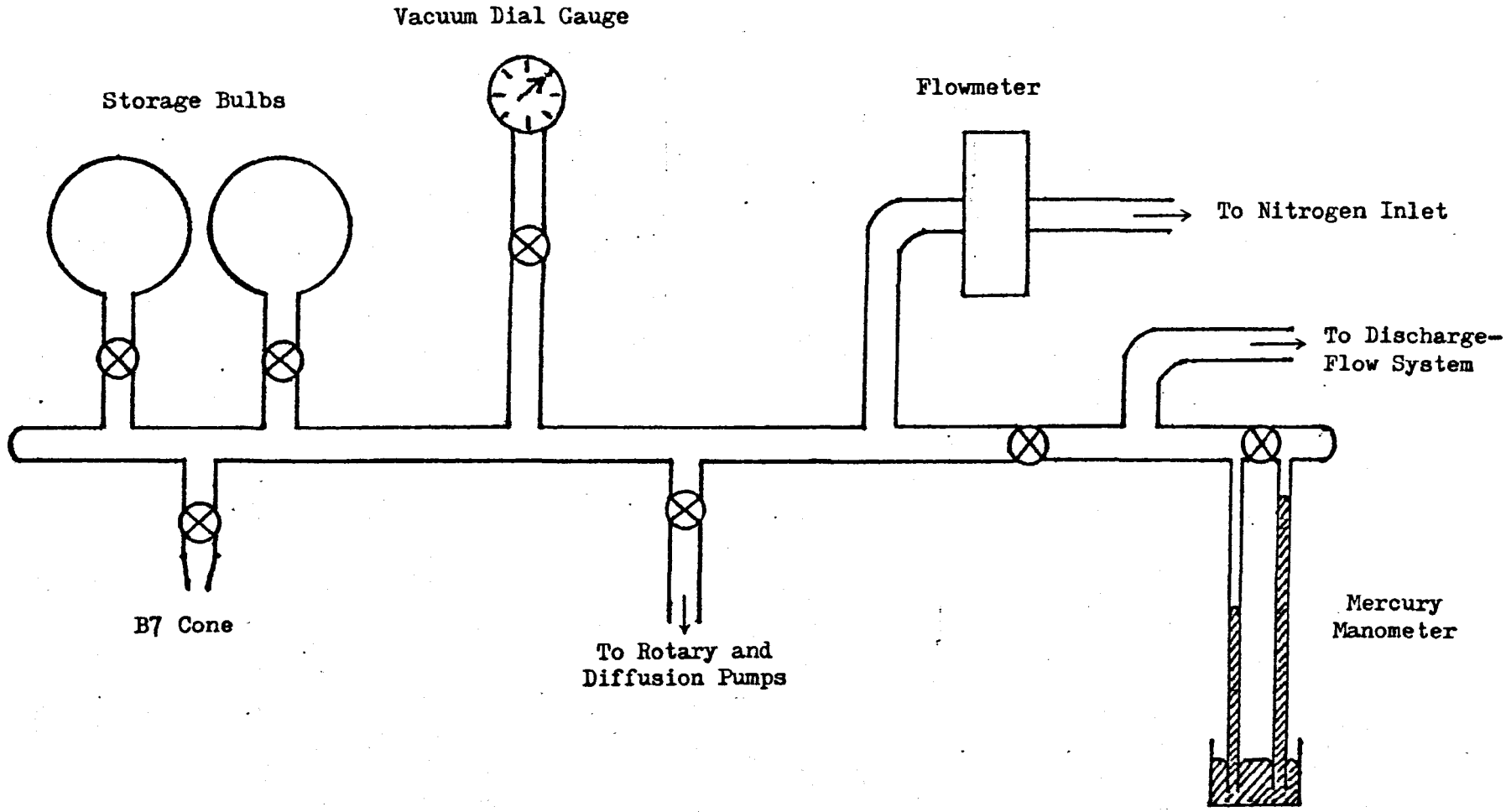

FIGURE 2.10 The Vacuum System

2.4. The Monitoring Apparatus

The concentrations of $O_2(^1\Sigma_g^+)$ and $O_2(^1\Delta_g)$ are followed using photomultiplier detectors together with the appropriate filters to observe the emissions from $O_2(^1\Sigma_g^+)$ at 762nm and from $O_2(^1\Delta_g)$ at 634nm (dimol emission).

The emission prior to the shock is measured using a digital voltmeter, and the changes during the short period of hot flow behind the shock front are recorded by a transient recorder.

2.4.1. Photomultiplier Detectors

EMI 9658B photomultipliers were chosen to follow the emissions at 762 and 634nm. These photomultipliers are of the 9558B parent type and have S20 cathodes; they combine a wide spectral response with low dark current and a relatively high quantum efficiency ($\sim$ 5% at 700nm[134]). In the 9658B photomultiplier the cathode is deposited on a surface of pyramid prisms which increases the quantum efficiency in the range 300-750nm over that of the parent type by up to 25%; this facilitates monitoring of the weak emission at 634nm.

The (0, 0) emission from $O_2(^1\Delta_g)$ at 1270nm is not easily detected by any technique; an EMI 9684B photomultiplier was used in early experiments to look at this emission. This photomultiplier uses an S1 cathode and has a low quantum efficiency (0.35% at 700nm), but a response which extends beyond 1000nm in the infrared region of the spectrum. Although 1270nm is well beyond the manufacturer's estimate of the high wavelength limit of response from this photomultiplier, the emission is detected very weakly. The dark current from the 9684B photomultiplier is high at room temperature and cooling in liquid nitrogen to 77 K is essential. An Oxford Instruments housing is used for this purpose; the other housing used was manufactured by Products for Research Inc. and can be cooled to -40 ^{o}C using a dry ice-propanol slurry.

For a typical shock experiment, the two 9658B photomultipliers are positioned in the above housings at the observation station. Photomultiplier A is mounted in the Oxford Instruments housing which is stationary, and the Products for Research housing containing Photomultiplier B is mounted on rails and able to monitor the emission in the observation section over a range of up to 2.5m. This latter detector is used to study the decrease in emission from the excited states as the oxygen passes along the tube. Neither photomultiplier is cooled as experiments showed that this produces no significant reduction of the dark current.

The photomultipliers operate at the maximum working voltage specified by the manufacturer; this varied by as much as 300 V (mean $\sim$ 1300 V). A single Brandenberg Model 472R EHT power supply operates both photomultipliers, the different individual working voltages being achieved by a simple circuit (figure 2.11).

The photomultiplier circuits (figure 2.12) were designed in accordance with the principles laid down in the manufacturer's handbook.[134] The rise time of the anode circuit is dependent on the anode load resistor, and a compromise must be made between a high load which gives a long rise time and large output voltage and a low load which gives a rapid rise but little output; a load of 51 kΩ was chosen because it allows a reasonably easily measured output voltage and gives a rise time of $\sim$ 5μs, which is not large compared with the overall rise time of the system in a typical shock ($\sim$ 15μs).

The voltage output is transmitted by a voltage follower circuit (figure 2.13). It is measured directly prior to each shock using a Solartron digital voltmeter (model 7040, sensitivity 0.01 mV or model 4440, sensitivity 0.1 mV) and then used as the recorder input. The photomultiplier voltage follower units saturate at an output of $\sim$ 8 V;

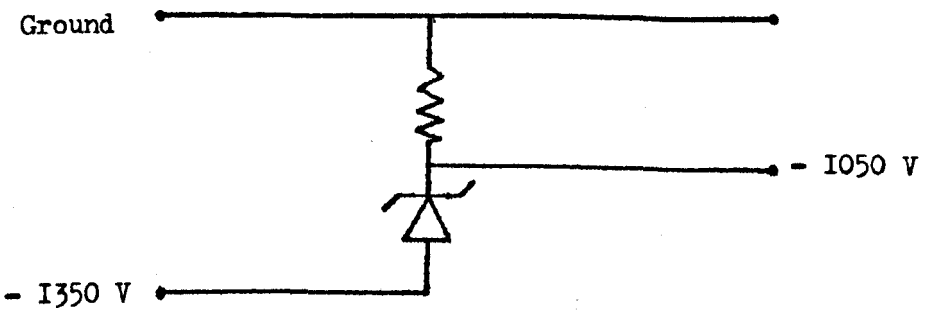

FIGURE 2.11 E.H.T. Voltage Reduction Circuit

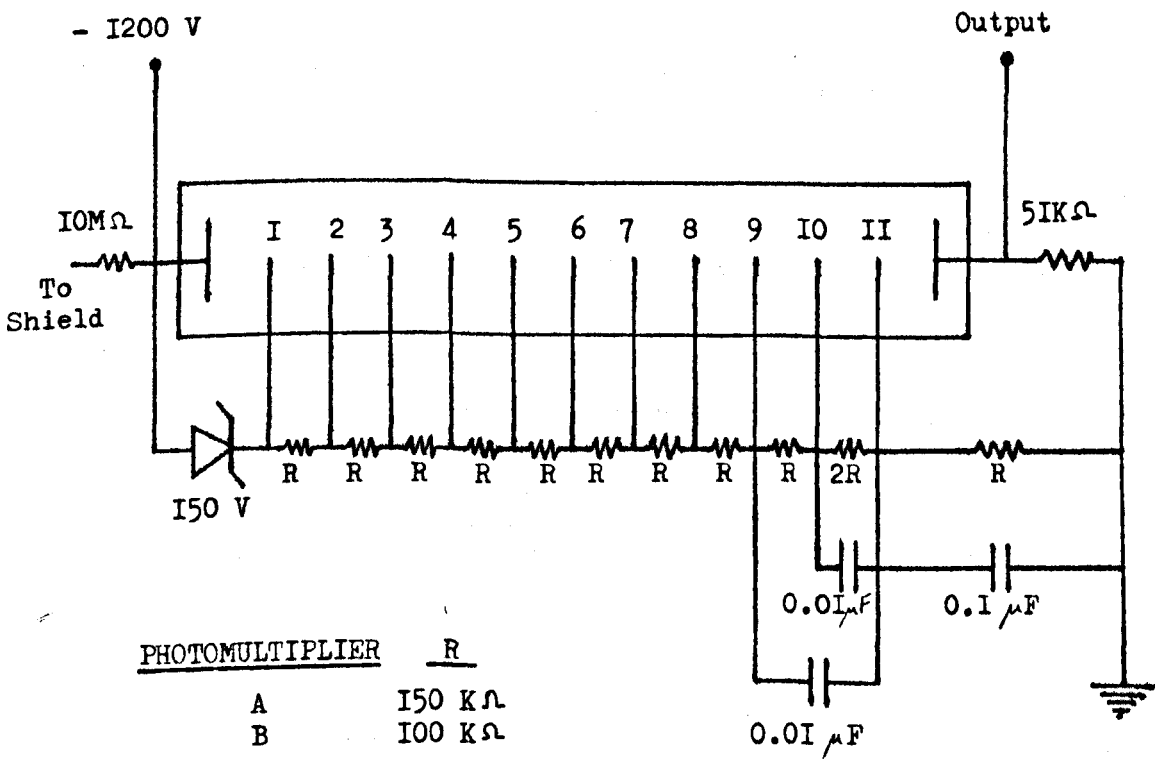

FIGURE 2.12 Photomultiplier Circuit

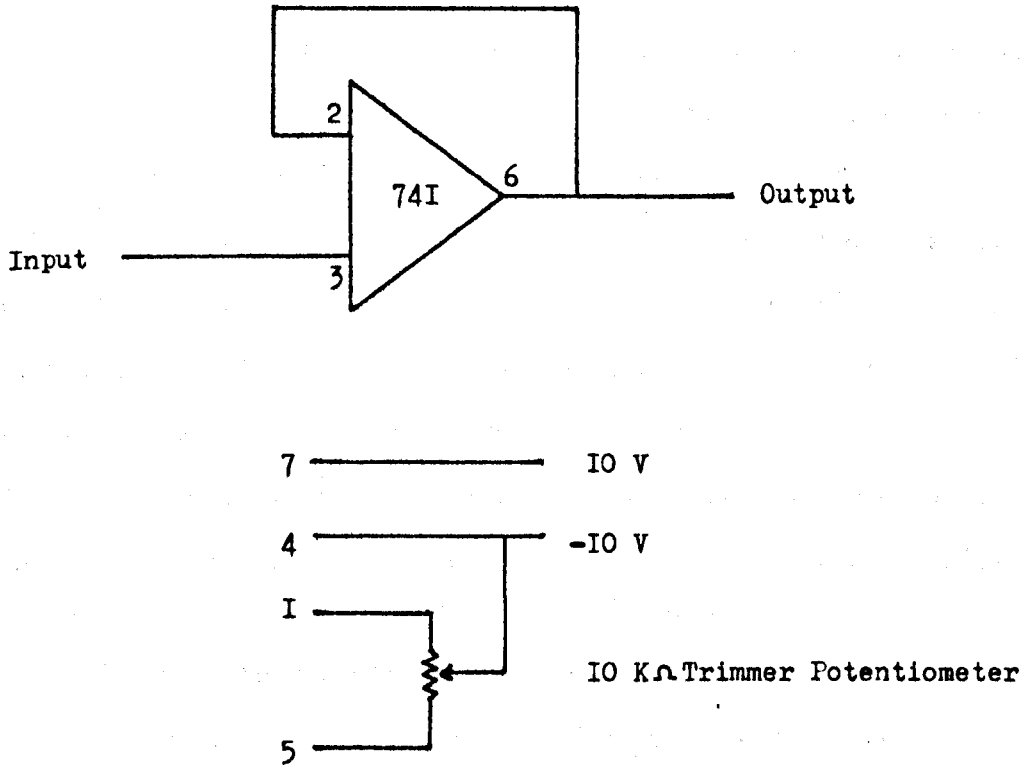

The numbers I - 7 refer to the Integrated Circuit connecting pins.

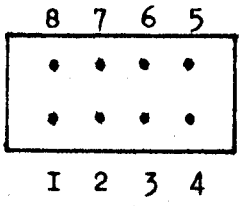

FIGURE 2.I3 Voltage Follower Circuit

experiments were designed so that the output voltage when following the hot gas behind the shock front was always less than 5 V.

The photomultiplier detectors were tested in position using a red light emitting diode (LED) placed inside the shock tube opposite the observation station. This LED was powered by the output of a Marconi pulse generator which provides excellent square pulses at any frequency up to 2.5 MHz or in the single shot mode. The liquid nitrogen cooled 9684B photomultiplier was found to have a significantly lower sensitivity when following a single pulse than when monitoring a continual stream of pulses. This was almost certainly a result of some electrical heating effect within the cold housing (the manufacturers confirmed that the tube itself was in perfect working order). Consequently this photomultiplier was used only for the study of the continuous room temperature emission in the system and not in single shock experiments.

The 9658B photomultipliers both gave satisfactory responses when tested in this way, confirming that the phenomenon was not an artefact of the LED testing system.

2.4.2. Filters and Optics

Narrow band interference filters supplied by Baltzer Ltd are used in these experiments. They have a maximum transmission of $\sim$ 50% at the requested wavelength; the transmission band has a half-width of $\sim$ 13nm.

The filters slot into holders strapped to the front of the photomultiplier detectors; at the front of each holder is an adjustable black paper slit of width between 0 and 3mm. Attempts to increase the amount of emission seen by the photomultipliers using lenses positioned between the shock tube and the detector to focus the emitted light on the photomultiplier slit were unsuccessful; the maximum sensitivity was obtained when the slit was right against the wall of the shock tube, and this configuration was used in all experiments.

The cathode of photomultiplier B is fixed in the housing at a distance of 8.4cm back from the slit. Although the Oxford Instruments housing allows photomultiplier A to be placed much closer to the shock tube, it too was set at this distance from the slit by means of a false front. This restricted the section of shock tube seen by both photomultipliers to the widest portion of the tube.

Figure 2.14 shows that the section of shock tube seen by the photomultiplier is far from square and varies between 4mm and 30mm for a 2mm slit (refraction through the glass wall of the tube is not considered, but its effect would be to broaden the segment seen by the detector still further, without changing its shape). Assuming a "square slit" of mean width 17mm, the rise time of a typical shock of velocity 1.4 kms^{-1} comes to about 12μs; the observed rise time is normally in the range 7-20μs, depending on the exact slit width. This good agreement is partially fortuitous as this estimate assumes the photomultiplier tube and shock tube to be of a rectangular (as opposed to cylindrical) cross section. The rise time of the photomultiplier anode current also contributes to the observed shock rise time.

A few experiments were performed using a double slit of width 2-3mm. The section of the shock tube seen by the detector when using this slit was much more "square" than when a single slit was used, but the intensity of emission was reduced unacceptably. As the analysis of the detector output in this work makes an allowance for the width of the slit, but assumes it to have a square cross section, an arrangement using a double slit of width $\sim$ 10mm (figure 2.15) might well be more suitable than the single slit of width $\sim$ 2mm.

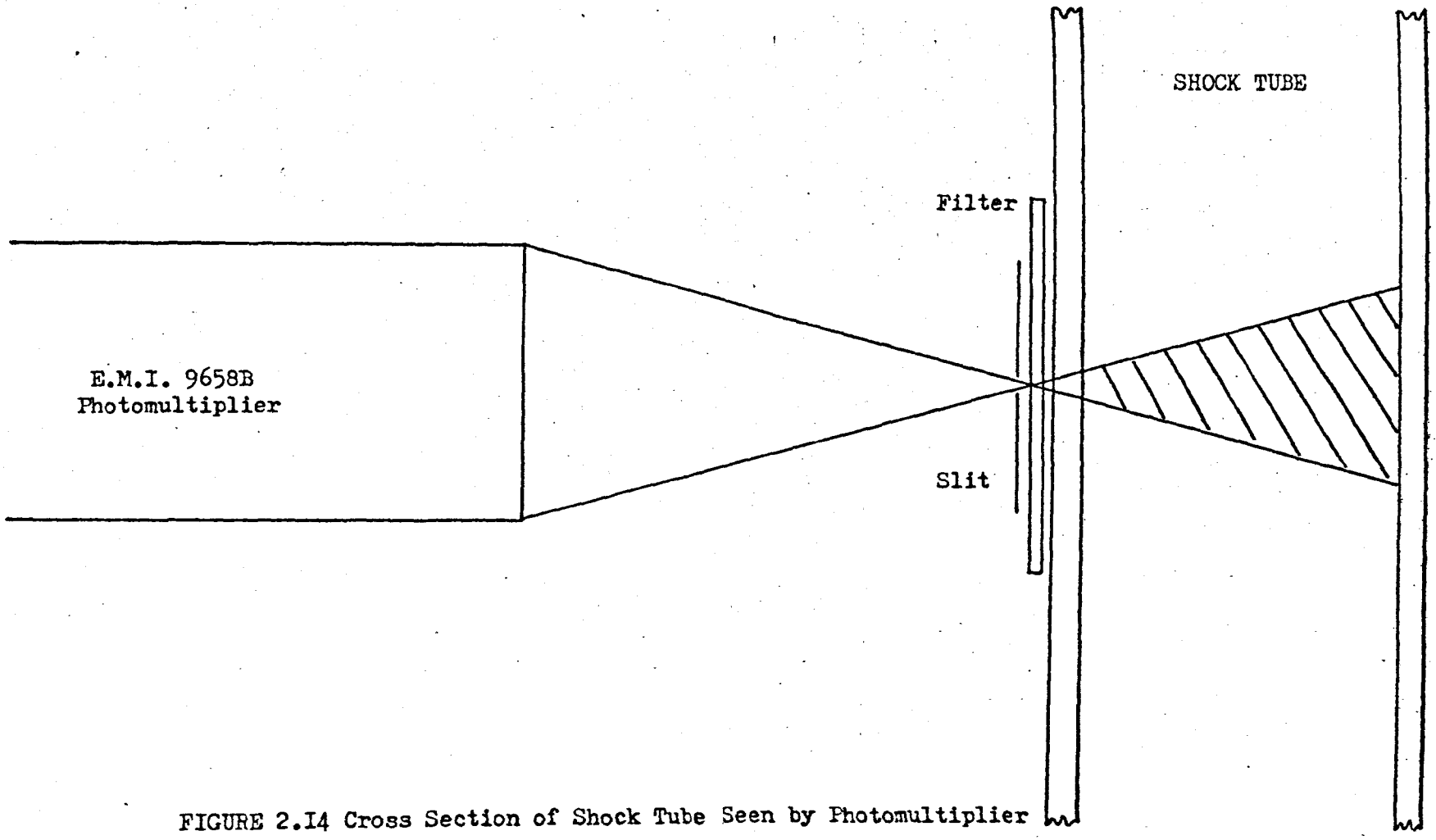

FIGURE 2.I4 Cross Section of Shock Tube Seen by Photomultiplier

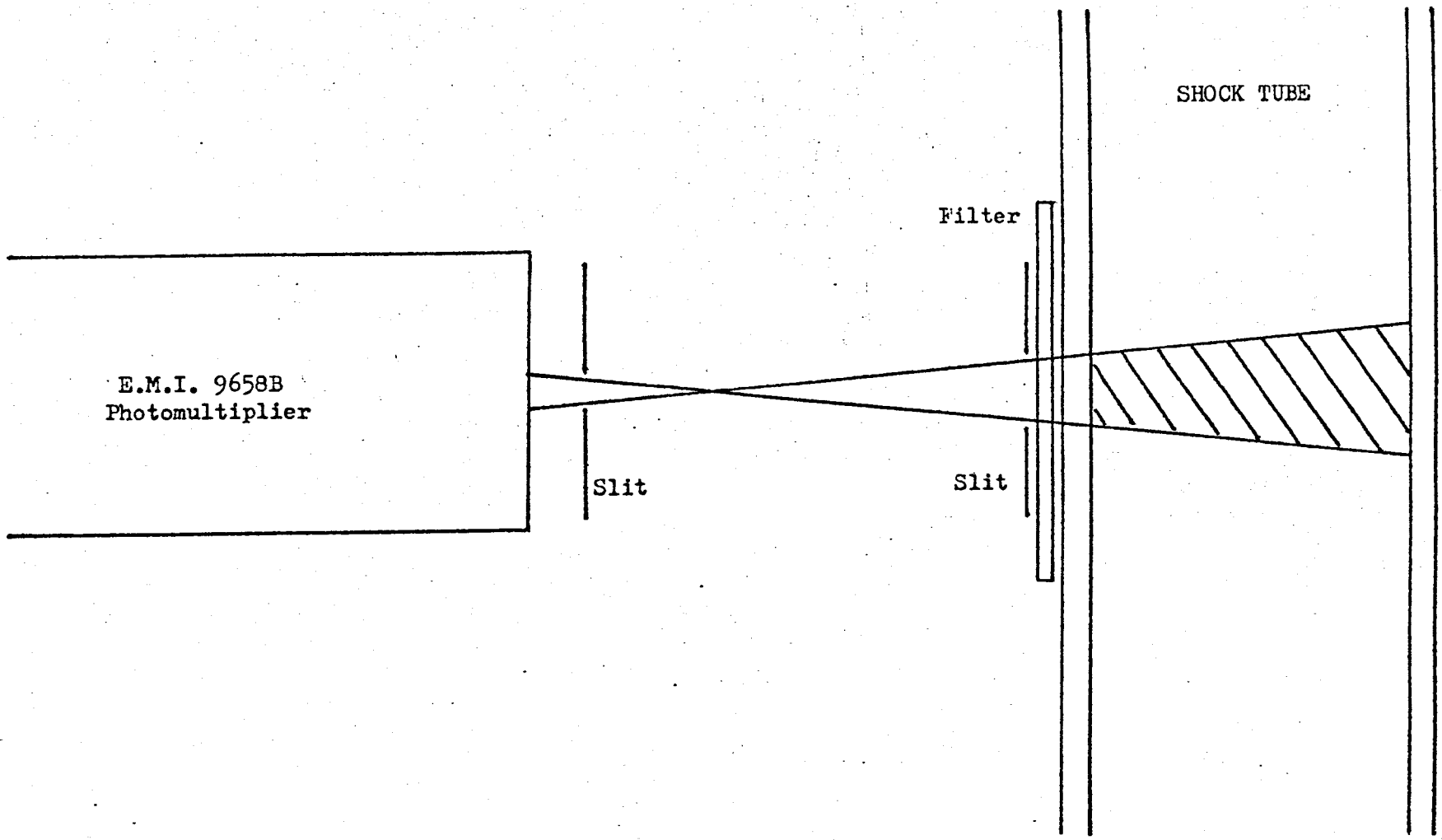

FIGURE 2.15 Cross Section of Shock Tube Seen Using a Double Slit

2.4.3. Measurement of the change in emission along the tube

As the gases flow along the observation region of the shock tube, the concentration of singlet molecular oxygen decreases owing to deactivation by gaseous collison or at the tube wall. The fall off in emission prior to the shock is studied by moving photomultiplier B along the rails and recording the detector output at 10cm intervals. Photomultiplier A remains at the observation station and monitors any overall fluctuations in the concentration of the excited species within the observation region; allowance for these fluctuations is made in the analysis of the results.

Two sources of inaccuracy in these measurements were found: variation in the effective height of the slit and electrical interference between the detector outputs when the two were close together.

The problems with the slit height arose from the great difficulty in setting the three sections of Handyangle rail, on which the travelling photomultiplier is mounted, at exactly the same height parallel to the shock tube. The curved wall of the shock tube results in a fall off in measured emission, if the detector is raised or lowered from the height at which the horizontal centre of the slit is the point in contact with the tube wall. A horizontal slit (width 22mm) of black paper was fixed along the entire length of the observation section and the slit on the detector was given a horizontal width of 16mm; these modifications make it easy to detect whether the photomultiplier is significantly away from its optimum position and adjust the apparatus accordingly.

Electrical interference between the two photomultiplier detectors results from the large short-term fluctuations in their output potentials. It was largely cured by trailing the output leads (all such leads use coaxial cable and BNC connectors) as far apart as possible. At its worst the magnitude of the "pick up" is never more than 10 mV and it is insignificant if wide slits are used to give an output potential of the order of 1 V.

2.4.4. Transient Recorders

The output from each voltage follower is connected to a Datalab DL905 transient recorder, which is triggered externally by the shock front using the output from light screen 1.

The transient recorder is ideally suited to shock tube experiments where the measurements must be made over a time period of less than 1 ms; the shock record is stored by the recorder as 1024 (2^{10}) individual data points, giving the intensity of emission at time intervals of 0.5μs for a 500μs sweep period or 1.0μs for a 1 ms sweep. A delay of up to ten times the sweep period allows efficient recording of the shock; this is usually set at 200-350μs in this work, depending on the velocity of the shock.

The data is displayed as a trace on the screen of an oscilloscope (Hewlett Packard Model 141A) triggered by the transient recorder; facilities are also available for output to a chart recorder or transfer of the data to paper tape. In practice a photographic record of the oscilloscope display is made using a Hewlett Packard 197A Oscilloscope Camera equipped with Polaroid film, and the data is then output to paper tape for computer analysis (the data is redisplayed after output to tape is complete).

The output to the tape punch (DL 2046) passes through an interface built in this department. The interface is equipped with a small keyboard which is used to type in the run number, sweep period and voltage sensitivity at the start of each tape. The tape is copied to a disc file capable of holding data from up to 23 shocks at a time for future analysis (chapter 6).

In many early experiments only one transient recorder was available; this was used to record the output from the better (less noisy) of the two detectors, and the output from the other detector was recorded by a storage oscilloscope. A hand analysis of this second

trace was possible, but the accuracy was too low for it to be of use other than as a very rough indication of what was happening.

2.5. Materials

Oxygen, nitrogen (oxygen free) and helium gases (all industrial grade) were supplied by B.O.C. Ltd., (Crewe). The oxygen purity is better than 99.5%, and impurities other than nitrogen and argon (both comparatively innocuous) are less than 0.01%; the nitrogen used has a purity better than 99.9%. Both these gases undergo further purification and drying before use as the test gases in the shock tube; ultra pure gases, while desirable, are prohibitively expensive. The purity of the helium and nitrogen used as driver gases is less important, although they are dried before use.

The danger of using test gases that are not ultra-pure in these experiments is a result of the rapid rate of deactivation of singlet molecular oxygen by impurities such as water (section 2.B(i)).

A small amount of nitric oxide was used for experiments on atomic oxygen; a litre bulb of the gas at atmospheric pressure was prepared by the reaction of potassium nitrite and potassium iodide in a strongly acidic solution.

$$2NO_2^- + 2I^- + 4H^+ \rightarrow 2NO + I_2 + 2H_2O \qquad (2.7)$$

The gas was then transferred to a storage bulb in the vacuum system.

Other materials, used without further purification are tabulated below:

Table 2.2

Material	Supplier
Aluminium foil (50 and 150μm)	G.W. Aluminium Co.†
Aluminium foil (other thicknesses)	Multifoil
Melinex (several thicknesses)	Bostik
Diethyl Ether (CPR SLR)	Koch-Light
Diethyl Phthalate	Mersey Chemicals
Mercury	Belgrave

† These suppliers have now ceased trading.

2.6. Experimental Procedure

The following procedure is adopted in a typical experimental run:

(i) An aluminium foil diaphragm of the required thickness is clamped in its holder and both driver and test sections are evacuated for approximately 15 minutes.

(ii) The Dewars on the two traps are filled with liquid nitrogen. When they have cooled, the gas inlet taps immediately before the needle valves are opened and the test gases allowed to flow through the system; the needle valves are adjusted to give the correct flows.

(iii) The discharge is lit and the cooling gas turned on; the power is adjusted to 100 W; the pressure in the test section is adjusted using the QVF flow control valve, and the system is left to settle for about twenty minutes at room temperature.

(iv) The overhead lights are switched off and the EHT photomultiplier power supply turned on; the fall in emission from $O_2(^1\Sigma_g^+)$ or $O_2(^1\Delta_g)$ along the observation section is recorded using the travelling photomultiplier.

(v) The room temperature and the exact pressure in the shock tube test section are recorded (the manometer is then shut off from the shock); the lasers are switched on and the light screen detectors and time interval meters are adjusted for optimum sensitivity.

(vi) The level of emission observed by each detector prior to the shock is measured using the digital voltmeters, and the detector outputs transferred to the transient recorder inputs; the transient recorders, time interval meters and digital counters are armed.

(vii) The vacuum pump connected to the driver section is shut off and the driver gas let in at a steady, fairly slow rate until the

diaphragm bursts and fires the shock; the driver gas inlet is closed immediately the shock fires. When mixed driver gases are used, the pressure in the driver section is raised to about one atmosphere by letting in nitrogen, and helium is then let in slowly until the diaphragm bursts (bursting pressure 275 KNm^{-2}).

(viii) The EHT power supplies, lasers and microwave discharge are switched off and the overhead lights turned back on.

(ix) The test gas inlet taps and flow control valve are shut off and the shock tube is opened to the atmosphere through the driver section. The diaphragm is replaced as quickly as possible (provided that the tube does not require cleaning) and the system re-evacuated as in (i). This entire operation takes about a minute.

(x) The times for the shock front to travel between the light screens are noted, the transient recorder trace on the oscilloscope screen is photographed, and the stored data is output to paper tape for future analysis.

3. Studies of the collisional deactivation of singlet molecular oxygen at room temperature

3.1. Introduction

The discharge flow shock tube may be used as a simple discharge flow apparatus. Hence the rates of quenching reactions of $O_2(^1\Sigma_g^+)$ and $O_2(^1\Delta_g)$ may be measured at room temperature; the accuracy of such measurements provides an excellent test of the discharge flow part of our apparatus. Compared with systems designed for such studies, the test section of the shock tube has the advantage of allowing measurements to be made over a considerable distance; the wide tube used in these experiments also reduces the effects of deactivation at the wall. The principal disadvantages of this system are the difficulty of keeping the gases perfectly dry inside the shock tube test section, and the absence of facilities for measuring the absolute concentrations of the excited species.

In this chapter the kinetic equations describing the reactions of singlet molecular oxygen are laid down for use in both the room temperature studies and in the high temperature work (the theory of which is outlined in chapter 4). In the room temperature studies, the rate constant for quenching of $O_2(^1\Delta_g)$ by oxygen has been measured with considerable precision, and approximate values have been obtained for the rates of deactivation of $O_2(^1\Sigma_g^+)$ by oxygen and nitrogen.

3.2. Deactivation of $O_2(^1\Delta_g)$

3.2.1. Theory

$O_2(^1\Delta_g)$ is formed in (or just after) the discharge, and, as it passes along the tube, it is removed by collisional quenching in the gaseous phase and by collisions with the wall

$$O_2(^1\Delta_g) + M \xrightarrow{k_q} O_2(^3\Sigma_g^-) + M \qquad (1.33)$$

$$O_2(^1\Delta_g) \xrightarrow{k_w} O_2(^3\Sigma_g^-) \qquad (3.1)$$

$O_2(^1\Delta_g)$ is also removed by the radiative processes

$$O_2(^1\Delta_g) + O_2(^1\Delta_g) \xrightarrow{k_D} O_2(^3\Sigma_g^-) + O_2(^3\Sigma_g^-) + h\nu(634nm) \qquad (1.12)$$

$$O_2(^1\Delta_g) \longrightarrow O_2(^3\Sigma_g^-) + h\nu(1270nm) \qquad (1.4)$$

and by the energy pooling reaction

$$O_2(^1\Delta_g) + O_2(^1\Delta_g) \xrightarrow{k_1} O_2(^1\Sigma_g^+) + O_2(^3\Sigma_g^-) \qquad (1.13)$$

Reactions (1.12) and (1.4) are very slow, and the energy pooling reaction becomes significant in comparison with (1.33) and (3.1) only at high concentrations of $O_2(^1\Delta_g)$; consequently only reactions (1.33) and (3.1) are rate determining. Thus, the rate equation for deactivation of $O_2(^1\Delta_g)$ may be written:

$$\frac{d[O_2(^1\Delta_g)]}{dt} = -\left\{k_q [O_2(^1\Delta_g)][M] + k_w[O_2(^1\Delta_g)]\right\} \qquad (3.2)$$

$$= -K^*[O_2(^1\Delta_g)] \qquad (3.3)$$

where K^* is the first order rate constant for deactivation of $O_2(^1\Delta_g)$ at a given pressure of oxygen.

As part of the measurements prior to each shock the decrease in concentration of $O_2(^1\Delta_g)$ along the test section is measured by following the dimol emission (1.12) or the emission from $O_2(^1\Sigma_g^+)$. Experiments, in which the emissions from $O_2(^1\Delta_g)$ at 1270 and 634nm are compared over a range of pressures[135], have shown that the intensity, I_D, of the dimol

emission varies with the square of the concentration of $O_2(^1\Delta_g)$

$$I_D = k_D[O_2(^1\Delta_g)]^2 \tag{3.4}$$

as is expected from equation (1.12).

By plotting ln I_D against distance from the observation station, the first order decay constant, α_ℓ, for the dimol emission is obtained:

$$\ln \frac{I_D}{I_D^o} = 2 \ln \frac{[O_2(^1\Delta_g)]}{[O_2(^1\Delta_g)]_o} = -\alpha_\ell \ell \tag{3.5}$$

$$\therefore \quad [O_2(^1\Delta_g)] = [O_2(^1\Delta_g)]_o \, e^{-\alpha_\ell \ell/2} \tag{3.6}$$

$$\frac{d[O_2(^1\Delta_g)]}{d\ell} = -\frac{\alpha_\ell}{2}[O_2(^1\Delta_g)]_o \, e^{-\alpha_\ell \ell/2} = \frac{-\alpha_\ell}{2}[O_2(^1\Delta_g)] \tag{3.7}$$

The decay of $O_2(^1\Delta_g)$ with distance along the tube is related to the decay rate (3.2) by

$$\frac{d[O_2(^1\Delta_g)]}{dt} = \frac{d[O_2(^1\Delta_g)]}{d\ell} \frac{d\ell}{dt} \tag{3.8}$$

where $\frac{d\ell}{dt}$ is simply the gas flow velocity v.

Thus from (3.7) and (3.8)

$$\frac{d[O_2(^1\Delta_g)]}{dt} = \frac{-\alpha_\ell v}{2} [O_2(^1\Delta_g)] \tag{3.9}$$

and from equation (3.2) it follows that

$$K^* = k_w + k_q[M] = \frac{\alpha_\ell v}{2} \tag{3.10}$$

The flow velocity, v, is related to the observed flow rate at atmospheric pressure by

$$v = \frac{\text{(flow rate)} \times 101.32}{\pi r^2 P_1} \text{ ms}^{-1} \tag{3.11}$$

where r is the tube radius (mm) and P_1 the pressure in the test gas.

The rate of collisional deactivation of $O_2(^1\Delta_g)$ by oxygen may be

obtained by following the decay of the dimol emission at a number of different pressures. In practice it is easier to follow the emission from $O_2(^1\Sigma_g^+)$, which also may be shown to vary with $[O_2(^1\Delta_g)]^2$: $O_2(^1\Sigma_g^+)$ is formed by the energy pooling reaction (1.13) and removed by collisional quenching and deactivation at the wall

$$O_2(^1\Sigma_g^+) + M \xrightarrow{k_2} O_2(^1\Delta_g) + M \qquad (1.32)$$

$$O_2(^1\Sigma_g^+) \xrightarrow{k'_w} O_2(^1\Delta_g) \text{ or } O_2(^3\Sigma_g^-) \qquad (3.12)$$

and also by the emissions

$$O_2(^1\Sigma_g^+) \xrightarrow{k_\Sigma} O_2(^3\Sigma_g^-) + h\nu(762nm) \qquad (1.3)$$

$$O_2(^1\Sigma_g^+) \rightarrow O_2(^1\Delta_g) + h\nu(1900nm) \qquad (3.13)$$

both of which are very weak. Hence (1.32) and (3.12) are rate determining and we may write

$$\frac{d[O_2(^1\Sigma_g^+)]}{dt} = k_1[O_2(^1\Delta_g)]^2 - k_2[O_2(^1\Sigma_g^+)][M] - k'_w[O_2(^1\Sigma_g^+)] \qquad (3.14)$$

At any point along the tube, $[O_2(^1\Delta_g)]$ and [M] are constant and the steady state approximation gives:

$$[O_2(^1\Sigma_g^+)] = \frac{k_1[O_2(^1\Delta_g)]^2}{k_2[M] + k'_w} \qquad (3.15)$$

Depending on the rate at which this equilibrium is reached and on the flow velocity of the gas, the concentration of $O_2(^1\Sigma_g^+)$ at any point, ℓ_2, in the tube will correspond to the concentration of $O_2(^1\Delta_g)$ a short distance upstream at ℓ_1. As $(\ell_2-\ell_1)$ is constant for a steady flow,

$$[O_2(^1\Delta_g)]_{\ell_2} = [O_2(^1\Delta_g)]_{\ell_1} \; e^{-\alpha_\ell(\ell_2-\ell_1)/2} \qquad (3.16)$$

or

$$[O_2(^1\Delta_g)]_{\ell_2} \propto [O_2(^1\Delta_g)]_{\ell_1} \qquad (3.17)$$

Hence from (3.15) and (3.17), at all points along the tube,

$$[O_2(^1\Sigma_g^+)] \quad \alpha \quad [O_2(^1\Delta_g)]^2 \tag{3.18}$$

As, at low pressures, the rate of (1.3) varies only with the concentration of $O_2(^1\Sigma_g^+)$, the intensity of emission from $O_2(^1\Sigma_g^+)$ varies with the square of the concentration of $O_2(^1\Delta_g)$

$$I_\Sigma \quad \alpha \quad [O_2(^1\Sigma_g^+)] \quad \alpha \quad [O_2(^1\Delta_g)]^2 \tag{3.19}$$

and relations (3.5)-(3.10) follow as before.

Figure (3.1) shows a first order plot of the decay of the $O_2(^1\Sigma_g^+)$ and the dimol emissions along the tube; although the gradient is identical for the two, the emission from $O_2(^1\Sigma_g^+)$ is of far greater intensity at the low pressures used in these experiments. Nearly all measurements reported here were made with the emission from $O_2(^1\Sigma_g^+)$; fluctuations in the emission and in the voltage follower zero levels (chapter 2) sometimes caused significant errors when following the dimol emission.

3.2.2. Results

The first order rate constant, K^*, for the collisional deactivation of $O_2(^1\Delta_g)$ was measured in pure oxygen over the pressure range 0.25-2.0 KN m^{-2}. At pressures greater than $\sim$ 0.8 KN m^{-2}, K^* was found to vary linearly with pressure; at lower pressures, however, the measured rate constant was increasingly greater than expected. Ogryzlo[55] has suggested that the mercury/mercuric oxide system is not completely effective at removing atomic oxygen, a species which, if present, would increase the rate of quenching considerably. Possible solutions to this problem include reduction of the discharge power from its usual value of 100W, reduction of the flow rate and addition of most of the oxygen quencher after the discharge.

Reduction of the power of the microwave discharge had a dramatic effect on the results, shown schematically in figure (3.2). It is clear that the species causing this high quenching rate at low pressures is

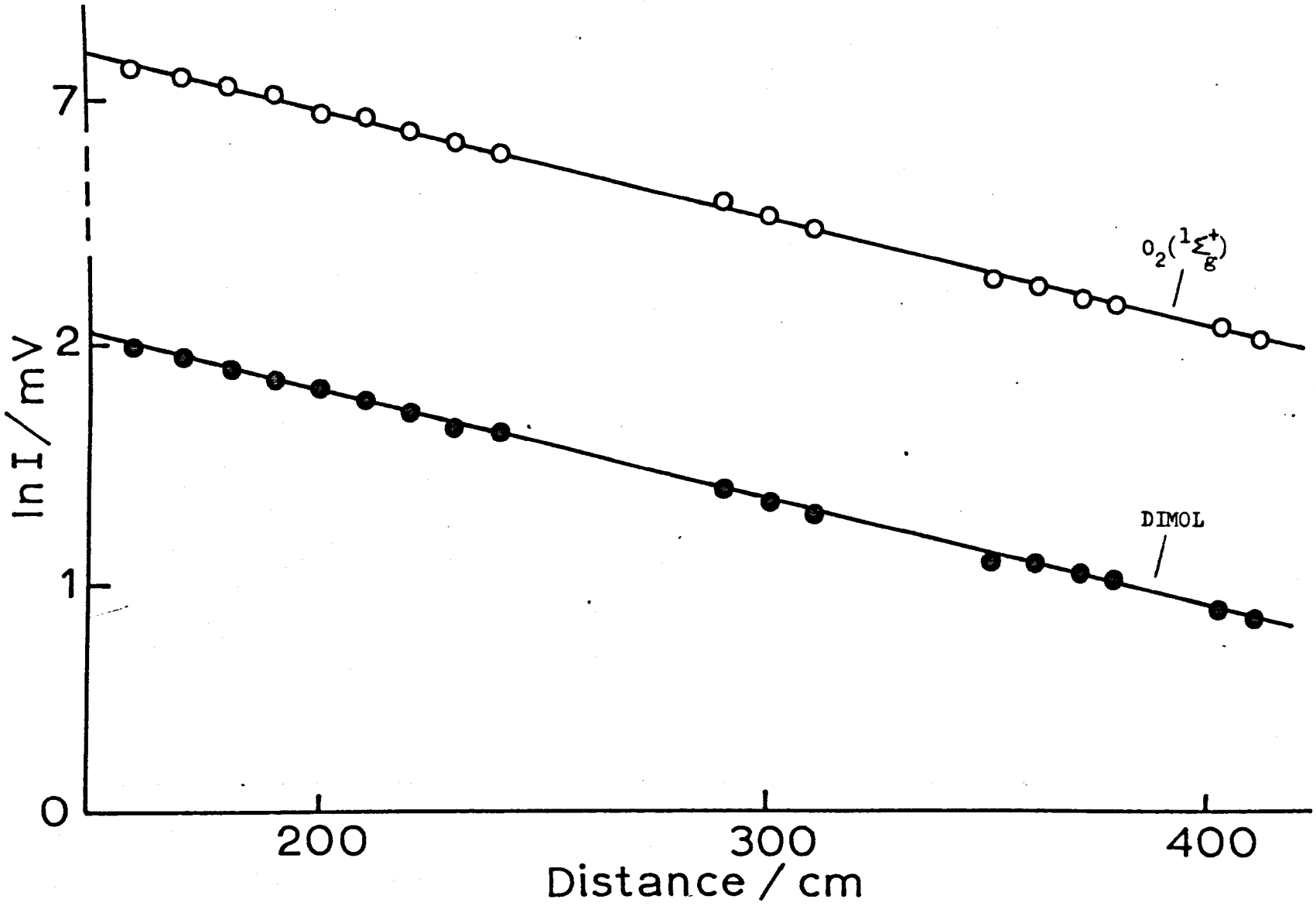

FIGURE 3.1 Decay of Emission along the Test Section

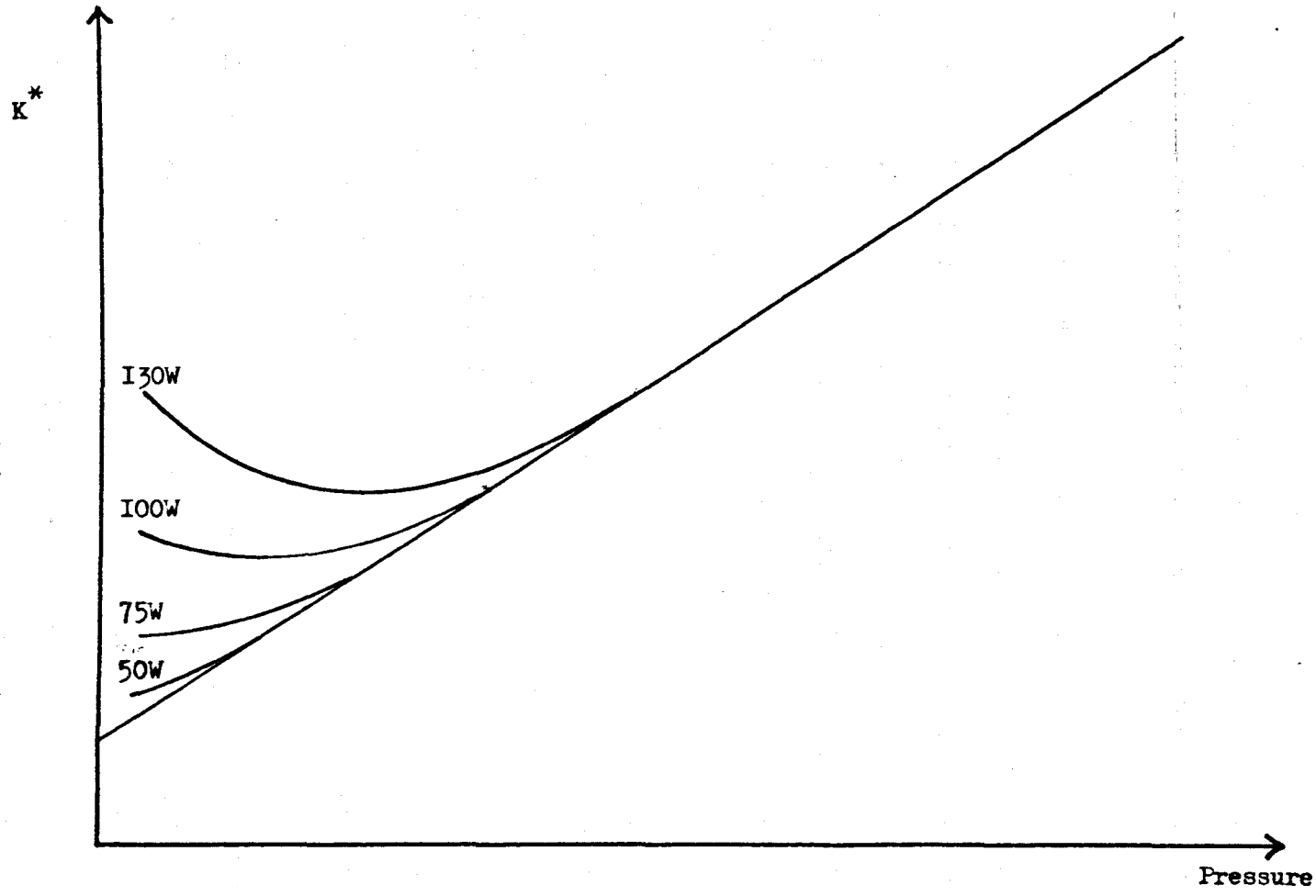

FIGURE 3.2 High Rate of Deactivation of $O_2(^1\Delta_g)$ at Low Pressure and High Discharge Powers.

removed more completely before the flowing gas enters the shock tube test section when low discharge powers are used. This is in accordance with the suggestion that the species is atomic oxygen; oxygen atoms are known to be formed in the discharge and removed by the mercury vapour in the oxygen flow and the mercuric oxide surface beyond the discharge. A reduction in discharge power decreases the quantity of atomic oxygen to be removed (naturally, the concentration of singlet molecular oxygen is also reduced).

A similar effect is expected if the flow rate is decreased; at the flow rate of 17.5 ml s^{-1} (at atmospheric pressure) used in early experiments, the flow velocity is approximately 1.1 ms^{-1} at a pressure of 0.8 KN m^{-2}, but rises to 3.5 ms^{-1} at 0.25 KN m^{-2}. Reduction of the flow velocity should give the mercury vapour and mercuric oxide layer more time to remove the atomic oxygen before the test section is reached. It was found that measurements at pressures of 0.25-0.4 KN m^{-2}, using a discharge power of 35W (the minimum power at which it remained alight) and a flow rate of only 9.3 ml s^{-1} at atmospheric pressure, gave values of K^* in good agreement with the values extrapolated from the linear region at higher pressures. At the low flow rate and very low discharge powers used, the intensity of emission is significantly reduced; as a result, the values of K^* obtained at these pressures are rather less precise than those obtained at pressures greater than 0.8 KN m^{-2}.

A few measurements were performed at very high flow rates (30.4 ml s^{-1} at atmospheric pressure); at pressures greater than 0.8 KN m^{-2} the first order decay constant obtained was unchanged from that found at the lower flow rates. The pumping rate is too low to allow measurements at lower pressures with this flow rate; presumably atomic oxygen would again give rise to errors.

The third option mentioned above was to pass only a small proportion of the oxygen through the discharge. Wayne[74] and Pitts[75] both added 90%

of the oxygen after the discharge in their measurements of the rate of quenching of $O_2(^1\Delta_g)$; their equations show that even if considerable quantities of atomic oxygen are formed in the discharge, the concentration will be negligible once the oxygen mainstream is mixed in. Experiments in which only 10% of the oxygen was discharged showed no detectable change in the first order rate constants at pressures between 0.5 KN m^{-2} and 1.2 KN m^{-2} from those observed when all the oxygen was discharged. This process gave rise to much lower concentrations of singlet molecular oxygen than before, and consequently accurate measurements at pressures outside this range were not possible.

After all the sources of error had been eliminated, a very good linear relation between K^* and the concentration of oxygen was obtained from the first order rate constants in Table 3.1 (figure 3.3). The rate constant for collisional quenching of $O_2(^1\Delta_g)$ was estimated from the gradient to be $(0.936 \pm 0.029) \times 10^3 dm^3$ mole^{-1} s^{-1} at 294 K, and that for deactivation at the wall, from the intercept, to be 0.106 ± 0.013 s^{-1} in our system. The wall deactivation efficiency, γ_Δ, calculated from k_w using the relation

$$\gamma_\Delta = \frac{2k_w r}{\bar{c}} \qquad (3.20)$$

(where r is the tube radius and $\bar{c}$ the mean molecular speed of oxygen gas), was estimated to be $(1.23 \pm 0.14) \times 10^{-5}$.

These estimates are compared with those reported by other workers in Table 1.1 (chapter 1). Our value of the rate of quenching is significantly lower than those of earlier authors, but of greater precision. It is in reasonable agreement with the early measurement of Schurath[62] and in excellent agreement with his most recent estimate[78], for which a technique entirely different from ours was used (his more recent results have been reported since ours were published). The rough estimate of Matheson et. al.[40], made using $O_2(^1\Delta_g)$ generated by laser excitation at

TABLE 3.1

Deactivation of $O_2(^1\Delta_g)$ by oxygen-first order rate constants at 294 K

PRESSURE ($KN\ m^{-2}$)	FLOW RATE ($ml\ s^{-1}$ at 1 atm)	$\alpha_\ell (m^{-1})$	$K^*(s^{-1})$
1.88	17.5	3.575	0.838
1.63	20.2	2.304	0.715
1.59	9.3	4.840	0.709
1.48	20.2	1.983	0.677
1.43	17.5	2.170	0.665
1.31	9.3	3.400	0.604
1.15	23.05†	1.018	0.511
1.14	30.4	0.863	0.575
1.12	30.0	0.800	0.536
1.01	20.2	0.958	0.477
0.97	9.3	2.070	0.495
0.93	30.0	0.601	0.483
0.87	9.3	1.650	0.443
0.85	30.4	0.498	0.443
0.77	10.1	1.146	0.373
0.75	23.05†	0.480	0.371
0.71	8.7	1.218	0.372
0.63	10.1	0.867	0.349
0.63	6.9	1.165	0.321
0.63	30.4	0.287	0.349
0.56	30.0†	0.265	0.355
0.49	6.9	1.165	0.321
0.40	11.3	0.431	0.312
0.40	11.3	0.443	0.305
0.33	9.3	0.304	0.212
0.27	9.3	0.181	0.158

† 90% of oxygen added after the discharge

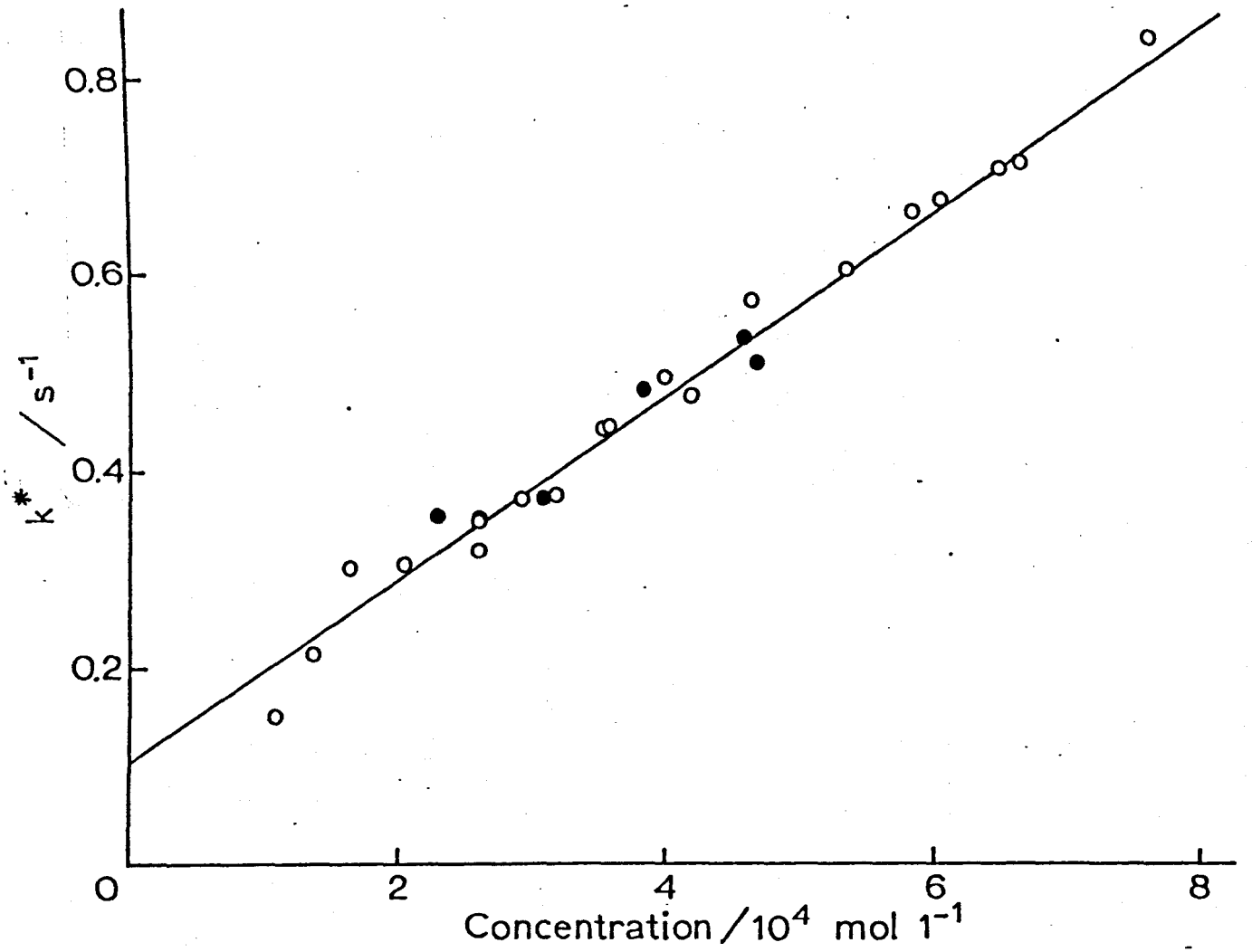

FIGURE 3.3 The Collisional Deactivation of $O_2(^1\Delta_g)$ at Room Temperature;

$K^* = k_q[O_2] + k_w$

high pressures (chapter 1), is also in agreement with ours; they had ascribed the low value obtained to unknown systematic errors in their system. Errors in the earlier measurements probably result from the choice of the weak atmospheric band at 1270nm to follow the concentration of $O_2(^1\Delta_g)$. This band comes in a region of the spectrum for which there is no really sensitive detection apparatus; in comparison the emissions at 634nm and in particular that at 762nm are very easily monitored. In general, it is found with such measurements that the presence of impurities tends to raise the measured rate constant compared with the true value, as was mentioned for the quenching of $O_2(^1\Sigma_g^+)$ (chapter 1), and this may be another factor contributing to these high values.

The wall deactivation efficiency for quenching of $O_2(^1\Delta_g)$ in the discharge flow shock tube is lower than that reported by other authors for Pyrex glass, but similar to that obtained by Wayne[74] using a reaction tube freshly rinsed in HF. Considering the simple method used to clean the tube (section 2), the low rate of deactivation at the wall is a pleasant surprise; the effect of dirt in the system is to increase the rate of this wall deactivation and hence the measured decay along the tube.

These experiments give us considerable information about the conditions most suitable for high temperature studies:

(i) The most suitable initial pressures are in the range 0.8-1.0 KN m^{-2}.

(ii) The discharge power may be set at 100W only at pressures $\geq$ 0,8 KN m^{-2}; at lower pressures a reduction in power is essential.

(iii) High flow rates are the most satisfactory except at very low pressures.

(iv) There is no advantage in passing only 10% of the oxygen through the discharge .

3.2.3. Application to quenching by other species

In principle, there is no reason why this system should not be used to study the quenching of $O_2(^1\Delta_g)$ by other species. Although no full scale measurements have been made, the decay of $O_2(^1\Delta_g)$ along the shock tube test section is always measured prior to each shock, and it should be possible to make an approximate estimate of the rate of quenching by nitrogen in oxygen/nitrogen mixtures from the relation

$$K^* = \frac{\alpha_\ell v}{2} = k_w + k_{qO_2}[O_2] + k_{qN_2}[N_2] \qquad (3.21)$$

and the values of k_{qO_2} and k_w obtained before. However, in practice it is quite impossible to maintain the walls as clean while performing shock experiments as when performing room temperature experiments only. Although there does seem to be some internal consistency between the measurements at each composition, k_w changes too much between experiments for satisfactory estimates to be made. If one takes the accepted rate constant for quenching of $O_2(^1\Delta_g)$ by nitrogen ($\sim$ 50 dm^3 $mole^{-1}$ s^{-1}) and works backwards to k_w, values in the region of 0.28 ± 0.06 s^{-1} are obtained. These do not compare very favourably with our earlier estimate of 0.106 ± 0.013 s^{-1}, and this illustrates the problem of maintaining a perfectly clean system while firing shocks into it.

In conclusion, it should be possible to study the quenching of $O_2(^1\Delta_g)$ by other species in our system, but, unless the rate of quenching is large in comparison with that of deactivation at the wall, it is not realistic to perform accurate room temperature measurements and shock studies at the same time.

3.3. The Deactivation of $O_2(^1\Sigma_g^+)$

3.3.1. Quenching by oxygen

By studying the ratios of the $O_2(^1\Sigma_g^+)$ emission at 762 nm and the dimol emission at 634nm, it is possible to estimate the room temperature rate of deactivation of $O_2(^1\Sigma_g^+)$.

Equation (3.15) shows that the steady state concentration of $O_2(^1\Sigma_g^+)$ is given by

$$[O_2(^1\Sigma_g^+)] = \frac{k_1[O_2(^1\Delta_g)]^2}{k_2[M] + k'_w} \qquad (3.15)$$

and it follows from equations (3.4) and (3.19) that

$$\frac{I_\Sigma}{I_D} = \frac{C[O_2(^1\Sigma_g^+)]}{[O_2(^1\Delta_g)]^2} \qquad (3.22)$$

where C is a proportionality constant, which is a function of the probabilities of the emissions at 762 and 634nm, the sensitivities of the two photomultipliers at the different wavelengths, and the width of the photomultiplier slits.

Equations (3.15) and (3.22) may be combined to give

$$\frac{I_\Sigma}{I_D} = \frac{Ck_1}{k_2[M] + k'_w} \qquad (3.23)$$

Of the seven variables in equation (3.23), I_Σ and I_D may be measured directly, [M] is a straightforward function of the pressure in the test gas, the value of k_1 is well known (chapter 1), and k'_w, although a complex function, can be calculated at any given pressure as outlined below. Thus there are two unknowns, C and k_2, and by measuring I_Σ/I_D at two pressures, two simultaneous equations are obtained; these are easily solved for k_2 (in fact, a value for k_1 is needed only if an estimate of C is required). Preliminary measurements in pure oxygen at pressures ~ 0.8 KN m^{-2} gave a value for k_2 of $(1.0 \pm 0.5) \times 10^5$ dm^3 $mole^{-1}$ s^{-1}. This estimate, although

of low precision, is quite reasonable, considering the difficulty of maintaining completely dry test gases (chapters 1 and 2); assuming a rate constant for quenching by dry oxygen of 2.6×10^4 dm^3 $mole^{-1}$ s^{-1} and a rate constant for deactivation by water of 2.4×10^9 dm^3 $mole^{-1}$ s^{-1}, about 30 ppm of water would give a value for k_2 of 1×10^5 dm^3 $mole^{-1}$ s^{-1}. This rate constant has been used throughout this work, but recently it has been remeasured with more precision; by measuring I_Σ/I_D at many different pressures (Table 3.2) and using the fitting optimisation computer program, ITERAT (Chapter 6) to obtain the best values of the two unknowns, k_2 was estimated to be $(1.07 \pm 0.42) \times 10^5$ dm^3 $mole^{-1}$ s^{-1}.

The rate of deactivation of $O_2(^1\Sigma_g^+)$ at the wall, k'_w, was calculated for these experiments as follows: Derwent and Thrush have shown that in a flowing gas system, k'_w is given by the relation

$$k'_w = \frac{1}{\frac{r^2(P/P_o)}{8D_o} + \frac{2r}{\gamma_\Sigma \bar{c}}} \qquad (3.24)$$

where r is the radius of the tube (2.54 cm), P the downstream pressure (and P_o atmospheric pressure), γ_Σ is the probability of surface quenching of $O_2(^1\Sigma_g^+)$ (measured by several authors to be 1.0×10^{-2} for a pyrex surface[92]), and $\bar{c}$ is the mean speed of the molecules of the gas (441 ms^{-1} in pure oxygen at 293 K). D_o is the diffusion coefficient for the gas at atmospheric pressure; the reported self diffusion coefficients of oxygen and nitrogen are similar ($\sim 2 \times 10^{-5}$ m^2 s^{-1}), and, as no measurements on diffusion in oxygen/nitrogen mixtures have been recorded, the value measured by Wayne et. al.[136] for the rate of diffusion of $O_2(^1\Delta_g)$ in oxygen (2.01×10^{-5} m^2 s^{-1}) was chosen. Although we have seen that γ_D, the probability of surface quenching of $O_2(^1\Delta_g)$, is sensitive to the state of the tube wall ($\gamma_D = 1\text{-}4 \times 10^{-5}$), the effect on the far more efficient quenching of $O_2(^1\Sigma_g^+)$ at the wall was considered to be much less important,

TABLE 3.2

Deactivation of $O_2(^1\Sigma_g^+)$ in pure oxygen at 295 K

PRESSURE (KN m^{-2})	I_Σ (mv)	I_D (mv)	I_{Σ/I_D}
0.87	7910	38.7	216.1
0.93	7650	38.7	209.0
0.995	6050	31.0	209.3
1.135	4280	23.9	196.3
1.24	2930	17.5	190.3
1.315	2220	14.2	183.5
1.44	1460	10.4	175.9

and the value quoted above was used in all calculations.

At room temperature, equation (3.24) reduces to

$$k'_w = \frac{10^2}{3.960P + 1.152} \qquad (3.25)$$

where P has units of KN m^{-2}. At a typical pressure in pure oxygen of 0.9 KN m^{-2}, k'_w is approximately 21 s^{-1} and $k_2[O_2(^3\Sigma_g^-)]$ approximately 37 s^{-1}, showing that the two processes of removal of $O_2(^1\Sigma_g^+)$ are of similar importance. The mean speed of nitrogen molecules is 472 ms^{-1} at 293 K, but equation (3.25) was not corrected for experiments using oxygen/nitrogen mixtures as the effect on k_w is very small. This correction is, in fact, made in the computer analysis of our high temperature studies as part of subroutine RATES (Chapter 6).

3.3.2. Quenching by nitrogen

The rate constant for quenching of $O_2(^1\Sigma_g^+)$ by nitrogen could be measured by a technique similar to that outlined in the previous section; by measuring k_2 in several oxygen/nitrogen mixtures of known composition, the rate constant in pure nitrogen should be easily estimated. However, because k_2 is obtained from such experiments only with difficulty, a slightly different technique was used: equation (3.23) was written in the more precise version

$$\frac{I_\Sigma}{I_D} = \frac{Ck_1}{k_2[O_2] + k_3[N_2] + k'_w} \qquad (3.26)$$

and, using the values of C and k_2 obtained from experiments in pure oxygen, k_3 was calculated by measuring I_Σ/I_D in mixtures of changing composition. Experiments were performed at a constant partial pressure of oxygen, using mixtures containing up to 65% N_2. Because the pressure dependence of the wall reaction is not a simple function, the results could not be analysed graphically; consequently a rate constant was calculated at each composition (Table 3.3) and the estimates averaged. In this way the rate constant for

TABLE 3.3

The rate of quenching of $O_2(^1\Sigma_g^+)$ by nitrogen at 295 K

$[N_2]/10^{-5}$ mole dm^3	I_Σ/I_Δ	$k_3/10^6$ dm^3 $mole^{-1}$ s^{-1}	
		$k_2 = 1.0 \times 10^5$ $mole^{-1}$ s^{-1}	$k_2 = 2.6 \times 10^4$ dm^3 $mole^{-1}$ s^{-1}
8.21	15.67	1.14	1.26
15.59	10.91	1.07	1.15
19.43	9.09	1.02	1.08
22.17	8.04	1.03	1.09
24.63	7.72	0.98	1.03
28.73	6.61	1.01	1.05

In all measurements: $[O_2] = 1.587 \times 10^{-4}$ mole dm^{-3}

$C = 5.763$ dm^3 $mole^{-1}$ s^{-1}

quenching of $O_2(^1\Sigma_g^+)$ by nitrogen was estimated to be $(1.04 \pm 0.05) \times 10^6$ dm^3 $mole^{-1}$ s^{-1}. The accepted value of this rate constant is 1.3×10^6 dm^3 $mole^{-1}$ s^{-1} (Table 1.1); the agreement is quite satisfactory considering the simple nature of the measurements.

Calculations using the rate constant for quenching of $O_2(^1\Sigma_g^+)$ by dry oxygen, gave a very similar result ($(1.11 \pm 0.08) \times 10^6$ dm^3 $mole^{-1}$ s^{-1}). Thus it appears that, despite the uncertain rate constant for quenching of $O_2(^1\Sigma_g^+)$ by oxygen in our apparatus, this method will give reasonable results for quenchers that deactivate $O_2(^1\Sigma_g^+)$ significantly faster than oxygen.

The rate constants for deactivation of $O_2(^1\Sigma_g^+)$ at room temperature are required in the high temperature analysis (Chapter 4). The rate constant for quenching by oxygen measured in this apparatus has been used in the high temperature work as it is certainly more reasonable than the accepted value in perfectly dry oxygen. However, the accepted value for the rate of quenching by nitrogen is more satisfactory than the rough estimate in this section, and has been preferred for the later studies.

4. REACTIONS TAKING PLACE BEHIND THE SHOCK FRONT

4.1. Introduction

Reactions of singlet molecular oxygen that it should be of interest to study in the shock tube include the collisional deactivation processes

$$O_2(^1\Delta_g) + M \longrightarrow O_2(^3\Sigma_g^-) \qquad (1.33)$$

$$O_2(^1\Sigma_g^+) + M \longrightarrow O_2(^1\Delta_g) \qquad (1.32)$$

the energy pooling reaction

$$O_2(^1\Delta_g) + O_2(^1\Delta_g) \longrightarrow O_2(^1\Sigma_g^+) + O_2(^3\Sigma_g^-) \qquad (1.13)$$

and the dimol emission

$$O_2(^1\Delta_g) + O_2(^1\Delta_g) \longrightarrow O_2(^3\Sigma_g^-) + O_2(^3\Sigma_g^-) + h\nu(634nm) \qquad (1.12)$$

In this chapter the changes in emission from $O_2(^1\Sigma_g^+)$ and $O_2(^1\Delta_g)$ behind the shock front, are compared with the emission prior to the shock, and related to the rates at which these reactions take place. The basic equations derived here are used in the computer analysis of our data (Chapter 6); the results obtained from such analysis are discussed in Chapters 7 and 8.

4.2. The deactivation of $O_2(^1\Delta_g)$

In Chapter 3 it was shown that the decrease in concentration of $O_2(^1\Delta_g)$ along the shock tube test section is first order

$$\frac{d[O_2(^1\Delta_g)]}{d\ell} = \frac{\alpha_\ell}{2}[O_2(^1\Delta_g)] \qquad (3.7)$$

and that the decay constant, α_ℓ, is a function of the gas flow velocity. When a shock is fired into the test gas, the heated, compressed gas behind the shock front is driven back down the tube at a velocity of ~ 1 Km s^{-1}, in comparison with which the initial flow velocity is negligible. Thus, if no reaction occurs in the time it takes the shock heated gas to pass the observation station, it will give a record of the decay along the tube prior to the shock.

It follows from conservation of mass across the shock front that the gas particle velocity, W_p, is related to the shock velocity, U, and the densities, ρ_1 and ρ_2, in the test gas before and behind the shock front (see figure (1.7)):

$$\rho_1 U_1 = \rho_2 U_2 \qquad (1.47)$$

$$U_1 = -U \qquad (4.1)$$

$$U_2 = -(U-W_p) \qquad (4.2)$$

$$W_p = U(1-{}^1/\rho_{21}) = \frac{d\ell}{dt_p} \qquad (4.3)$$

where ρ_{21} is the ratio $({}^{\rho 2}/\rho_1)$. By definition, W_p is equal to $\frac{d\ell}{dt_p}$, where ℓ is the distance travelled by a section of gas in order to pass the observation station at a particle time, t_p, after the shock front has passed. The time of flight of the section of shock-heated gas is significantly different on the particle time scale from that measured on the laboratory time scale: the particle time is given by[102]

$$W_p = {}^\ell/t_p \qquad (4.4)$$

$$\therefore \quad t_p = \frac{\ell}{W_p} \qquad (4.5)$$

and the laboratory time, t_ℓ, by

$$t_\ell = \frac{\ell}{W_p} - \frac{\ell}{U} \tag{4.6}$$

where $^{\ell}/_{W_p}$ gives the time of arrival of the section of gas and $^{\ell}/_{U}$ the time of arrival of the shock front.

$$\frac{t_p}{t_\ell} = \frac{\ell/W_p}{\ell/W_p - \ell/U} = \frac{U}{(U-W_p)} = \frac{U_1}{U_2} \tag{4.7}$$

From equation (1.47)

$$\frac{U_1}{U_2} = \rho_{21} \tag{4.8}$$

and hence

$$t_p = \rho_{21}\, t_\ell \tag{4.9}$$

This result is valid for ideal shocks only (Chapter 5); it is important because all experimental measurements are made in laboratory time, and the time scale is converted to particle time for analysis of the data.

By analogy with equation (3.7), the decay of the emission from the shock-heated gas with time, α_t, is given by

$$\frac{d[O_2(^1\Delta_g)]}{dt_p} = -\frac{\alpha_t}{2}[O_2(^1\Delta_g)] \tag{4.10}$$

$$\frac{d[O_2(^1\Delta_g)]}{dt_p} = \frac{d[O_2(^1\Delta_g)]}{d\ell}\,\frac{d\ell}{dt_p} \tag{4.11}$$

α_ℓ and α_t are related by equations (3.7), (4.10) and (4.3):

$$\frac{d[O_2(^1\Delta_g)]}{dt_p} = -\frac{U\alpha_\ell}{2}\,(1-{}^1/\rho_{21})\,[O_2(^1\Delta_g)] \tag{4.12}$$

$$\alpha_t = U\alpha_\ell\,(1-{}^1/\rho_{21}) \tag{4.13}$$

This treatment assumes that the decay in emission seen as the shock passes the observation station is purely a reflection of the decay prior to the shock and that no $O_2(^1\Delta_g)$ is removed by collisonal quenching and

by deactivation at the wall in the time, t_p, that it takes the section of gas to reach the observation station. The effect of these reactions may be calculated using equation (3.2):

$$\frac{d[O_2(^1\Delta_g)]}{dt} = -\{k_q[O_2(^1\Delta_g)][M] + k_w[O_2(^1\Delta_g)]\} \tag{3.2}$$

(where k_q and k_w are now the rate constants for the reactions taking place at the temperature behind the shock front)

$$\int_{[O_2(^1\Delta_g)]_o}^{[O_2(^1\Delta_g)]_t} \frac{1}{[O_2(^1\Delta_g)]}\, d[O_2(^1\Delta_g)] = \int_o^{tp} -\{k_q[M] + k_w\}\, dt \tag{4.14}$$

$$\ln \frac{[O_2(^1\Delta_g)]_t}{[O_2(^1\Delta_g)]_o} = -t_p\{k_q[M] + k_w\} \tag{4.15}$$

$$\frac{[O_2(^1\Delta_g)]_t}{[O_2(^1\Delta_g)]_o} = e^{-\{k_q[M] + k_w\}t_p} \tag{4.16}$$

$[O_2(^1\Delta_g)]_o$ is the concentration of $O_2(^1\Delta_g)$ at a point along the shock tube immediately after the shock front has passed, while $[O_2(^1\Delta_g)]_t$ is the concentration after the time t_p. $[O_2(^1\Delta_g)]_o$ is related to the initial post-shock concentration of $O_2(^1\Delta_g)$ at the observation station, $[O_2(^1\Delta_g)]_{o,o}$, by the first order decay equation

$$[O_2(^1\Delta_g)]_o = [O_2(^1\Delta_g)]_{o,o}\, e^{-(\alpha_t t_p/2)} \tag{4.17}$$

Equations (4.10) and (4.11) may be combined to give:

$$\frac{[O_2(^1\Delta_g)]_t}{[O_2(^1\Delta_g)]_{o,o}} = e^{-\{k_q[M] + k_w + \frac{\alpha_t}{2}\}t_p} \tag{4.18}$$

$$\ln \frac{[O_2(^1\Delta_g)]_t}{[O_2(^1\Delta_g)]_{o,o}} = -\{k_q[M] + k_w + \frac{\alpha_t}{2}\}t_p \tag{4.19}$$

The concentration of $O_2(^1\Delta_g)$ is monitored using the dimol emission, I_D, which varies with $[O_2(^1\Delta_g)]^2$:

$$\therefore \quad \ln \frac{I_D}{I_D^o} = -\{2k_q[M] + 2k_w + \alpha_t\}t_p \qquad (4.20)$$

(where I_D^o is the initial post-shock emission at the observation station). The rate constant for quenching of $O_2(^1\Delta_g)$ at the temperature of the shock is obtained by plotting $\ln(I_D/I_D^o)$ against t_p and measuring the increase of the gradient from that prior to the shock, which is obtained using equation (4.13)(Fig.4.1). In shock-heated oxygen at temperatures greater than 1000 K, α_t has a value of $\sim 10^3$ s^{-1}. Assuming that the temperature of the wall is not significantly different from that prior to the shock, k_w will be ~ 0.2 s^{-1} and may be neglected. The value of $k_q[M]$ will be comparable with that of α_t if $k_q \sim 5 \times 10^5$ dm^3 $mole^{-1}$ s^{-1}. If k_q is less than $\sim 5 \times 10^4$ dm^3 $mole^{-1}$ s^{-1} (about fifty times the rate constant at room temperature), the change in gradient is not likely to be significant.

Preliminary measurements showed no significant change of the decay from that observed prior to the shock, and many other measurements since then have confirmed this to be the case. This negative result is very important, and is given here, because it allows us to neglect the collisional deactivation of $O_2(^1\Delta_g)$ when studying the dimol emission and the formation and removal of $O_2(^1\Sigma_g^+)$ behind the shock front.

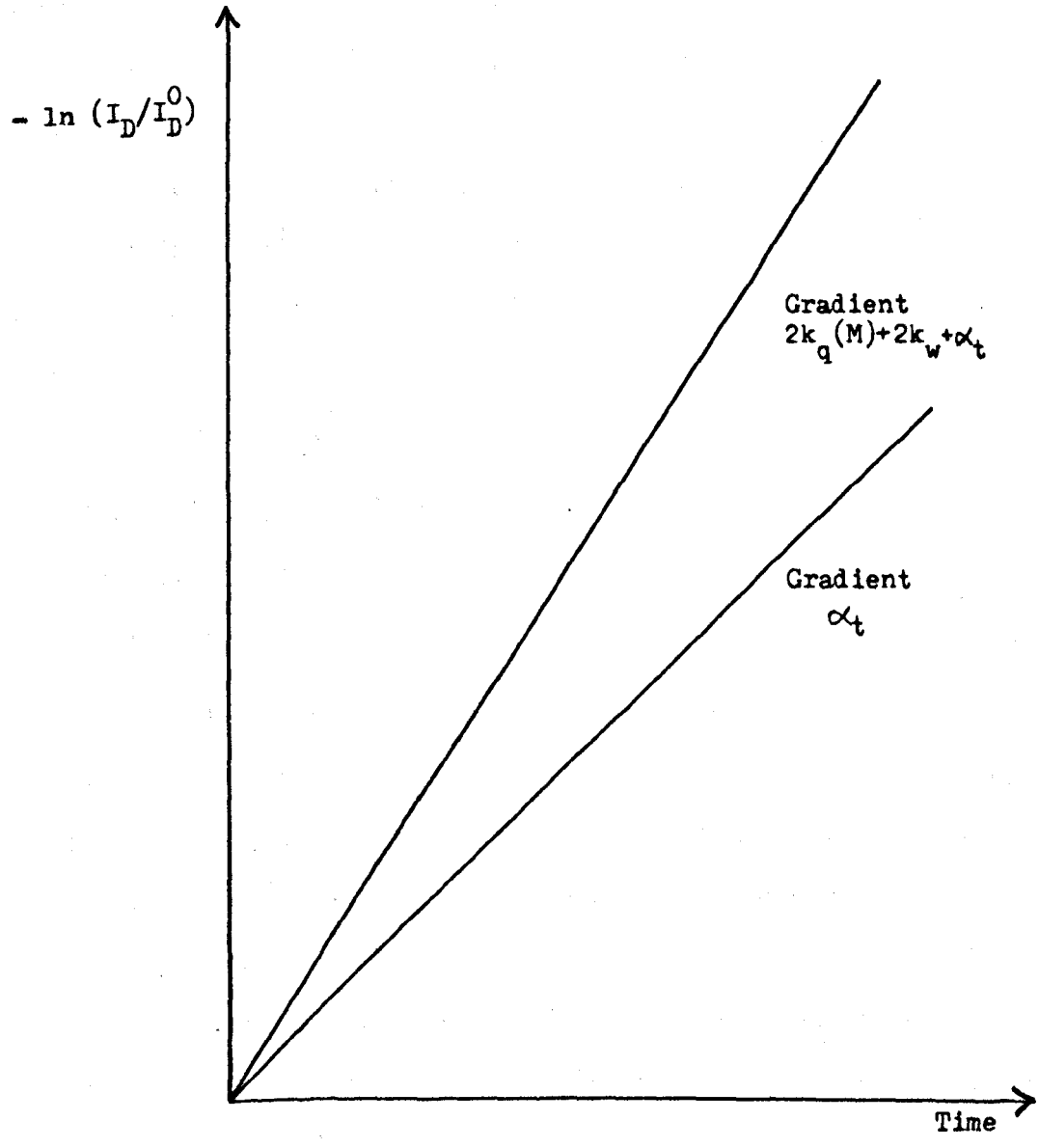

FIGURE 4.I Measurement of the Rate of Quenching of $O_2(^1\Delta_g)$ Behind the Shock Front

4.3. The Dimol Emission

In section 4.2. no account was taken of the change in the level of emission from $O_2(^1\Delta_g)$ that results from the shock compression. This was acceptable because in an ideal shock the density and temperature behind the shock front are constant, and their effect on the level of emission should be the same at all points along the tube. The intensity of the emission from $O_2(^1\Delta_g)$ should be a function of its concentration; for the dimol emission at 634nm, it was indicated in Chapter 3 that the relation is:

$$I_D = k_D[O_2(^1\Delta_g)]^2 \qquad (3.4)$$

As $[O_2(^1\Delta_g)]$ is proportional to the density of the gas, the dimol emission should vary with the density squared:

$$I_D \alpha \rho^2 \qquad (4.21)$$

The nature of this emission was discussed in Chapter 1, and it was concluded that the dimol reaction is probably a simple collisional process, in the gaseous phase at least. If this is the case, the reaction will be collision controlled, with a zero activation energy:

$$k = CT^{\frac{1}{2}} \qquad (1.2)$$

Thus the intensity of emission, I_{D2}, from the shock-heated gas should be related to that prior to the shock, I_{D1}, by the equation

$$\frac{I_{D2}}{I_{D1}} = \left(\frac{\rho_2}{\rho_1}\right)^2 \left(\frac{T_2}{T_1}\right)^{\frac{1}{2}} = \rho_{21}^{\ 2}\, T_{21}^{\frac{1}{2}} \qquad (4.22)$$

(where T_1, T_2 are the temperatures before and behind the shock front), if the dimol reaction is a collisonal process.

The calculations refer to the emission at any point along the shock tube, immediately after the shock front has passed. Because it was shown in the previous section that

$$\alpha_t \gg 2\{k_q[M] + k_w\} \qquad (4.23)$$

equation (4.18) may be rewritten

$$\frac{[O_2(^1\Delta_g)]_t}{[O_2(^1\Delta_g)]_{o,o}} = e^{-\alpha_t t_p/2} \tag{4.24}$$

and the dimol emission, I_{D2}, seen at the observation station at a time t_p after the shock front has passed is given by:

$$I_{D2} = I^o_{D2}\, e^{-\alpha_t t_p} \tag{4.25}$$

or, using equation (4.22) for a simple collisional process:

$$\frac{I_{D2}}{I^o_{D1}} = \rho_{21}{}^2 T_{21}{}^{\frac{1}{2}} e^{-\alpha_t t_p} \tag{4.26}$$

where I^o_{D1} is the level of emission at the observation station prior to the shock, and I^o_{D2} is the emission immediately after the shock front has passed.

For the analysis of real shocks, the relation

$$\frac{I_{D2}}{I^o_{D1}} = K\rho_{21}{}^2 T_{21}{}^{\frac{1}{2}} e^{-\alpha_t t_p} \tag{4.27}$$

is used to fit a line to the experimental data. By comparison with equation (4.22), it may be seen that K should be equal to one for a purely collisional process.

The temperature dependence of the reaction will be different if an O_4 molecule of reasonable stability is formed as an intermediate. If the reaction

$$O_2(^1\Delta_g) + O_2(^1\Delta_g) \rightleftharpoons O_4 \tag{4.28}$$

is considered to be at equilibrium, the intensity of the dimol emission behind the shock front, given by equations (3.4) and (4.21) is related to the concentration of $O_2(^1\Delta_g)$ and temperature by[29]

$$I_{D2} = k' \rho_2{}^2 e^{\Delta H/RT_2} \tag{4.29}$$

where k' is a constant directly related to the equilibrium constant of

equation (4.28), ρ_2 is the density of the gas and ΔH the enthalpy change for reaction (4.28).

Similarly, at room temperature, the emission is given by

$$I_{D1} = k' \rho_1^{\,2} e^{\Delta H/RT_1} \tag{4.29a}$$

Equations (4.29) and (4.29a) combine with equation (4.27) to give the relation

$$KT_{21}^{\frac{1}{2}} = e^{\frac{\Delta H}{R}\left[\frac{1}{T_2} - \frac{1}{T_1}\right]} \tag{4.30}$$

By plotting $\ln(K\, T_{21}^{\frac{1}{2}})$ against $^1/T_2$, the dissociation energy of the O_4 molecule is found; it will have a physical significance only if the dimol reaction is not a simple collisional process.

4.4. Formation and removal of $O_2(^1\Sigma_g^+)$

The processes in which $O_2(^1\Sigma_g^+)$ is formed from $O_2(^1\Delta_g)$ and removed by quenching and radiative processes, were outlined in Chapter 3.2.1. The rate of change in the concentration of $O_2(^1\Sigma_g^+)$ is given by

$$\frac{d[O_2(^1\Sigma_g^+)]}{dt} = k_1[O_2(^1\Delta_g)]^2 - k_2[O_2(^1\Sigma_g^+)][M] - k'_w[O_2(^1\Sigma_g^+)] \quad (3.14)$$

Under the steady state conditions in Chapter 3, $\frac{d[O_2(^1\Sigma_g^+)]}{dt}$ was equal to 0, and thus

$$[O_2(^1\Sigma_g^+)] = \frac{k_1[O_2(^1\Delta_g)]^2}{k_2[M] + k'_w} \quad (3.15)$$

When a shock wave is passed through the test gas, the initial effect of the shock compression is to increase the concentration of $O_2(^1\Sigma_g^+)$ by a factor of the density ratio, ρ_{21}, across the shock front. Following the initial compression, there will be a relaxation zone in which the concentration of $O_2(^1\Sigma_g^+)$ is changing to its new steady state level at the temperature behind the shock front. At the new level, the concentration of $O_2(^1\Sigma_g^+)$ is again governed by equation (3.15), but the rate constants now describe the reactions at the temperature behind the shock front.

The relaxation may be treated mathematically by integration of equation (3.14), using the form

$$\int_{[O_2(^1\Sigma_g^+)]_o}^{[O_2(^1\Sigma_g^+)]_{t_p}} \frac{1}{k_1[O_2(^1\Delta_g)]^2 - [O_2(^1\Sigma_g^+)]\{k_2[M] + k'_w\}} \, d[O_2(^1\Sigma_g^+)] = \int_o^{t_p} dt \quad (4.31)$$

where all the rate constants apply to the shock-heated gas, to give

$$\ln\left\{\frac{k_1[O_2(^1\Delta_g)]^2 - [O_2(^1\Sigma_g^+)]_o\{k_2[M] + k'_w\}}{k_1[O_2(^1\Delta_g)]^2 - [O_2(^1\Sigma_g^+)]_{t_p}\{k_2[M] + k'_w\}}\right\} = \{k_2[M] + k'_w\}_{t_p} \quad (4.32)$$

or, in exponential form

$$\left\{k_1[O_2(^1\Delta_g)]^2 - [O_2(^1\Sigma_g^+)]t_p \{k_2[M] + k'_w\}\right\}$$
$$= \left\{k_1[O_2(^1\Delta_g)]^2 - [O_2(^1\Sigma_g^+)]_o \{k_2[M] + k'_w\}\right\} e^{-\{k_2[M] + k'_w\}t_p} \quad (4.33)$$

At this stage, it is necessary to make certain simplifications. It was shown in Chapter 3 that at room temperature and the initial pressure, $k_2[M]$ and k'_w are of the same order of magnitude. However, the pressure ratio across the shock front in a shock of velocity 1.4 Km s^{-1} is $\sim$ 20 and the rate of diffusion of $O_2(^1\Sigma_g^+)$ to the walls is reduced by this factor. Hence k'_w has a value only 6-7% that in the gas prior to the shock. At the same time the density, and hence the concentration of the gas, behind the shock front is a factor of 3.5-6 greater than that prior to the shock. As a result, if k_2 is unchanged at the temperature of the shock, k'_w is only of the order of 1% of $k_2[M]$. Preliminary results showed that k_2 is in fact 1-2 orders of magnitude greater at the temperature of the shock than at room temperature, and thus that k'_w is negligible in comparison with $k_2[M]$.

Equation (4.33) may then be re-written

$$\left\{k_1[O_2(^1\Delta_g)]^2 - k_2[M][O_2(^1\Sigma_g^+)]t_p\right\} =$$
$$\left\{k_1[O_2(^1\Delta_g)]^2 - k_2[M][O_2(^1\Sigma_g^+)]_o\right\} e^{-k_2[M]t_p} \quad (4.34)$$

and by rearrangement the relation

$$\frac{[O_2(^1\Sigma_g^+)]t_p}{[O_2(^1\Sigma_g^+)]_o} = \left\{\frac{k_1[O_2(^1\Delta_g)]^2}{k_2[M][O_2(^1\Sigma_g^+)]_o}\left[1 - e^{-k_2[M]t_p}\right] + e^{-k_2[M]t_p}\right\} \quad (4.35)$$

is obtained.

As the initial change in the concentrations of $O_2(^1\Delta_g)$, M and $O_2(^1\Sigma_g^+)$ across the shock front are merely a reflection of the shock

compression, the ratio $\frac{[O_2(^1\Delta_g)]^2}{[M][O_2(^1\Sigma_g^+)]_o}$ is the same as that at room temperature where, using T_1 and T_2 in parentheses to indicate the rate constants at the temperatures before and behind the shock front

$$\frac{[O_2(^1\Delta_g)]^2}{[M][O_2(^1\Sigma_g^+)]_o} = \frac{k_2(T_1) + k'_w/[M]}{k_1(T_1)} \tag{4.36}$$

Equation (4.35) may then be simplified to give the form

$$\frac{[O_2(^1\Sigma_g^+)]_t}{[O_2(^1\Sigma_g^+)]_o}p = K\left[1 - (1-^1/K)\, e^{-k_2(T_2)[M]t_p}\right] \tag{4.37}$$

where

$$K = \frac{k_1(T_2)}{k_2(T_2)} \cdot \frac{k_2(T_1) + k'_w/[M]}{k_1(T_1)} \tag{4.38}$$

As the emission from $O_2(^1\Sigma_g^+)$ varies directly with its concentration, equation (4.37) may be rewritten

$$\frac{I_{\Sigma 2}}{I^o_{\Sigma 2}} = K\left[1 - (1-^1/K)\, e^{-k_2(T_2)[M]t_p}\right] \tag{4.39}$$

where $I^o_{\Sigma 2}$ and $I_{\Sigma 2}$ are respectively the emission immediately after the shock compression and the emission after a time, t_p has passed.

A plot of equation (4.39) is shown schematically in figure (4.2). The relaxation time, τ_{rel}, observed in the zone where the level of emission relaxes to the new equilibrium level at the high temperature, is, by definition, equal to $^1/k_2(T_2)[M]$; when relaxation is complete, the ratio $I_{\Sigma 2}/I^o_{\Sigma 2}$ will be equal to K. Thus the new rate of collisional deactivation of $O_2(^1\Sigma_g^+)$, $k_2(T_2)$, is obtained from the relaxation time, and this estimate, together with the value of K and the room temperature rate constants discussed in Chapter 3, is used to calculate the rate constant, $k_1(T_2)$, for the energy pooling reaction at temperature T_2.

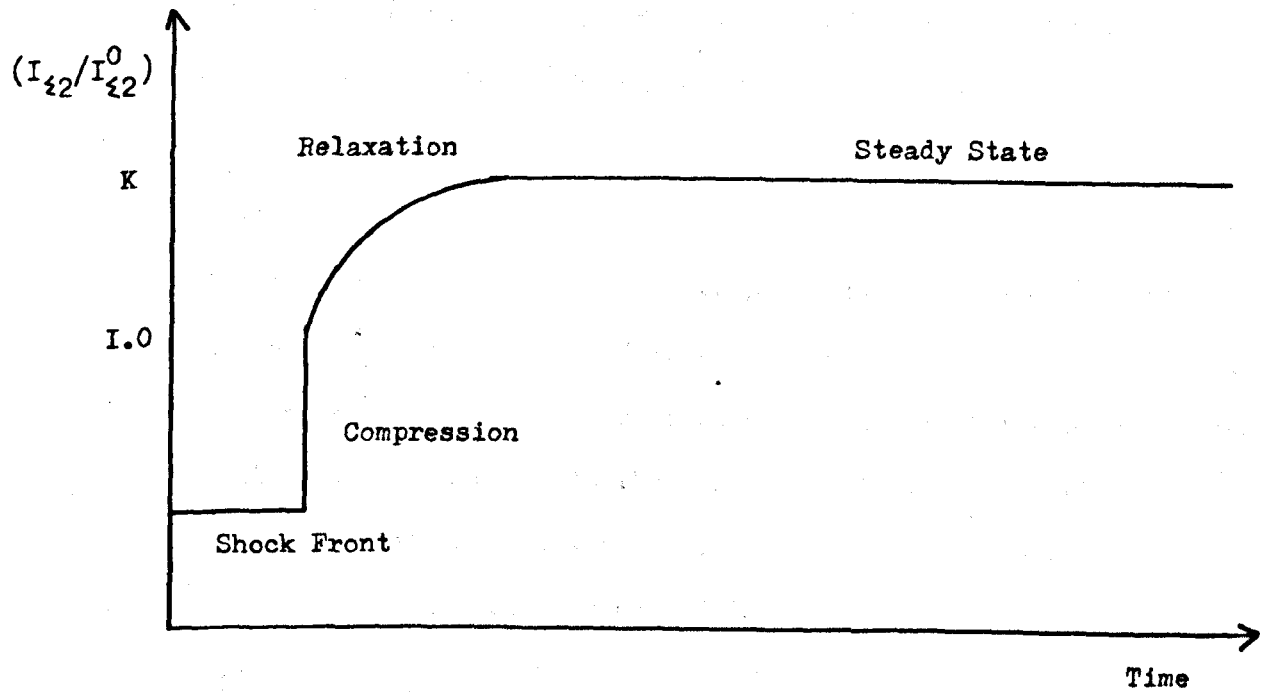

FIGURE 4.2 Post-Shock Emission From $O_2(^1\Sigma_g^+)$.

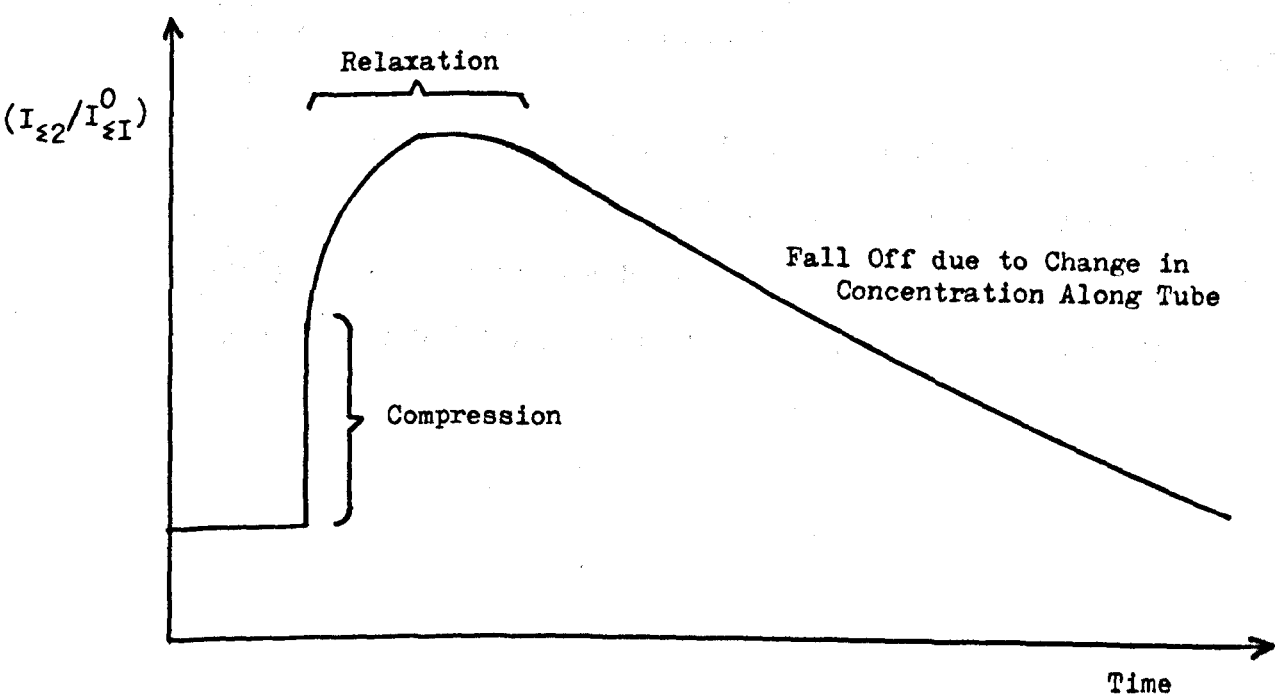

FIGURE 4.3 Post-Shock Emission From $O_2(^1\Sigma_g^+)$; Decay Included

If the ratio of the high temperature and room temperature rate constants, K, is equal to unity, equation (4.39) reduces to

$$\frac{I_{\Sigma 2}}{I^{o}_{\Sigma 2}} = 1 \qquad (4.40)$$

and relaxation measurements will not be possible. However, useful information may still be obtained in certain circumstances (Chapter 8).

Again, no account has been taken of the decay of the emission from $O_2(^1\Sigma_g^+)$ along the tube prior to the shock; it follows from Chapter 3 and equation (4.21) that the emission at any point along the shock tube immediately after the shock has passed is given by

$$I^{o}_{\Sigma 2} = \rho_{21} I^{o}_{\Sigma 1} e^{-\alpha_t t_p} \qquad (4.41)$$

where $I^{o}_{\Sigma 1}$ is the level of emission at the observation station immediately prior to the shock. Hence, equation (4.39) becomes

$$\frac{I_{\Sigma 2}}{I^{o}_{\Sigma 1}} = K\left[1-(1-^1/K)\ e^{-t_p \tau_{rel}}\right] \rho_{21} e^{-\alpha_t t_p} \qquad (4.42)$$

Equation (4.42) is shown schematically in figure (4.3); there are now three obvious zones: compression; relaxation, and the decay of emission from $O_2(^1\Sigma_g^+)$ along the tube, which is again a reflection of the fall off in concentration of $O_2(^1\Delta_g)$ prior to the shock, as in section (4.2).

5. PROCESSES LEADING TO NON-UNIFORM CONDITIONS BEHIND THE SHOCK FRONT

5.1. Introduction

In chapter 4 the equations describing the reactions taking place behind the shock front were derived assuming the density and temperature to be constant. However, in a real gas, vibrational relaxation and non-uniform flow behind the shock front give rise to significant changes in these conditions. As an example of the effect of vibrational relaxation, when a shock of velocity 1.4 Km s^{-1} is passed into pure oxygen, the temperature, T, and the density ratio, ρ_{21}, immediately behind the shock front are 1323 K and 4.718 respectively. At long times, when vibrational relaxation is complete, the temperature is significantly lower (1183 K), and the density ratio has risen to 5.448. It is clear that such changes may, if not corrected, give rise to large errors in the equations derived in chapter 4. In this chapter, the importance of the effects of these non-uniform conditions is discussed, and corrections are made to the equations in chapter 4.

5.2. Vibrational Relaxation

In experimental measurements of the temperature dependence of vibrational relaxation rates, it is common practice to follow the changes in density of the gas behind the shock front. As the relaxation is a first order process, in a pure gas the density may be expressed in the form

$$\rho_{t1} = \rho_{A1} + (\rho_{21} - \rho_{A1})(1 - e^{-t_p/\tau_{vib}}) \qquad (5.1)$$

where ρ_{A1} and ρ_{21} are the frozen and relaxed density ratios across the shock front and ρ_{t1} is the density ratio at any given time. τ_{vib} is the vibrational relaxation time; if this is long in comparison with the

period of study, the gas will be effectively vibrationally frozen, whereas, if τ_{vib} is short, a relaxation zone, in which the density ratio rises from that immediately after the shock has passed (ρ_{A1}) to that when the gas is totally relaxed, will be observed.

Equation (5.1) is complicated by the changes in temperature and pressure that also accompany vibrational relaxation. As τ_{vib} is temperature dependent, measurements of the density changes give a mean value of the relaxation rate at the mean temperature behind the shock front.

The rate of vibrational relaxation of oxygen has been measured many times; Borrell's review[109] gives the temperature dependence of the relaxation time as

$$\ln \tau_{vib} = 126.0T^{-1/3} - 21.955 \ (\text{atm s}^{-1}) \qquad (5.2)$$

or, in a more general form

$$\tau_{vib} = \frac{101.32}{P_2} e^{(126T^{-1/3} - 21.955)} (\text{s}) \qquad (5.3)$$

where P_2 is the pressure behind the shock front (KN m^{-2}). Table 5.1 shows the mean vibrational relaxation times of oxygen at three temperatures under typical conditions used in these experiments; the initial pressure of the test gases was $\sim$ 0.87 KN m^{-2}

TABLE 5.1

RUN NUMBER	TEMPERATURE (K)	ρ_{21}	P_{21}	τ_{vib} (μs)
M129	663	3.563	8.05	7897.8
M146	1219	5.358	21.87	206.3
M147	1656	6.034	33.50	43.7

τ_{vib} is expressed in particle time; on this time scale it is usually possible to study the gas behind the shock front for 2000-2500 μs. Thus, at the two higher temperatures, vibrational relaxation will be important in the early part of the shock, but the gas is effectively

relaxed for most of the period under study; in contrast, at 663 K the conditions behind the shock front change very little from the frozen conditions and vibrational relaxation is nowhere near completion during the period of hot flow.

What then are the effects of the vibrational relaxation? If the rate constants that are being measured were to show an Arrhenius temperature dependence, the changes in temperature behind the shock front would cause considerable errors; however, our preliminary measurements show the expected temperature dependence of these reactions to be small, so the use of the mean temperature should be satisfactory for these experiments. The density ratio across the shock front is, however, of considerable importance; in the equations

$$\frac{I_{\Sigma 2}}{I^{o}_{\Sigma 1}} = K[1-(1-{}^{1}/K)e^{-tp/\tau_{rel}}]\rho_{21}e^{-\alpha_t t_p} \qquad (4.42)$$

$$\frac{I_{D2}}{I^{o}_{D1}} = K\rho_{21}{}^{2}T_{21}{}^{\frac{1}{2}}e^{-\alpha_t t_p} \qquad (4.27)$$

ρ_{21} was assumed to be constant, α_t was given by the relation

$$\alpha_t = U\alpha_{\ell}(1-{}^{1}/\rho_{21}) \qquad (4.13)$$

and t_p by

$$t_p = \rho_{21}t_{\ell} \qquad (4.9)$$

where t_{ℓ} is the laboratory time used in experimental observations.

To allow for a changing density behind the shock front, these equations must be rewritten

$$\frac{I_{\Sigma 2}}{I\Sigma^{o}_{1}} = K[1-(1-{}^{1}/K)e^{-t_p/\tau_{rel}}]\rho_{t1}e^{-\alpha_t t_p} \qquad (5.5)$$

$$\frac{I_{D2}}{I^{o}_{D2}} = K\rho_{t1}{}^{2}\left(\frac{T_t}{T_1}\right)^{\frac{1}{2}}e^{-\alpha_t t_p} \qquad (5.6)$$

where $$\alpha_t = U\alpha_\ell \int_0^{t_p} (1-{}^1/\rho_{21})\,dt_p \qquad (5.7)$$

and

$$t_p = \int_0^{t_\ell} \rho_{t1}\; dt_\ell \qquad (5.8)$$

Equation (5.5) is still an approximation, because K is a function of the density of the gas, as shown by equation (4.38); however, a full treatment, starting from equation (3.14)

$$\frac{d[O_2(^1\Sigma_g^+)]}{dt} = k_1[O_2(^1\Delta_g)]^2 - k_2[O_2(^1\Sigma_g^+)][M] - k_w'[O_2(^1\Sigma_g^+)] \qquad (3.14)$$

and allowing the concentrations of $O_2(^1\Delta_g)$, $O_2(^1\Sigma_g^+)$, and M to vary with the density behind the shock front, gives rise to an insoluble series of differential equations.

The effects of the changes in density due to vibrational relaxation on the high temperature rate constant for formation and removal of $O_2(^1\Sigma_g^+)$ are shown schematically in figure (5.1) (cf. figure (4.2)). The ratio $(^I\Sigma/I^o_\Sigma\rho_{21})$ rises less rapidly with time than if vibrational relaxation were instantaneous. Thus, if the gas behind the shock front is assumed to be fully relaxed, the rate of relaxation to the chemical equilibrium (where $\frac{d[O_2(^1\Sigma_g^+)]}{dt} = 0$) will be underestimated. The magnitude of the errors so introduced will depend on the relative values of τ_{vib} and τ_{rel} and on the equilibrium ratio of levels, K.

Non-uniform flow, caused by the formation of a boundary layer behind the shock front, also gives rise to changes in the density and temperature. Equations (5.5)-(5.8) will still hold in such circumstances, and in consequence the effects of flow non-uniformities are examined before these equations are evaluated.

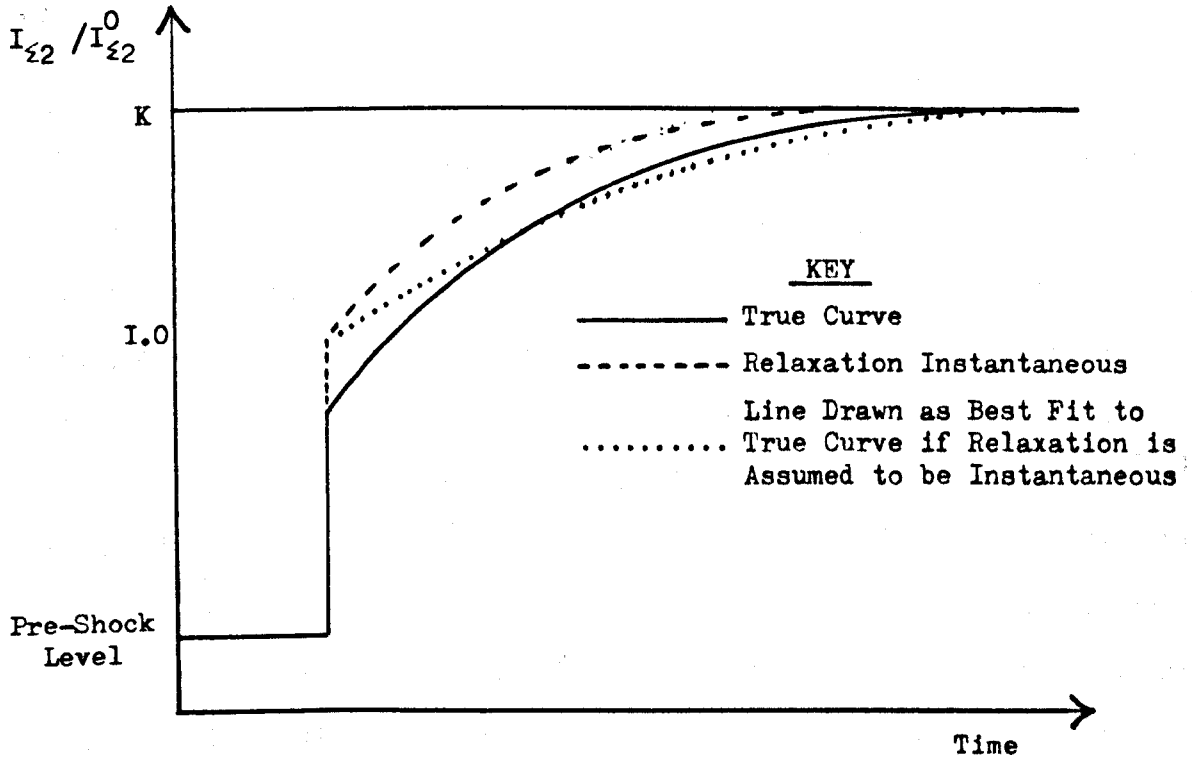

FIGURE 5.I The Effect of Vibrational Relaxation on the Post-Shock Emission from $O_2(^1\Sigma^+_g)$.

(a) Laboratory Coordinates

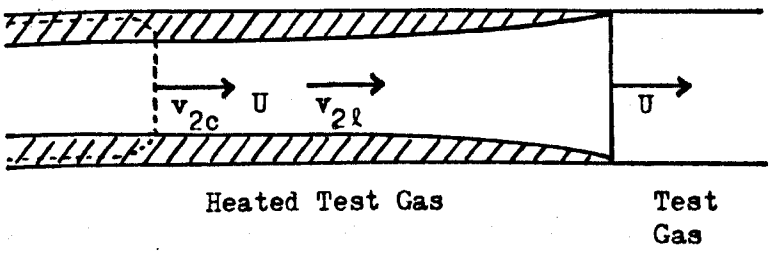

(b) Shock Coordinates

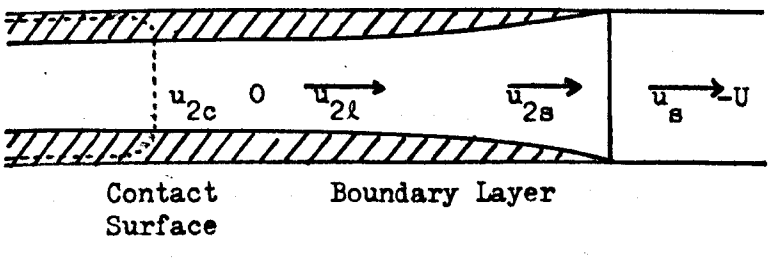

FIGURE 5.2 Shock Tube Flow in Presence of Boundary Layer (after Limiting Flow Has Been Attained)

5.3. Non-Uniform Flow

Several workers have suggested that the effects of non-uniform flow in a shock-heated gas are considerable[125,137], and that estimates of rate constants which fail to take them into account may be seriously in error. However, it is extremely difficult to make such corrections, because our experimental knowledge of the physical changes that result from boundary layer formation, is poor. Mirels has produced a series of papers[138,139,140,141] which predict the theoretical changes in density and temperature behind the shock front, but these have little experimental basis. His equations are unwieldy, and Belford and Strehlow[125,142] have simplified them considerably by approximation; the approximations are valid only in the early part of the shock and are not suitable for the experiments on singlet molecular oxygen in which studies are made during almost the whole time of hot flow.

In order to estimate the changes taking place behind the shock front, a computer program, FLOCOR, which used the equations of Mirels with only minor approximations, was developed (Appendix C1). This program was in fact a major extension of one written some years earlier by G.E. Millward[128], which used Belford and Strehlow's approximations. Several measurements of shock deceleration and hot flow duration were also made in order to provide some experimental basis for the results obtained.

In this section, the changes in density and temperature behind the shock front are assumed to be negligible in comparison with the initial density, and the gas is assumed to be vibrationally relaxed at all times. Such assumptions are obviously approximations, but easy solution of the equations that are set up would not otherwise be possible.

5.3.1. Maximum Flow Duration in the Shock Tube

The situation in an ideal shock, where the hot flow time increases linearly with the distance travelled by the shock front, was discussed in Chapter 1, and in Chapter 2, where it was noted that the ideal shock

equations gave a poor estimate of the duration of hot flow. In any real shock tube, a boundary layer of cold gas is formed at the wall (figure (5.2)); momentum is transferred through this boundary layer from the shock front to the contact surface, causing a deceleration of the shock front and a consequent acceleration of the contact surface. Figure (5.3) shows that in the limiting situation the shock front and contact surface travel at a constant separation and the same velocity, and that the hot flow time at an observation station is significantly less than in the ideal case.

In the real gas, the hot flow time, t_m, depends on the nature of the flow; this is known to be laminar in the early stages, but becomes turbulent at long distances from the shock front. Mirels has produced semi-theoretical plots relating the maximum separation of the shock front and the contact surface, ℓ_m, to the shock Mach number (M_s) for pure laminar[138] and pure turbulent[140] flows. Belford and Strehlow suggest that a plot of ln (maximum separation) against ln M_s is very nearly linear over the range M_s = 2-5. The data of Mirels is plotted in this way in figures (5.4)-(5.6). A is the separation distance for shocks into a tube of unit diameter, containing test gas initially at a pressure of one atmosphere. For laminar flow

$$A = \frac{\ell_m}{d^2} \frac{P_{atm}}{P_1} \tag{5.9}$$

and from figure (5.4)

$$\ell_m = \frac{3.916\ d^2\ P_1 \times 10^{-1}\ mm}{P_{atm}\ M_s^{0.7}} \tag{5.10}$$

As figure (5.2) shows that

$$v_{2c} = U \tag{5.11}$$

$$t_m = \frac{\ell_m}{U} = \frac{\ell_m}{a_1 M_s} \tag{5.12}$$

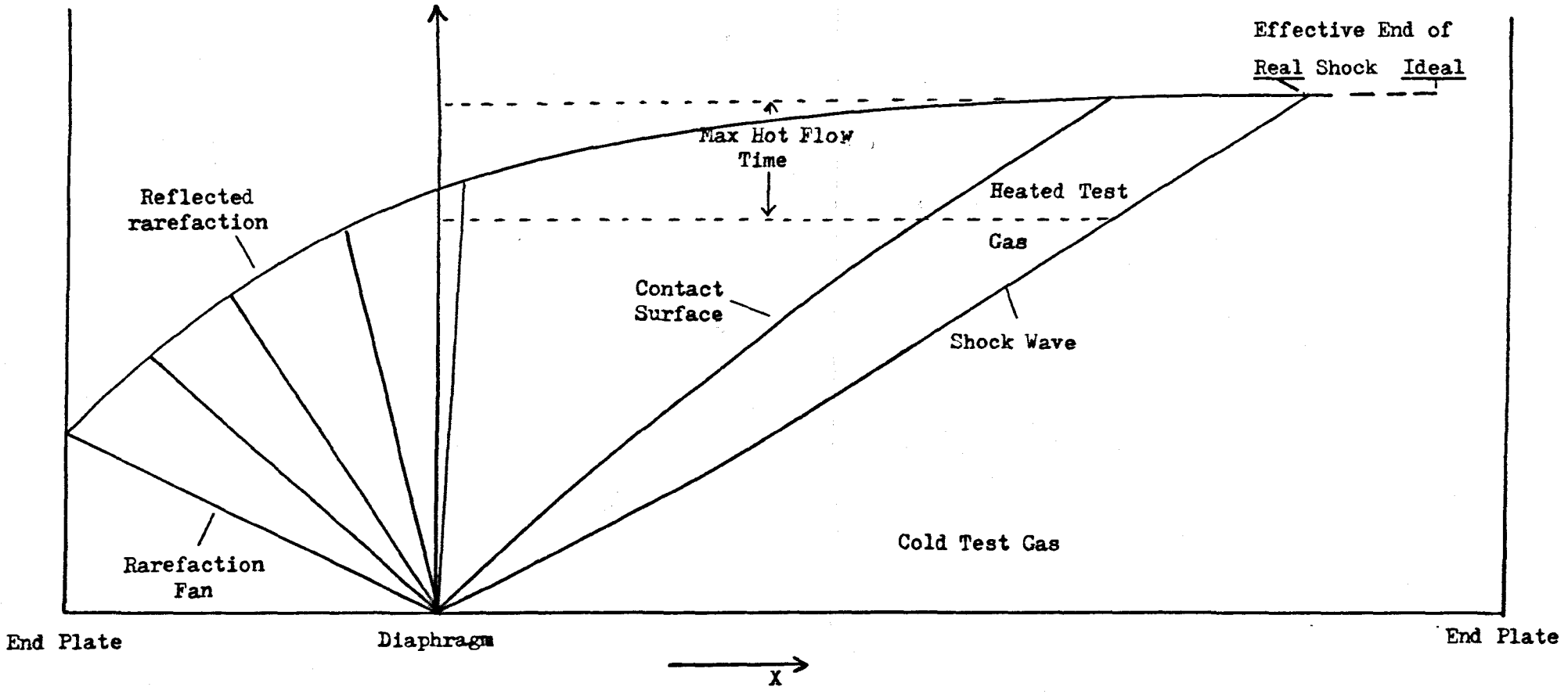

FIGURE 5.3 Reduced Hot Flow Time and Hot Flow Duration in Presence of Boundary Layer

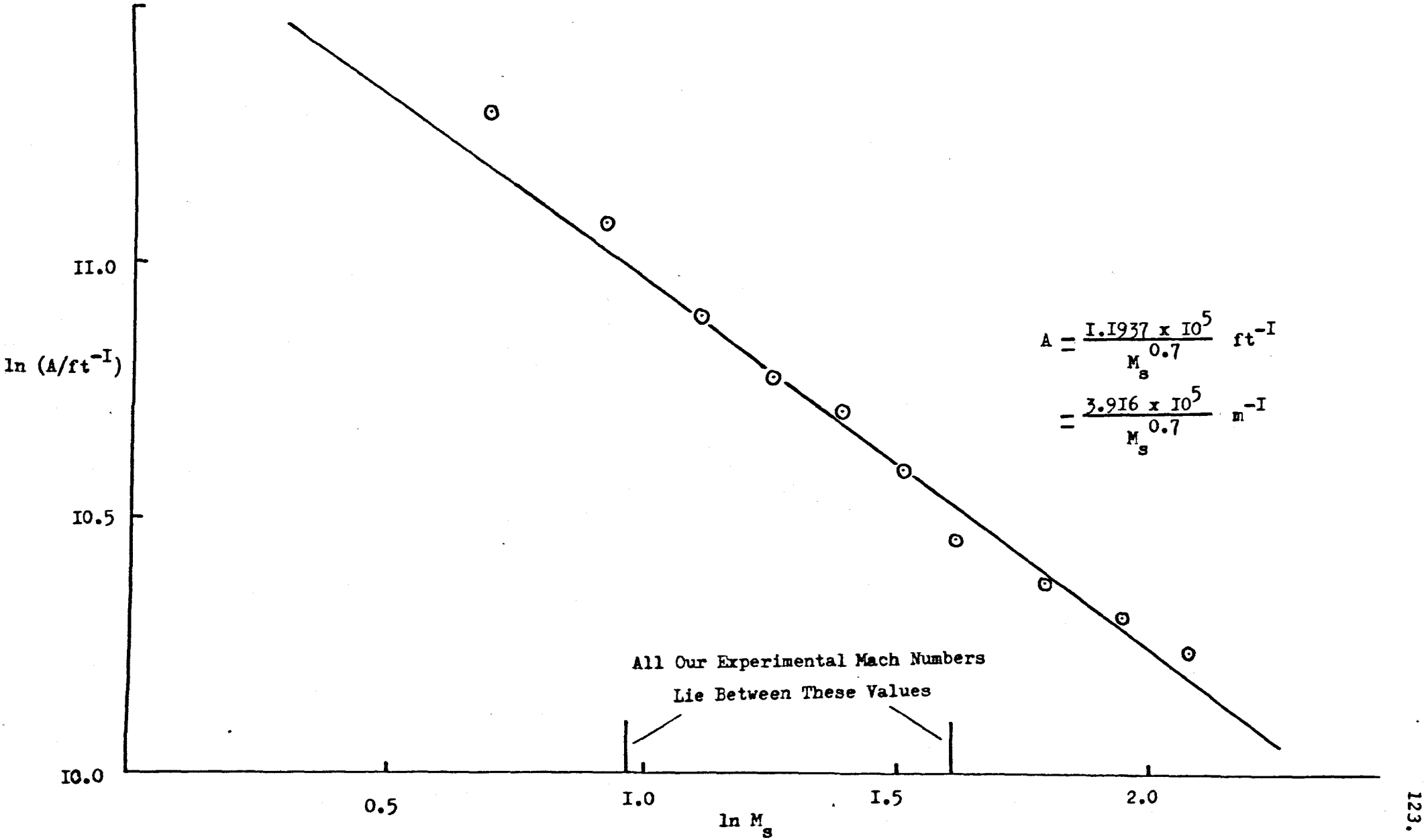

Figure 5.4 Maximum Test Time for Laminar Flow in a Shock Tube

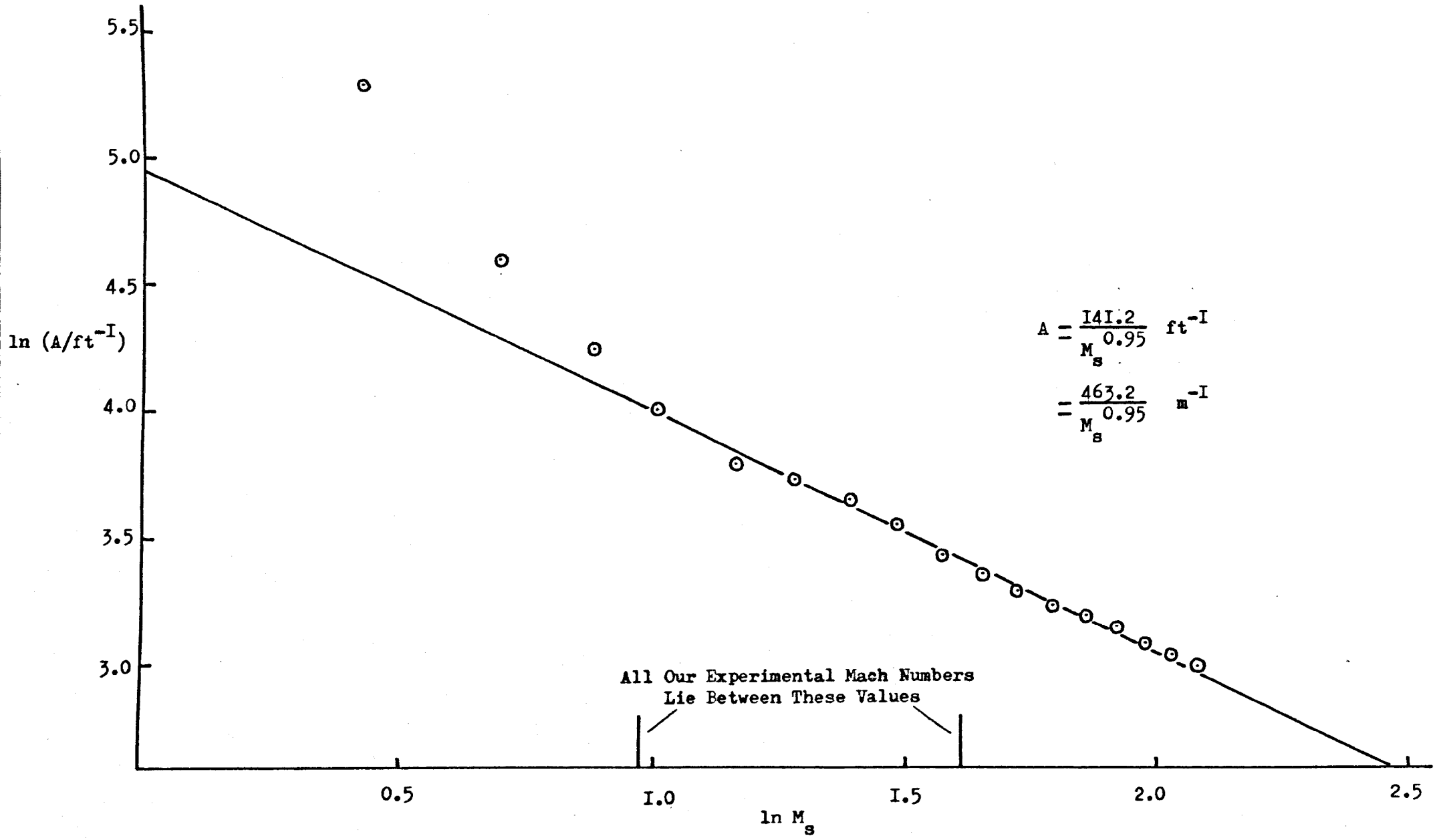

FIGURE 5.5 Maximum Test Time for Turbulent Flow in a Shock Tube - AIR

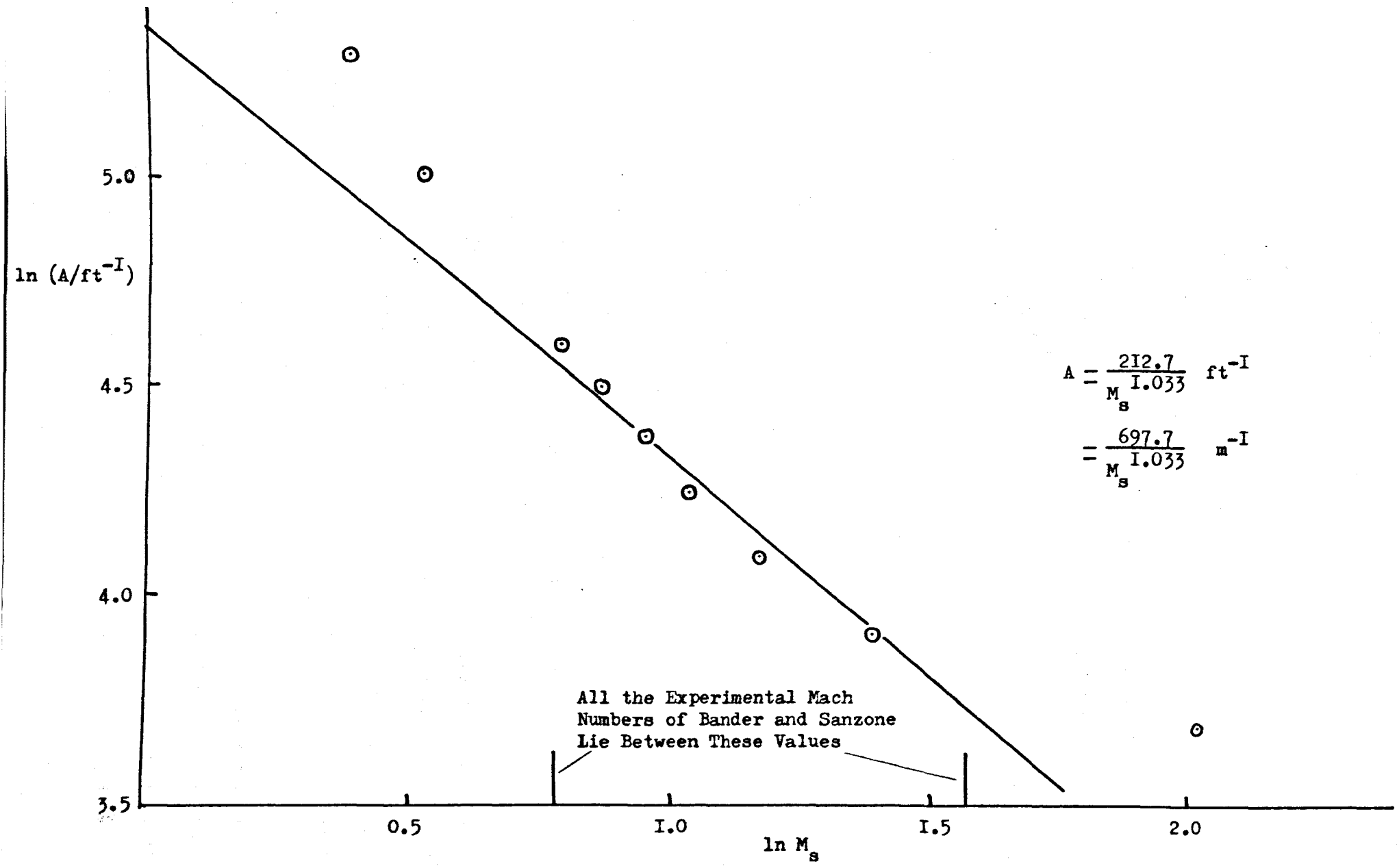

FIGURE 5.6 Maximum Test Time For Turbulent Flow - ARGON

Hence, using $P_{atm} = 101.3 \text{ KN m}^{-2}$,

$$t_m = \frac{3.86\ d^2\ P_1}{a_1 M_s^{1.7}} \times 10^{-6} \text{ s} \qquad (5.13)$$

where P_1 is the initial pressure in KN m^{-2}, a_1 the velocity of sound in the test gas (Km s^{-1}), and d the hydraulic diameter (mm), which, for a tube of cylindrical cross section, is the same as the natural diameter. For turbulent flow, A in figures (5.5) and (5.6) is given by

$$A = \frac{\ell_m}{d^{5/4}} \left(\frac{P_{atm}}{P_1}\right)^{\frac{1}{4}} \qquad (5.14)$$

and by a similar procedure we obtain the relations

$$t_m = \frac{1.065\ d^{5/4}\ P_1^{\frac{1}{4}}}{a_1\ M_s^{1.95}} \times 10^{-5} \text{ s} \qquad (5.15)$$

for shocks into air, and

$$t_m = \frac{1.608\ d^{5/4}\ P_1^{\frac{1}{4}}}{a_1\ M_s^{2.033}} \times 10^{-5} \text{ s} \qquad (5.16)$$

for shocks into argon. In the case of laminar flow, t_m, shows little dependence on the nature of the test gas; with turbulent flow, the hot flow time should be little different for shocks into oxygen from the figures in equation (5.15).

The hot flow time is considerably greater for laminar than for turbulent flow; a shock into oxygen of Mach No 4.0 (velocity 1.32 Km s^{-1}) in our apparatus will have a maximum hot flow time of 2574μs for laminar flow, but only 286μs when the flow is turbulent. Experimentally observed hot flow times inevitably lie between these values.

In the early part of a shock, the hot flow time is less than t_m, and the deceleration of the shock front gives rise to increases in the temperature, density and pressure of the shock-heated gas. Even when the shock front and contact surface are at their maximum separation, the

increases are not insignificant.

5.3.2. Conditions behind the Shock Front

The gas parameters associated with the shock wave in both laboratory-fixed and shock-fixed coordinates are shown in figure 5.2. The suffices, s, ℓ, and c refer respectively to sections of gas immediately behind and at a distance, ℓ, from the shock front, and the section of gas at the contact surface.

Equation (1.47) is now written

$$\rho_{2s}U_{2s} = \rho_1 U_s \tag{5.17}$$

where $U_s = -U$ (5.18)

$$U_{2s} = v_{2s} - U = Wp - U \tag{5.19}$$

and $U_{2\ell} = v_{2\ell} - U$ (5.20)

Mirels[141] has shown that, after the limiting separation, ℓ_m has been reached, conservation of mass indicates that

$$\rho_{2\ell}\, U_{2\ell}/\rho_{2s}\, U_{2s} = 1-(\ell/\ell_m)^{\frac{1}{2}} \tag{5.21}$$

for laminar flow. From (5.17) and (5.21)

$$\rho_{2\ell}\, U_{2\ell} = \rho_1 U_s\, [1-(\ell/\ell_m)^{\frac{1}{2}}] \tag{5.22}$$

$$U_{2\ell} = U_s\, \rho_{2\ell 1}^{-1}[1-(\ell/\ell_m)^{\frac{1}{2}}] \tag{5.23}$$

$$v_{2\ell} = U\left\{1-\rho_{2\ell 1}^{-1}[1-(\ell/\ell_m)^{\frac{1}{2}}]\right\} \tag{5.24}$$

When $\ell = 0$, equation (5.24) reduces to the ideal relation (4.3)

$$v_{2s} = U[1-1/\rho_{21}] \tag{5.25}$$

but when $\ell = \ell_m$

$$v_{2c} = U \tag{5.26}$$

as was predicted. The conditions in the gas at a distance ℓ behind the

shock front are then given by

$$\frac{T_2}{T_{2s}} = \frac{2 + (\gamma-1)M_{2s}^2}{2 + (\gamma-1)M_2^2} \tag{5.27}$$

where M_{2s}, the Mach number of the flow immediately behind the shock front in shock-fixed coordinates, is related to the shock Mach number, M_s, by

$$M_{2s} = \frac{(\gamma-1)M_s^2 + 2}{2\gamma M_s^2 - (\gamma-1)} \tag{5.28}$$

and M_2 is given by

$$M_2 = \left[1-(\ell/\ell_m)^{\frac{1}{2}}\right] M_{2s}\left[\frac{2 + (\gamma-1)M_2^2}{2 + (\gamma-1)M_{2s}^2}\right]^{(\gamma-1)/2(\gamma-1)} \tag{5.29}$$

which is solved by iteration. γ is the ratio of specific heats of the gas. The density and pressure at ℓ are found by assuming these changes to be isentropic:

$$\frac{T_2}{T_{2s}} = \left(\frac{\rho_2}{\rho_{2s}}\right)^{\gamma-1} = \left(\frac{P_2}{P_{2s}}\right)^{(\gamma-1)/\gamma} \tag{5.30}$$

For turbulent flow, the term $(\ell/\ell_m)^{\frac{1}{2}}$ in equations (5.21)-(5.24) and (5.29) is replaced by $(\ell/\ell_{mt})^{4/5}$, where ℓ_{mt} is the limiting separation for turbulent flow. As ℓ_{mt} is far less than ℓ_m, the increases in temperature and density are far more rapid for a turbulent than for a laminar boundary layer.

In the period before the shock wave reaches a constant velocity, the deceleration gives rise to an entropy gradient in the gas flow. The contribution of shock deceleration to the change in temperature behind the shock front is given by[128]

$$\frac{\Delta T}{T_{2s}} = t_p\left[\frac{2(M_s^2-1)}{\{1+[(\gamma-1)/2]M_s^2\}\{[2\gamma M_s^2/(\gamma-1)]-1\}}\right]\frac{d \ln M_s}{dt_\ell} \tag{5.31}$$

where t_p is the gas particle time and

$$\frac{d \ln M_s}{dt_\ell} = \frac{\gamma a_1 M_s}{\gamma M_s a_1 t_m + 1} \tag{5.32}$$

in which Y is the velocity decrement in % m^{-1}, and t_m is taken to be the maximum hot flow time (although the limiting separation has not yet been reached). This contribution to the change in temperature may, provided that the overall increase is small, be added to that found at constant velocity; equation (5.30) is again used to calculate the changes in density and pressure.

Equation (5.31) is solved using the measured experimental parameters and the expressions relating t_p and t_ℓ for non-uniform flow:

Ideal flow: $$t_p = \rho_{21} t_\ell \qquad (4.9)$$

Laminar flow[143]: $$t_p = 2\rho_{21} t_\ell \left(\frac{\ell}{\ell_m}\right)^{-1} \left\{\left(\frac{\ell}{\ell_m}\right)^{\frac{1}{2}} + \ln\left[1-(\ell/\ell_m)^{\frac{1}{2}}\right]\right\} \qquad (5.33)$$

Turbulent flow[141]: $$t_p = \frac{5}{4}\rho_{21} t_\ell \left(\frac{\ell}{\ell_{mt}}\right)^{-1} \left\{2\tan^{-1}(\ell/\ell_{mt})^{1/5} + \ln\left[\frac{1 + (\ell/\ell_{mt})^{1/5}}{1 - (\ell/\ell_{mt})^{1/5}}\right] - 4\left(\frac{\ell}{\ell_{mt}}\right)^{1/5}\right\} \qquad (5.34)$$

Again, solution of these equations is greatly simplified by assuming ρ_{21} to be constant.

To calculate the contributions of shock deceleration and limiting flow, the ratio, (ℓ/ℓ_m) or (ℓ/ℓ_{mt}), is required. Experimental measurements follow the laboratory time, t_ℓ, and it is necessary to relate (t_ℓ/t_m) to (ℓ/ℓ_m) and (ℓ/ℓ_{mt}); the increase in the velocity of the shocked gas from the shock front to the contact surface means that the transfer from time to distance is no longer the simple relation

$$\frac{t_\ell}{t_m} = \frac{1}{(1 - 1/\rho_{21})} \frac{\ell}{\ell_m} \qquad (5.35)$$

obtained from equations (5.25) and (5.26).

For laminar flow, equation (5.24) is written

$$\frac{d\ell}{dt_\ell} = U_s \left\{1 - \rho_{21}^{-1}\left[1-(\ell/\ell_m)^{\frac{1}{2}}\right]\right\} \qquad (5.36)$$

$$\int_0^{t_\ell} dt_\ell = \int_0^{\ell} \frac{1}{U_s\{1-\rho_{21}^{-1}[1-(\ell/\ell_m)^{\frac{1}{2}}]\}}\, d\ell \qquad (5.37)$$

By making use of the relation

$$v_{2c} = \frac{\ell_m}{t_m} = U_s \qquad (5.26)$$

the expression

$$\frac{t_\ell}{t_m} = 2\rho_{21}\left\{\left(\frac{\ell}{\ell_m}\right)^{\frac{1}{2}} + (\rho_{21}-1)\ln\left[\frac{(\rho_{21}-1)}{\rho_{21}^{-1} + (\ell/\ell_m)^{\frac{1}{2}}}\right]\right\} \qquad (5.38)$$

is obtained. When (ℓ/ℓ_m) is small, expansion of the log term gives the ideal relation (5.30)

$$\frac{t_\ell}{t_m} \simeq 2\rho_{21}\left\{\left(\frac{\ell}{\ell_m}\right)^{\frac{1}{2}} - \left(\frac{\ell}{\ell_m}\right)^{\frac{1}{2}} + \frac{1}{2(\rho_{21}-1)}\left(\frac{\ell}{\ell_m}\right) - \cdots\cdots\right\}$$

$$\simeq \frac{1}{(1 - 1/\rho_{21})}\left(\frac{\ell}{\ell_m}\right) \qquad (5.39)$$

When the flow is turbulent, equation (5.36) becomes

$$\frac{d\ell}{dt_\ell} = v_{2\ell} = U_s\left[1 - \rho_{21}^{-1}[1-(\ell/\ell_{mt})^{4/5}]\right] \qquad (5.40)$$

$$\int_0^{t_\ell} dt_\ell = \int_0^{\ell} \frac{1}{U_s\{1-\rho_{21}^{-1}[1-(\ell/\ell_{mt})^{4/5}]\}}\, d\ell \qquad (5.41)$$

Equation (5.41) is integrated by making the substitution

$$a = 1 - \rho_{21}^{-1} \qquad (5.42)$$

$$b = \rho_{21}^{-1} \qquad (5.43)$$

$$c = (a/b)^{\frac{1}{4}} \qquad (5.44)$$

$$x = (\ell/\ell_{mt})^{1/5} \; ; \; \frac{dx}{d\ell} = 5\,\ell_{mt}\,x^4 \qquad (5.45)$$

$$\therefore \quad t_\ell = \frac{5\,\ell_{mt}}{U_s}\int_0^x \frac{x^4}{a + bx^4}\, dx \qquad (5.46)$$

$$\frac{t_\ell}{t_m} = \frac{5}{b} \int_0^x 1 - \frac{a}{b} \frac{1}{c^4 + x^4} \, dx \tag{5.47}$$

Tables of integrals[144] give the relation

$$\int_0^x \frac{1}{c^4 + x^4} \, dx = \frac{1}{4c^3\sqrt{2}} \ln \frac{x^2 + cx\sqrt{2} + c^2}{x^2 - cx\sqrt{2} + c^2} + \frac{1}{2c^3\sqrt{2}} \tan^{-1} \frac{cx\sqrt{2}}{c^2 - x^2} = \text{INT} \tag{5.48}$$

$$\therefore \quad \frac{t_\ell}{t_m} = 5\rho_{21} \left[x - (\rho_{21} - 1) \text{ INT} \right] \tag{5.49}$$

Equations (5.38) and (5.49) are solved for (ℓ/ℓ_m) by iteration in subroutines GRAVE and HEARSE of the flow corrections program.

At this stage, all the basic equations have been set up, but satisfactory estimates of the effects of non-uniform flow will only be possible if the point of transition from laminar to turbulent flow is known.

5.3.3. The Transition from Laminar to Turbulent Flow

Mirels describes the transition from laminar to turbulent flow[141] in some detail, but makes no attempt to predict the distance from the shock front at which this will occur. The ratio of the excess mass flow in a laminar boundary layer at station (ℓ/ℓ_m) to the mass flow through the shock varies with $(\ell/\ell_m)^{\frac{1}{2}}$. It follows that the shock flow is equivalent to inviscid flow through a channel with an area distribution defined by

$$A_{2s}/A_2 = 1 - (\ell/\ell_m)^{\frac{1}{2}} \tag{5.50}$$

For a turbulent boundary layer, the area distribution of the channel is defined by

$$A_{2s}/A_2 = 1 - (\ell/\ell_{mt})^{4/5} \tag{5.51}$$

As there is obviously no discontinuity in the boundary layer at the transition point, it follows that at this point

$$(\ell/\ell_m)^{\frac{1}{2}}_{LAM} = (\ell/\ell_{mt})^{4/5}_{TURB} \tag{5.52}$$

or $$(\ell/\ell_{mt})_{TURB} = (\ell/\ell_m)^{5/8}_{LAM} \tag{5.53}$$

Hence we may use our knowledge of the limiting separation, ℓ_m, for both laminar and turbulent flows to calculate an effective origin for the turbulent boundary layer. Pure turbulent flow starting from this origin will have the same value of A_{2s}/A_2 at the transition point as is observed for laminar flow starting at the true time origin. Thus the total hot flow time in any shock is given by the sum of the maximum duration of turbulent flow and the duration of laminar flow to the point of transition to turbulent flow, less the time for a pure turbulent flow to reach the conditions at the transition point. This is illustrated by the graphs of density ratio against time in figure (5.7); it may be seen that the temperature and density ratios increase much more rapidly when the flow is turbulent.

Bander and Sanzone[145] assume the total test time, t_m to be a weighted sum of fractions of a fully laminar test time L and a fully turbulent test time T:

$$t_m = (\tau_{trans}/t_m)L + (1 - \tau_{trans}/t_m)T \tag{5.54}$$

where τ_{trans} is the laboratory time at which the transition from laminar to turbulent flow occurs. This argument is naive and for a given value of τ_{trans} predicts test times far longer than the model of Mirels, which considers the basic physics of the flow at the transition point. Unfortunately, no other workers have attempted to predict this transition point.

To make some rough estimate of the transition point, the hot flow time at the observation station in our apparatus was measured from the

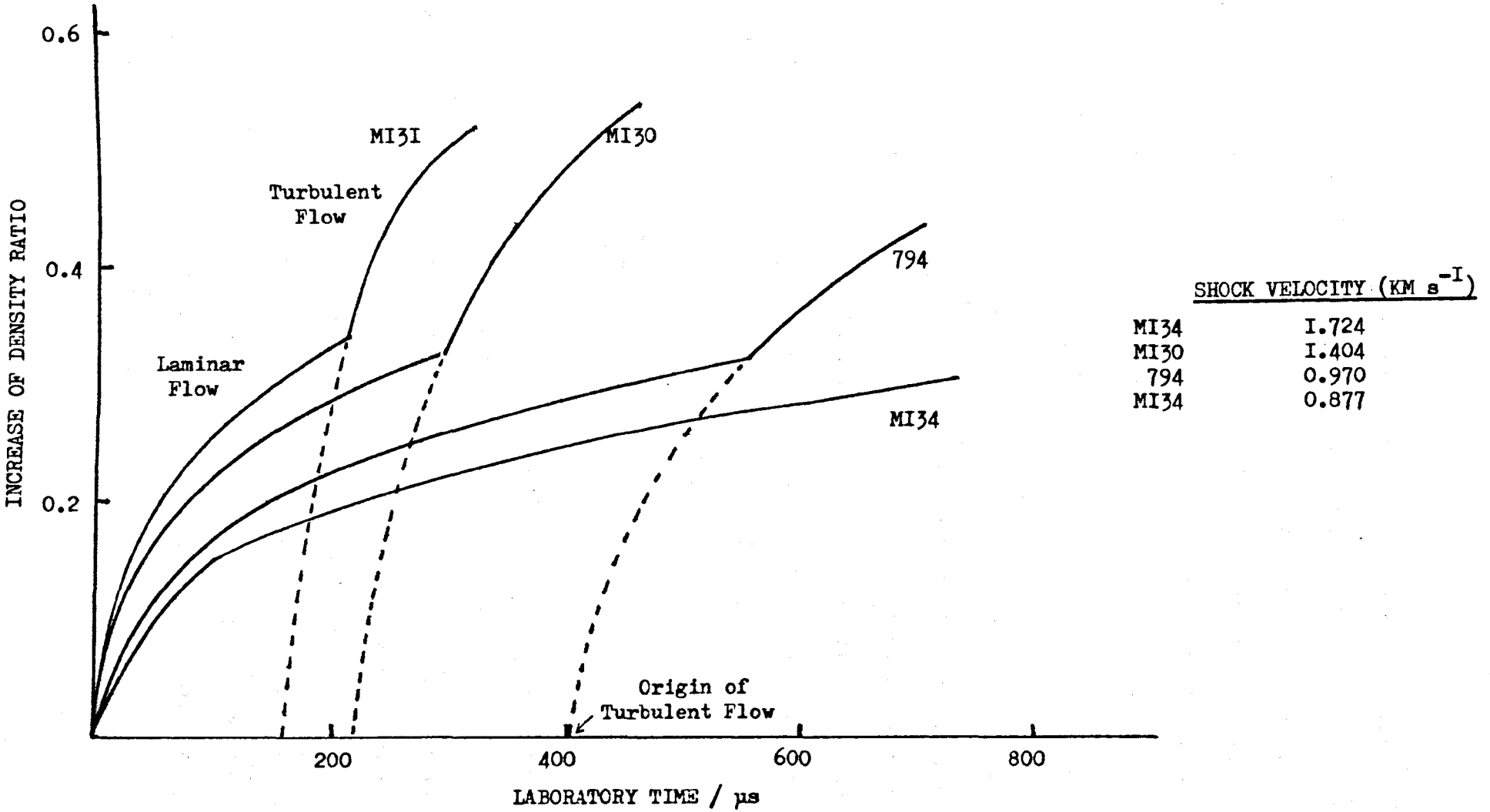

FIGURE 5.7 The Effect of Non-Uniform Flow on the Density Behind the Shock Front; $\tau_{trans} = \frac{2\pi d(U-v_{2\ell})}{Uv_{2\ell}}$

photographic records of the emission from shock-heated oxygen. Empirical formulae, based on the relations obtained by Bander and Sanzone by equating flow and transition Reynolds numbers, were then used to obtain the best fit to the crude experimental data. The fits found using the two most satisfactory formulae for τ_{trans} are shown in figure (5.8); for subsequent experiments the relation

$$\tau_{trans} = \frac{20\pi\, d(U - v_{2\ell})}{U\, v_{2\ell}} \qquad (5.55)$$

(where d is again the hydraulic diameter) was used.

It should be possible to fit the experimental data on shocks into argon, reported by Bander and Sanzone, in the same way. Figures (5.9) and (5.10) show that equation (5.55) gives a very poor fit; the scatter of the results is very large, and limits attempts to find a more satisfactory relation. None of the forms suggested by Bander and Sanzone fit very well; the most satisfactory overall fit is

$$\tau_{trans} = \frac{3dU}{v_{2\ell}^2} \qquad (5.56)$$

Referring back to figure (5.7), in which τ_{trans} was given by equation (5.55) and the shock deceleration was assumed to be zero, it is apparent that the changes in density ratio predicted by these equations are large in comparison with the absolute density ratio of 3.5-6, and that except for slow shocks, the transition from laminar to turbulent flow occurs well within the period of observation. The effects of deceleration of the shock front may be still greater than this; as the changes in density, temperature etc. are highly sensitive to the shock deceleration, it was necessary to measure this in our apparatus.

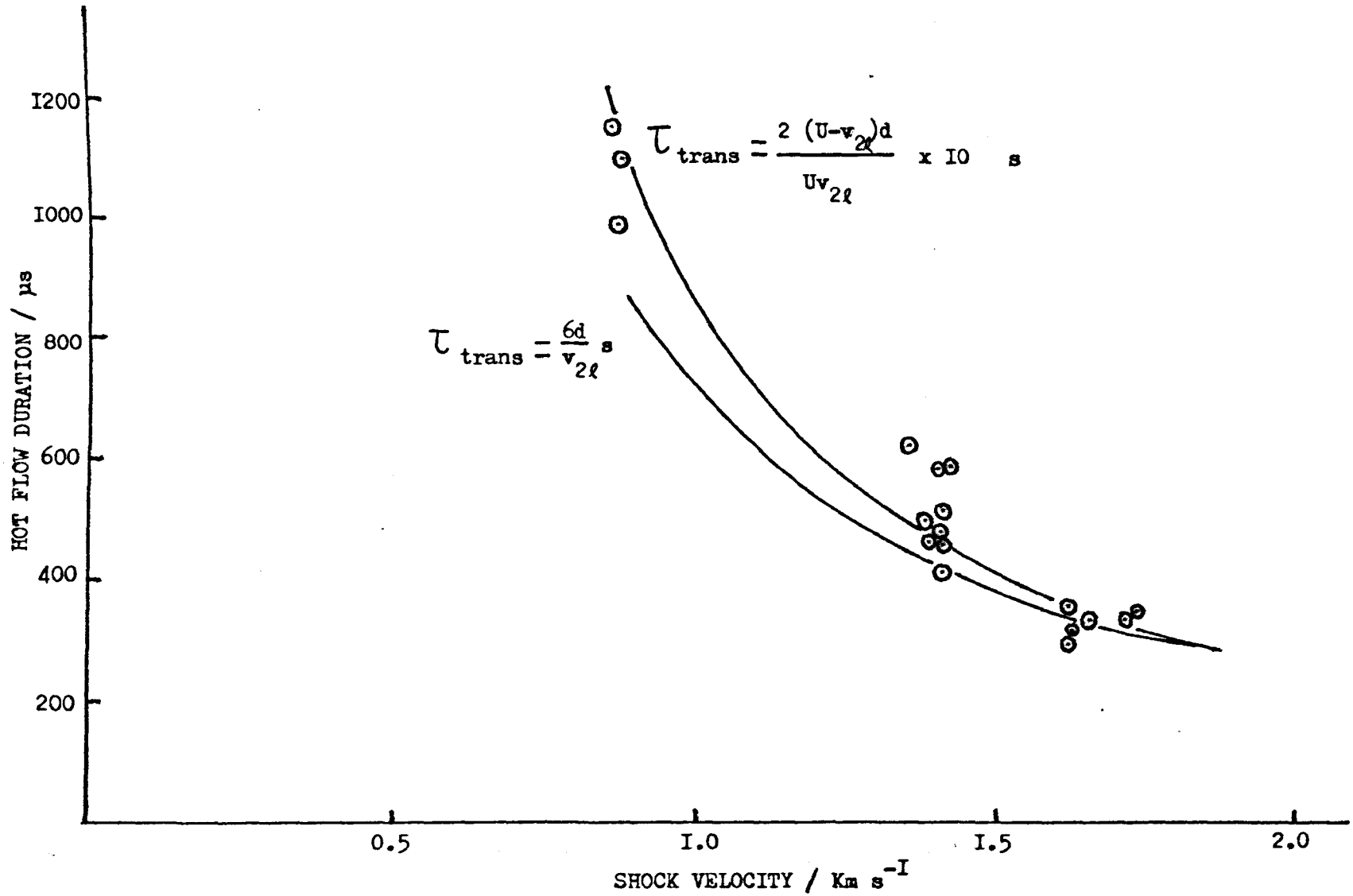

FIGURE 5.8 Hot Flow Duration in Our Shock Tube: Experimental Data and Empirical Fits

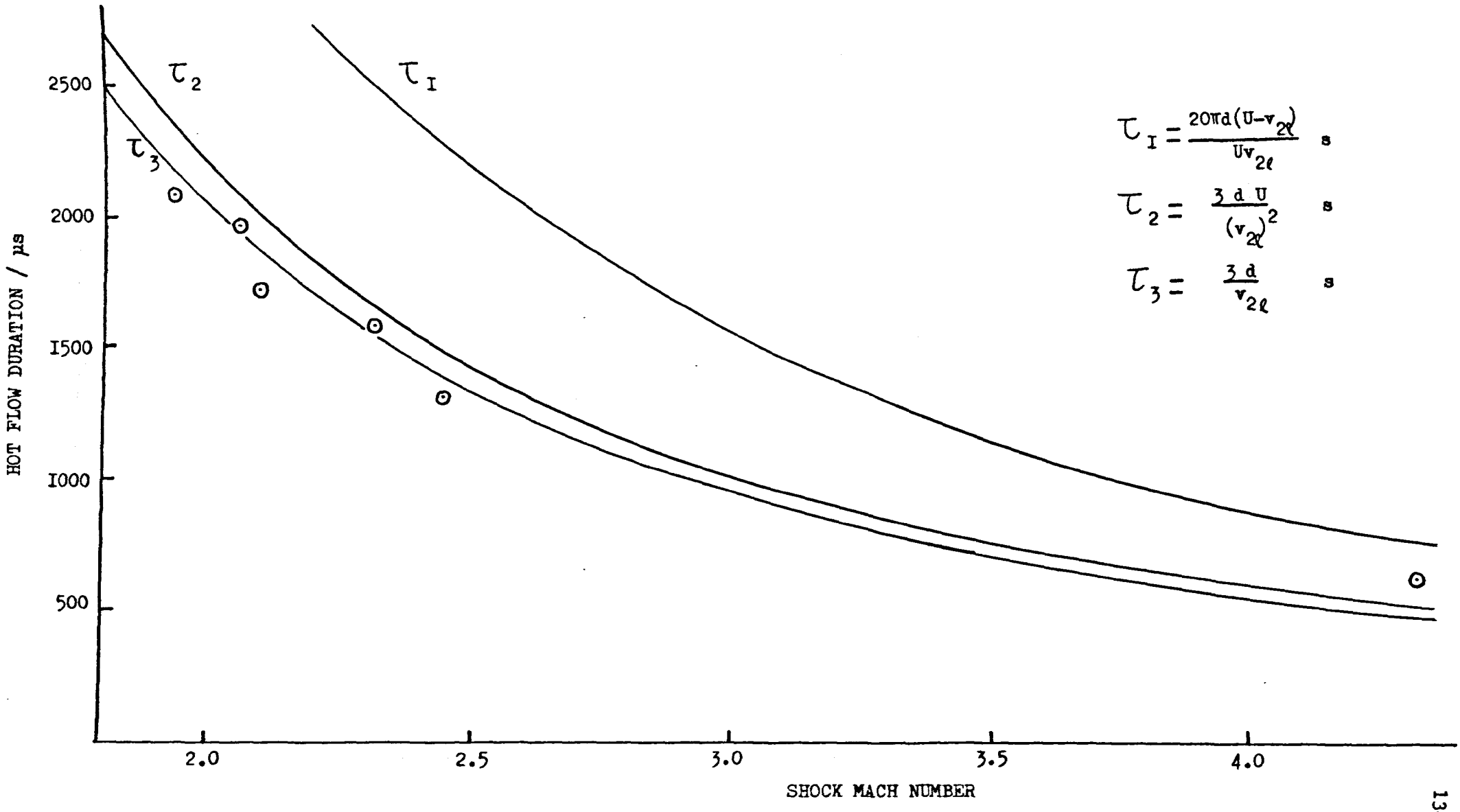

FIGURE 5.9 Total Hot Flow Time for Shock-Heated Argon

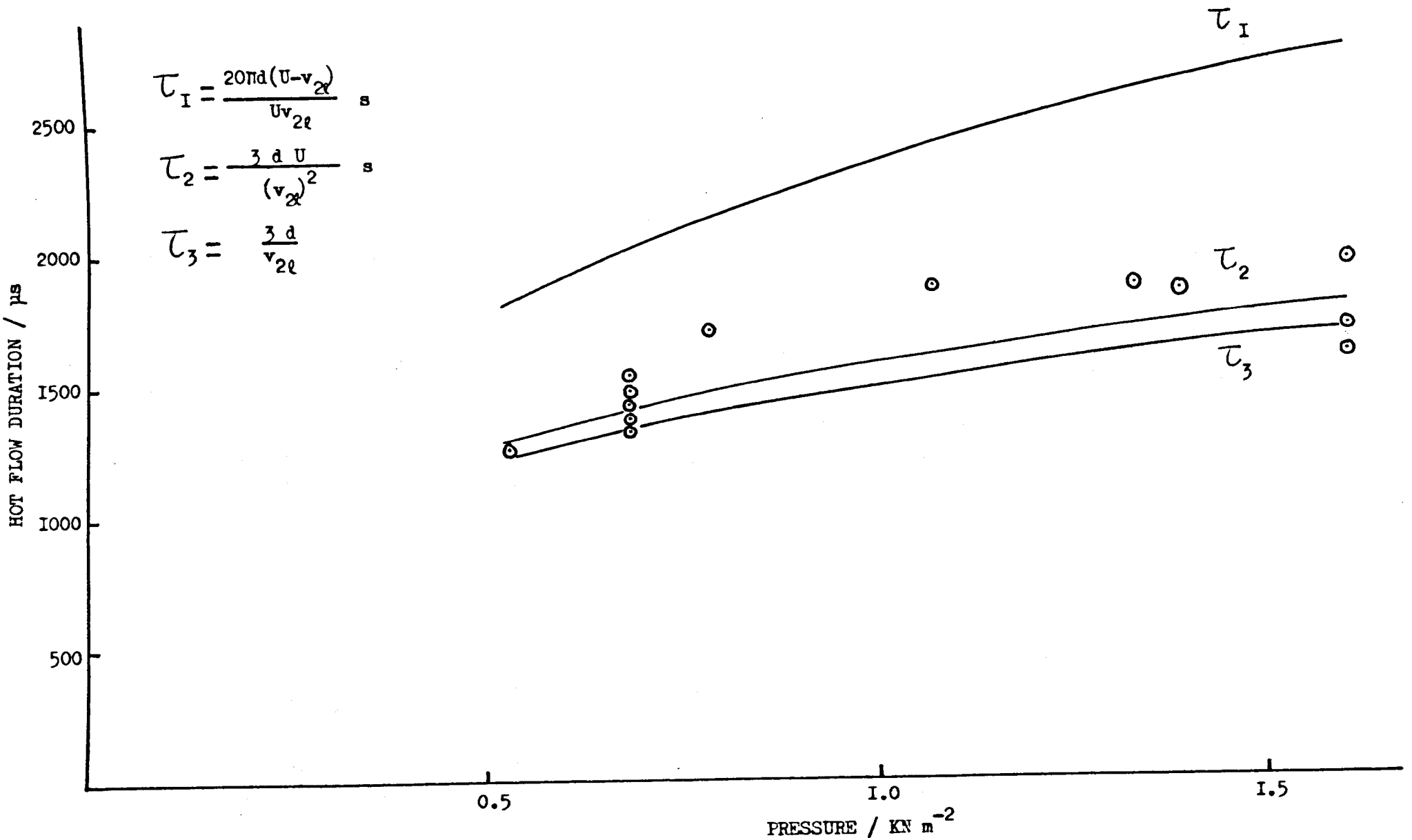

FIGURE 5.10 Total Hot Flow Time for Shock-Heated Argon : Pressure Dependence

5.3.4. Measurements of shock deceleration

Measurements were made by moving light screen 2 to a position much nearer to the diaphragm. The distances between light screens 2-3 and light screens 1-3 were then 2.617 and 0.815m respectively. The deceleration was found to vary considerably from one shock to another, lying between 0.3 and 2.9% m^{-1}. Although the scatter of measurements was considerable, some dependence on the shock velocity was noted; slow shocks generally showed greater deceleration than fast.

Light screen 2 was then moved towards the observation station and the deceleration remeasured with the distance 2-3 now 1.176m. It was now much smaller than before (0-1.0% m^{-1}), and for fast shocks no significant deceleration was detected.

The two sets of measurements estimate the rates of deceleration at distances of 0.50m and 0.15m from the observation station. The deceleration of the shock wave is certainly decreasing as it travels away from the diaphragm; the tube dimensions do not allow measurements of any significance to be made at the observation station itself, but the deceleration should be very small at this point.

Because the deceleration of the shock front is small and uncertain, it has been neglected in subsequent calculations; this assumption will be further justified later. Mirels' model of limiting flow predicts that the total time of hot flow behind the shock front should now be independent of the position of the observation station.

An interesting result of these measurements of the shock velocity was found when using mixtures of helium and nitrogen as the driver gas; a persistent acceleration of the shock front was observed, except when the driver gases were mixed extremely slowly. Nobody has attempted to predict the flow non-uniformities in such a case, and it is apparent that, unless a cylinder of the mixed gases is available, great care must

be taken in experiments which use mixed drivers.

5.3.5. The effects of non-uniform flow

The changes in temperature and density behind the shock front are predicted, by Mirels' equations for non-uniform flow, to be large (up to $\sim$ 8% if there is no deceleration of the shock front; this is approximately doubled for a shock deceleration of 1% m^{-1}). Unlike the changes due to vibrational relaxation, there is no experimental evidence that demonstrates their occurrence. Our considerable experimental experience of the emissions observed behind the shock front, suggests that the changes resulting from non-uniform flow are much smaller than is predicted by the calculations in this section.

A further piece of evidence that casts doubt on the applicability of Mirels' equations to our apparatus is the hot flow time behind the shock front. The deceleration of the shock front is zero in two cases: the limiting case of Mirels when the shock front and contact surface are moving with the same velocity, and the ideal situation, in which no boundary layer is formed and the hot flow time increases linearly with the distance travelled by the shock front. By setting the travelling photomultiplier at a distance 1m from the observation station (which is approximately 4m from the diaphragm), it was possible to detect any increase of hot flow time with distance. The results showed the time at the new observation station (3m from the diaphragm) to be about 3/4 that observed by the stationary photomultiplier. Thus the limiting situation has certainly not been reached, and the behaviour of the shock-heated gas is very nearly that expected for an ideal flow.

This result is surprising as all authors seem agreed that there is no way in which boundary layer formation can be avoided. The effects of non-uniform flow appear to have been exaggerated by the theoretical treatments; the total hot flow time at the observation station is

significantly shorter for fast shocks than is predicted by the ideal shock relations, but reasonably correct for shocks of velocity less than 1 Km s^{-1}.

Because it was apparent that the effect of boundary layer formation, derived in this section, are seriously overestimated, they were not included when correcting equations (5.5) and (5.6) for changes in the conditions behind the shock front. The experimental study of shock non-uniformities is clearly a fertile and necessary field of research; although the apparatus used here has some convenient features for such measurements (e.g. the measurement of hot flow time by following the emission from $O_2(^1\Sigma_g^+)$ or $O_2(^1\Delta_g)$), it is not suitable for the precise experiments required in such work.

5.4. Corrections for the non-uniform conditions

5.4.1. Shocks into pure oxygen

The process of making corrections for the changes in density, temperature and pressure behind the shock front is simplified considerably by the conclusion that the effects of boundary layer formation may be ignored. The computer program, VIBREL (Appendix C2) has been written to calculate the corrections for vibrational relaxation.

The conditions behind the shock front for the gas in its frozen and relaxed states are calculated by incorporating a version of Millikan's program (chapter 1) into VIBREL as the routine, DISHOCK. The relations

$$\rho_{t1} = \rho_{A1} + (\rho_{21} - \rho_{A1})(1 - e^{-t_p/\tau_{vib}}) \qquad (5.1)$$

$$T_t = T_A + (T_2 - T_A)(1 - e^{-t_p/\tau_{vib}}) \qquad (5.57)$$

$$P_{t1} = P_{A1} + (P_{21} - P_{A1})(1 - e^{-t_p/\tau_{vib}}) \qquad (5.58)$$

are used, together with equation (5.3), in an iterative cycle to calculate the conditions at a particle time, t_p, after the shock front has passed. An estimate of the rate of vibrational relaxation of the shock-heated gas at the time, t_p, is also obtained. The particle time is a function of the density (equation (5.8)), and is estimated from the laboratory time, t_ℓ, by numerical integration of the density, using Simpson's rule (Appendix B and subroutine NUMINT) and the trapezium rule. To facilitate the numerical integration, calculations are made with a constant increment of laboratory time, and the small error that results from using the density calculated in one cycle to estimate the particle time for the next is ignored.

α_t, defined in equation (5.7) is more conveniently expressed in terms of laboratory time :

$$\alpha_t = U\alpha_\ell \int_0^{t_\ell} (\rho_{t1}^{-1})\, dt_\ell \qquad (5.59)$$

$$= U\alpha_\ell \left\{ -t_\ell + \int_0^{t_\ell} \rho_{t1}\, dt_\ell \right\} \tag{5.60}$$

Thus at each laboratory time, it is a simple matter to calculate the functions $\rho_{t1}\, e^{-\alpha_t t_p}$ in equation (5.5) for studies of $O_2(^1\Sigma_g^+)$ and $\rho_{t1}^2 \left(\frac{T_t}{T_1}\right)^{\frac{1}{2}} e^{-\alpha_t t_p}$ in equation (5.6) for studies of the dimol emission. Figures (5.11) and (5.12) show the changes in the function $\rho_{t1} e^{-\alpha_t t_p}$ with time; the assumption that the gas is fully relaxed is clearly unsatisfactory in the early part of the shock.

It is not convenient to store the values of these functions at each t_ℓ; instead, the polynomial curve fitting routine (subroutine CURFIT), written by W.R. Graves, is used to find the coefficients in the equation

$$Y = a_o + a_1 t_p + a_2 t_p^2 + a_3 t_p^3 + a_4 t_p^4 + a_5 t_p^5 \tag{5.61}$$

where

$$Y = \rho_{t1}\, e^{-\alpha_t t_p} \quad \text{or} \quad \rho_{t1}^2 \frac{T_t}{T_1}^{\frac{1}{2}} e^{-\alpha_t t_p} \tag{5.62}$$

The coefficients obtained are used in the computer analysis to calculate the corrected values of the rate constants from equations (5.5) and (5.6). The true curve of (density ratio x decay) in figures (5.11) and (5.12) actually crosses the "relaxed" curve as vibrational relaxation approaches completion; at times after the two curves have met, equation (5.61) is replaced by the relation

$$Y = \rho_{21}\, e^{-U\alpha_\ell (1-\rho_{21}^{-1}) t_p} \tag{5.63}$$

or

$$Y = \rho_{21}^2 T_{21}^{\frac{1}{2}}\, e^{-U\alpha_\ell (1-\rho_{21}^{-1}) t_p} \tag{5.64}$$

where t_p is still the true particle time. These equations are perfectly satisfactory in such circumstances and the function obtained by polynomial curve fitting to the true curve in the early part of the shock is much more satisfactory than when the whole curve is fitted.

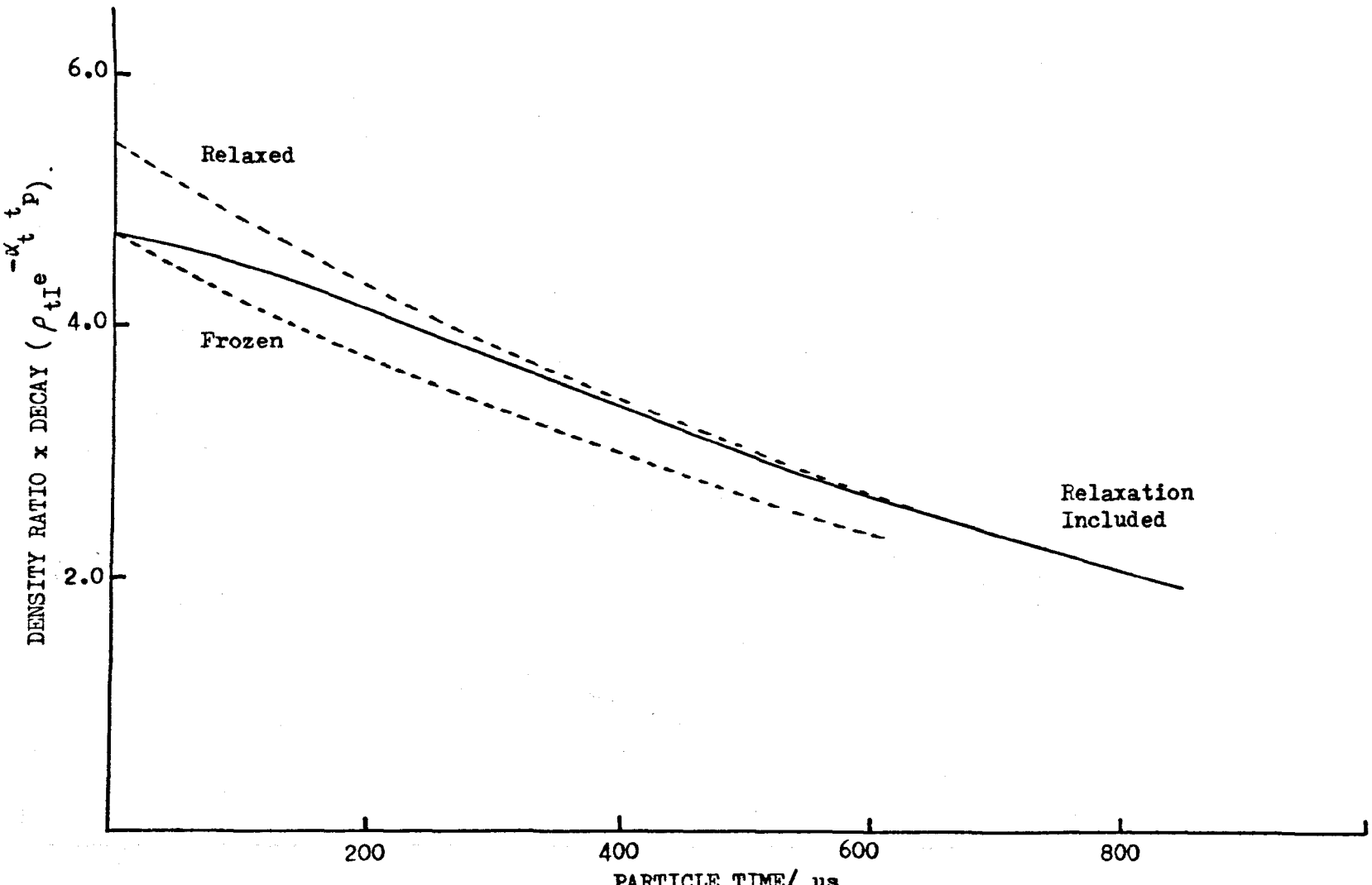

FIGURE 5.II Vibrational Relaxation of Oxygen: Effect on the Function $\rho_{tI} e^{-\alpha_t t_p}$ (T_2 = 1195 K)

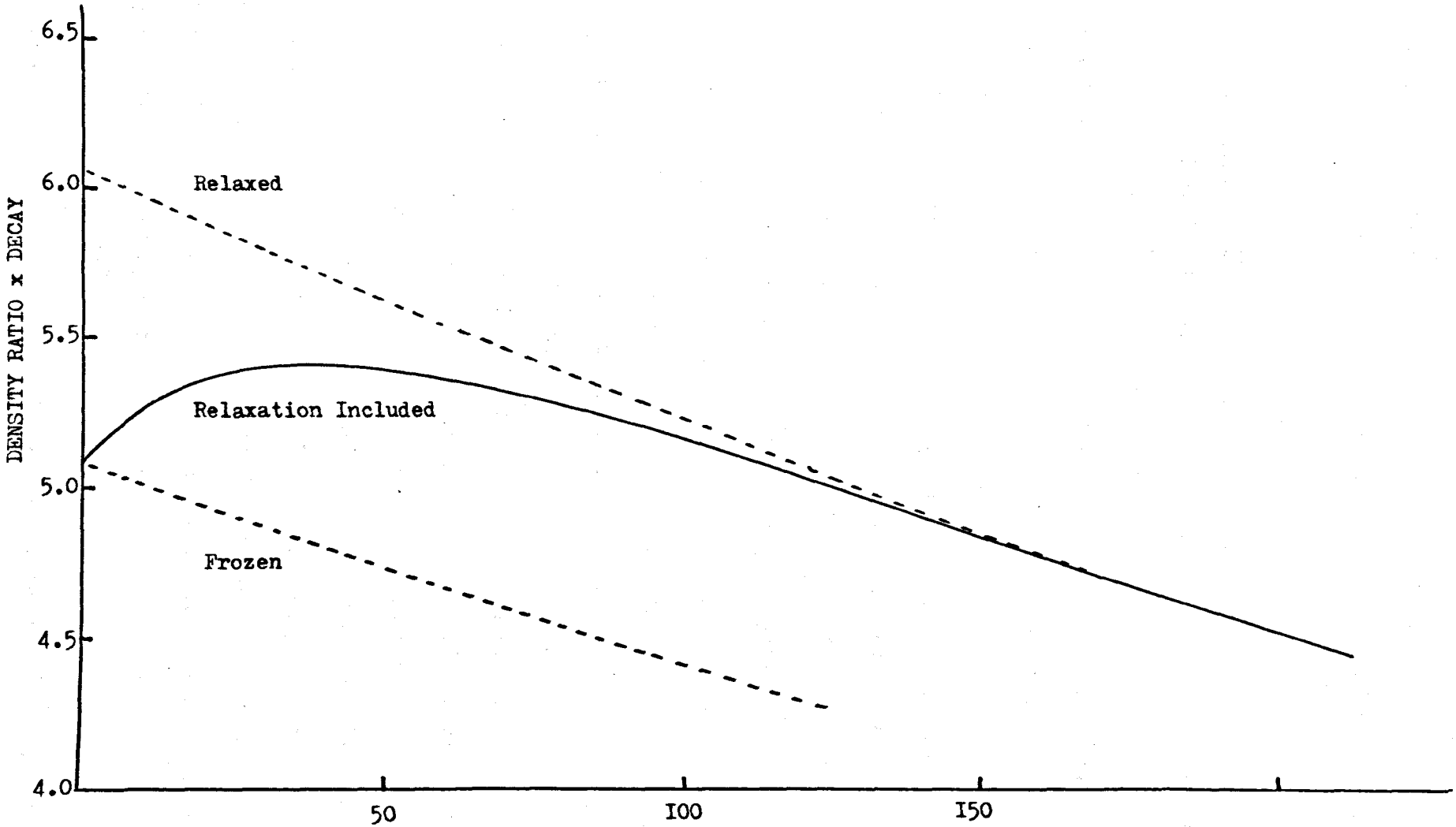

FIGURE 5.12 Vibrational Relaxation of Oxygen - T_2 = 1643 K

VIBREL also calculates (again by numerical integration) the mean density, temperature and pressure behind the shock front and the mean vibrational relaxation time, for the period of study of the shock-heated gas.

5.4.2. Shocks into oxygen/nitrogen mixtures

The vibrational relaxation time of pure nitrogen is given by[109]

$$\ln \tau_{vib} = 235\ T^{-1/3} - 25.88 \text{ (atm s)} \qquad (5.65)$$

The relaxation is much slower than that of oxygen (a factor of $\sim 10^3$ at 1000 K), and as a result the vibrational relaxation of oxygen/nitrogen mixtures is less rapid than that of pure oxygen.

The only worker to study experimentally the vibrational relaxation of oxygen/nitrogen mixtures is White (1968)[146]. He interpreted the observed changes of density as the sum of two exponential decays:

$$\rho_{t1} = \rho_{A1} + (\rho_{B1}-\rho_{A1})(1-e^{-t/\tau_{O2}}) + (\rho_{21}-\rho_{B1})(1-e^{-t/\tau_{N2}}) \qquad (5.66)$$

where ρ_{B1} is the hypothetical density ratio in state B, when oxygen is completely relaxed and the nitrogen is still frozen. This interpretation, if correct, means that the two species effectively relax separately; the oxygen was found to relax at the same rate as when pure, but the rate of nitrogen relaxation was increased by added oxygen as a result of vibrational energy exchange with excited O_2. At high temperatures ($\sim$ 5000 K), the rate of relaxation tended back to that of pure nitrogen.

Doubt has been cast on White's interpretation of his data, as a result of more recent studies of vibrational energy exchange. Nevertheless, his results should still be suitable for calculating the density etc. behind the shock front in these experiments. Measurements of the coefficients, C and D, in the equation

$$\ln \tau_{N_2} = CT^{-1/3} + D \text{ (atm s)} \qquad (5.67)$$

were made in mixtures containing 50, 67, 79, 90 and 95 % N_2; the values

of each coefficient were related to the composition by a simple polynomial curve fit:

$$C = 130.49 - 128.3\ X_{O_2} + 102.7\ X_{O_2}^2 \qquad (5.68)$$

$$D = 17.97 + 2.118\ X_{O_2} - 0.7918\ X_{O_2}^2 \qquad (5.69)$$

where X_{O_2} is the mole fraction of oxygen. White's data was not sufficiently precise to justify the inclusion of terms in higher powers of X_{O_2}, and equations (5.68) and (5.69) were not very satisfactory when extrapolated to concentrations of oxygen greater than 50%. In the absence of more suitable data, they were used for mixtures containing less than 80% O_2; at higher concentrations the relation

$$\ln \tau_{vib} = 86.5\ T^{1/3} - 16.896 \text{ (atm s)} \qquad (5.70)$$

was more satisfactory.

Once all this has been worked out, it is a simple matter to calculate the corrections for oxygen/nitrogen mixtures, using VIBREL. The conditions in the gas when frozen, relaxed and in state B are calculated by the DISHOCK routine, equations (5.57) and (5.58) are replaced by relations of the form of equation (5.66), in order to calculate the conditions at each t_p, and all subsequent calculations follow as before.

6. ANALYSIS BY COMPUTER GRAPHICS

6.1 Introduction

The transient recorder output is analysed, in terms of the equations derived in Chapters 4 and 5, by an interactive computer graphics program developed by Dr. P. Borrell[147] for use on the ICL 4130 computer at Keele University.

The interactive nature of the program allows the operator to exercise a considerable degree of control over the calculations made at each stage; in doing so he develops a "feel" for the calculations and an understanding of the steps involved. After each action of the program, a number of options on the next step are shown on the screen of a visual display unit (V.D.U.), together with a display of the partially treated data; the required option is selected by a sense switch. Such features are of particular value in the early stages of development of the computer analysis, as the effects of alterations in the program are easily tested directly. Once the analysis is working satisfactorily, they become less important, but even then it is desirable to remain in contact with the calculations as they are made. Many parameters throughout the program are specified by eye; although in a "blind" system all could be set adequately at the start, the interactive operations are generally more convenient and more accurate.

The program is written as a series of short subroutines; the ten principal subprograms are called in order by the main program, GRAPH2, and the data analysis is performed within these subroutines, frequently by making use of one of the many other subroutines available. Figure (6.1) shows the main sections of the program and gives a brief description of the nature of the calculations performed at each stage; all the subroutines (a total of eighty eight) are shown, together with an indication of their use, in Table 6.1. The early sections of the program, BEGIN to VRELAX

FIGURE 6.1

Principal subroutines of the Mainprogram, GRAPH2

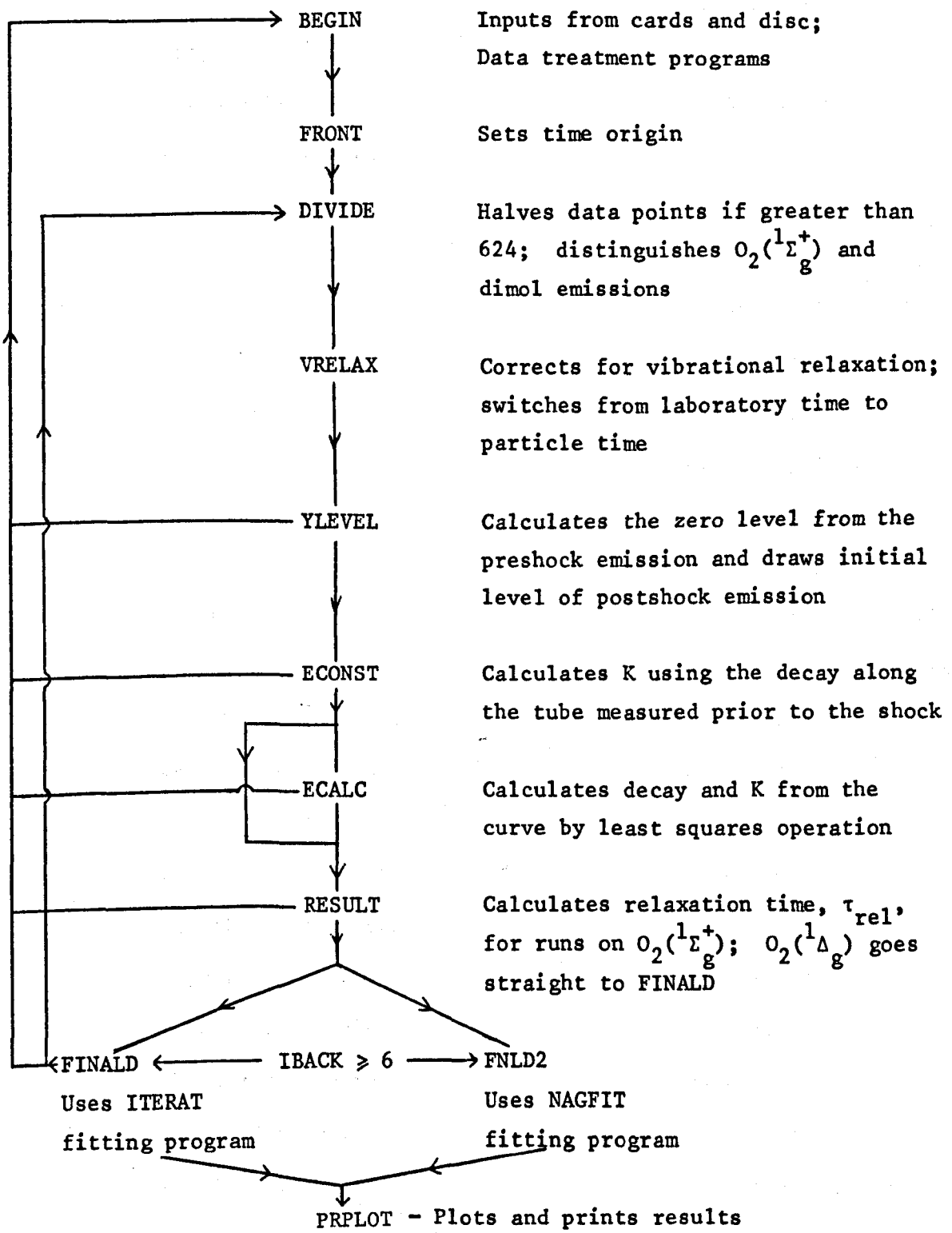

TABLE 6.1.

SUBROUTINE	USE	AUTHOR
GRAPH2	main program	P. Borrell
DEPICT	graphics	P. Borrell
BEGIN	reads data	P. Borrell
TFILE	stores ordered data	P. Borrell
TREAD	reads data from disc	P. Borrell
GAXES	graphics	M. Sturdy & P. Collis
GSCALS	graphics	M. Sturdy & P. Collis
GDAREA	graphics	M. Sturdy & P. Collis
GXLIN	graphics	M. Sturdy & P. Collis
GYLIN	graphics	M. Sturdy & P. Collis
GXLABL	graphics	M. Sturdy & P. Collis
GYLABLE	graphics	M. Sturdy & P. Collis
ZCROSS	graphics	M. Sturdy & P. Collis
ZSCALE	graphics	M. Sturdy & P. Collis
REJECT	rejects data points	P. Borrell
SCARY	rejects data points	P. Borrell
SELECT	rejects data points	P. Borrell
CARTES	rejects data points	P. Borrell
POLAR	rejects data points	P. Borrell
RORDER	rejects data points	P. Borrell
RANGE	rejects data points	P. Borrell
FRONT	chooses time origin	P. Borrell
DIVIDE	halves data points	P. Borrell
VRELAX	switches to particle time	P. Borrell & M.D. Pedley
VIBREL	calculates vibrational relaxation	M.D. Pedley
HSHOCK	calculates shock conditions	R.C. Millikan
TIMDIS	calculates changes from ideal function	M.D. Pedley

Table 6.1. continued:

NUMINT	numerical integration	M.D. Pedley
CURFIT	polynomial curve fit	W.R. Graves
SFLINE	sets "start" and "finish" lines	P. Borrell
YLEVEL	calculates zero and initial rise	P. Borrell
ECALC	calculates K from card decay	P. Borrell
LEASTQ	least squares program	P. Borrell
BIGDIS	economises big displays	P. Borrell
ECONST	calculates K and decay from curve	P. Borrell
RESULT	calculates quenching rate	P. Borrell
FNLD2	final display for NAGFIT	P. Borrell
PAVARY	varies parameters	P. Borrell
RESIDS	used for NAGFIT	P. Borrell
FNFIT2	used for NAGFIT	P. Borrell
NAGFIT	used for NAGFIT	P. Borrell
MONIT	used for NAGFIT	P. Borrell
E04GAF	N.A.G. library program[148]	
E04GAZ	N.A.G. library program	
P01AAF	N.A.G. library program	
F01AAF	N.A.G. library program	
F03AEF	N.A.G. library program	
F04AGF	N.A.G. library program	
F03AFF	N.A.G. library program	
F04AJF	N.A.G. library program	
F01ARF	N.A.G. library program	
DIFSIG	numerical differentiation	K.E. Newman & P. Borrell
FINALD	final display for ITERAT	P. Borrell
FINFIT	used for ITERAT	P. Borrell
EQUATA	integrated equations	P. Borrell & M.D. Pedley

Table 6.1. continued:

CA34	calculates exponentials	P. Borrell
CA134	calculates exponentials	P. Borrell
EQUAT3	integrated equations compensated for vibrational rel.	M.D. Pedley
YDELA	functions compensated for vibrational rel.	M.D. Pedley
YSIGA	functions compensated for vibrational rel.	M.D. Pedley
ITERAT	fitting program	K.E. Newman
MATMPY	used for ITERAT	K.E. Newman
INVERT	used for ITERAT	K.E. Newman
DETERM	used for ITERAT	K.E. Newman
SETUP	used for ITERAT	K.E. Newman
STORE	graphics	P. Borrell
PRPLOT	plots and prints results	P. Borrell
RATES	calculates rate constants	M.D. Pedley
DPLOTA	files data for plotting	P. Borrell
DATE	writes data on plots	P. Collis
GERROR	graphics	M. Sturdy & P. Collis
DELETE	deletes large displays	P. Borrell
RUN	graphics	P. Borrell
CHECK	prints check points	P. Borrell
MENU	controls some switch options	P. Borrell
NAME	graphics	P. Borrell
ZREAL	graphics	M. Sturdy & P. Collis
ZINT	graphics	M. Sturdy & P. Collis
ZINTCP	graphics	M. Sturdy & P. Collis
GCHOUT	graphics	M. Sturdy & P. Collis
ZCLEAR	graphics	M. Sturdy & P. Collis
GDRAW	graphics	M. Sturdy & P. Collis

Table 6.1. continued:

ZDIGTS	graphics	M. Sturdy & P. Collis
ZTRAK	graphics	M. Sturdy & P. Collis
ZSETP	graphics	M. Sturdy & P. Collis
ZPOINT	graphics	M. Sturdy & P. Collis
ZVECTR	graphics	M. Sturdy & P. Collis
ZRESET	graphics	P. Borrell
RESET	graphics	P. Borrell

treat the data so that it is in a suitable form for the calculation of the rate constants; the subroutines YLEVEL to RESULT then calculate approximate values of each of the parameters in the equations for use as initial values in the non-linear curve fitting programs in FINALD and FNLD2.

The graphics routines were written for use in conjunction with the ICL 4130 computer and are used extensively throughout the analysis. Parameters are set at each stage by a tracking cross on the V.D.U. screen, the position of which is controlled by a light pen.

There is no question of reproducing the graphics program in full, instead, the principal actions of each of the subprograms in figure (6.1) are described in detail, together with some of the general features of the program.

6.2. Subroutine BEGIN

Subroutine BEGIN reads the data card, which for each run supplies the following information: the run number, density ratio, pre-shock emission from $O_2(^1\Sigma_g^+)$, pre-shock emission from $O_2(^1\Delta_g)$, temperature ratio (T_{21}), shock velocity, decay along the tube, initial pressure, and the mole fraction of nitrogen. The density and temperature ratios are read from tables and the values for either the relaxed or frozen conditions used on the card, depending on the shock velocity (Chapter 5); neither is essential if vibrational relaxation is to be included later in the calculations.

The run number is compared with those of the experimental data stored on disc (Chapter 2), and the correct set of data selected and displayed on the screen as emission (mV) against laboratory time (μs). At this stage it is possible to abandon the run and read a new card, to continue if the data looks satisfactory, or to reject some of the data points. The rejection of data points is justified

(i) where the hot flow behind the shock front has ended well before the end of the transient recorder record;

(ii) with some fast shocks which display large, random peaks superimposed on the later parts of the trace. The source of such peaks is not known; combustion of dirt on the walls and reflections from fragments of diaphragm material have been suggested as possibilities.

The data points are rejected by subroutine REJECT; it allows the deletion of individual points, or parts of the X or Y range, selected by the light pen using subroutine RANGE. A further option, sometimes used for situation (ii) is the deletion of areas of points (subroutine SCARY).

The data, in its ordered form, may be filed on to a new disc, using subroutine TFILE; this is particularly valuable if the program is returned to BEGIN from a later stage in the calculations (figure (6.1)), at which point the data has been further ordered in subroutine DIVIDE.

6.3. Subroutine FRONT

In this routine, the operator sets the start of the rise in emission that results from the arrival of the shock front. The cross is set approximately on the main display using the light pen; an enlargement of the region of the initial rise is then displayed in the top right hand corner of the screen, and is used to obtain a more precise setting (figure (6.2)). The time of arrival of the shock front can be calculated from the measured shock velocity with a precision of ± 2.0 μs; by setting it manually, the accuracy is improved to ± 0.5 μs (i.e. ± one data point). The time origin set in this subprogram is referred to as TORIG in later sections.

6.4. Subroutine DIVIDE

In subroutine DIVIDE, the operator selects the correct form of analysis of the data for the emission under study. If the number of data points rejected in BEGIN is less than 400 (as is normally the case), the remaining data is halved by discarding alternate points. This operation, originally necessary because of a shortage of storage space, is performed to reduce the time taken by the calculations in the non-linear curve fitting programs; the effect on the final results is negligible.

An option that allows the study of the output from two photomultiplier detectors, using only one transient recorder, is also available at this stage. The output from the two detectors is fed into an oscilloscope operating in the chopped mode, and the potential supplied to the oscilloscope screen is recorded by the transient recorder; the two emissions are separated out in DIVIDE. This technique proved unsatisfactory because switching transients are present when the oscilloscope operates in the chopped mode (the data rejection programs were originally designed to eliminate such errors).

FIGURE 6.2 Graphics Display of the Program at Subroutine FRONT; the Time Origin Is Set with an Accuracy of ±One Data Point.

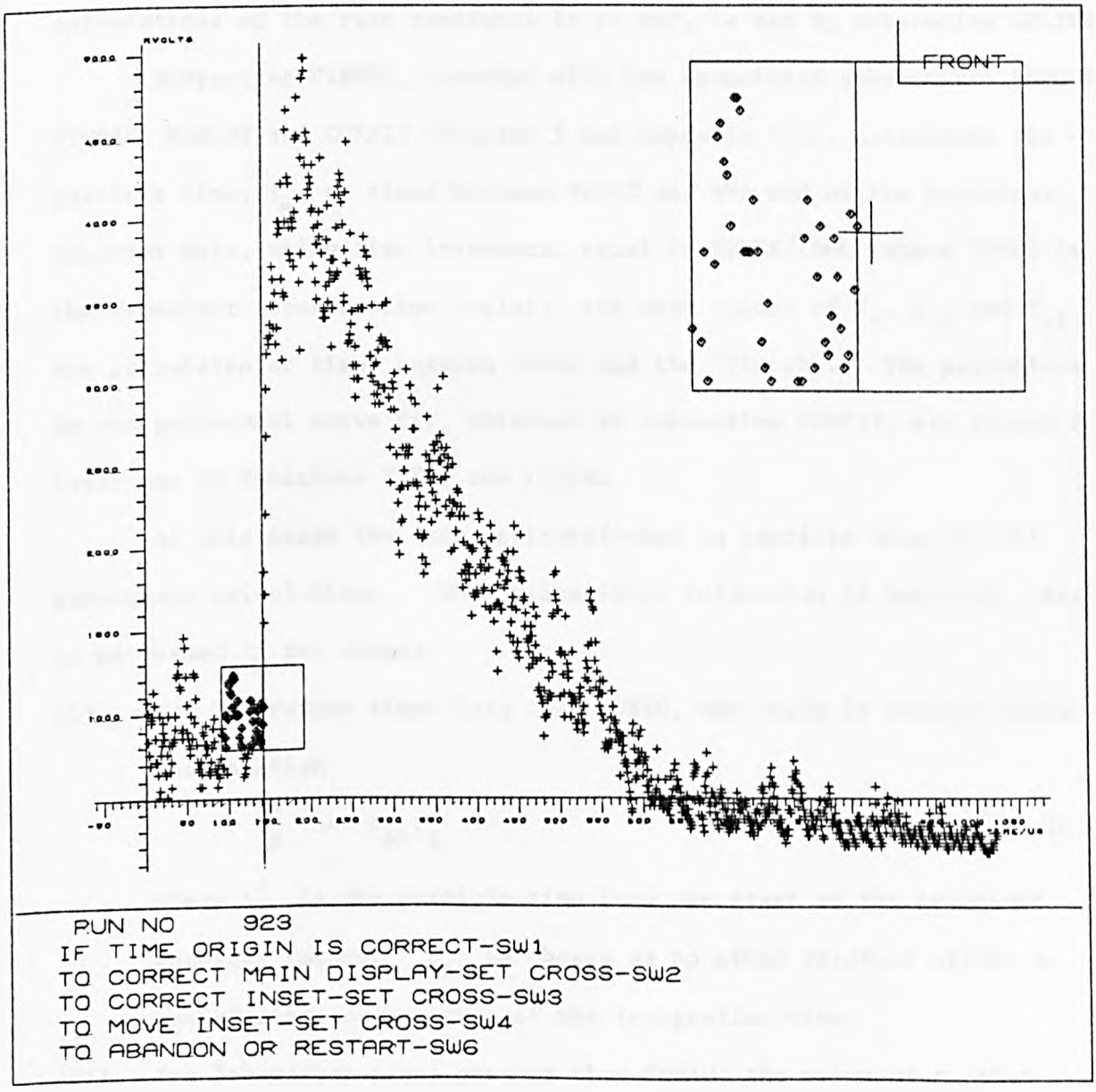

6.5. Subroutine VRELAX

The inclusion of corrections for the effects of vibrational relaxation is an option at this stage. If vibrational relaxation is to be included, it is necessary to designate the period of hot flow time for which calculations are to be made, in order to obtain the correct mean values of the temperature behind and the density and pressure ratios before and behind the shock front; the "finish", the time at which calculations of the rate constants is to end, is set by subroutine SFLINE.

Subroutine VIBREL, together with the associated subroutines HSHOCK, TIMDIS, NUMINT and CURFIT (Chapter 5 and Appendix C.2), calculates the particle time, t_p, at times between TORIG and the end of the transient recorder data, using time increments equal to XSENS/1000 (where XSENS is the transient recorder time scale); the mean values of T_t, ρ_{t1} and P_{t1} are calculated at times between TORIG and the "finish". The parameters in the polynomial curve fit, obtained in subroutine CURFIT, are stored for later use in functions YSIGA and YDELA.

At this stage the data is transformed to particle time for all subsequent calculations. When vibrational relaxation is included, this is performed in two stages:

(i) for laboratory times less than TORIG, the scale is changed using the relation

$$t_p' = \rho_{A1} t_\ell \qquad (6.1)$$

where t_p' is the particle time from the start of the transient recorder record. ρ_{A1} is chosen as no other relation allows a satisfactory calculation of the integration time.

(ii) for laboratory times greater than TORIG, the value of t_ℓ that corresponds to each data point is exchanged for the value of t_p calculated by VIBREL. To set TORIG in a position consistent with (i), each value of t_p is changed to t_p', where

$$t_p' = t_p + \rho_{A1}(\text{TORIG}) \qquad (6.2)$$

When vibrational relaxation is neglected, the transition to particle time is made by setting ρ_{A1} equal to ρ_{21}, using (i) as before, and the ideal relation

$$t_p = \rho_{21} t_\ell \tag{4.9}$$

(where ρ_{21} is the density ratio read from the data card in BEGIN) for times greater than TORIG. Equation (6.2) is again used to calculate t'_p from t_p.

6.6. Subroutine YLEVEL

The analysis of the experimental data starts at this stage; each data point is considered to have coordinates on the graphical display, (t'_{pi}, Y_i), where Y_i is the level of emission in millivolts at particle time t'_{pi}, and the data is analysed by fitting equations of the form

$$Y = f(t'_p) \tag{6.3}$$

Subroutine YLEVEL calculates, and draws a horizontal line through, the mean value of those data points that come before the time origin; the pre-shock emission on the data card is then used to draw the line corresponding to zero emission.

An approximate value of the initial level of emission from the shock-heated gas (SAFTGL) is calculated using the relation

$$\text{SAFTGL} = I^o_{\Sigma 1}\rho_{21} \tag{6.4}$$

or

$$\text{SAFTGL} = I^o_{D1}\rho_{21}T_{21}^{\frac{1}{2}} \tag{6.5}$$

depending on the nature of the emission. The initial level is displayed on the oscilloscope screen; this level and the voltage zero level may be reset (not independently) by the light pen, but this option should only be used if there is evidence to suggest that the measured pre-shock emission is incorrect.

6.7. Subroutine ECONST

Subroutines ECONST, ECALC and RESULT calculate approximate values of the ratios K in equations (4.27) and (4.42), and the relaxation time τ_{rel}, in equation (4.42), for use as initial values of the parameters in the curve fitting programs, NAGFIT and ITERAT. As the accuracy of these initial estimates is not of great importance, the ideal relations are used, and the effects of vibrational relaxation are ignored.

Thus in ECONST, the decay on the data card, α_ℓ, is converted to the decay with time, α_t, by equation (4.13)

$$\alpha_t = U\alpha_\ell \left(1-{}^1/\rho_{21}\right) \tag{4.13}$$

A line is drawn on the graphical display of the function

$$Y = KI^o_{\Sigma 1}\rho_{21}e^{-\alpha_t t_p} \tag{6.6}$$

or

$$Y = KI^o_{D1}\rho_{21}{}^2T_{21}{}^{\frac{1}{2}}e^{-\alpha_t t_p} \tag{6.7}$$

depending on the nature of the emission. Initially, K is set equal to unity and the line passes through the SAFTGL, but its value is changed by moving the line up or down with the light pen to give the best fit to the experimental data.

If the gradient obtained from the pre-shock decay is clearly unsatisfactory, α_t may be re-estimated by moving to subroutine ECALC. Otherwise the "finish" is set (if not preset in VRELAX) and, for studies of $O_2(^1\Sigma^+_g)$, the "start" (the time at which the relaxation of the chemical equilibrium is considered to be complete) is chosen (subroutine SFLINE) and the program moves on to the start of subroutine RESULT.

6.8. Subroutine ECALC

The "start" amd the "finish" (providing it is not preset) are set using subroutine SFLINE. In the region of the curve between these times, the experimental data is fitted by a function of the form

$$Y = Ae^{-\alpha_t t_p} \tag{6.8}$$

and by performing a least squares operation to fit the data points to the linear equation

$$\ln Y = \ln A - \alpha_t t_p \tag{6.9}$$

the value of α_t, which is the best fit to the experimental data, is obtained. K is estimated from equation (6.6) or (6.7), by the pertinent relation

$$A = K I^o_{\Sigma 1} \rho_{21} \tag{6.10}$$

or

$$A = K I^o_{D1} \rho_{21}{}^2 T_{21}{}^{\frac{1}{2}} \tag{6.11}$$

At the conclusion of the calculations, the program normally moves to RESULT. However, if vibrational relaxation is to be included, it is necessary to return to BEGIN in order to recalculate the parameters in VRELAX using the new decay.

Although the value of α_t calculated in ECALC is inevitable a better fit to the data than that obtained from the decay prior to the shock, the latter is preferred for several reasons:

(i) the equations in ECONST and ECALC are not corrected for the effects of vibrational relaxation;

(ii) the rate of relaxation of the level of emission behind the shock front has not been estimated at this stage;

(iii) no integration to allow for the width of the photomultiplier slit has been performed.

These effects all tend to distort the gradient appreciably from that

which gives the best fit to equation (6.6) or (6.7). Thus, what appears to be a poor fit in ECONST may well turn out to be quite satisfactory when analysis is complete, and the recalculation of the decay at this stage may give rise to unnecessary systematic errors.

6.9. Subroutine RESULT

Subroutine RESULT calculates the relaxation time, τ_{rel}, for the emission from $O_2(^1\Sigma_g^+)$ and then offers a choice of fitting routines for the final part of the program. Initially, the level of emission, Y_i, at each data point (Y_i, t_{pi}) is converted to a new value, Y_i' by the function

$$Y_i' = Y_i / K e^{-\alpha_t t_p} \qquad (6.12)$$

Figure (6.3) shows the results of this calculation; at this stage several options are available:

(i) for runs which follow the dimol emission, there is no relaxation time to be estimated and the program moves on to the final part of RESULT;

(ii) for runs following the emission from $O_2(^1\Sigma_g^+)$ where the ratio of levels, K, is less than or very near to unity, it is impossible to calculate τ_{rel} at this stage and, as for (i) the program moves to the final part of RESULT with τ_{rel} set equal to zero;

(iii) if the values of K and the decay are clearly unsatisfactory, they may be re-estimated by returning to DIVIDE;

(iv) if the situation is as in figure (6.3), τ_{rel} is calculated from the experimental points which lie inside the rectangle formed by the time origin, the "start" line and the lines corresponding to $Y' = 1/K$ and $Y' = 1$. The experimental points inside the relaxation zone should fit the relation

$$Y' = (1 - e^{-t_p/\tau_{rel}}) \qquad (6.13)$$

and the fitting is accomplished by taking the logarithms of $(1-Y')$ and t_p and performing a least squares operation as in ECALC.

The relaxation time estimated in (iv) is frequently of low accuracy as the scatter of the experimental data results in an unrepresentative sample being selected for study when $K < 1.5$. As a result, it is not impossible

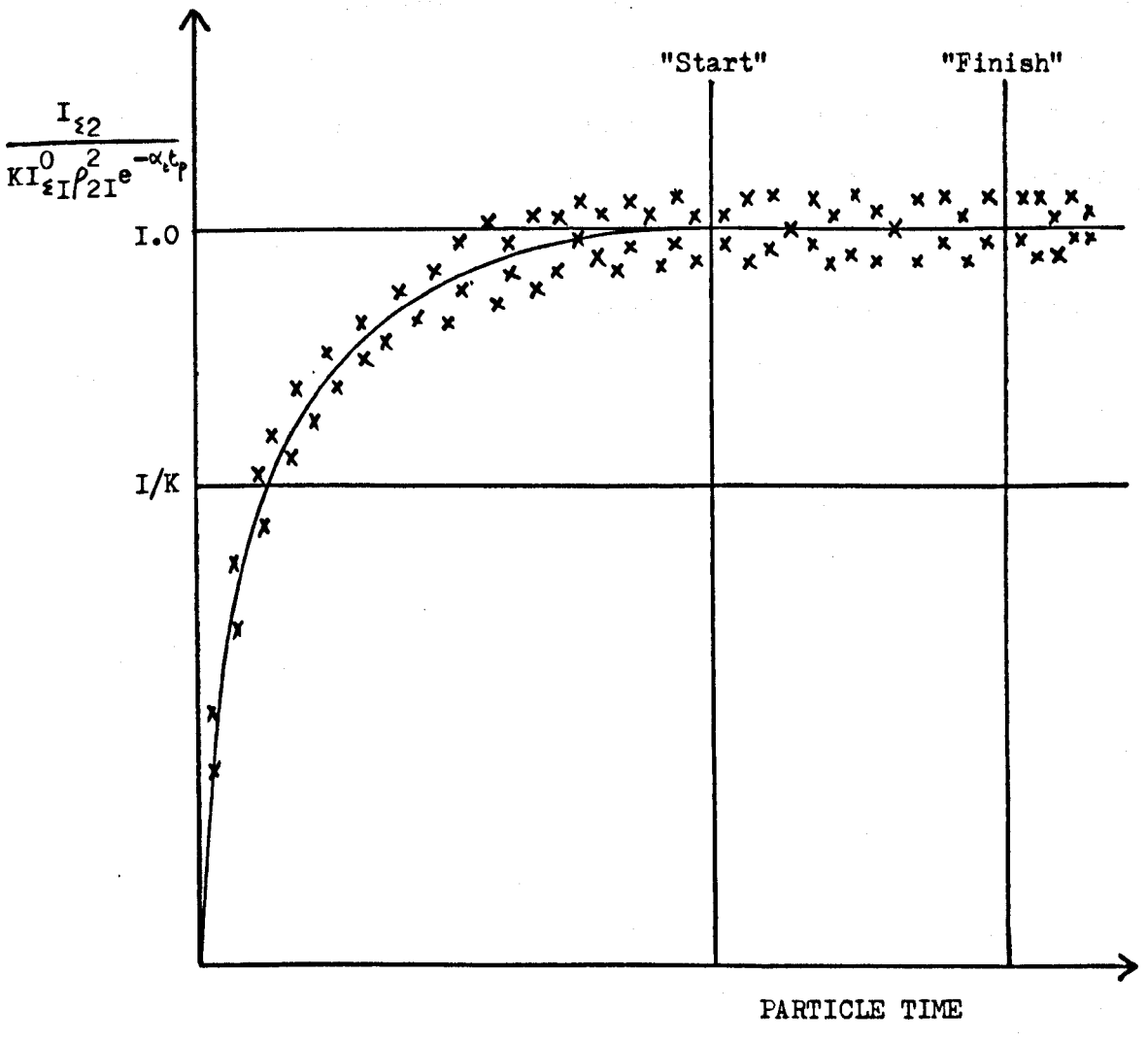

FIGURE 6.3 Calculation of Rate of Collisional Deactivation of $O_2(^I\Sigma_g^+)$ Behind the Shock Front

to calculate a least squares line which gives a negative value of τ_{rel}; if this happens, it is necessary to go back to YLEVEL and return to the end of RESULT, missing out the calculations in (iv).

In all our early experiments, the ratio of levels of emission from $O_2(^1\Sigma_g^+)$, K, was greater than or equal to unity. As this is a measure of the relative temperature dependence of the energy pooling and collisonal quenching reactions (equation (4.38)), it is possible for K to be less than one in some cases. However, RESULT does not allow the calculation of the relaxation time in such circumstances, and calculations of the relaxation time must be left to the non-linear curve-fitting part of the program.

6.10. Subroutines FINALD, FNLD2, and PRPLOT

The subroutines FINALD and FNLD2 control the final display of the results; they differ only in the fitting programs that they use. The programs used to optimise the fit of equations (5.5) and (5.6) to the experimental data are ITERAT, written by Dr. K.E. Newman, and NAGFIT, which uses program E04GAF from the Nottingham Algorithms Group Library.

Consider an analysis of the emission from shock-heated $O_2(^1\Sigma_g^+)$. The program has arrived at FINALD with the approximate values of K and τ_{rel} (or possibly with $\tau_{rel} = 0$) calculated at an earlier stage. FINALD calls subroutine EQUATA to calculate the line given by using these parameters in equation (4.39) or (4.22); if vibrational relaxation is to be included, subroutine EQUAT3, which uses the functions YSIGA and YDELA to calculate the emission from equations (5.5) and (5.6)

$$\frac{I_{\Sigma 2}}{I^o_{\Sigma 1}} = K\left[1 - (1-{}^1/K)e^{-t_p/\tau_{rel}}\right] \rho_{t1} e^{-\alpha t t_p} \qquad (5.5)$$

$$\frac{I_{D2}}{I^o_{D1}} = K \rho_{t1}{}^2 \left(\frac{T_t}{T_1}\right)^{\frac{1}{2}} e^{-\alpha_t t_p} \qquad (5.6)$$

is called instead.

At this stage, for the first time, the equations are integrated to take into account the width of the photomultiplier slit. The integration assumes a simple model in which the slit is of rectangular cross section (Chapter 2); the three possible situations are shown in figure (6.4) and outlined below.

Both the particle time after the arrival of the shock front, t_p, and the particle time after the start of the transient recorder record, t'_p (defined in equation (6.2)), are used in the integrations. Figure (6.4) shows that the integration time, τ_{int}, is negative; the following relations follow:

$\underline{t'_p < \text{TORIG}}$

$$Y = I^o_{\Sigma 1} \tag{6.14}$$

$\underline{t'_p + \tau_{int} \leq \text{TORIG}}$

$$Y = \frac{1}{\tau_{int}} \left\{ I^o_{\Sigma 1}(t'_p + \tau_{int} - \text{TORIG}) + \int_{t'_p}^{\text{TORIG}} \left\{ I^o_{\Sigma 1} K \left[1-(1-^1/_K) e^{-t_p/\tau_{rel}} \right] \rho_{t1} e^{\int_o^{t_p} -\alpha_t dt_p} \right\} dt'_p \right\} \tag{6.15}$$

$\underline{t'_p + \tau_{int} > \text{time origin}}$

$$Y = \frac{1}{\tau_{int}} \int_{t_p}^{t_p + \tau_{int}} \left\{ I^o_{\Sigma 1} K \left[1-(1-^1/_K) e^{-t_p/\tau_{rel}} \right] \rho_{t1} e^{\int_o^{t_p} -\alpha_t dt_p} \right\} dt_p \tag{6.16}$$

The integrals in equations (6.15) and (6.16) may be obtained by calculating the exact integrated form of the equations, or by numerical integration using Simpson's rule (Appendix B); the two methods give similar results, but the exact solution cannot be obtained when vibrational relaxation is taken into account.

Figure (6.4b) shows that the integration time will be of greatest importance in the intermediate situation when $(t'_p + \tau_{int}) <$ time origin, and that the finite rise time is a direct result of the width of the slit; the integration time is approximately related to the mean slit width ($\Delta\ell$)

$$\tau_{int} = \rho_{21} \frac{\Delta\ell}{W_p} \tag{6.17}$$

but is also a function of the rise time of the electronic equipment (Chapter 2).

On the laboratory time scale, the integration time, τ_{lab}, is constant; the conversion to particle time is made using the relation

$$\tau_{int} = \int_{t_\ell}^{t_\ell + \tau_{lab}} \tau_{lab} \rho_{t1} dt_\ell \tag{6.18}$$

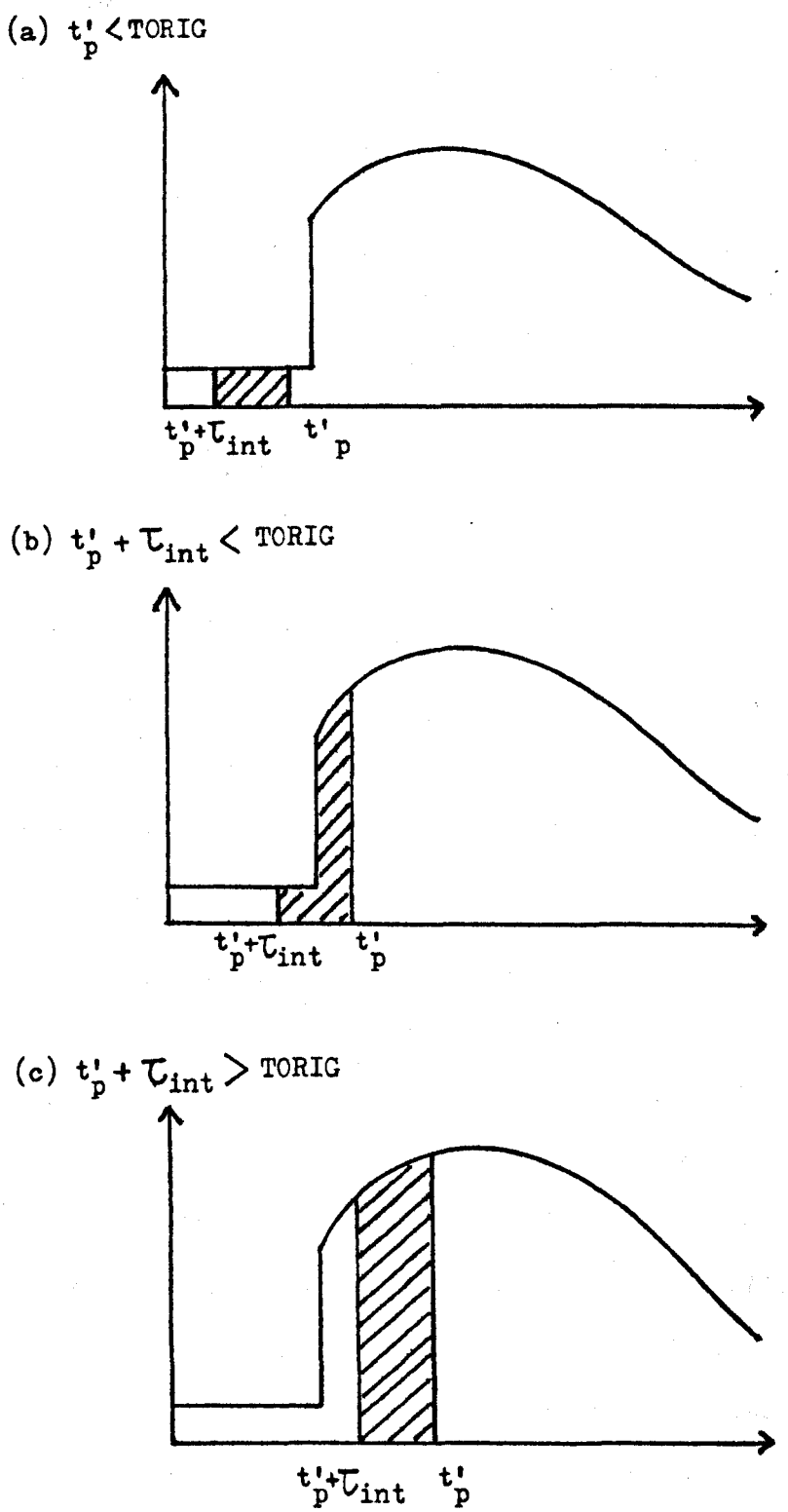

FIGURE 6.4 Shock Profile: Area Under Curve Seen by Slit of Rectangular Cross-Section

As $t_\ell + \tau_{lab} \simeq t_\ell$, equation (6.18) may be rewritten

$$\tau_{int} \simeq \rho_{tl}\, \tau_{lab} \qquad (6.19)$$

(where ρ_{tl} is the density ratio at laboratory time t_ℓ)
In fact, considering the approximate nature of the slit function, it is reasonable to make the approximation

$$\tau_{int} = \rho_{Al}\, \tau_{lab} \qquad (6.20)$$

as the integration time is of greatest importance in the early part of the curve where $\rho_{tl} \simeq \rho_{Al}$.

The parameters to be varied in the non-linear fitting routine, ITERAT, are then chosen; the possible variables are K, τ_{rel}, τ_{int} and α_t, but the decay cannot be iterated if vibrational relaxation is included, because the parameter

$$Y = a_o + a_1 t_p + a_2 t_p^{\,2} + \ldots. \qquad (5.61)$$

calculated from the polynomial expression derived in CURFIT in YSIGA no longer includes any function of α_t. These parameters may be incremented or decremented by 1% or 5% (subroutine PAVARY) to improve the initial fit. ITERAT, together with its associated subroutines, FINFIT, SETUP, DIFSIG, MATMPY and INVERT optimises the fit of equations (6.14) - (6.16) to the experimental data by varying the chosen parameters. The subroutine and the alternative fitting routine, NAGFIT, operate by minimising the sum of the squares of the residuals left when the calculated emission at each point is subtracted from the experimental value, Y_i. Both routines require

the differentials of the functions; the function values are calculated numerically in EQUATA and EQUAT3 and the differentials are estimated by numerical differentiation (subroutine DIFSIG).

The number of iterative cycles required for the parameters to reach a consistency of ± 1% varies between about 4 and 12. The values of those parameters which are being varied are displayed on the V.D.U. screen together with the values after the previous iteration. Occasionally, the iteration does not converge; the cycle is then stopped manually and the parameters may be re-estimated by subroutine PAVARY or by going back to DIVIDE. Alternatively, NAGFIT may be chosen instead; the two fitting routines are controlled in much the same way. NAGFIT uses the subroutines RESIDS, FNFIT2 and several library routines called by the principal library routine, E04GAF; it performs more rapidly than ITERAT and is inherently far more stable in that the iterative cycle always converges. However, NAGFIT appears to give a far less satisfactory fit to the experimental data; it always confirms the optimum values of the parameters calculated by ITERAT from the approximate estimates obtained earlier in the program, but the reverse is rarely true. The sum of the squares of the residuals will have more than one minimum; presumably NAGFIT settles for a shallow, local minimum, while ITERAT seeks out a deeper minimum which satisfies both routines. Certainly the parameters calculated using ITERAT give a much better fit to the experimental data than do those obtain in NAGFIT.

When the iteration is complete, the program returns to FINALD. If the parameters now give a satisfactory fit to the data, subroutine PRPLOT is called by a sense switch.

PRPLOT displays the final fit to the data on the V.D.U. screen, together with the optimised parameters and the associated errors. If a permanent record is required, this trace is filed on disc for subsequent plotting; an example of the plotter output is shown in figure (6.5).

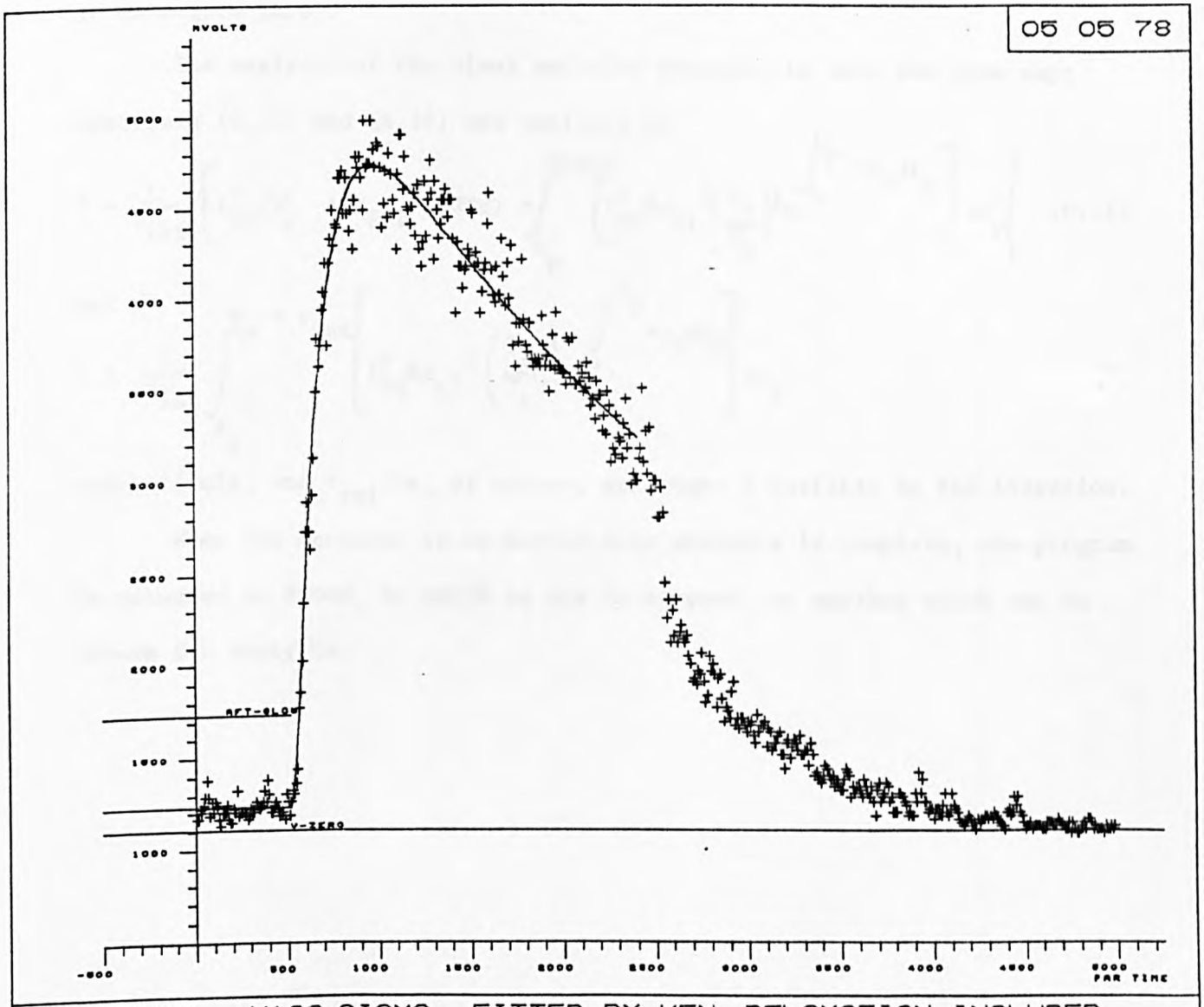

FIGURE 6.5 Analysis by Computer Graphics - Plotter Output.

Subroutine RATES calculates the rate constants from τ_{rel}, K and the room temperature rate constants; these, together with the values of all the other useful parameters in the program, are automatically printed, as in figure (6.6).

The analysis of the dimol emission proceeds in much the same way; equations (6.15) and (6.16) are replaced by

$$Y = \frac{1}{\tau_{int}} \left\{ I^o_{D1}(t'_p + \tau_{int} - TORIG) + \int_{t'_p}^{TORIG} \left[I^o_{D1} K \rho_{t1} \left(\frac{T_t}{T_1} \right)^{\frac{1}{2}} e^{\int_o^{t_p} -\alpha_t dt_p} \right] dt'_p \right\} \quad (6.21)$$

and

$$Y = \frac{1}{\tau_{int}} \int_{t_p}^{t_p + \tau_{int}} \left[I^o_{D1} K \rho_{t1}{}^2 \left(\frac{T_t}{T_1} \right)^{\frac{1}{2}} e^{\int_o^{t_p} -\alpha_t dt_p} \right] dt_p \quad (6.22)$$

respectively, and τ_{rel} is, of course, no longer a variable in the iteration.

When the operator is satisfied that analysis is complete, the program is returned to BEGIN, in which it may be stopped or another shock may be chosen for analysis.

```
            ANALYSIS FROM GRAPHICAL DISPLAY                    26 04 78

            RUN NUMBER   H165    SIGMA RUN                      FITTED BY KEN

    RESULTS                                                     VIBRATIONAL RELAXATION INCLUDED

FITTED      QUENCHING CONST      :    0.002377  ERROR    0.000174 USEC-1  420.72862  ERROR  30.85032   USEC
FITTED      RATIO(K)             :    2.312313  ERROR    0.029364
PROVIDED    DECAY CONSTANT       :   -0.000344   USEC-1                        -0.00551  CM-1
FITTED      INTEGRATION TIME     :   32.258507  ERROR    7.740748 USEC

   RATE CONSTANTS

FITTED      ENERGY POOLING(K1)   :  0.4715E+05  ERROR 0.8501E+03 L MOLE-1 S-1       LOG(K1) = 4.827
FITTED      COLL. QUENCHING(K2)  :  0.1907E+07  ERROR 0.1398E+06 L MOLE-1 S-1       LOG(K2) = 6.280

   DATA PROVIDED

            PRE-SHOCK GLOW-GIVEN :    239.00    USED   239.00
            AFTER GLOW     GIVEN :    853.91    USED   853.91

            RDAVG =  3.423   TAVG =  646.   SPEED =     0.0868 CM/US   PERCENT OXYGEN =  46.30
            X ORIGIN =   575.07 US
            Y ORIGIN =  2020.11 MVOLTS

            NO OF ITERATIONS =  3                              NO OF DATA POINTS =  472

            SUM OF THE SQUARES OF THE RESIDUALS = 0.12300E+03

            FITTING COMPLETED
```

FIGURE 6.6 Analysis by Computer Graphics - Printout of Results

6.11. Options available throughout the program

At any of the principal stages of the program, a sense switch allows the operator to return to BEGIN. The sense switch sets IBACK equal to one; at later stages in the program, it is also possible to return only as far as DIVIDE, by setting IBACK equal to five. Normally, IBACK has a value of zero or two, which indicates whether the emission from $O_2(^1\Sigma_g^+)$ or the dimol emission is under study.

Test routines are available throughout the calculation, but may be set and reset only in BEGIN and YLEVEL. They give a printout of the title of each subroutine entered and of the detailed calculations in VIBREL, CURFIT, ECALC, RESULT and ITERAT. As this reduces the speed of the program significantly, they are only used when testing a new section.

CHAPTER 7

RESULTS OF THE HIGH TEMPERATURE STUDIES OF SINGLET MOLECULAR OXYGEN

In this chapter the results obtained from the high temperature discharge flow shock tube experiments are presented together with a discussion of their accuracy. Results are reported for our studies of the dimol emission and the formation and removal of $O_2(^1\Sigma_g^+)$ in pure oxygen and in oxygen/nitrogen mixtures.

7.1. Accuracy of the Results

The precision of the rate constants calculated from the computer analysis of each experiment is much greater than the overall precision of the results. The error limits defined by the scatter of the transient recorder data for a slow shock such as M165 (Figure (6.5)) are only about ± 7.5%; for a shock of average velocity such as M192 (Figure (6.6)), where there is little noise on the transient recorder data, the error is less than ± 4%. In each case the principal source of error is in the calculation of the rate constant for collisional deactivation from the relaxation zone; the precision of the ratio of levels, K, is ± 1.3% for M165 and ± 0.4% for M192.

The results of a series of shock tube experiments inevitably show a wider scatter; the accuracy is generally good but the precision of the data is poor. Factors contributing to the scatter of the results are the finite opening time of the diaphragm when the bursting pressure is reached, variable shock deceleration (although the deceleration in these experiments has been shown to be small) and errors in the measurement of the parameters required in the computer analysis. The errors in the measured values of the shock velocity, initial pressure, initial temperature, pre-shock emission and pre-shock decay will probably give rise to an error of ± 3-4% in the calculated rate constant. Thus the precision of the results of the slow shocks such as M165 is unlikely to

be better than ± 10%. The scatter of the results increases with temperature as the other factors increase in importance; because it is not possible to estimate the magnitude of these sources of error for a single shock, no error bars are shown in the plots of the data in Chapters 7 and 8.

7.2. The Dimol Emission

The emission from $O_2(^1\Delta_g)$ at 634 nm is used to study both the rate of quenching of $O_2(^1\Delta_g)$ and the nature of the dimol reaction, behind the shock front.

Figure (7.1) shows a typical photographic record of the emission from shock-heated $O_2(^1\Delta_g)$. The initial computer analysis took no account of the vibrational relaxation behind the shock front, and the decay in emission, α_t, was chosen as a variable in the non-linear least squares fitting routines. This allowed comparison of the decay prior to the shock with the post-shock decay, as described in Chapter 4.1; the estimate of the post-shock decay made in this way is of limited accuracy as the effects of vibrational relaxation on the particle time and the density behind the shock front (Chapter 5) are neglected. However, when vibrational relaxation is included, the decay cannot be varied in the fitting part of the program (Chapter 6).

The computer analysis also calculates the ratio K in equation (4.27)

$$\frac{I_{D2}}{I^o_{D1}} = K \rho_{21}^2 T_{21}^{\frac{1}{2}} e^{-\alpha_t t_p} \qquad (4.27)$$

and in this case the equations corrected for vibrational relaxation may be used instead. However, the effect of the corrections on K is expected to be small, and this is confirmed by the results recently obtained by Mr. K. Grant (Figures (7.2) and (7.3)). As the change in K is well within the experimental scatter of the results, the data in Table 7.1

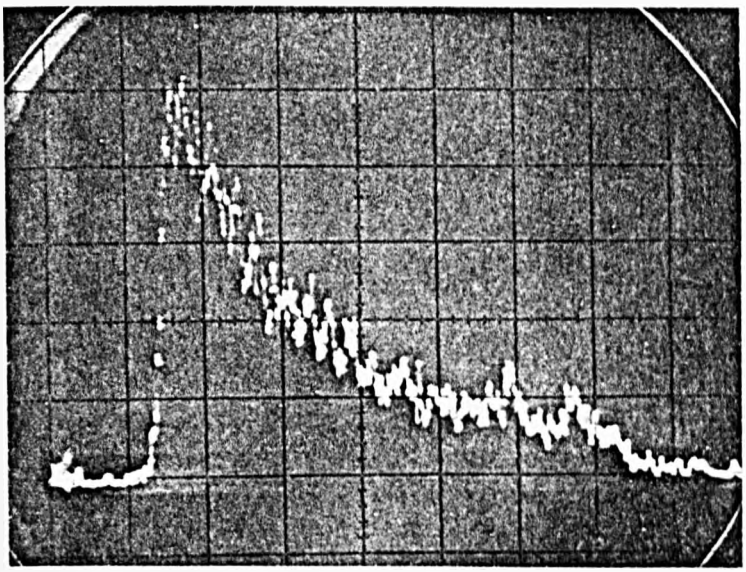

RUN NUMBER M124

Sweep Speed 50 us cm^{-1}

Sensitivity 2 V cm^{-1}

Pre-Shock Emission 6.28 mV

Shock Velocity 1.629 Km s^{-1}

FIGURE 7.1 The Dimol Emission in 100% Oxygen

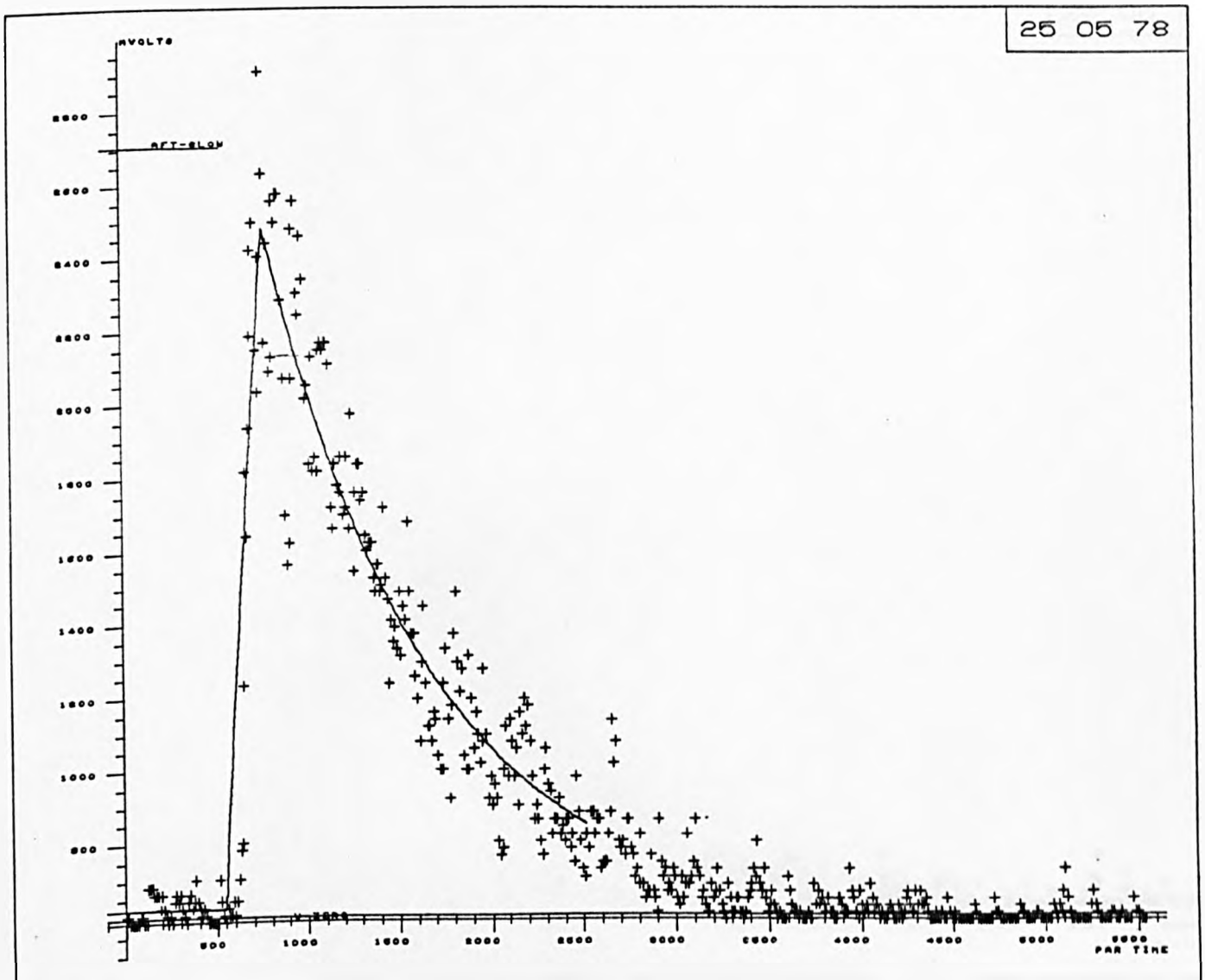

RUN NO A C14 DELTA FITTED BY KEN RELAXATION NOT INCLUDED

RATIO (K)	: 1.018093	ERR	.024518	FITTED
DECAY CONSTANT	: -.001139	ERR	.0000419	FITTED
INTEGRATION TIME	: 228.0308	ERR	8.485357	FITTED

FIGURE 7.2 Emission from $O_2(^1\Delta_g)$ in Pure Oxygen - Effects of Vibrational Relaxation Not Included.

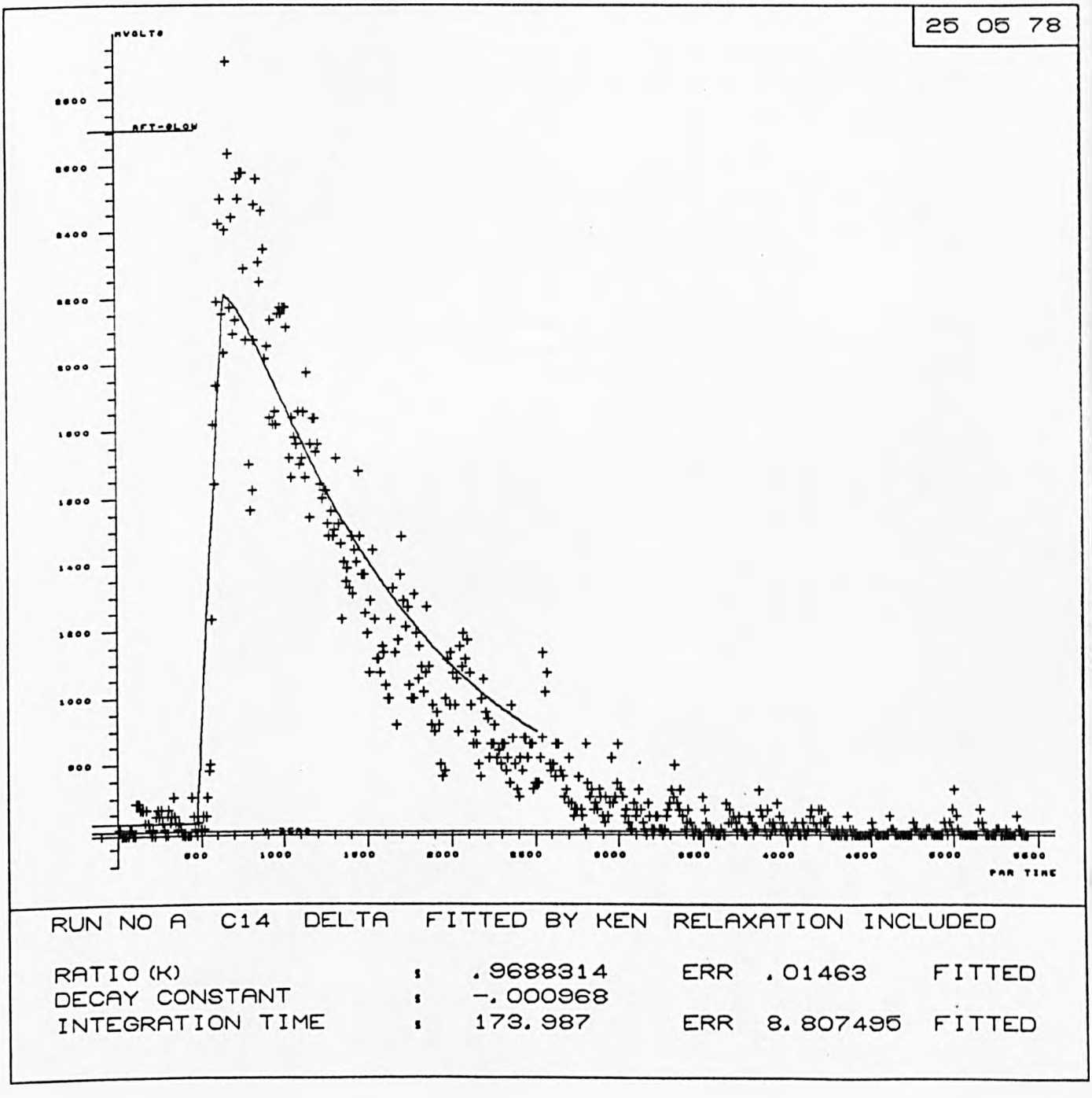

FIGURE 7.3 Emission from $O_2(^1\Delta_g)$ in Pure Oxygen - Effects of Vibrational Relaxation Taken into Account.

do not include any correction for vibrational relaxation behind the shock front; it may be seen that in most cases K lies close to unity as is expected for a reaction with little or no activation energy. This will be discussed further in Chapter 8.

TABLE 7.1 Analysis of the Dimol Emission

100% Oxygen; Initial temperature = 293 K; Flow Velocity 17.5 ml s^{-1}; All measurements used Photomultiplier A; Vibrational Relaxation not included

Run No.	Initial Pressure (KN m^{-2})	Shock Velocity (KM s^{-1})	Discharge Power (W)	Pre-shock Emission (mV)	T_2(K)	ρ_{21}	Decay (m^{-1}) Pre-Shock	Decay (m^{-1}) Post-Shock	τ_{int} (μs)	K
M116	0.87	1.620	40	0.56	1471	5.880	-	0.787	12.3	1.03
M117	0.87	1.631	130	17.9	1490	5.903	-	1.375	105.7	1.25
M118	0.87	1.408	100	13.4	1191	5.462	-	1.221	157.9	0.86
M119	0.87	1.400	80	9.0	1183	5.448	-	1.331	116.0	0.92
M120	0.87	1.411	60	4.27	1195	5.469	-	0.974	214.4	0.75
M121	0.87	1.414	50	1.33	1199	5.476	-	0.924	151.7	0.49
M122	0.88	1.411	130	16.7	1195	5.469	-	1.329	95.7	0.94
M126	0.87†	1.403	100	7.8	1187	5.455	1.000	1.178	82.9	0.92
M130	0.87	1.404	60	1.44	1187	5.455	0.910	1.254	38.4	1.01
M131	0.87	1.724	60	1.36	1621	6.058	0.878	0.741	55.7	2.19
M137	0.85†	0.885	100	30.2	689	3.570	1.328	1.155	24.6	0.74
M139	0.90	0.870	100	20.6	676	3.522	1.285	1.12	79.6	0.83
M140	0.88	0.864	100	21.1	671	3.505	1.287	1.105	80.6	0.91
M145	0.865	1.416	100	22.4	1203	5.483	1.092	1.123	53.7	1.11
758	0.88	1.609	100	15.6	1458	5.862	-	1.312	125.4	1.19
762	0.87	1.605	60	5.7	1453	5.856	-	0.912	67.9	0.96
771	0.87	1.586	100	13.6	1426	5.821	1.035	1.15	79.2	1.30
791	0.88	1.586	100	5.3	1426	5.821	1.125	1.113	55.9	1.24
793	0.87	1.593	100	6.4	1435	5.833	1.017	1.074	70.0	1.39

Run No.	Initial Pressure (KN m^{-2})	Shock Velocity (KM s^{-1})	Discharge Power (W)	Pre-Shock Emission (mV)	T_2(K)	ρ_{21}	Decay (m^{-1}) Pre-Shock	Post-Shock	τ_{int} (μs)	K
795	0.88	0.947†	100	6.0	751	3.763	1.100	1.492	55.7	0.83
805	0.85	0.874†	100	4.5	680	3.537	0.867	1.294	25.0	1.04
807	0.895	1.687	100	5.3	1569	5.999	1.083	1.160	96.0	1.54
810	0.87	1.416	75	3.1	1203	5.483	0.913	0.952	72.4	0.75
811	0.87	1.004†	75	3.2	812	3.929	0.996	0.932	127.2	0.67
821	0.79	1.438	100	28.7	1230	5.527	0.871	1.203	144.8	1.16
823	0.88	1.520†	100	21.2	1333	5.691	1.101	1.092	91.6	1.05
825	0.795	0.875	100	25.1	680	3.538	1.048	1.140	65.8	0.79
827	0.775	0.876	100	25.4	680	3.537	1.013	1.158	70.4	0.96
829	0.80	1.740	100	25.3	1646	6.085	1.050	1.201	125.4	4.22
830	0.835	1.428	100	14.9	1217	5.507	1.492	1.736	88.1	1.70
831	0.800	1.632	100	15.8	1490	5.903	1.342	1.036	85.0	3.75

Runs 758 - 831 were performed in conjunction with, and analysed by, Mrs. P.M. Borrell.

† Shock velocity measured from the photographic record.

7.3. Formation and Removal of $O_2(^1\Sigma_g^+)$ in Pure Oxygen

7.3.1. Vibrational Relaxation not Included

Figure (7.4) shows a typical photographic record of the emission from shock-heated $O_2(^1\Sigma_g^+)$ in pure oxygen; the shape differs from that of Figure (7.1) as a result of the relaxation in the early part of the shock (Chapter 4.3.). Analysis in which vibrational relaxation is ignored again allows us to compare the post-shock decay with that observed prior to the shock. The relaxation time, τ_{rel}, for collisonal deactivation in equation (4.42)

$$\frac{I_{\Sigma 2}}{I^o_{\Sigma 1}} = K\left[1-(1-{}^1/K)e^{-t_p\tau_{rel}}\right] \rho_{21}\, e^{-\alpha_t t_p} \qquad (4.42)$$

and the rate constant for collisonal quenching of $O_2(^1\Sigma_g^+)$ obtained using the relation defined in Chapter 4.

$$\tau_{rel} = {}^1/K_2(T_2)[M] \qquad (7.1)$$

where

$$[M] = \frac{1}{22.4}\ \frac{P_1}{P_{atm}}\ \frac{273}{T_1}\ \text{mole dm}^{-3} \qquad (7.2)$$

should be underestimated in these calculations, but the error in the ratio, K, will be quite small. The results are shown in Table 7.2; it can be seen that for slow shocks K in equation (4.42) is very close to unity and consequently k_1 and k_2 are not estimated (Chapter 6). The large amount of data in Table 7.2 is a result of the use of these experiments to test the apparatus; measurements have been made using a wide range of discharge powers, initial pressures and photomultiplier slit widths, and show that the settings have no significant effect on the results.

The rate constants, k_1 and k_2, are plotted against temperature in Figures (7.5) and (7.6); the results show a large scatter, but indicate that the rates of both quenching and energy pooling increase slowly with increasing temperature. These plots and many others in Chapters 7 and

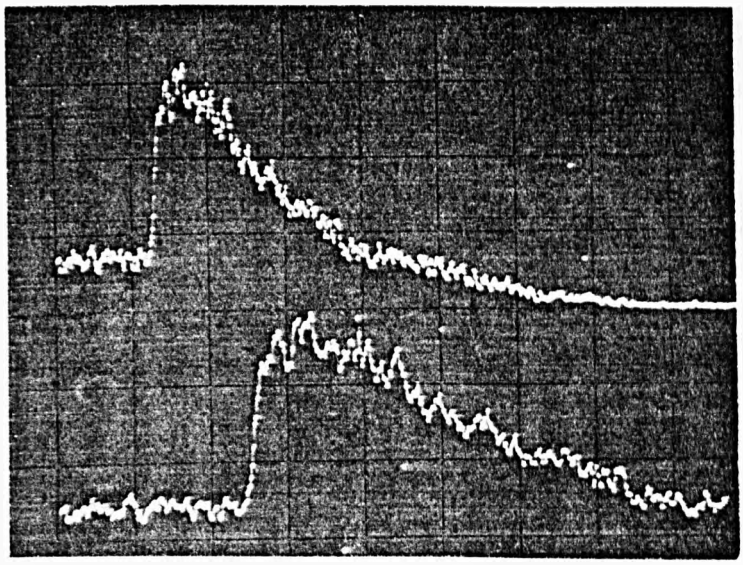

RUN NUMBER M110

Sweep Speed 100 us cm^{-1} (top) 50 us cm^{-1} (bottom)

Sensitivity 2 V cm^{-1}

Pre-Shock Emission 1238 mV

Shock Velocity 1.352 Km s^{-1}

FIGURE 7.4 Emission from $O_2(^1\Sigma_g^+)$ - 100% Oxygen

TABLE 7.2 Analysis of the Emission from $O_2(^1\Sigma_g^+)$. Shocks into Pure Oxygen

100% Oxygen; Flow Velocity 17.5 ml s^{-1}; All measurements used Photomultiplier A; Vibrational Relaxation Included

Run No.	Initial Pressure (KN m^{-2})	Initial Temp. (K)	Shock Velocity (Km s^{-1})	Discharge Power (W)	Pre-shock Emission (mV)	T_2(K)	ρ_{21}	Decay (m^{-1}) Pre-shock	Decay (m^{-1}) Post-shock	τ_{int} (μs)	K	$k_{1/10^5}$ ($dm^3 mole^{-1} s^{-1}$)	$k_{1/10^5}$ ($dm^3 mole^{-1} s^{-1}$)
M110	0.865	293	1.352	100	1238	1123	5.338	-	1.068	97.7	1.304	1.13	1.157
M111	0.865	293	1.400	75	824	1183	5.448	-	1.064	160.7	1.467	2.29	2.080
M112	0.865	293	1.391	50	69.2	1170	5.426	-	0.918	31.5	3.582	2.50	0.930
M113	0.865	293	1.653	80	350.2	1517	5.937	-	1.004	234.5	1.809	1.80	1.325
M124	0.865	293	1.629†	100	940	1485	5.897	1.002	1.049	110.3	1.380	3.62	3.449
M125	0.88	293	0.872†	100	915	677	3.527	1.049	1.084	117.1	1.000	-	-
M127	0.895	293	0.882†	100	863	686	3.559	1.085	1.074	60.1	1.034	-	-
M128	0.865	293	0.860†	100	973	666	3.489	1.025	1.104	82.7	1.000	-	-
M129	0.88	293	0.864†	100	886	671	3.505	1.040	1.118	47.3	1.000	-	-
M146	0.875	298	1.411	75	317	1195	5.469	1.022	1.047	39.4	1.242	2.05	2.194
M147	0.855	298	1.738	75	263	1643	6.082	1.007	1.029	59.6	1.967	7.09	4.854
M150	0.865	294	1.734	75	204	1636	6.074	1.090	1.123	32.2	2.316	12.26	7.061
M151	0.875	294	1.705	75	163	1593	6.026	1.300	1.298	20.5	2.893	8.35	3.831
M152	1.125	294	1.343	100	505	1111	5.315	-	1.519	134.5	1.333	0.817	0.703
M153	1.125	294	1.327	100	645	1093	5.279	1.70	-	147.8	1.253	0.435	0.398
M154	1.18	296	1.321	60	203	1088	5.269	1.570	-	67.4	1.009	0.122	0.135
M155	1.165	296	1.319	60	179	1084	5.261	1.545	-	63.1	1.284	0.163	0.143
M157	0.655	295	1.455	100	895	1253	5.566	0.935	0.865	66.8	1.489	1.08	1.209

Run No.	Initial Pressure (KN m^{-2})	Initial Temp. (K)	Shock Velocity (Km s^{-1})	Discharge Power (W)	Pre-shock Emission (mV)	T_2(K)	ρ_{21}	Decay (m^{-1}) Pre-shock	Decay (m^{-1}) Post-shock	τ_{int} (μs)	K	$k_1/10^5$ ($dm^3 mole^{-1} s^{-1}$)	$k_2/10^5$ ($dm^3 mole^{-1} s^{-1}$)
M158	0.655	295	1.450	100	898	1244	5.553	0.970	0.900	88.8	1.315	0.956	1.238
753	0.87	293	1.631	50	58.3	1490	5.903	-	0.994	100.2	5.64	8.26	1.953
755	0.88	293	1.634	100	178.5	1494	5.909	-	1.078	146.1	2.996	3.79	1.669
764*	0.85	293	1.620	100	70.0	1471	5.880	-	0.992	132.6	1.605	5.80	4.857
766*	0.87	293	1.623	50	10.3	1476	5.886	-	0.758	97.2	2.822	2.97	1.404
768*	0.87	293	1.627	50	9.6	1483	5.894	-	1.332	195.2	4.880	3.54	0.967
770	0.87	293	1.616	75	977	1467	5.874	-	1.190	112.7	2.147	2.38	1.476
777	0.88	293	1.604	100	902	1449	5.851	1.008	1.070	107.2	1.420	2.24	2.084
797	0.87	293	1.618	100	352	1471	5.880	1.100	1.086	70.9	1.545	2.10	1.803
799	0.87	293	1.579	100	354	1417	5.809	1.113	1.231	73.1	1.702	1.28	1.390
801	0.88	293	1.383	100	340	1162	5.412	1.092	1.152	73.8	1.262	0.966	1.010
839	0.755	293	1.431	100	265	1219	5.511	0.942	1.006	192.1	1.234	0.719	0.859
840	0.825	293	1.397	100	198	1179	5.441	1.102	1.119	22.9	1.249	1.08	1.192
842	0.785	293	1.386	75	122	1166	5.419	1.267	1.134	47.8	1.344	0.681	0.723
843	0.745	293	1.452	75	236	1248	5.559	0.879	0.966	91.7	1.507	2.62	0.872
844	0.825	293	1.592	100	338	1435	5.833	1.196	1.227	44.9	2.117	2.03	1.322
845	0.775	293	1.544	100	337	1368	5.741	1.175	1.108	85.5	1.826	1.49	1.176
846	0.765	293	1.614	50	20.5	1462	5.868	1.063	0.914	38.5	2.150	1.92	1.309
847	0.86	293	1.524	60	319	1342	5.704	0.975	0.911	130.8	1.614	1.36	1.124
853	0.825	293	1.162	60	1280	953	4.543	1.306	1.600	97.0	1.000	-	-

Run No.	Initial Pressure (KN m^{-2})	Initial Temp. (K)	Shock Velocity (Km s^{-1})	Discharge Power (W)	Pre-shock Emission (mV)	T_2(K)	ρ_{21}	Decay (m^{-1}) Pre-shock	Decay (m^{-1}) Post-shock	τ_{int} (μs)	K	$k_1/10^5$ ($dm^3 mole^{-1} s^{-1}$)	$k_2/10^5$ ($dm^3 mole^{-1} s^{-1}$)
854	0.825	293	1.142	60	1180	931	4.268	1.313	1.736	46.3	1.237	0.536	0.836
855	0.865	293	1.152	100	1145	898	4.282	1.160	1.279	63.6	1.170	0.229	0.251
856	0.825	293	1.154	100	1150	900	4.285	1.213	1.378	39.3	1.227	0.295	0.348
859	0.865	293	1.253	100	1190	1009	5.099	1.396	1.286	61.2	1.043	0.405	0.520
870	0.88	293	1.269	100	1134	1027	5.141	1.480	1.389	61.7	1.024	0.256	0.308
880	0.89	293	1.385	100	750	1162	5.412	1.240	-	63.9	1.330	1.416	1.387
881	0.825	293	1.385	100	805	1162	5.412	1.131	-	64.9	1.174	0.724	0.855
881A	0.825	293	1.385	100	860	1162	5.412	1.131	-	86.6	1.196	0.879	1.016
883	0.88	293	1.367	100	683	1141	5.371	1.208	-	64.5	1.184	1.130	1.265
884	0.84	293	1.596	100	634	1426	5.821	1.142	1.164	77.5	1.388	3.069	3.027
884A	0.84	293	1.596	100	688	1426	5.821	1.142	1.183	94.4	1.475	3.319	3.581

* EMI 9663B photomultiplier detector

Shocks 753-847 were performed in conjunction with Mrs. P.M. Borrell, and runs 853-884 by Mrs. Borrell working alone; all were analysed by her.

Runs 881A and 884A were performed using a second transient recorder to analyse the output from photomultiplier B.

† Shock velocity measured from photographic record.

8 have been made using the plotting routines available on the ICL 4130 computer (Appendix C.3).

FIGURE 7.5

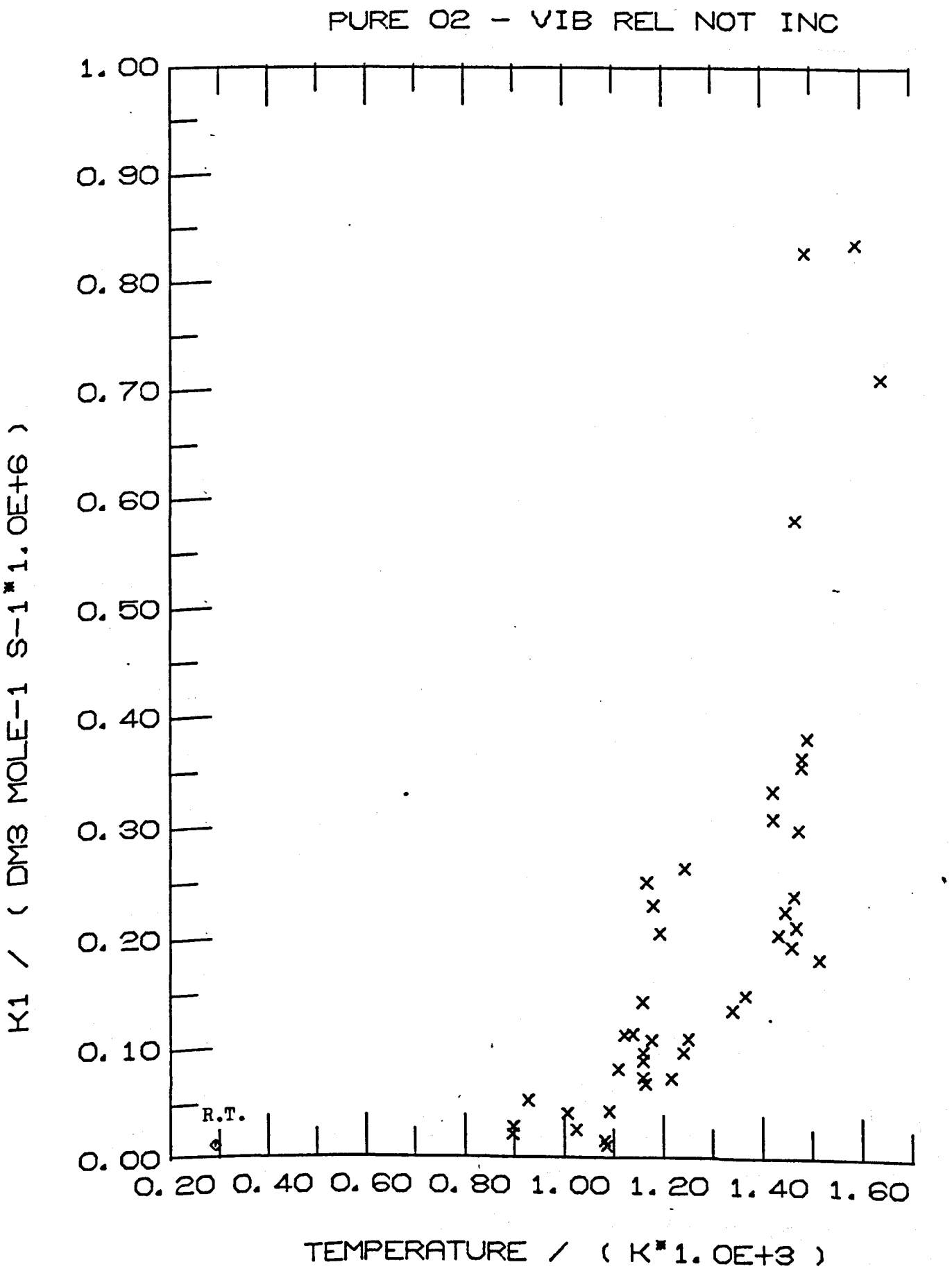
PURE O2 - VIB REL NOT INC
1.00
0.90
0.80
0.70
0.60
0.50
0.40
0.30
0.20
0.10
0.00
K1 / (DM3 MOLE-1 S-1*1.0E+6)
R.T.
0.20 0.40 0.60 0.80 1.00 1.20 1.40 1.60
TEMPERATURE / (K*1.0E+3)

FIGURE 7.6

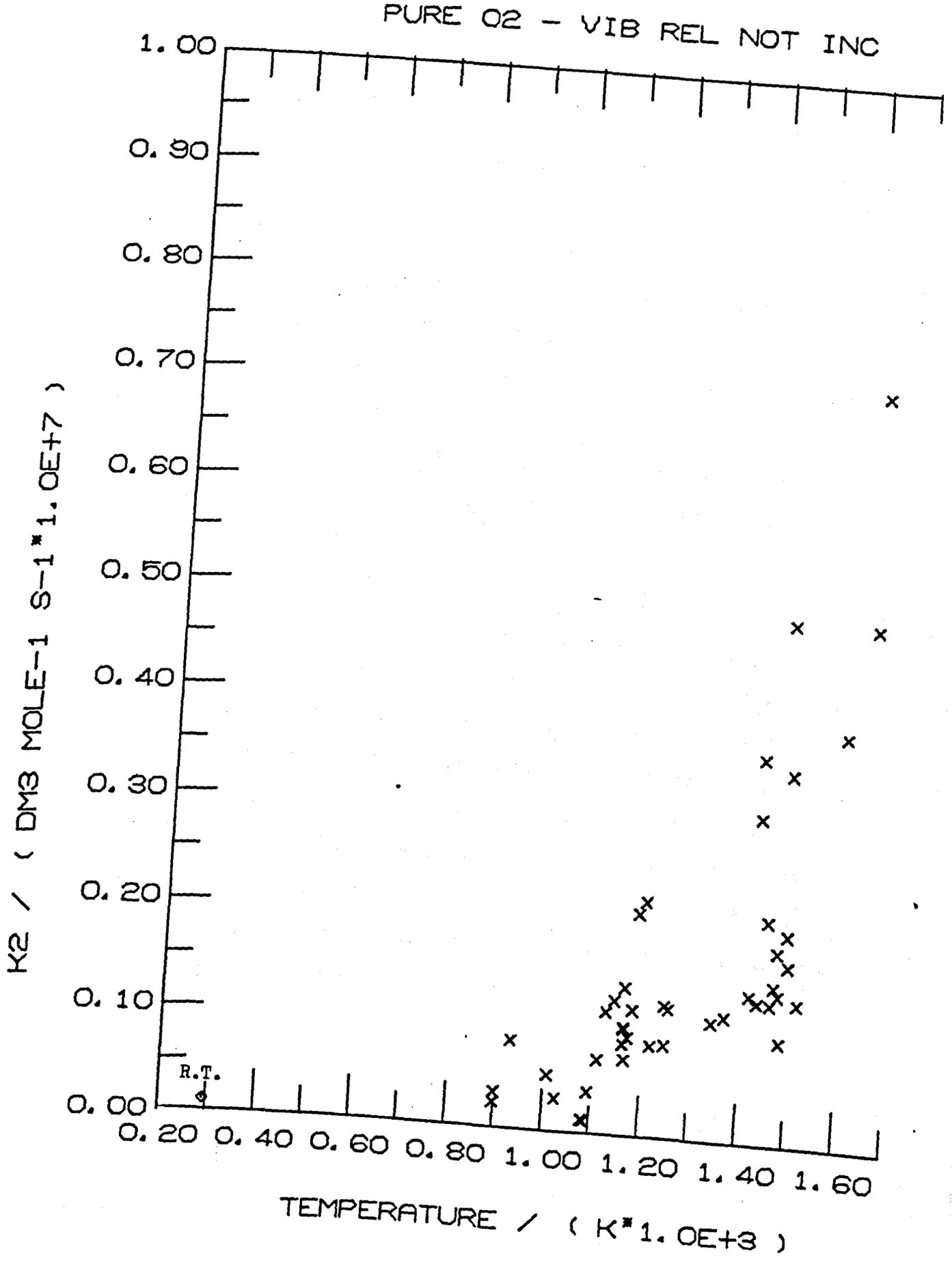
PURE O2 - VIB REL NOT INC
1.00
0.90
0.80
0.70
0.60
0.50
0.40
0.30
0.20
0.10
0.00
K2 / (DM3 MOLE-1 S-1 * 1.0E+7)
R.T.
0.20 0.40 0.60 0.80 1.00 1.20 1.40 1.60
TEMPERATURE / (K * 1.0E+3)

7.3.2. Vibrational Relaxation Included

The results of most runs for which the decay down the tube was measured prior to the shock were recalculated to take into account the effects of vibrational relaxation (Table 7.3). Table 7.2 contains more experimental data than is required to define the temperature dependence of the rate constants; for this reason, shocks that gave results in Table 7.2 which were in poor agreement with those from other shocks of a similar velocity, were discarded.

Table 7.3 and Figures (7.7) and (7.8) show that for a shock of average velocity, the rate of quenching is approximately twice the value calculated when vibrational relaxation is ignored, but that the ratio of levels, K, changes only slightly. As the rate of the energy pooling reaction varies with $(K.k_2(T_2))$ (equation (4.38)), the rate constant for energy pooling is underestimated by a similar amount if vibrational relaxation is not included.

For slow shocks, K is still very near to unity and the rate constants for collisonal quenching may not be calculated without prior knowledge of the rate constant for energy pooling at that temperature. The results which can be analysed show that the effect of vibrational relaxation is to increase the observed temperature dependence of the rate constants for energy pooling (Figure (7.9)) and collisonal deactivation (Figure (7.10)) significantly in comparison with figures (7.5) and (7.6), except at the highest temperatures ($\sim$ 1600 K) where little change is observed. This confirms the expectation outlined in Chapter 5 that the effect of neglecting vibrational relaxation would be greatest when K is small.

TABLE 7.3 ANALYSIS OF EMISSION FROM $O_2(^1\Sigma_g^+)$ RECALCULATED TO INCLUDE EFFECTS OF VIBRATIONAL RELAXATION

Run No.	Initial Pressure (KN m^{-2})	Shock Velocity (Km s^{-1})	Discharge Power (W)	Pre-Shock Emission (mV)	T_{AV} (K)	ρ_{AV}/ρ_1	τ_{int} (μs)	K Relax Not Inc.	K Relax Inc.	k_1/dm^3 $mole^{-1}$ s^{-1} x10^5 Relax Not Inc.	k_1/dm^3 $mole^{-1}$ s^{-1} x10^5 Relax Inc.	k_2/dm^3 $mole^{-1}$ s^{-1} x10^6 Relax Not Inc.	k_2/dm^3 $mole^{-1}$ s^{-1} x10^6 Relax Inc.
M110	0.865	1.352	100	1238	1140	5.256	85.3	1.304	1.243	1.13	2.558	1.157	2.730
M124	0.865	1.629	100	940	1498	5.847	84.0	1.380	1.294	3.62	6.676	3.449	6.839
M125	0.88	0.872	100	915	673	3.567	111.9	1.000	0.987	-	-	-	-
M127	0.895	0.882	100	863	681	3.613	68.8	1.034	1.001	-	-	-	-
M129	0.88	0.864	100	886	666	3.540	75.8	1.000	0.971	-	-	-	-
M146	0.875	1.411	75	317	1220	5.353	36.2	1.242	1.042	2.05	-	2.194	-
M147	0.855	1.738	75	263	1655	6.035	39.1	1.967	1.951	7.09	7.285	4.854	5.026
M150	0.865	1.734	75	204	1655	6.049	20.1	2.316	2.261	12.26	13.89	7.061	8.135
M151	0.875	1.705	75	163	1608	5.975	17.9	2.893	3.057	8.35	7.818	3.831	3.370
770	0.87	1.616	75	977	1475	5.844	79.1	2.15	1.654	2.38	4.314	1.476	3.485
777	0.88	1.604	100	902	1460	5.814	88.4	1.42	1.302	2.24	4.180	2.084	4.244
797	0.87	1.618	100	352	1480	5.834	55.9	1.55	1.453	2.10	4.490	1.803	4.129
799	0.87	1.579	100	354	1429	5.771	53.4	1.702	1.427	1.28	3.088	1.390	2.891
801	0.88	1.383	100	340	1185	5.286	54.7	1.262	1.130	0.966	2.677	1.010	3.133
839	0.755	1.431	100	249	1238	5.432	72.0	1.234	1.098	0.719	2.543	0.859	3.382
842	0.785	1.386	75	122	1184	5.318	35.1	1.344	1.328	0.681	2.108	0.723	2.244
844	0.825	1.592	100	338	1447	5.796	32.7	2.117	1.860	2.03	3.057	1.322	2.239
853	0.825	1.162	60	1280	961	4.543	84.7	1.000	0.939	-	-	-	-
854	0.825	1.146	60	1180	935	4.508	47.5	1.237	0.957	0.536	-	0.836	-

Run No.	Initial Pressure (KN m^{-2})	Shock Velocity (Km s^{-1})	Discharge Power (W)	Pre-Shock Emission (mV)	T_{AV} (K)	ρ_{AV}/ρ_1	τ_{int} (μs)	K		$k_1/dm^3 mole^{-1} s^{-1} x10^5$		$k_2/dm^3 mole^{-1} s^{-1} x10^6$	
								Relax Not Inc.	Relax Inc.	Relax Not Inc.	Relax Inc.	Relax Not Inc.	Relax Inc.
855	0.865	1.152	100	1145	937	4.577	57.8	1.170	1.080	0.229	1.631	0.251	2.002
856	0.825	1.154	100	1150	943	4.574	36.3	1.227	1.033	0.295	-	0.348	-
870	0.88	1.269	100	1133	1054	4.982	56.7	1.024	1.035	0.256	-	0.308	-
881A	0.825	1.385	100	860	1179	5.333	68.5	1.196	1.096	0.879	2.951	1.016	3.676
884A	0.84	1.596	100	688	1438	5.792	71.0	1.475	1.409	3.319	5.017	3.581	4.708
910	0.815	1.607	100	461	1473	5.817	33.2	Not Measured	2.211	-	6.293	-	3.912
910A	0.851	1.607	100	458	1472	5.820	52.7	Not measured	2.184	-	6.987	-	4.398
911	0.87	1.382	100	546	1175	5.330	62.4	Not measured	1.434	-	4.994	-	4.600
882	0.865	1.385	100	621	1181	5.327	73.6	Not measured	1.077	-	2.214	-	2.717
835	0.775	0.947	100	972	738	3.867	47.1	1.483	1.127	-	-	-	-

Runs 910, 910a, 911 and 882 were not included in Table 7.2;
the pre-shock decays (m^{-1}) were 1.050, 1.050, 1.173 and 1.192 respectively.

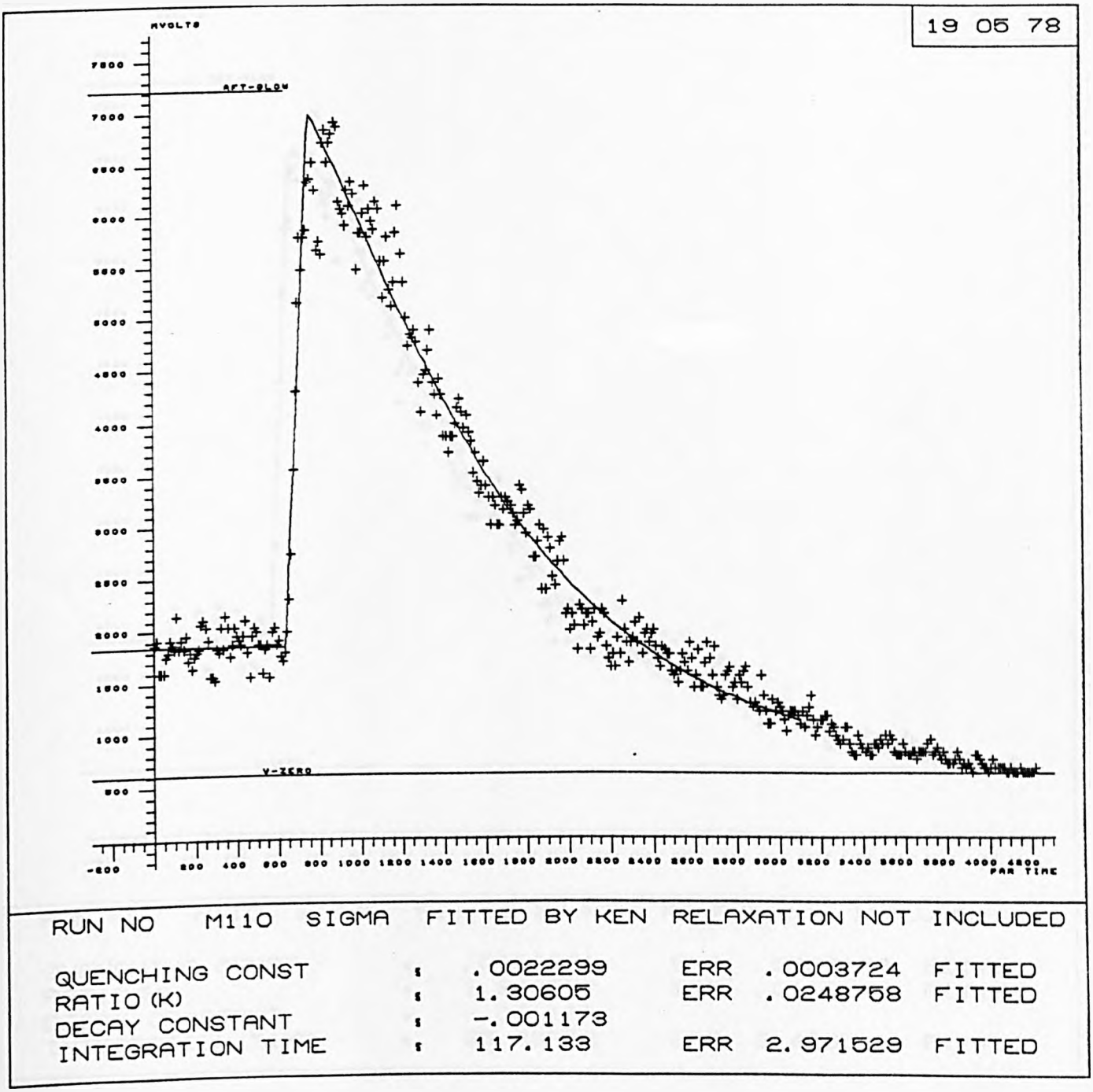

RUN NO M110 SIGMA FITTED BY KEN RELAXATION NOT INCLUDED

QUENCHING CONST	: .0022299	ERR .0003724	FITTED
RATIO (K)	: 1.30605	ERR .0248758	FITTED
DECAY CONSTANT	: -.001173		
INTEGRATION TIME	: 117.133	ERR 2.971529	FITTED

FIGURE 7.7 Emission from $O_2(^1\Sigma_g^+)$ in Pure Oxygen - Effects of Vibrational Relaxation Not Included.

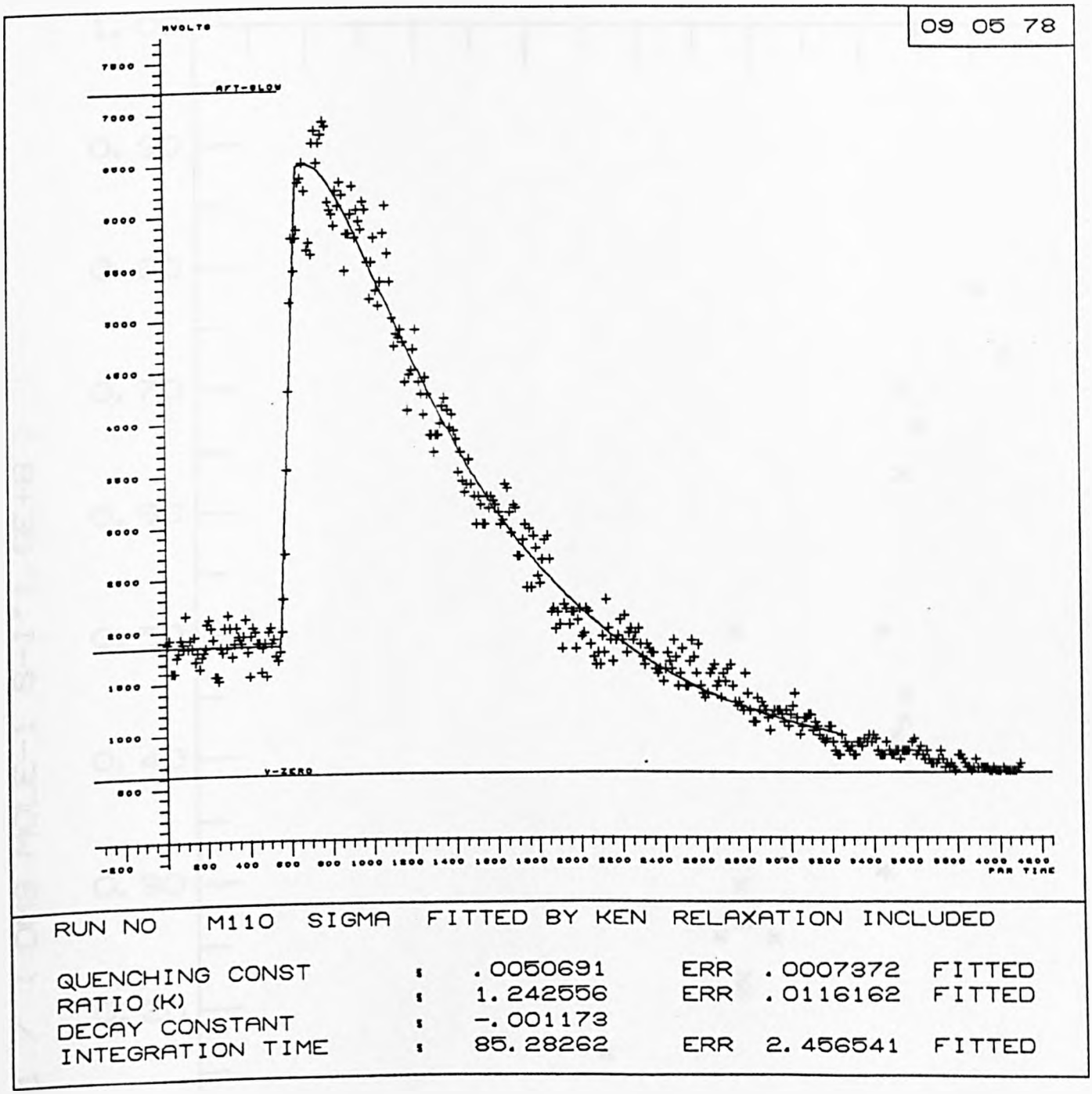

FIGURE 7.8 Emission from $O_2(^1\Sigma_g^+)$ in Pure Oxygen - Effects of Vibrational Relaxation Taken into Account.

FIGURE 7.9

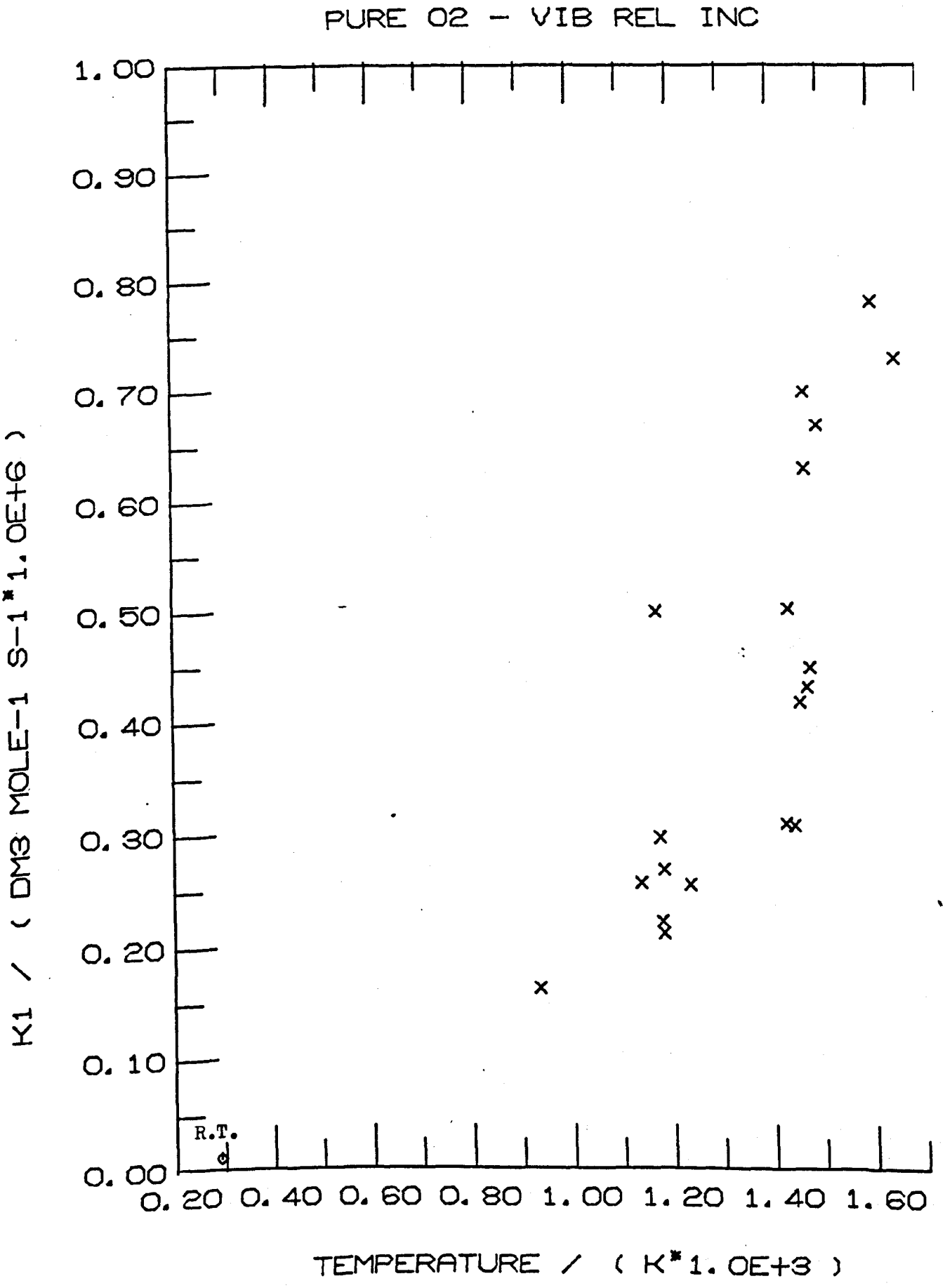
PURE O2 - VIB REL INC
1.00
0.90
0.80
0.70
0.60
0.50
0.40
0.30
0.20
0.10
0.00
K1 / (DM3 MOLE-1 S-1 *1.0E+6)
R.T.
0.20
0.40
0.60
0.80
1.00
1.20
1.40
1.60
TEMPERATURE / (K*1.0E+3)

FIGURE 7.10

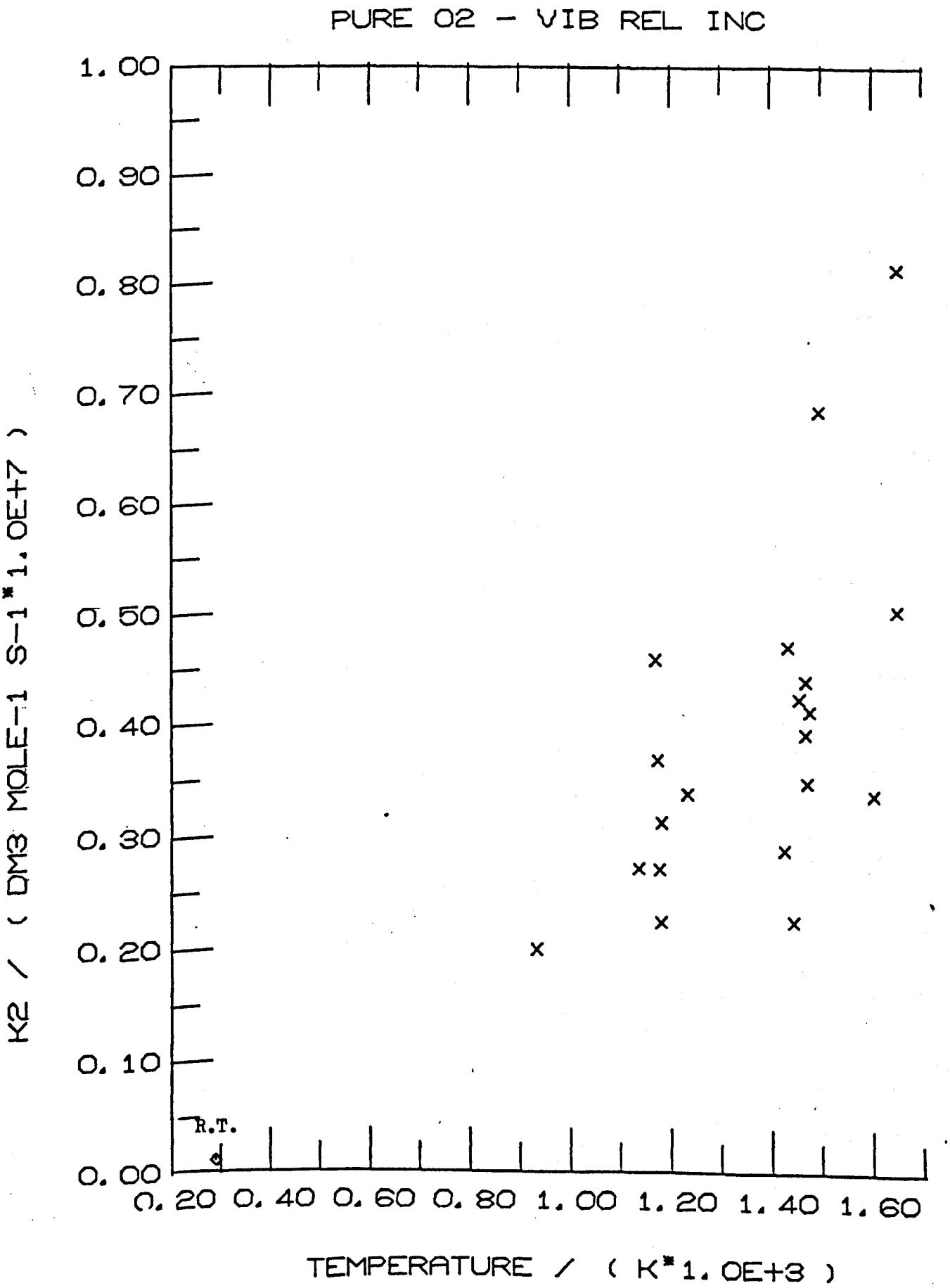
PURE O2 - VIB REL INC
1.00
0.90
0.80
0.70
0.60
0.50
0.40
0.30
0.20
0.10
0.00
K2 / (DM3 MOLE-1 S-1*1.0E+7)
R.T.
0.20 0.40 0.60 0.80 1.00 1.20 1.40 1.60
TEMPERATURE / (K*1.0E+3)

7.4. Formation and Removal of $O_2(^1\Sigma_g^+)$ in Oxygen/Nitrogen Mixtures

The most striking difference in the emission from $O_2(^1\Sigma_g^+)$ in oxygen/nitrogen mixtures from that in pure oxygen is the much greater value of the ratio of levels, K. Figures (7.11) and (7.12) show the emission resulting from slow shocks into approximately 50% oxygen; K is about 2.3 compared with 0.9-1.0 for a shock of similar velocity into pure oxygen. The greater intensity of post-shock emission has three important benefits: the data is far less noisy and hence is more easily analysed than for pure oxygen; the rate of collisional deactivation is easily measured even at $\sim$ 600 K; the effects of vibrational relaxation are not nearly as significant when K is large.

An examination of equation (4.38)

$$K = \frac{k_1(T_2)}{k_2(T_2)} \quad \frac{(k_2(T_1) + k_w'/[M])}{k_1(T_1)} \tag{4.38}$$

suggests that the higher value of K is due either to a disproportionate increase of k_1 or a disproportionate decrease of k_2. k_1 is likely to be the same for all systems; therefore k_2 is expected to increase with temperature less rapidly in oxygen/nitrogen mixtures than in pure oxygen.

All measurements were made at pressures of 0.85-0.95 KN m^{-2} with a discharge power of 100W; these conditions were considered to be the most satisfactory in light of our experience of discharge flow shock tube experiments in pure oxygen.

Table 7.4 compares rate constants calculated in oxygen/nitrogen mixtures with and without vibrational relaxation taken into account. The improvement of the approximate calculations that results from the high value of K, is to some extent countered by the slow vibrational relaxation of the nitrogen (Chapter 5), and the rate constants are underestimated by 10-50% if the relaxation is ignored. In consequence all the results presented in this section include the effects of vibrational relaxation.

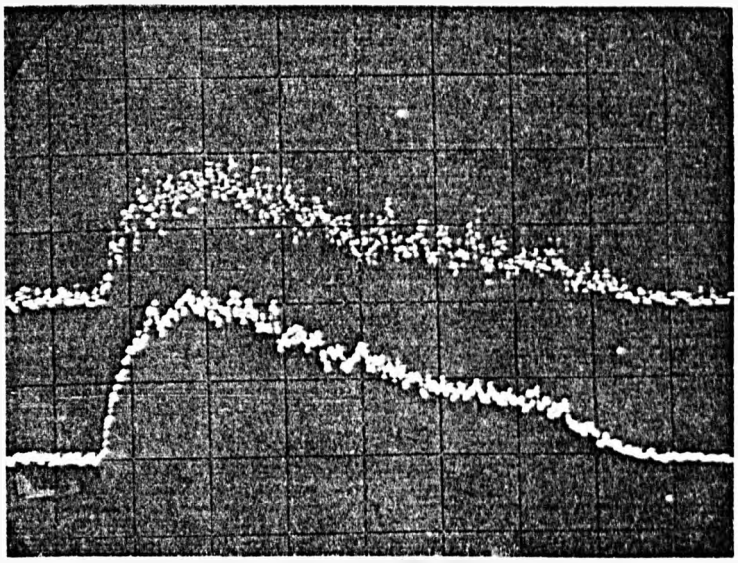

RUN NUMBER 895 A

Sweep Speed 100 us cm^{-1}

Sensitivity 1 V cm^{-1} 2 V cm^{-1}

Pre-Shock Emission 151 mV 415 mV

Shock Velocity 1.168 Km s^{-1}

FIGURE 7.11 Emission from $O_2(^1\Sigma_g^+)$ - 50% Oxygen

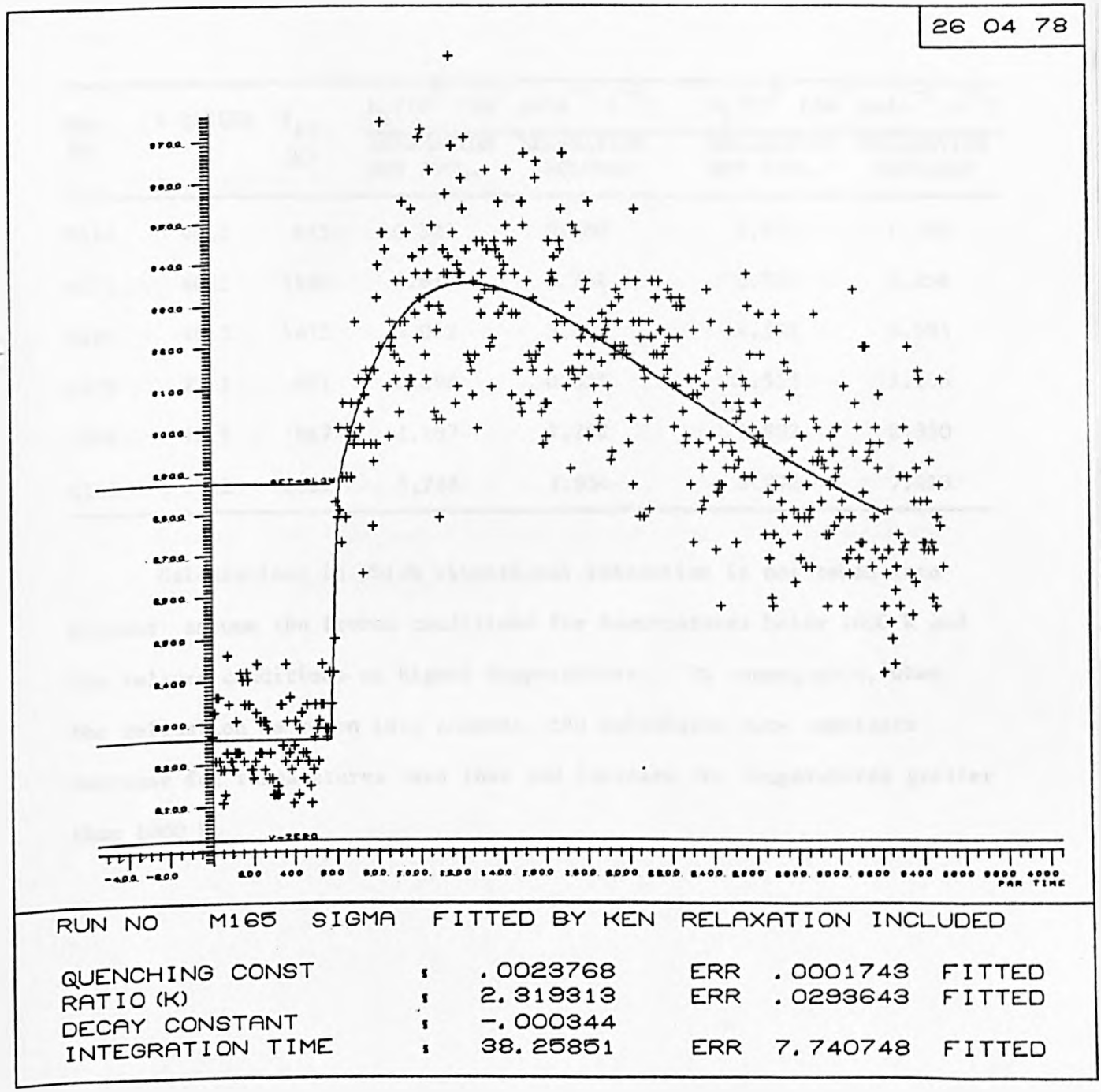

FIGURE 7.12 Emission from $O_2(^1\Sigma_g^+)$ in 50% Oxygen / 50% Nitrogen - Slow Shock, Velocity 0.868 Km s^{-1}.

TABLE 7.4

The effect of vibrational relaxation on the rate constant calculated for the formation and removal of $O_2(^1\Sigma_g^+)$ in oxygen/nitrogen mixtures

Run No.	% OXYGEN	T_{AV} (K)	$k_1/10^5$ (dm^3 $mole^{-1}$ s^{-1})		$k_2/10^6$ (dm^3 $mole^{-1}$ s^{-1})	
			RELAXATION NOT INCL.	RELAXATION INCLUDED	RELAXATION NOT INCL.	RELAXATION INCLUDED
M164	46.3	655	0.521	0.460	1.517	1.340
M172	46.3	1182	2.818	3.741	3.715	5.358
M166	46.3	1475	5.082	5.929	4.592	5.585
M179	72.1	627	0.698	0.525	1.553	1.205
886	72.1	847	1.167	1.262	1.982	2.350
M185	72.1	1322	5.728	7.834	5.272	7.413

Calculations in which vibrational relaxation is not taken into account assume the frozen conditions for temperatures below 1000 K and the relaxed conditions at higher temperatures. In consequence, when the relaxation is taken into account, the calculated rate constants decrease for temperatures less than and increase for temperatures greater than 1000 K.

7.4.1. 90% O_2 - 10% N_2

The results are shown in Table 7.5; the rate constants for energy pooling and collisonal quenching are plotted against temperature in Figures (7.13) and (7.14). It may be seen that the scatter of the data is far lower than with the measurements in pure oxygen, as a result of the much greater value of K; the rate constants are little different from those observed in pure oxygen.

In the later experiments with oxygen/nitrogen mixtures, the introduction of a second transient recorder allowed the analysis of the emission seen by both photomultiplier A and photomultiplier B. The results obtained for a single shock from the different photomultipliers were in excellent agreement, confirming that the detection systems were operating correctly. This greatly increased the ease with which results were obtained; runs designated numbers of the form M203A analysed the post-shock output from photomultiplier A.

TABLE 7.5

90% O_2 - 10% N_2 - Emission from $O_2(^1\Sigma_g^+)$; Flow = 28.0 ml s^{-1}; discharge power = 100W

Run No.	Initial Pressure (KN m^{-2})	Initial Temp. (K)	Shock Velocity (Km s^{-1})	Pre-Shock Emission (mV)	T_{AV} (K)	ρ_{AV}/ρ_1	Decay (m^{-1})	τ_{int} (μs)	K	k_1 /dm^3 $mole^{-1}s^{-1}$ x10^5	k_2 /dm^3 $mole^{-1}s^{-1}$ x10^6
M201	0.90	293	1.392	259	1186	5.279	0.730	75.0	2.017	2.956	3.333
M202	0.895	292	1.381	534	1172	5.254	0.845	93.9	1.990	3.072	3.518
M203	0.895	293	1.381	397	1174	5.245	0.834	71.1	2.001	3.483	3.971
M203A	0.895	293	1.381	379	1173	5.252	0.834	81.3	2.021	4.946	5.582
M204	0.88	294	1.571	380	1419	5.648	0.844	73.2	2.738	7.258	6.084
M204A	0.88	294	1.571	380	1416	5.661	0.844	67.1	2.810	10.70	8.738
M205	0.905	293	1.539	333	1380	5.565	0.879	56.1	2.496	6.765	6.148
M205A	0.905	293	1.539	328	1380	5.601	0.879	46.9	2.676	4.534	3.842
M206	0.885	294	1.574	349	1424	5.652	0.837	51.7	2.795	7.994	6.546
M206A	0.885	294	1.574	389	1424	5.681	0.837	43.9	3.001	7.366	5.619
M207	0.865	294	0.844	471	644	3.443	0.824	53.4	1.425	0.707	1.146
M207A	0.865	294	0.844	527	644	3.443	0.824	29.8	1.609	0.781	1.121
C4	0.875	291	0.867	578	661	3.541	0.726	52.3	1.484	1.097	1.692
C4A	0.875	291	0.867	585	661	3.544	0.726	86.0	1.586	0.808	1.167
C5	0.855	292	0.845	543	642	3.458	0.698	41.6	1.369	0.773	1.293
C5A	0.855	292	0.845	554	642	3.461	0.698	53.4	1.482	0.663	1.024
C6	0.865	293	0.932	575	720	3.781	0.752	137.6	1.418	1.052	1.714
C6A	0.865	293	0.932	578	720	3.781	0.752	94.9	1.577	1.178	1.725

Run No.	Initial Pressure ($KN\ m^{-2}$)	Initial Temp. (K)	Shock Velocity ($Km\ s^{-1}$)	Pre-Shock Emission (mV)	T_{Av} (K)	ρ_{AV}/ρ_1	Decay (m^{-1})	τ_{int}	K	k_1 $/dm^3\ mole^{-1}s^{-1}x10^5$	k_2 $/dm^3\ mole^{-1}s^{-1}x10^6$
C7	0.84	293	0.930	563	718	3.773	0.706	141.8	1.427	1.147	1.876
C7A	0.84	293	0.930	579	718	3.773	0.706	213.2	1.553	1.314	1.975
C8	0.865	294	0.925	568	714	3.756	0.719	39.8	1.435	1.191	1.917
C8A	0.865	294	0.925	550	714	3.752	0.719	114.6	1.517	1.080	1.645
C9	0.885	293	1.520	115	1345	5.574	0.800	89.3	2.931	7.119	5.560
C9A	0.885	293	1.520	100	1342	5.587	0.800	55.1	3.100	4.717	3.483
C10	0.875	294	1.620	122	1477	5.781	0.745	111.9	2.967	16.29	12.64
C10A	0.875	294	1.620	133	1477	5.782	0.745	103.6	3.329	12.33	8.522
912	0.87	294	1.204	791	975	4.767	0.739	64.1	1.513	2.858	4.357
912A	0.87	294	1.204	800	983	4.720	0.739	68.9	1.916	2.600	3.132
913A	0.845	295	0.966	787	752	3.900	0.744	60.1	1.543	1.416	2.139
914	0.83	294	1.192	854	969	4.694	0.751	78.4	1.785	2.341	3.079
914A	0.83	294	1.192	610	969	4.692	0.751	56.3	2.185	2.838	3.049
915	0.905	295	1.410	788	1204	5.342	0.917	102.5	2.314	3.920	3.847
915A	0.905	295	1.410	768	1213	5.295	0.917	68.3	2.636	3.589	3.093

Runs C4-C10A were performed and analysed by Mr. K. Grant

Runs 912-915A were performed and analysed by Mrs. P.M. Borrell

FIGURE 7.13

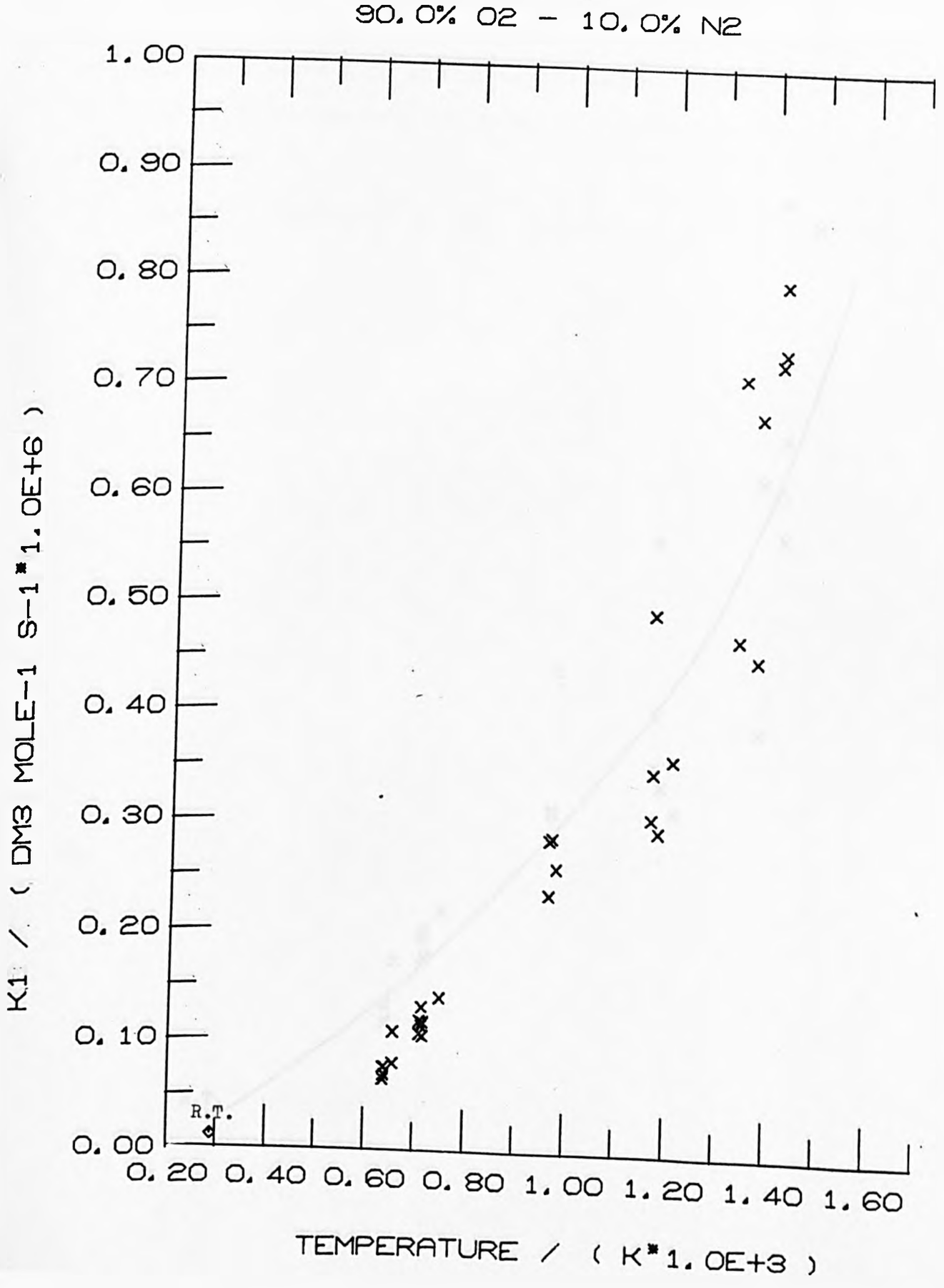
90.0% O2 - 10.0% N2
1.00
0.90
0.80
0.70
0.60
0.50
0.40
0.30
0.20
0.10
0.00
K1 / (DM3 MOLE-1 S-1 * 1.0E+6)
R.T.
0.20 0.40 0.60 0.80 1.00 1.20 1.40 1.60
TEMPERATURE / (K * 1.0E+3)

FIGURE 7.14

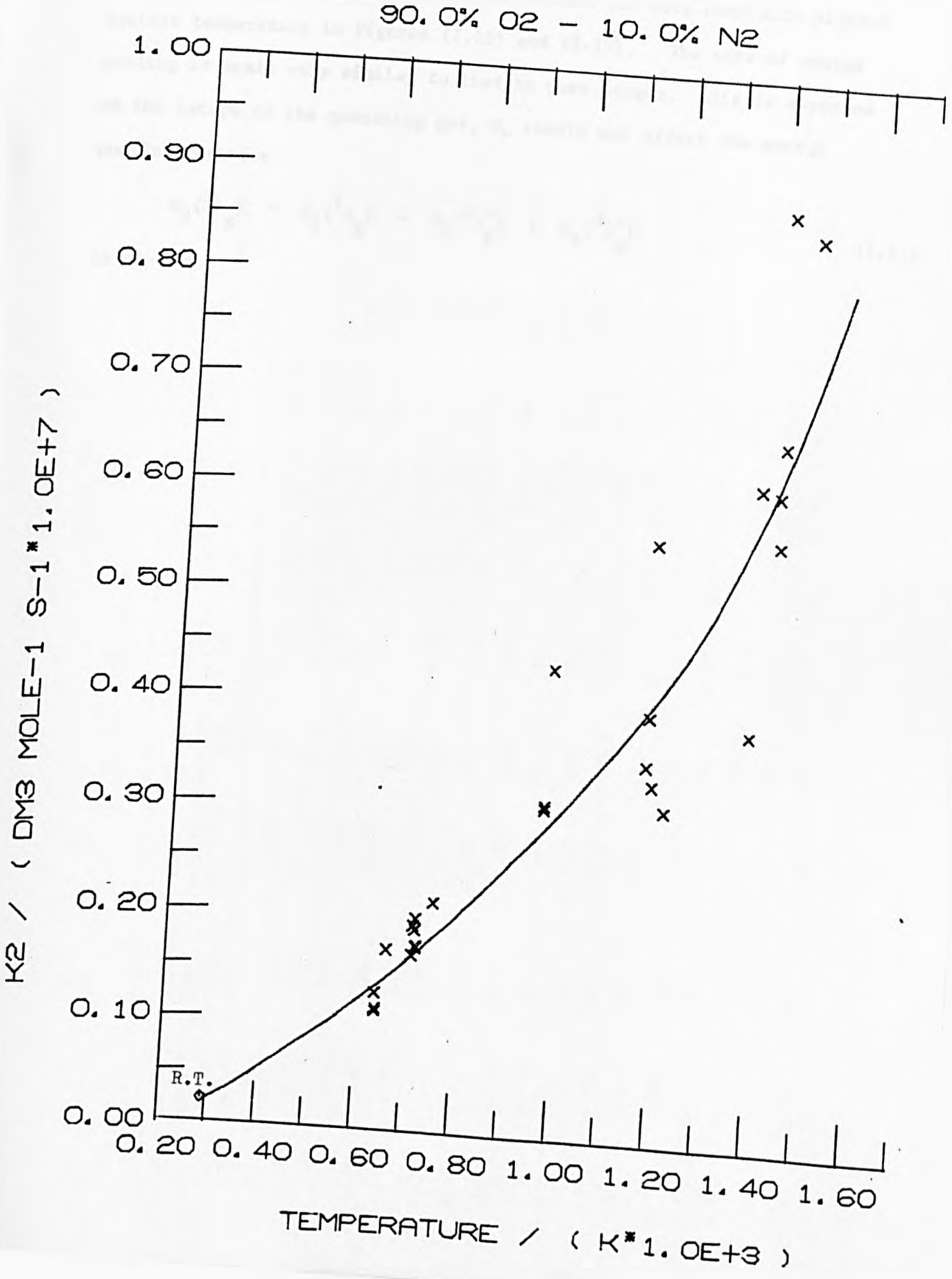
90.0% O2 - 10.0% N2
1.00
0.90
0.80
0.70
0.60
0.50
0.40
0.30
0.20
0.10
0.00
K2 / (DM3 MOLE-1 S-1 *1.0E+7)
R.T.
0.20 0.40 0.60 0.80 1.00 1.20 1.40 1.60
TEMPERATURE / (K*1.0E+3)

7.4.2. 72.1% O_2 - 27.9% N_2

The results are shown in Table 7.6 and the rate constants plotted against temperature in Figures (7.15) and (7.16). The rate of energy pooling is again very similar to that in pure oxygen; this is expected as the nature of the quenching gas, M, should not affect the energy pooling reaction

$$O_2(^1\Delta_g) + O_2(^1\Delta_g) \rightarrow O_2(^1\Sigma_g^+) + O_2(^3\Sigma_g^-) \qquad (1.13)$$

in any way.

TABLE 7.6

72.1% O_2 - 27.9% N_2 - Emission from $O_2(^1\Sigma_g^+)$; Flow = 29.1 ml s^{-1}; Discharge power = 100W

Run No.	Initial Pressure (KN m^{-2})	Initial Temp. (K)	Shock Velocity (Km s^{-1})	Pre-Shock Emission (mV)	T_{AV} (K)	ρ_{AV}/ρ_1	Decay (m^{-1})	τ_{int} (μs)	K	k_1 /$dm^3 mole^{-1} s^{-1} x10^5$	k_2 /$dm^3 mole^{-1} s^{-1} x10^6$
M175	0.92	296	1.353	197	1139	5.050	0.898	27.7	2.970	2.841	3.849
M176	0.935	298	1.361	262	1149	5.068	0.900	50.8	3.054	3.042	3.999
M177	0.915	294	1.338	216.5	1120	5.018	0.915	53.0	2.930	3.591	4.935
M178	0.92	296	0.853	344	645	3.425	0.890	50.4	1.740	0.590	1.367
M179	0.905	296	0.831	329	627	3.339	0.920	21.4	1.754	0.524	1.206
M180	0.92	297	0.836	323	632	3.354	0.930	64.2	1.692	0.607	1.445
M182	0.915	297	1.481	165	1302	5.308	0.897	35.9	3.657	5.737	6.324
M183	0.915	296	1.479	160	1289	5.356	0.946	42.7	4.099	4.615	4.536
M184	0.895	297	1.483	165	1297	5.352	0.935	55.3	3.696	6.067	6.648
M185	0.90	297	1.519	165	1347	5.431	0.980	70.6	4.266	7.828	7.420
M186	0.895	295	1.627	96.7	1488	5.658	0.975	67.6	4.038	11.11	11.13
M187	0.915	296	1.592	139.7	1441	5.564	1.305	0.0	8.787	5.569	2.554
M188	0.895	296	1.384	159	1177	5.133	0.717	50.6	2.838	3.073	4.383
M189	0.90	297	1.684	92.5	1569	5.732	0.449	55.3	3.318	4.964	6.049
M190	0.915	296	1.694	87.6	1583	5.779	0.715	57.6	4.424	4.951	4.510
885	0.83	293	1.367	201	1157	5.074	0.741	37.5	3.272	5.291	6.642
885A	0.83	293	1.367	181	1157	5.072	0.741	30.3	3.444	2.884	3.439

Run No.	Initial Pressure ($KN\ m^{-2}$)	Initial Temp.; (K)	Shock Velocity ($Km\ s^{-1}$)	Pre-Shock Emission (mV)	T_{AV} (K)	ρ_{AV}/ρ_1	Decay (m^{-1})	τ_{int} (μs)	K	k_1 $/dm^3 mole^{-1} s^{-1} x10^5$	k_2 $/dm^3 mole^{-1} s^{-1} x10^6$
886	0.91	293	1.077	294	847	4.236	0.717	61.4	2.165	1.263	2.348
886A	0.91	293	1.077	312	850	4.214	0.717	41.7	2.110	1.195	2.280
887	0.91	293	1.180	441	949	4.565	0.656	125.5	2.401	2.242	3.758
888	0.88	293	1.040	374	813	4.097	0.691	43.1	2.260	0.784	1.407
888A	0.88	293	1.040	685	814	4.092	0.691	98.9	2.198	0.999	1.843
889	0.83	293	1.228	375	1000	4.703	0.652	17.8	2.606	1.901	2.995
889A	0.83	293	1.228	707	1000	4.704	0.652	77.3	2.543	1.927	3.112
890	0.83	293	1.271	323	1047	4.827	0.633	71.7	2.603	2.364	3.730
890A	0.83	293	1.271	727	1047	4.827	0.633	80.5	2.569	2.179	3.484

Runs 885-890A were performed by Mrs. P.M. Borrell

FIGURE 7.15

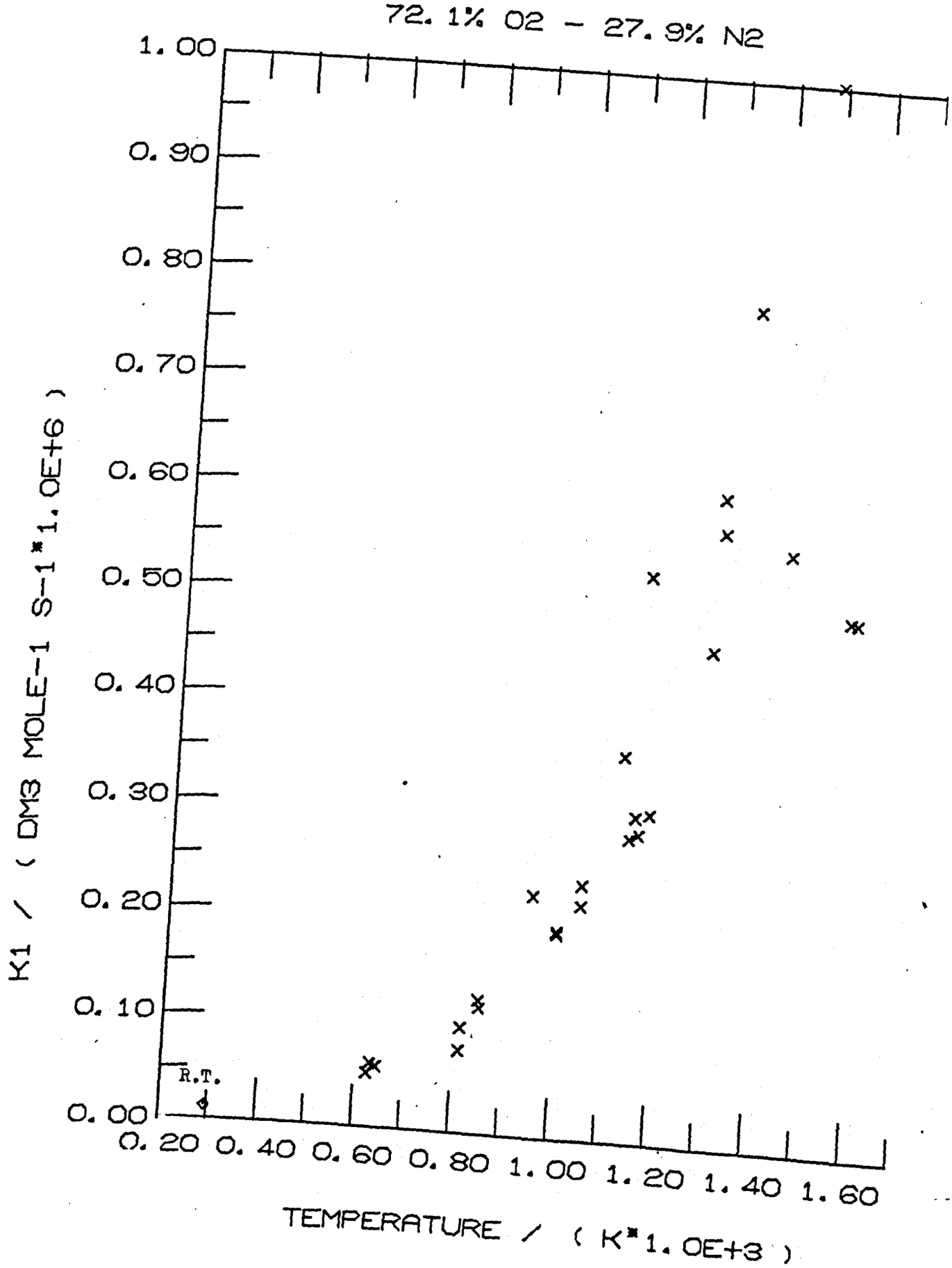
72.1% O2 – 27.9% N2
1.00
0.90
0.80
0.70
0.60
0.50
0.40
0.30
0.20
0.10
0.00
K1 / (DM3 MOLE-1 S-1*1.0E+6)
R.T.
0.20 0.40 0.60 0.80 1.00 1.20 1.40 1.60
TEMPERATURE / (K*1.0E+3)

FIGURE 7.16

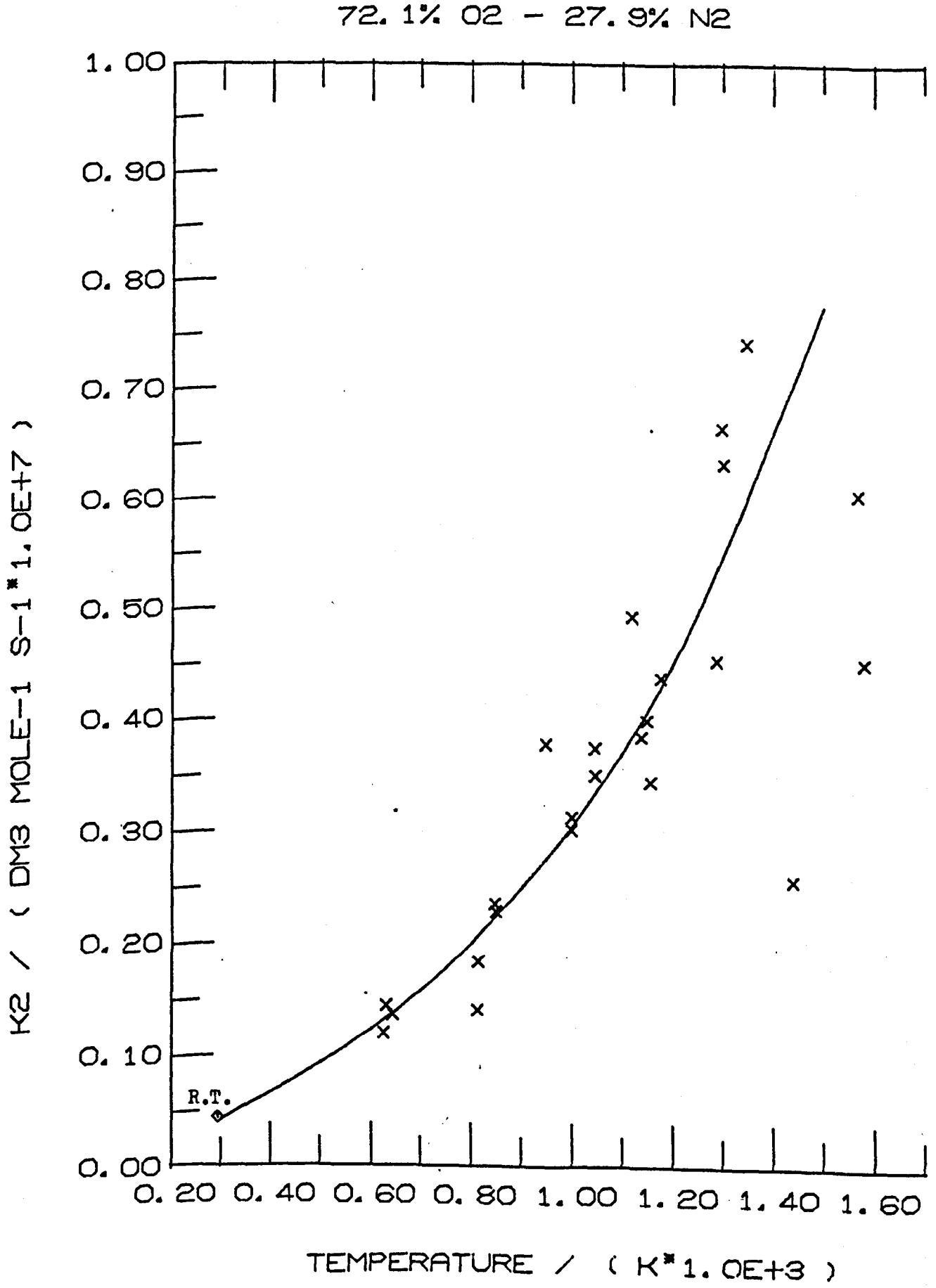
72.1% O2 - 27.9% N2
1.00
0.90
0.80
0.70
0.60
0.50
0.40
0.30
0.20
0.10
0.00
K2 / (DM3 MOLE-1 S-1*1.0E+7)
R.T.
0.20 0.40 0.60 0.80 1.00 1.20 1.40 1.60
TEMPERATURE / (K*1.0E+3)

7.4.3. 46.3% O_2 - 53.7% N_2

The results are shown in Table 7.7 and Figures (7.17) and (7.18). The scatter of the data is particularly low at this composition; the consistency is exceptionally good for shock tube experiments.

TABLE 7.7

46.3% O_2 - 53.7% N_2 - Emission from $O_2(^1\Sigma_g^+)$; Flow = 30.3 ml s^{-1}; Discharge power = 100W

Run No.	Initial Pressure (KN m^{-2})	Initial Temp. (K)	Shock Velocity (Km s^{-1})	Pre-Shock Emission (mV)	T_{AV} (K)	ρ_{AV}/ρ_1	Decay (m^{-1})	τ_{int} (μs)	K	k_1 /$dm^3 mole^{-1} s^{-1} x10^5$	k_2 /$dm^3 mole^{-1} s^{-1} x10^6$
M160	0.90	297	1.417	100.5	1208	5.028	0.507	49.9	4.507	3.598	5.255
M161	0.875	295	1.389	117	1175	4.961	0.532	68.3	4.566	3.389	4.903
M162	0.905	296	1.407	97.3	1195	5.012	0.531	34.8	4.925	2.698	3.602
M163	0.895	297	0.883	137	661	3.468	0.528	263.0	1.888	0.540	1.886
M164	0.895	297	0.877	266	655	3.446	0.533	25.9	2.266	0.461	1.339
M165	0.895	295	0.868	239	646	3.423	0.551	38.3	2.319	0.672	1.907
M166	0.895	296	1.629	94.1	1475	5.480	0.530	16.2	6.991	5.925	5.583
M167	0.90	296	1.701	40.6	1574	5.613	0.562	30.4	5.680	8.287	9.602
M168	0.915	297	1.590	88.9	1434	5.387	0.555	34.5	6.248	6.147	6.465
M169	0.92	295	1.540	81.9	1363	5.306	0.559	47.4	6.094	6.271	6.752
M170	0.895	297	1.582	85.7	1420	5.355	0.559	20.8	6.092	5.730	6.198
M171	0.885	298	1.730	110	1617	5.652	0.548	20.2	8.369	9.189	7.244
M172	0.92	296	1.398	121	1182	5.000	0.577	42.6	4.583	3.739	5.355
M173	0.90	297	1.396	130	1183	4.981	0.553	109.6	4.872	3.510	4.743
M174	0.895	298	1.718	68.8	1599	5.640	0.530	31.1	7.631	8.257	7.132
891	0.865	293	1.170	191	929	4.405	0.566	74.6	3.530	1.602	3.001
891A	0.865	293	1.170	388	930	4.402	0.566	38.5	3.669	1.271	2.290

Run No.	Initial Pressure (KN m^{-2})	Initial Temp. (K)	Shock Velocity (Km s^{-1})	Pre-Shock Emission (mV)	T_{AV} (K)	ρ_{AV}/ρ_1	Decay (m^{-1})	τ_{int} (μs)	K	k_1 /$dm^3 mole^{-1} s^{-1} x10^5$	k_2 /$dm^3 mole^{-1} s^{-1} x10^6$
892	0.845	293	1.097	176	867	4.295	0.515	26.2	3.394	2.207	2.660
892A	0.845	293	1.097	386	868	4.290	0.515	75.5	3.282	2.026	2.524
893	0.88	293	1.105	165	865	4.206	0.546	186.9	3.811	1.425	2.466
893A	0.88	293	1.105	398	865	4.205	0.546	74.5	3.713	1.200	2.131
894	0.895	293	1.070	152	829	4.106	0.544	23.1	2.982	1.276	2.815
894A	0.895	293	1.070	417	829	4.106	0.544	65.7	3.122	1.157	2.439
895	0.895	293	1.168	151	927	4.402	0.585	77.3	3.482	1.428	2.700
895A	0.895	293	1.168	415	930	4.383	0.585	122.0	3.598	1.358	2.485
896	0.905	293	1.012	139	774	3.922	0.587	11.8	2.856	0.879	2.022
896A	0.905	293	1.012	356	773	3.927	0.587	84.9	2.992	0.925	2.030
897	0.825	293	1.026	149	788	3.959	0.509	47.5	2.805	1.039	2.463
897A	0.825	293	1.026	401	788	3.956	0.509	89.6	2.929	1.125	2.555

Runs 891-897A were performed by Mrs. P.M. Borrell

FIGURE 7.17

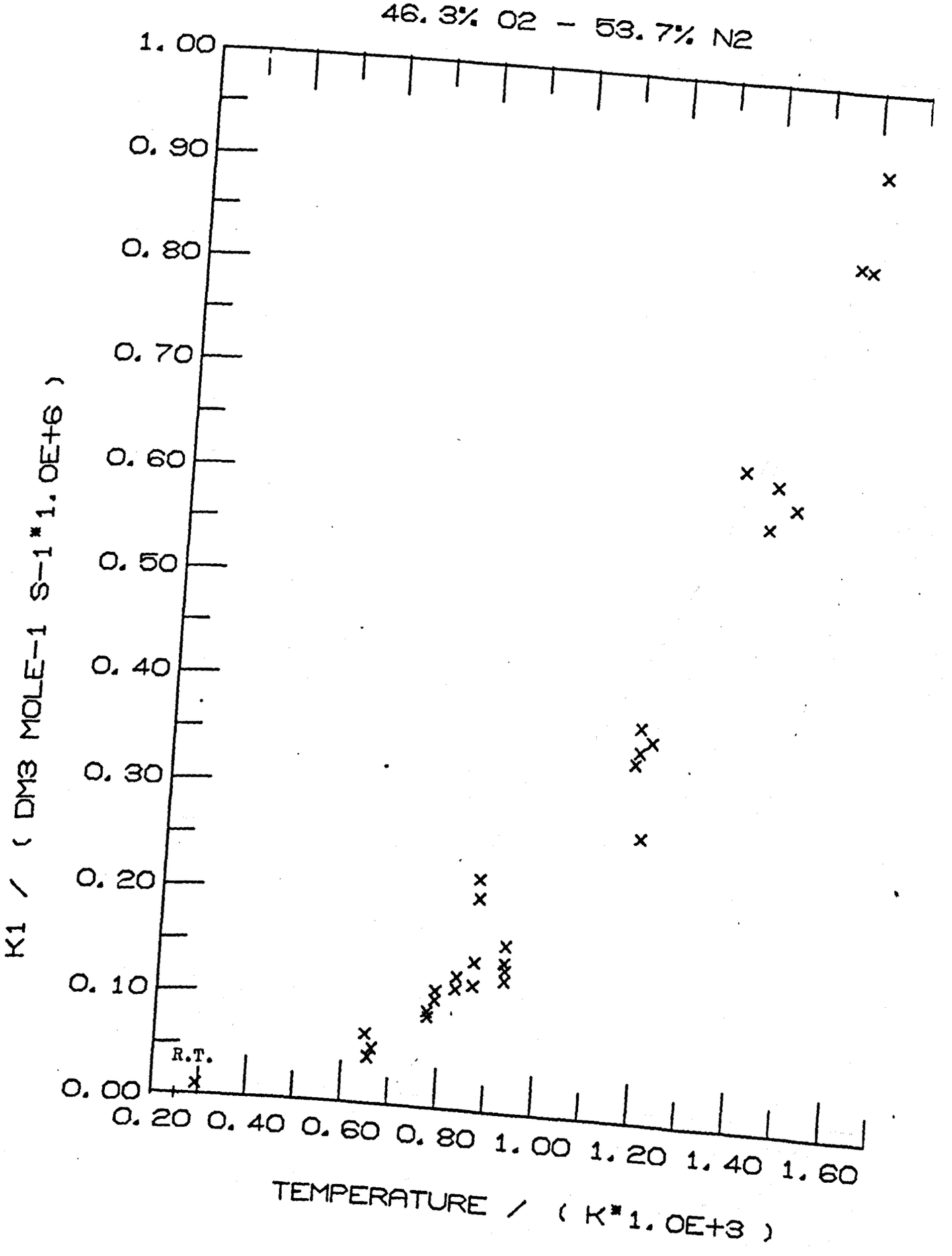
46.3% O2 - 53.7% N2
1.00
0.90
0.80
0.70
0.60
0.50
0.40
0.30
0.20
0.10
0.00
K1 / (DM3 MOLE-1 S-1*1.0E+6)
R.T.
0.20 0.40 0.60 0.80 1.00 1.20 1.40 1.60
TEMPERATURE / (K*1.0E+3)

FIGURE 7.18

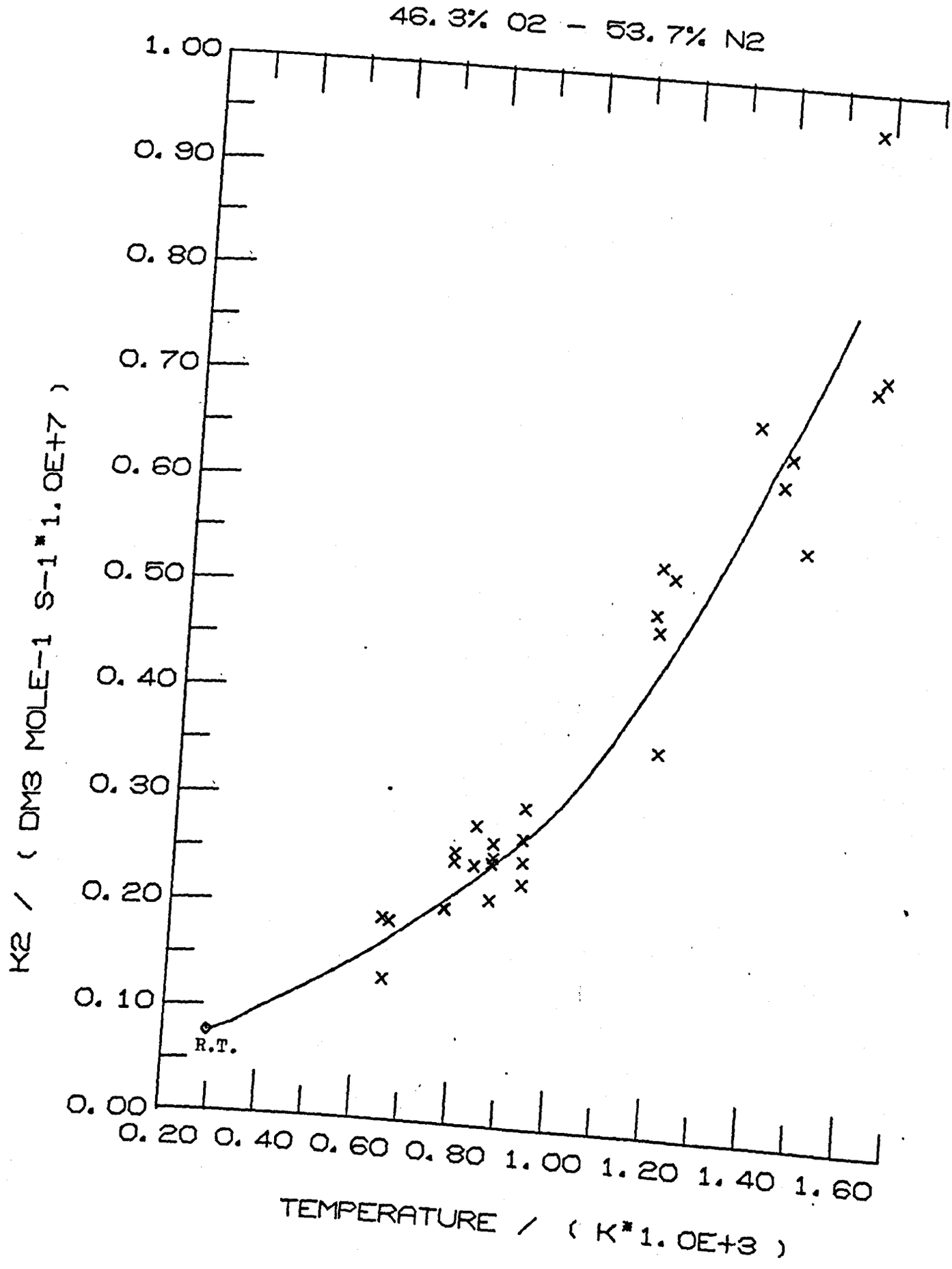
46.3% O2 - 53.7% N2
1.00
0.90
0.80
0.70
0.60
0.50
0.40
0.30
0.20
0.10
0.00
K2 / (DM3 MOLE-1 S-1 * 1.0E+7)
R.T.
0.20 0.40 0.60 0.80 1.00 1.20 1.40 1.60
TEMPERATURE / (K * 1.0E+3)

7.4.4. 25% O_2 - 75% N_2

The results are shown in Table 7.8 and in Figures (7.19) and (7.20). At low temperatures (less than 1000 K), the rate constant for quenching of $O_2(^1\Sigma_g^+)$ is now significantly greater than in pure or 90% oxygen (Figures (7.10) and (7.13)); at higher temperatures, the rates appear to be much the same at all compositions.

TABLE 7.8

25% O_2 - 75% N_2 - Emission from $O_2(^1\Sigma_g^+)$; Flow = 28.0 ml s^{-1}; discharge power = 100W

Run No.	Initial Pressure (KN m^{-2})	Initial Temp. (K)	Shock Velocity (Km s^{-1})	Pre-Shock Emission (mV)	T_{AV} (K)	ρ_{AV}/ρ_1	Decay (m^{-1})	τ_{int} (μs)	K	k_1 /$dm^3 mole^{-1} s^{-1} x10^5$	k_2 /$dm^3 mole^{-1} s^{-1} x10^6$
M192	0.865	291	1.406	125.9	1190		0.380	88.7	7.551	3.388	3.905
M192A	0.865	291	1.406	26.8	1191		0.380	35.6	7.056	4.045	4.989
M193	0.855	292	1.420	140.9	1207		0.381	117.1	7.657	2.931	3.337
M193A	0.855	292	1.420	29.7	1207		0.381	60.8	8.100	4.539	4.885
M194	0.855	292	1.592	143.2	1432		0.368	42.4	11.737	6.380	4.738
M194A	0.855	292	1.592	27.0	1433		0.368	107.9	11.049	6.121	4.829
M195	0.865	290	1.556	114.4	1387		0.403	48.6	13.434	5.130	3.322
M195A	0.865	290	1.556	21.0	1384	5.146	0.403	0.0	13.519	3.391	2.182
M196	0.895	291	1.598	110.3	1439	5.232	0.404	29.5	11.715	8.611	6.377
M196A	0.895	291	1.598	22.5	1437	5.218	0.404	20.2	13.026	6.612	4.404
M197	0.895	291	0.874	124.7	638	3.411	0.418	61.5	3.040	0.567	1.617
M197A	0.895	291	0.874	20.7	638	3.411	0.418	87.5	2.122	0.493	2.014
M198	0.885	292	0.869	131	634	3.391	0.404	42.1	2.901	0.558	1.669
M198A	0.885	292	0.869	124	634	3.391	0.404	37.4	2.908	0.514	1.534
M199	0.90	292	0.874†	124.7	639	3.406	0.403	47.5	2.951	0.553	1.625
M199A	0.90	292	0.874	123.1	639	3.406	0.403	75.2	3.337	0.597	1.551

Run No.	Initial Pressure ($KN\ m^{-2}$)	Initial Temp. (K)	Shock Velocity ($Km\ s^{-1}$)	Pre-Shock Emission (mV)	T_{AV} (K)	ρ_{AV}/ρ_1	Decay (m^{-1})	τ_{int} (μs)	K	k_1 $/dm^3 mole^{-1} s^{-1} x10^5$	k_2 $/dm^3 mole^{-1} s^{-1} x10^6$
M200	0.875	295	1.419	104.3	1210	4.854	0.383	35.7	8.701	3.425	3.425
M200A	0.875	295	1.419	95.6	1210	4.856	0.383	11.1	9.668	2.681	2.413
899	0.83	293	1.387	44.9	1173	4.776	0.392	33.2	7.023	4.226	5.264
899A	0.83	293	1.387	134	1173	4.776	0.392	51.4	7.134	2.931	3.595
900	0.835	293	1.105	40.7	856	4.107	0.421	32.1	3.965	1.418	3.124
900A	0.835	293	1.105	119.1	856	4.107	0.421	138.1	4.086	1.371	2.930
901	0.895	293	1.007	28.0	759	3.830	0.450	86.6	3.190	1.267	3.445
901A	0.895	293	1.007	87.0	759	3.830	0.450	83.3	3.424	0.945	2.395

Runs 899-901A were performed by Mrs. P.M. Borrell

† Shock velocity measured from the photographic record

FIGURE 7.19

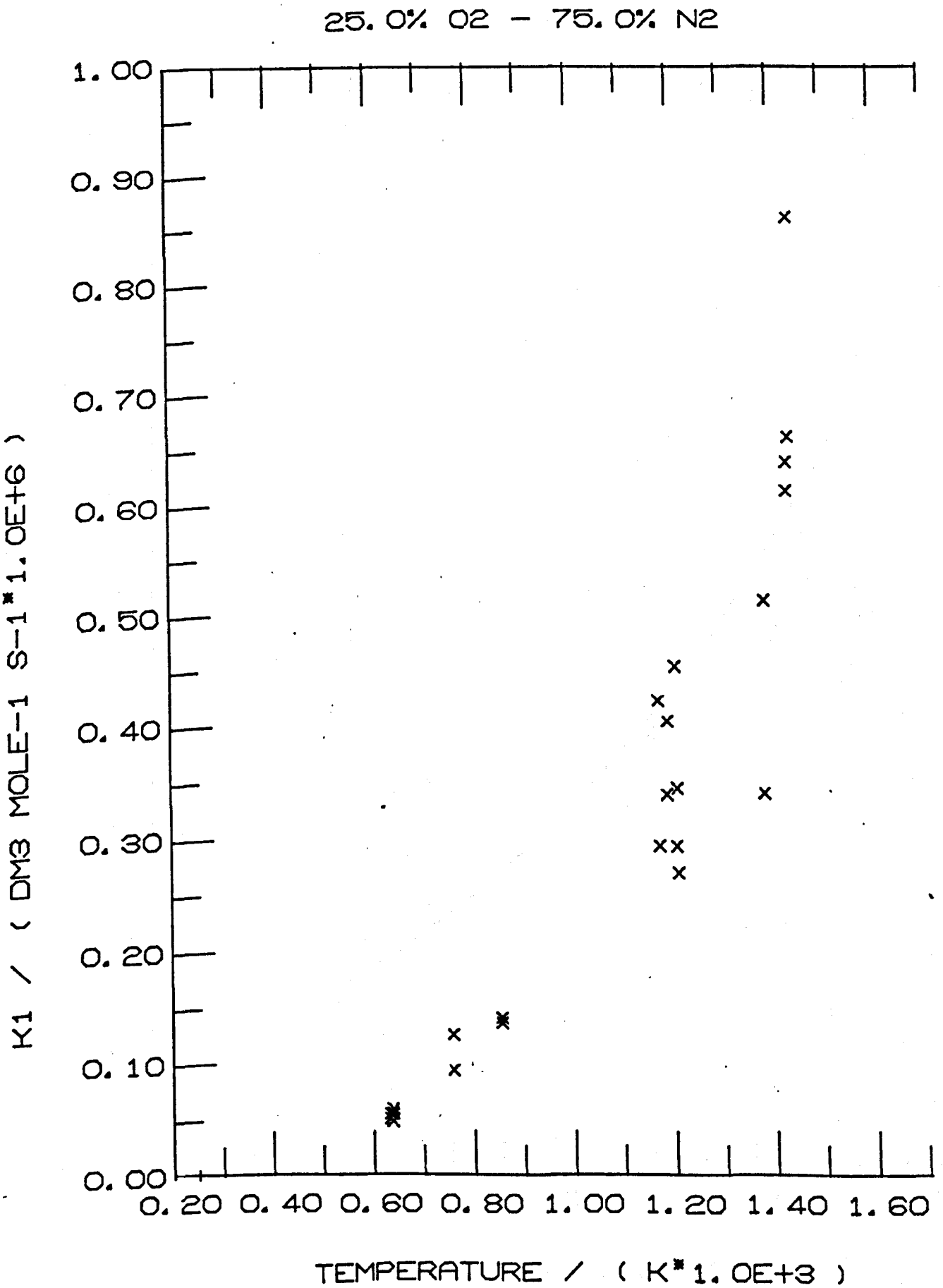
25.0% O2 - 75.0% N2
1.00
0.90
0.80
0.70
0.60
0.50
0.40
0.30
0.20
0.10
0.00
K1 / (DM3 MOLE-1 S-1*1.0E+6)
0.20
0.40
0.60
0.80
1.00
1.20
1.40
1.60
TEMPERATURE / (K*1.0E+3)

FIGURE 7.20

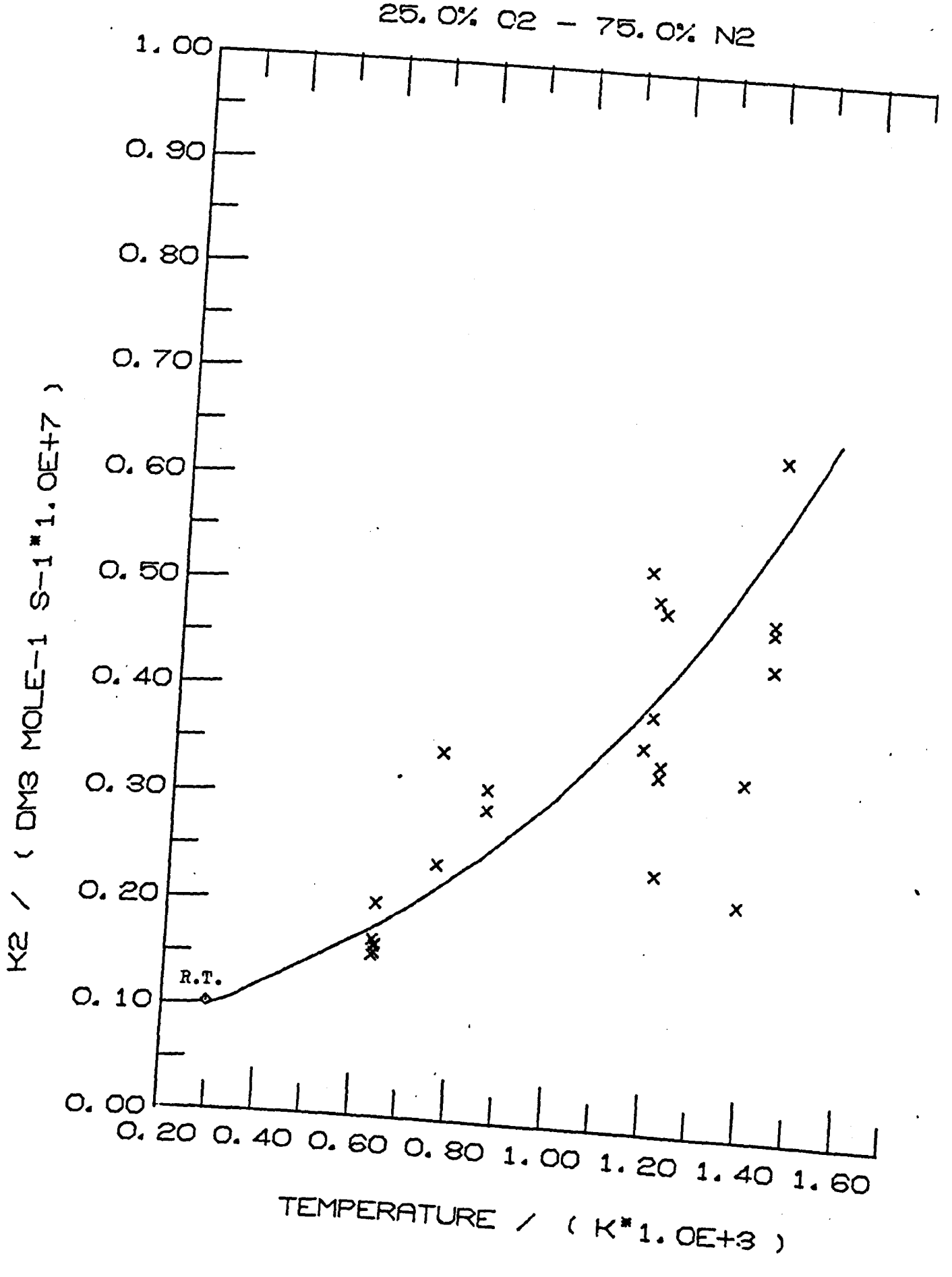
25.0% O2 - 75.0% N2
1.00
0.90
0.80
0.70
0.60
0.50
0.40
0.30
0.20
0.10
0.00
K2 / (DM3 MOLE-1 S-1 * 1.0E+7)
R.T.
0.20 0.40 0.60 0.80 1.00 1.20 1.40 1.60
TEMPERATURE / (K * 1.0E+3)

CHAPTER 8. ANALYSIS OF THE HIGH TEMPERATURE RESULTS

8.1. The Collisional Deactivation of $O_2(^1\Delta_g)$

The rate constants for the collisonal deactivation of $O_2(^1\Delta_g)$ in pure oxygen

$$O_2(^1\Delta_g) + O_2(^3\Sigma_g^-) \rightarrow O_2(^3\Sigma_g^-) + O_2(^3\Sigma_g^-) \tag{8.1}$$

at high temperatures, were calculated from the change in the decay of the post-shock emission from that observed prior to the shock, as was described in Chapter 4. The results showed considerable scatter, and in consequence only an upper limit to the rate of deactivation at high temperatures was obtained.

The rate constants were calculated as follows:

$$\ln \frac{I_D}{I_D^o} = -\left\{2k_q[M] + 2k_w + \alpha_t\right\} t_p \tag{4.20}$$

where α_t is related to the pre-shock decay, α_ℓ, by

$$\alpha_t = U\alpha_\ell(1-\rho_{21}^{-1}) \tag{4.13}$$

Equation (4.20) is rewritten

$$\ln \frac{I_D}{I_D^o} = -\beta_t t_p \tag{8.2}$$

where β_t is the measured post-shock decay. The post-shock decay, β_ℓ, given for each shock in Table 7.1, follows from the relation

$$\beta_\ell = \frac{\beta_t}{U(1-\rho_{21}^{-1})} \tag{8.3}$$

which is equivalent to (4.13). Hence, if

$$\beta_\ell - \alpha_\ell = \delta \tag{8.4}$$

we may write

$$k_q + k_w/[M] = \frac{U\delta(1-\rho_{21}^{-1})}{2[M]} \tag{8.5}$$

where

$$[M] = \rho_{21} \frac{P_1}{P_{atm}} \times \frac{1}{22.4} \text{ mole dm}^{-3} \qquad (8.6)$$

Table (8.1) and Figure (8.1) show the estimated rate constant for each shock. The results are of very low precision and suggest that for satisfactory analysis of discharge flow shock tube experiments of this type, the rates of the reactions under study must increase by 2-3 orders of magnitude over the room temperature rates.

As the temperature at the wall should not be significantly different from that prior to the shock, k_w is expected to be unchanged; the concentration of gas, [M], increases by a factor of the density ratio, and thus $k_w/[M]$ will be a factor of 3.5-6 less than at room temperature. In view of the scatter of the results in Figure (8.1), the wall deactivation of $O_2(^1\Delta_g)$ is neglected in the remainder of the discussion.

In the analysis of the results in Table 8.1, it is important to consider the statistical significance of the small changes in decay and also any systematic errors that may result from neglecting the effects of vibrational relaxation. Statistical calculations on the 22 runs in Table 7.1 for which the decay was measured prior to the shock, give a mean pre-shock decay of 1.083 ± 0.169 m^{-1}; the mean of the post-shock decays (β_ℓ), is 1.151 ± 0.194 m^{-1}. The difference between the two means, $\bar{\delta}$, is 0.068 m^{-1}, and the standard deviation, S_d, of the differences, δ, given by

$$S_d = \frac{\Sigma(\delta - \bar{\delta})^2}{(n-1)} \qquad (8.7)$$

(where n is the number of results), is 0.199 m^{-1}. The standard deviation, $S_{\bar{d}}$, of the mean difference, $\bar{\delta}$, is given by

$$S_{\bar{d}} = \frac{S_d}{n} = 0.0425 \text{ m}^{-1} \qquad (8.8)$$

and $$t = \frac{0.0681-0}{0.0425} = 1.604$$

TABLE 8.1

Calculated rates of collisonal deactivation of $O_2(^1\Delta_g)$ in pure oxygen

Run Number	Temperature /K	δ (m^{-1})	$k_q + k_w/[M]$ /10^5 dm^3 $mole^{-1}$ s^{-1}
M126	1187	+0.178	+0.53
M130	1187	+0.354	+1.05
M131	1621	-0.137	-0.46
M137	689	-0.173	-0.45
M139	676	-0.165	-0.40
M140	671	-0.182	-0.45
M145	1203	+0.031	+0.09
771	1426	+0.115	+0.37
791	1426	-0.012	-0.04
793	1435	+0.057	+0.18
795	751	+0.392	+1.01
805	680	+0.427	+1.10
807	1569	+0.077	+0.25
810	1203	+0.039	+0.12
811	812	-0.064	-0.17
821	1230	+0.332	+1.10
823	1333	-0.009	-0.03
825	680	+0.092	+0.25
827	680	+0.145	+0.41
829	1646	+0.151	+0.56
830	1217	+0.244	+0.76
831	1490	-0.306	-1.08

FIGURE 8. 1

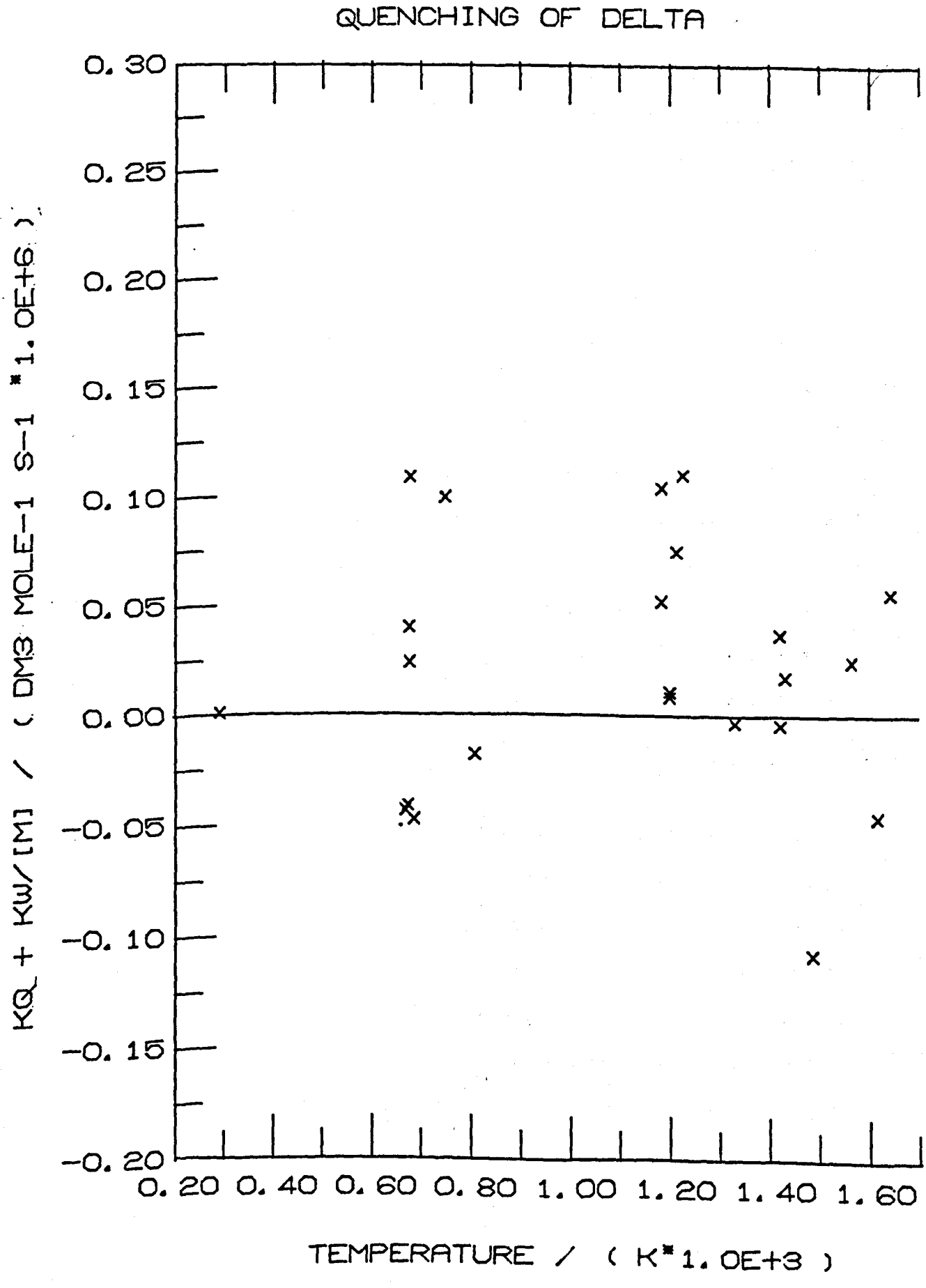
QUENCHING OF DELTA
0. 30
0. 25
0. 20
0. 15
0. 10
0. 05
0. 00
-0. 05
-0. 10
-0. 15
-0. 20
KQ + KW/[M] / (DM3 MOLE-1 S-1 *1. OE+6)
0. 20
0. 40
0. 60
0. 80
1. 00
1. 20
1. 40
1. 60
TEMPERATURE / (K*1. OE+3)

Statistical tables show that for n=22 the difference in pre- and post-shock decays is significant at the 95% confidence level if t is greater than 2.080, or at the 90% confidence level when this greater than 1.721. As t is only 1.604, this analysis does not allow us to say that the post-shock decay is significantly greater than that prior to the shock. However, if k_q increases appreciably with temperature, significant changes in the decay could be missed by this treatment.

Similarly, by neglecting the effects of vibrational relaxation we may be incorrectly estimating the difference in pre- and post-shock decays and also increasing the scatter of the results. Figure (8.2) shows the change in the function $(\rho_{t1}^{\ 2}\ T_{t1}^{\ \frac{1}{2}}\ e^{-\alpha_t t_p})$ with particle time for a typical shock (temperature ≈ 1220) K, both when the gas is assumed to be fully relaxed and when the effects of vibrational relaxation are included. If the gas is assumed to be fully relaxed, the "calculated" curve which gives the best fit to the true decay curve, has a greater gradient than that obtained from the pre-shock decay. For slow shocks, analysed assuming the conditions to be frozen, the gradient of the "calculated" curve will be less than that of the true curve; as vibrational relaxation at temperatures of 650-820 K is very slow, the observed decrease should be small.

Thus, if it were possible to take vibrational relaxation into account, the observed changes in gradient would be still less than has been observed. The scatter should also decrease if the negative rate constants calculated for some slow shocks are a result of choosing the frozen conditions. However, it is clear that discharge flow shock tube experiments are not suitable for the accurate measurement of the temperature dependence of the rate constants for collisonal deactivation of $O_2(^1\Delta_g)$.

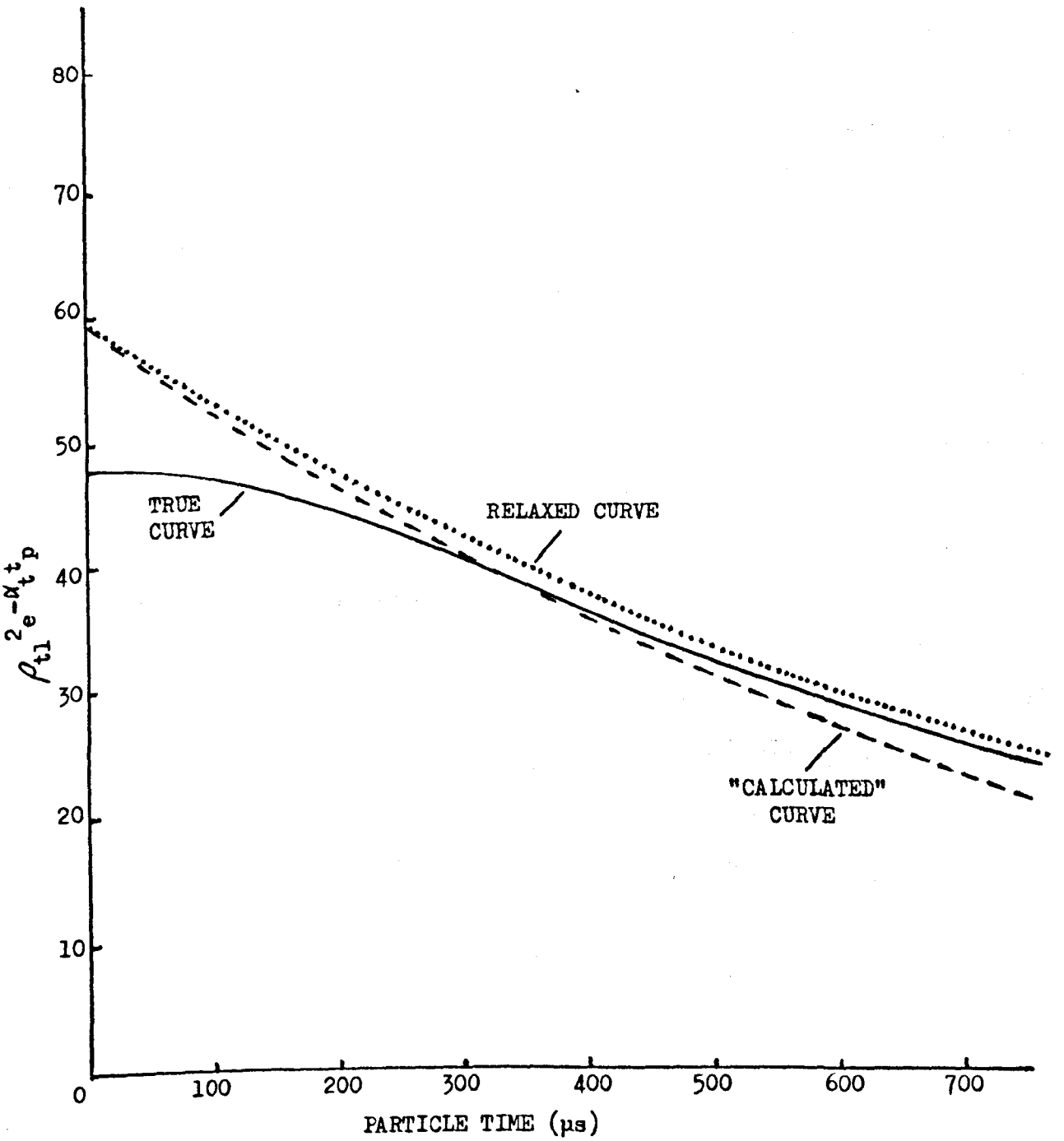

FIGURE 8.2 Overestimated Decay of "Calculated" Curve that Results from Trying to Fit Real Results (True Curve), Assuming Vibrational Relaxation to Be Complete.

These experiments do tell us that the rate of quenching of $O_2(^1\Delta_g)$ changes only slowly with temperature, an important result in itself. Assuming that systematic changes in the rate constant, greater than a factor of 50 (corresponding roughly to a 15% change in the decay) should be detectable in our apparatus, an upper limit of 5×10^4 dm^3 $mole^{-1}$ s^{-1} may be placed on the rate constant at 1500 K; the lower limit is zero.

The temperature dependence of this rate constant has been measured by Findlay and Snelling[66] over the narrow range 285-324 K; their results showed the rate of deactivation to increase slowly with temperature. By plotting log k_q against log T they obtained an approximate relation

$$k_q = (1.34 \pm 0.05) \times 10^3 \, (T/300)^n \qquad (8.9)$$

where $n = 0.78 \pm 0.32$ and T is the absolute temperature. Their measured rate constants are significantly greater than the recent room temperature estimates of ourselves[77] and of Schurath et al.,[78] suggesting that there are systematic errors in the experiments; the observed changes with temperature are probably approximately correct over the temperature range studied, but extrapolation of equation (8.9) to temperatures of $\sim$ 1500 K is unlikely to be satisfactory. Such extrapolations do, however predict the rate constant at 1500 K to lie somewhere between 2×10^3 and 10^4 dm^3 $mole^{-1}$ s^{-1}, which is well within the range suggested by our results.

8.2. The Dimol Emission

Information on the nature of the dimol reaction

$$O_2(^1\Delta_g) + O_2(^1\Delta_g) \rightarrow O_2(^3\Sigma_g^-) + O_2(^3\Sigma_g^-) + h\nu(634\ nm) \qquad (1.12)$$

is obtained by comparing the change in the level of the dimol emission behind the shock front from the level observed prior to the shock with that predicted by a simple collisional model; the results confirm the generally accepted view that the collision complex formed in (1.12) cannot be regarded as a stable O_4 molecule.

It was shown in Chapter 4 that the emission observed at time t_p after the shock front has passed is related to the pre-shock emission by

$$\frac{I_{D2}}{I_{D1}^o} = K \rho_{21}^{\ 2} T_{21}^{\frac{1}{2}} e^{-\alpha_t t_p} \qquad (4.27)$$

where the constant, K, is the ratio of the observed level of emission to that expected if (1.12) was a simple collisional process. The values of this ratio, K, given in Table 7.1 are plotted against temperature in Figure (8.3). It may be seen that, with a few exceptions, the ratio lies very close to unity; the anomalous results are from runs M121 and M131, in which the pre-shock level of emission is extremely low, and from the last three runs, 829-831, for which the high pre-shock decay suggests that a dirty shock tube has given rise to spurious emissions. If these are excluded, the mean value of K is equal to 1.005 ± 0.217, very nearly that expected for a simple collisional reaction. K does show a small systematic increase with temperature; this may be due to systematic errors in the experimental measurements or to reaction (1.12) having a small activation energy.

The conclusion of Arnold et al.[29] that the collision complex formed in the dimol reaction has a lifetime too short for the reaction

FIGURE 8.3

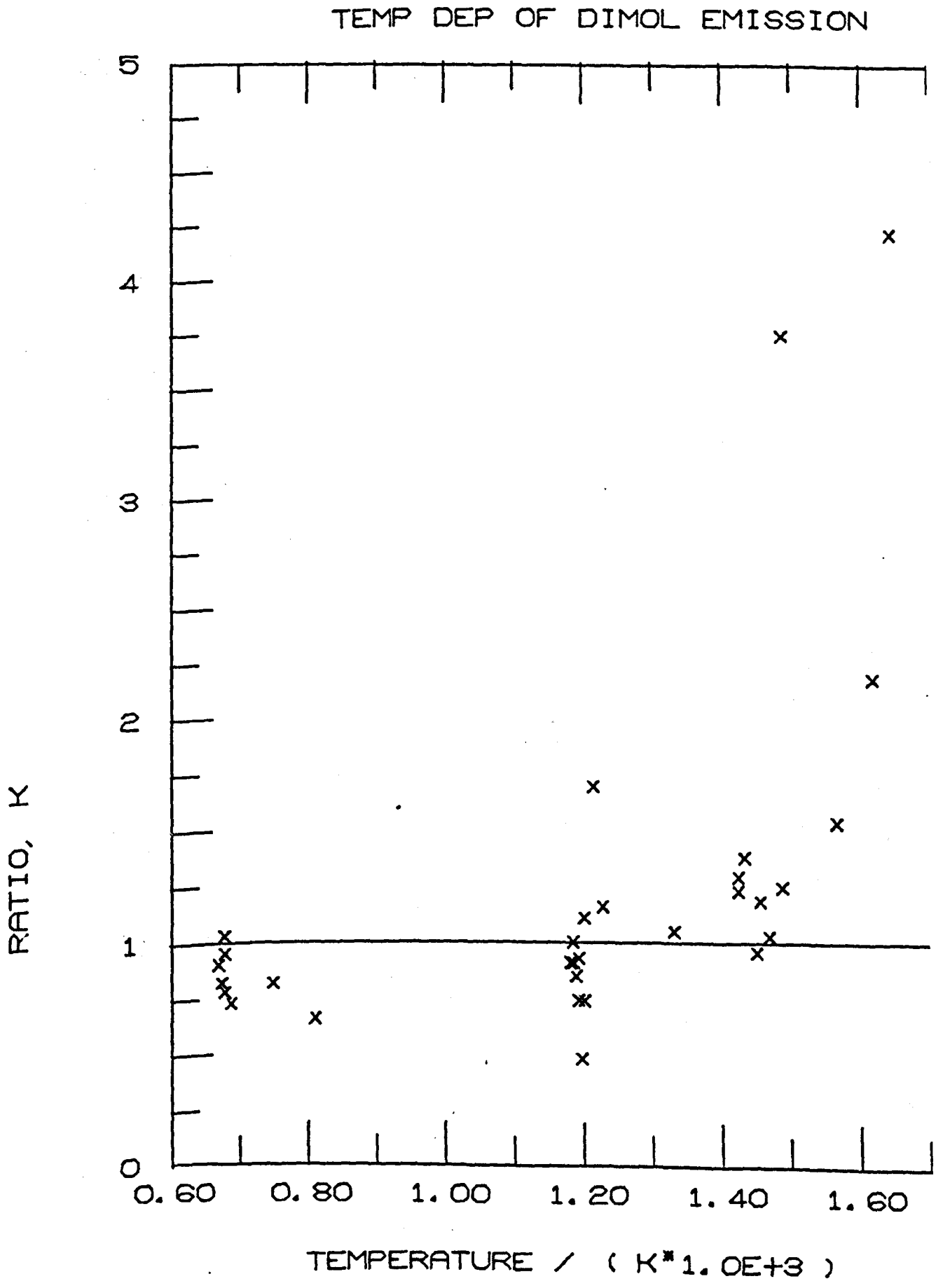
TEMP DEP OF DIMOL EMISSION
RATIO, K
5
4
3
2
1
0
0.60
0.80
1.00
1.20
1.40
1.60
TEMPERATURE / (K*1.0E+3)

$$O_2(^1\Delta_g) + O_2(^1\Delta_g) \rightleftharpoons O_4 \qquad (4.28)$$

to be at equilibrium is confirmed by the results shown in Figure 8.4; it was shown in Chapter 4 that if a stable O_4 molecule is formed

$$KT_{21}^{\frac{1}{2}} = e^{\frac{\Delta H}{R}\left[\frac{1}{T_2} - \frac{1}{T_1}\right]} \qquad (4.30)$$

or

$$\ln KT_{21}^{\frac{1}{2}} = C + \frac{\Delta H}{RT_2} \qquad (8.10)$$

where ΔH is the dissociation energy of the O_4 molecule. The gradient of the least squares line through the experimental data is negative (-373 K) and greater than the value of -63 K obtained by Arnold et al. over the temperature range 221-475 K; this is to be expected if the O_4 molecule is not stable and K is equal to unity, because equation (8.10) then reduces to the function

$$\log T = A + \frac{B}{T} \qquad (8.11)$$

the differential of which is a function of the temperature.

The above result is not unexpected; the existence of $(O_2)_2$ dimers has been demonstrated only when they are isolated in a neon matrix at 4 K,[32] and the dissociation energy of such species must be little greater than that produced by Van der Waals type forces. The emission spectrum of singlet molecular oxygen (Figure 1.4) shows the dimol band to be broad and diffuse, with an absence of fine structure; this again supports the idea that the emitting species is a loosely bound collision complex. As was pointed out in Chapter 1, the dimol emission is not restricted to the collision of molecules of $O_2(^1\Delta_g)$, and other two-molecule transitions have been observed:

$$O_2(^1\Sigma_g^+)(v=o) + O_2(^1\Delta_g)(v=o) \rightarrow O_2(^3\Sigma_g^-)(v=o) + O_2(^3\Sigma_g^-)(v=o) + h\nu(477\ nm) \qquad (1.10)$$

FIGURE 8.4

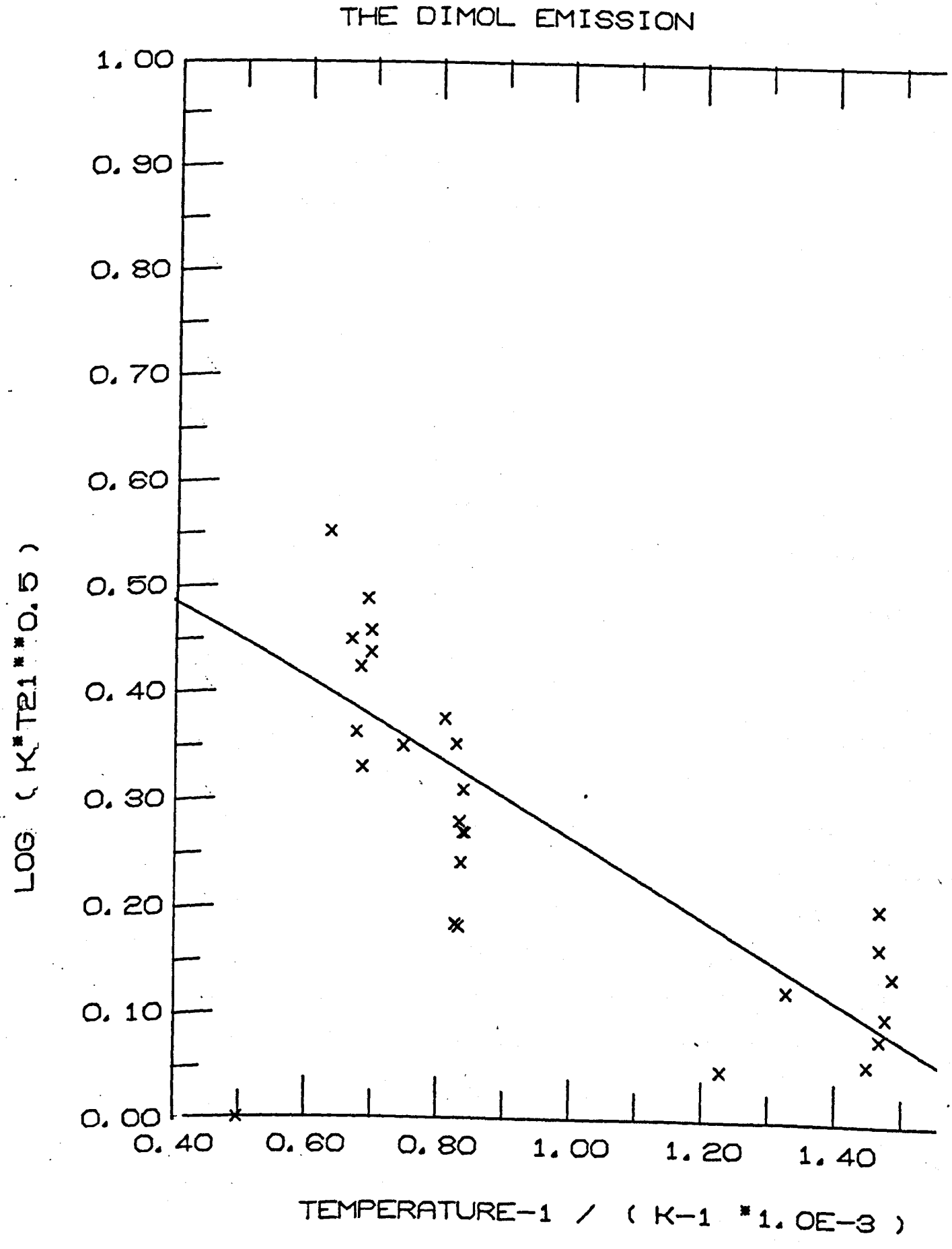
THE DIMOL EMISSION
1.00
0.90
0.80
0.70
0.60
0.50
0.40
0.30
0.20
0.10
0.00
LOG (K*T2**0.5)
0.40
0.60
0.80
1.00
1.20
1.40
TEMPERATURE-1 / (K-1 *1.0E-3)

$$O_2(^1\Sigma_g^+)(v=o) + O_2(^1\Sigma_g^+)(v=o) \rightarrow O_2(^3\Sigma_g^-)(v=o) + O_2(^3\Sigma_g^-)(v=o) + h\nu(380\ nm) \quad (1.11)$$

Arnold, Kubo and Ogryzlo[65] have estimated the radiative lifetime of the collision complex in the three reactions to be 1.5s, 1.7s and 0.3s respectively; such estimates are approximate because the duration of the collision complex is not known. In their calculations, an estimate of about 10^{-13}s for the collision time was used; the radiative lifetimes obtained are shorter than those of the magnetic dipole transitions in $O_2(^1\Sigma_g^+)$ and $O_2(^1\Delta_g)$

$$O_2(^1\Sigma_g^+)(v=o) \rightarrow O_2(^3\Sigma_g^-)(v=o) + h\nu(762\ nm) \quad (1.3)$$

$$O_2(^1\Delta_g)(v=o) \rightarrow O_2(^3\Sigma_g^-)(v=o) + h\nu(1270\ nm) \quad (1.4)$$

which are 12s and 45 min respectively. This is reasonable as the possibility of electric dipole transitions is increased in a collision with another molecule; similar calculations of the rates of the reactions

$$O_2(^1\Delta_g) + O_2(^3\Sigma_g^-) \rightarrow O_2(^3\Sigma_g^-) + O_2(^3\Sigma_g^-) + h\nu(1270\ nm) \quad (8.12)$$

$$O_2(^1\Sigma_g^+) + O_2(^3\Sigma_g^-) \rightarrow O_2(^3\Sigma_g^-) + O_2(^3\Sigma_g^-) + h\nu(762\ nm) \quad (8.13)$$

give radiative lifetimes of 4s and 15s respectively;[65] which explains the observation in Chapter 1 that the emission at 1270 nm is collision enhanced, whereas that at 762 nm is collision enhanced only at high pressures.

As the lifetime of the collision complex is small (e.g. $\sim 10^{9}$-10^{-13}s), the equilibrium approach described in Chapter 4 is clearly not applicable. Since the ratio, K, shows a small temperature dependence, it should in principle be possible to estimate the activation energy of reaction (1.12); while for a simple collisional process K is equal to unity, if the reaction has a finite activation energy, E_{act}

$$K = e^{\frac{-E_{act}}{R}\left[\frac{1}{T_1} - \frac{1}{T_2}\right]} \quad (8.14)$$

where T_1, T_2 are the initial temperature of the test gas and the temperature of the shock-heated gas. K will then increase with temperature. Figure (8.3) shows that K is generally less than unity at temperatures $\sim$ 650 K and greater than unity at temperatures above 1300 K; as a result, it is not possible to make a satisfactory estimate of the activation energy from equation (8.14). As an indication of the order of magnitude of the activation energies involved, for E_{act} = 1 kJ mole^{-1}, K should be 1.24 at 650 K and 1.38 at 1500 K; for E_{act} = 0.5 kJ mole^{-1}, K becomes 1.12 at 650 K and 1.18 at 1500 K. Thus the activation energy of the dimol reaction will certainly be small.

The emission bands of stable molecules such as $O_2(^1\Sigma_g^+)$ are broadened at high temperatures as a result of the increase in the population of the higher rotational energy levels; although the dimol collision complex is too loosely bound for rotational levels to be observed, Arnold et al.[29] have suggested that the emission band at 634 nm is broadened by increasing the temperature. This broadening is probably a result of the increased rotational energy of the molecules of $O_2(^1\Delta_g)$ which form the collision complex.

Arnold et al. consider the broadening of the dimol band over the temperature range 220-475 K to be important. However, the results of our experiments in which a simple narrow band optical filter is used to select the correct wavelength give a value of the ratio, K, that is close to unity, showing that the broadening is not significant in the temperature range 295-1650 K. In confirmation of this result, a few experiments, performed using a broad band filter which transmitted light of wavelengths between 625 and 675 nm, did not show the increase in the ratio of levels, K, from that observed with a narrow band filter which would be expected if the emission band were appreciably broadened at high temperatures. Our results suggest that the broadening of the dimol band at high temperatures is far smaller than expected by Arnold et al., and that the use

of a narrow band filter in these experiments to monitor the dimol emission is satisfactory.

In conclusion, it may be said that the dimol emission is confirmed to be a simple collision controlled reaction with an activation energy unlikely to be greater than 1 kJ $mole^{-1}$. The collision complex formed in the reaction is short-lived and cannot reasonably be described as an O_4 molecule. The broadening of the dimol band at high temperatures has not been studied directly, but the results of the present work suggest that the effect is small.

8.3. The Energy Pooling Reaction

The rate constants for the energy pooling reaction

$$O_2(^1\Delta_g) + O_2(^1\Delta_g) \rightarrow O_2(^1\Sigma_g^+) + O_2(^3\Sigma_g^-) \qquad (1.13)$$

should not depend on the composition of the bulk carrier gas. The results shown in Tables 7.5 - 7.8 for oxygen/nitrogen mixtures containing 10-75% nitrogen are obtained by rearranging equation (4.38) to give

$$k_1(T_2) = \frac{K.k_1(T_1) \cdot k_2(T_2)}{k_2(T_1) + k'_w/[M]} \qquad (8.15)$$

The ratio, K, of the level of emission behind the shock front to that which is expected from the shock compression alone, and the rate constant for collisional deactivation of $O_2(^1\Sigma_g^+)$, calculated from the relaxation zone in the early part of the shock, both show a composition dependence. As an example of this, for a series of shocks at temperatures 1185 ± 10 K into oxygen/nitrogen mixtures, K is ∿ 1.2 in pure oxygen, 2.0 at 90% oxygen, 2.8 at 72.1%, 4.9 at 46.3%, and 7.5 at 25%. The rate constant, $k_2(T_1)$, for collisional deactivation of $O_2(^1\Sigma_g^+)$ at room temperature also varies with composition according to the relation

$$k_2(T_1) = 1.0 \times 10^5 X_{O_2} + 1.3 \times 10^6 X_{N_2} \qquad (8.16)$$

where 1.0×10^5 and 1.3×10^6 dm^3 $mole^{-1}$ s^{-1} are the room temperature rate constants for deactivation by oxygen and nitrogen and X_{O_2}, X_{N_2} are the mole fractions of each species.

The rate constants for energy pooling at the temperatures behind the shock front, that are calculated from the widely differing values of the parameters in equation (8.15), are shown in Figure (8.5). The results show no detectable composition dependence. This is powerful confirmation that our apparatus is working properly; if the results contained significant systematic errors, the calculated rate constants for energy pooling would

FIGURE 8.5

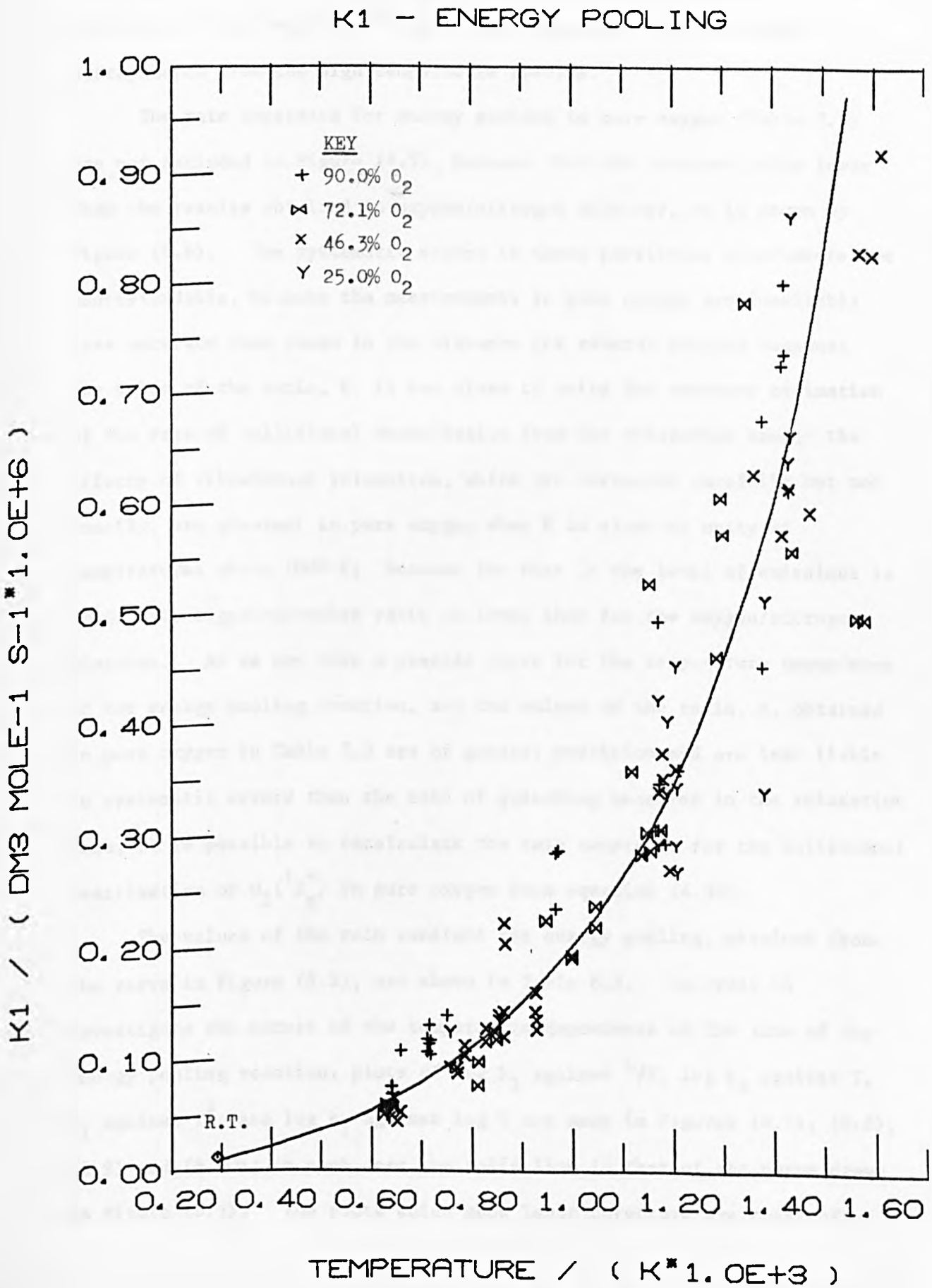
K1 - ENERGY POOLING
KEY
+ 90.0% O_2
⋈ 72.1% O_2
× 46.3% O_2
Y 25.0% O_2
R.T.
1.00
0.90
0.80
0.70
0.60
0.50
0.40
0.30
0.20
0.10
0.00
0.20 0.40 0.60 0.80 1.00 1.20 1.40 1.60
K1 / (DM3 MOLE-1 S-1 * 1.0E+6)
TEMPERATURE / (K * 1.0E+3)

almost certainly vary with the composition. The best line through the experimental data is drawn by eye; the room temperature rate constant[92] of 1.22×10^4 dm^3 $mole^{-1}$ s^{-1} is in good agreement with the curve extrapolated from the high temperature results.

The rate constants for energy pooling in pure oxygen (Table 7.3) are not included in Figure (8.5), because they are systematically lower than the results obtained in oxygen/nitrogen mixtures, as is shown by Figure (8.6). The systematic errors in these particular experiments are understandable, because the measurements in pure oxygen are inevitably less accurate than those in the mixtures for several related reasons: the value of the ratio, K, is too close to unity for accurate estimation of the rate of collisional deactivation from the relaxation zone; the effects of vibrational relaxation, which are corrected carefully but not exactly, are greatest in pure oxygen when K is close to unity at temperatures above 1000 K; because the rise in the level of emissions is small, the signal-to-noise ratio is lower than for the oxygen/nitrogen mixtures. As we now have a precise curve for the temperature dependence of the energy pooling reaction, and the values of the ratio, K, obtained in pure oxygen in Table 7.3 are of greater precision and are less liable to systematic errors than the rate of quenching measured in the relaxation zone, it is possible to recalculate the rate constants for the collisional deactivation of $O_2(^1\Sigma_g^+)$ in pure oxygen from equation (4.38).

The values of the rate constant for energy pooling, obtained from the curve in Figure (8.5), are shown in Table 8.2. In order to investigate the nature of the temperature dependence of the rate of the energy pooling reaction, plots of $\log k_1$ against $^1/T$, $\log k_1$ against T, k_1 against $T^{\frac{1}{2}}$, and $\log k_1$ against $\log T$ are made in Figures (8.7), (8.8), (8.9) and (8.10); in each case the solid line is that of the curve drawn in Figure (8.5). The plots which show least curvature are those of

FIGURE 8.6

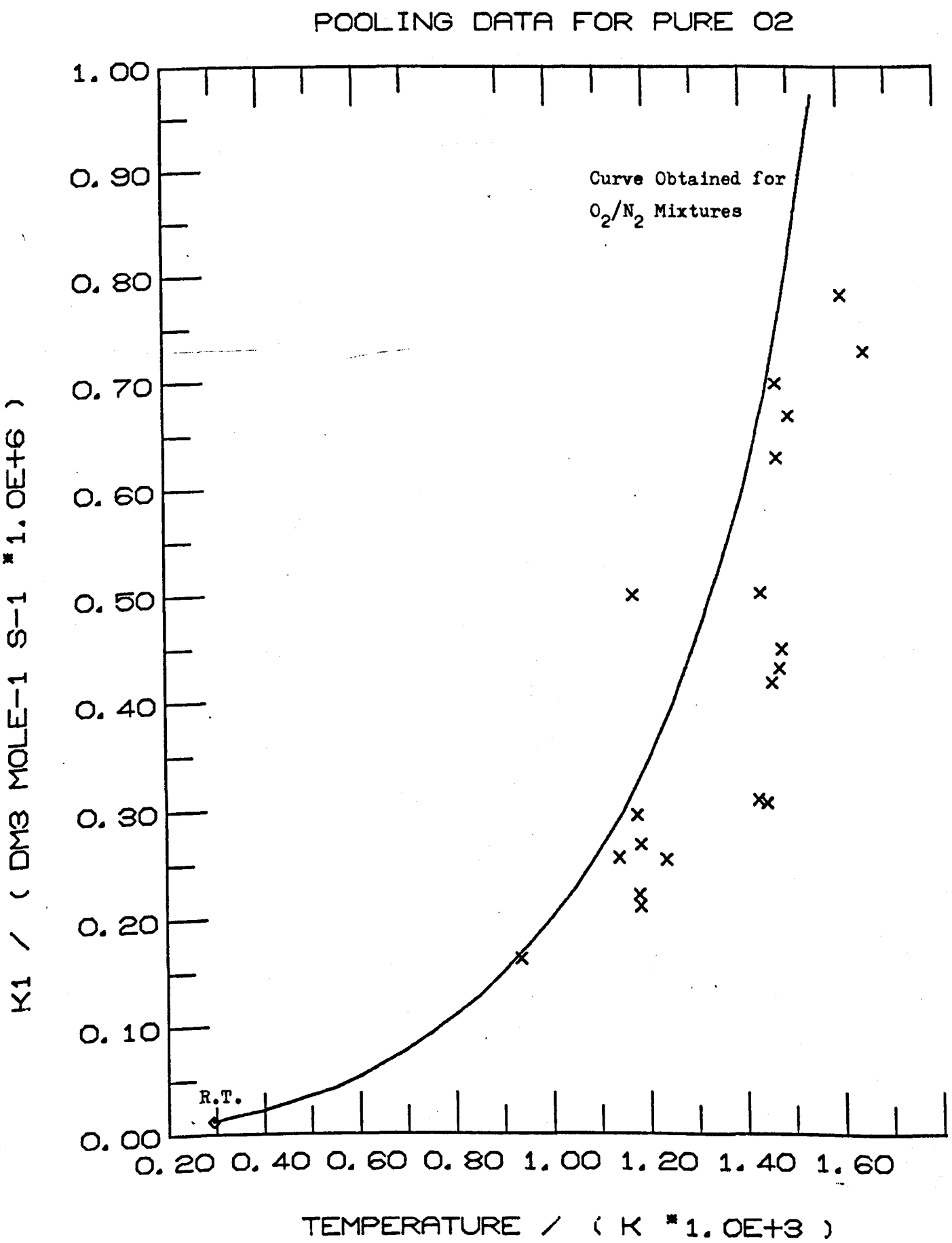
POOLING DATA FOR PURE O2
Curve Obtained for
O_2/N_2 Mixtures
R.T.
K1 / (DM3 MOLE-1 S-1 *1.0E+6)
1.00
0.90
0.80
0.70
0.60
0.50
0.40
0.30
0.20
0.10
0.00
0.20 0.40 0.60 0.80 1.00 1.20 1.40 1.60
TEMPERATURE / (K *1.0E+3)

TABLE 8.2

Rate constants for the energy pooling reaction at temperatures 300-1600 K, obtained from Figure (8.5)

TEMPERATURE/K	$k_1/10^5$ dm^3 mole^{-1} s^{-1}
300	0.12
400	0.23
500	0.36
600	0.53
700	0.78
800	1.10
900	1.50
1000	2.00
1100	2.62
1200	3.43
1300	4.56
1400	5.96
1500	8.17
1600	11.95

FIGURE 8.7

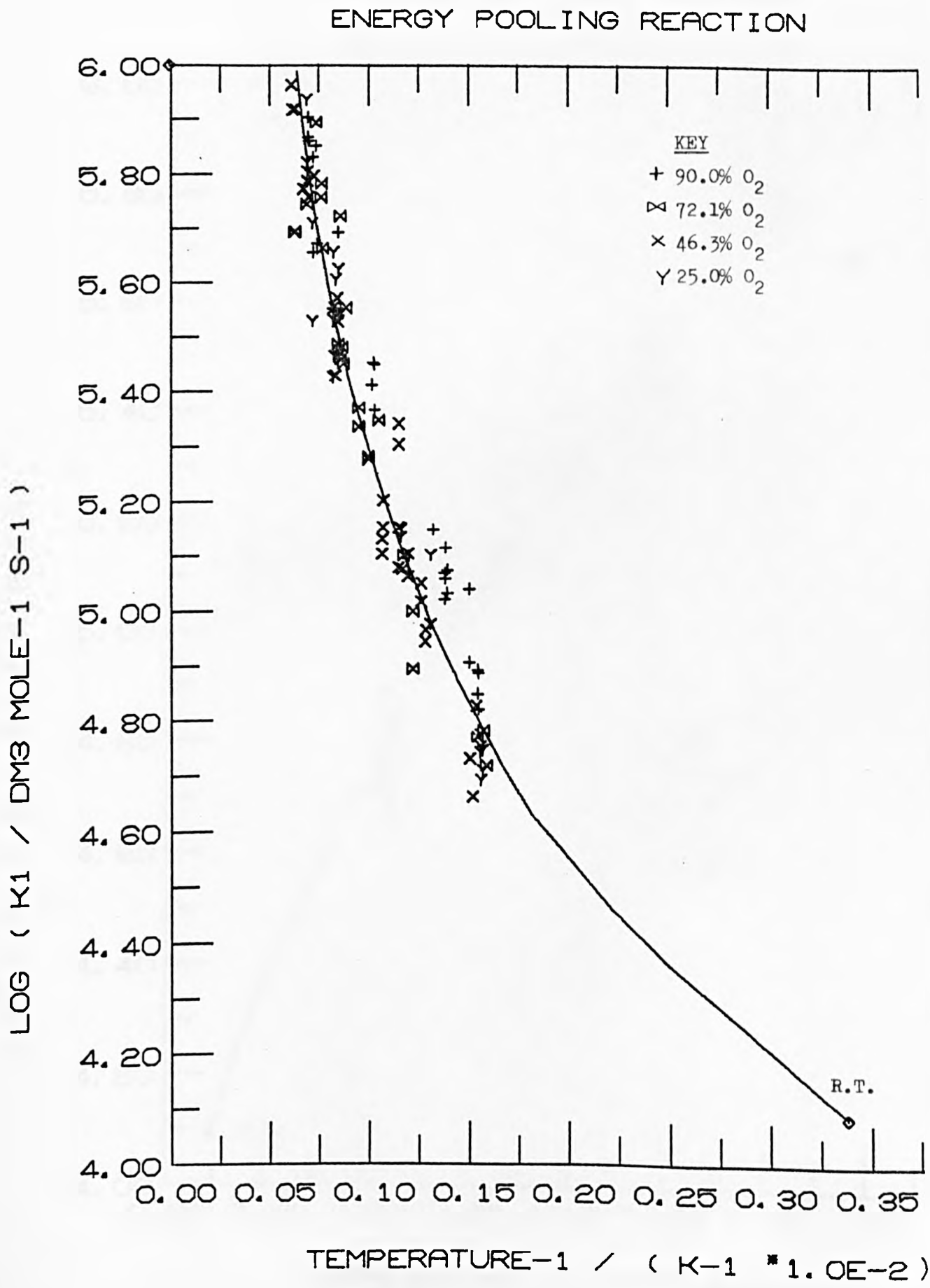
ENERGY POOLING REACTION
KEY
+ 90.0% O2
⋈ 72.1% O2
× 46.3% O2
Y 25.0% O2
R.T.
LOG (K1 / DM3 MOLE-1 S-1)
6.00
5.80
5.60
5.40
5.20
5.00
4.80
4.60
4.40
4.20
4.00
0.00 0.05 0.10 0.15 0.20 0.25 0.30 0.35
TEMPERATURE-1 / (K-1 *1.0E-2)

FIGURE 8.8

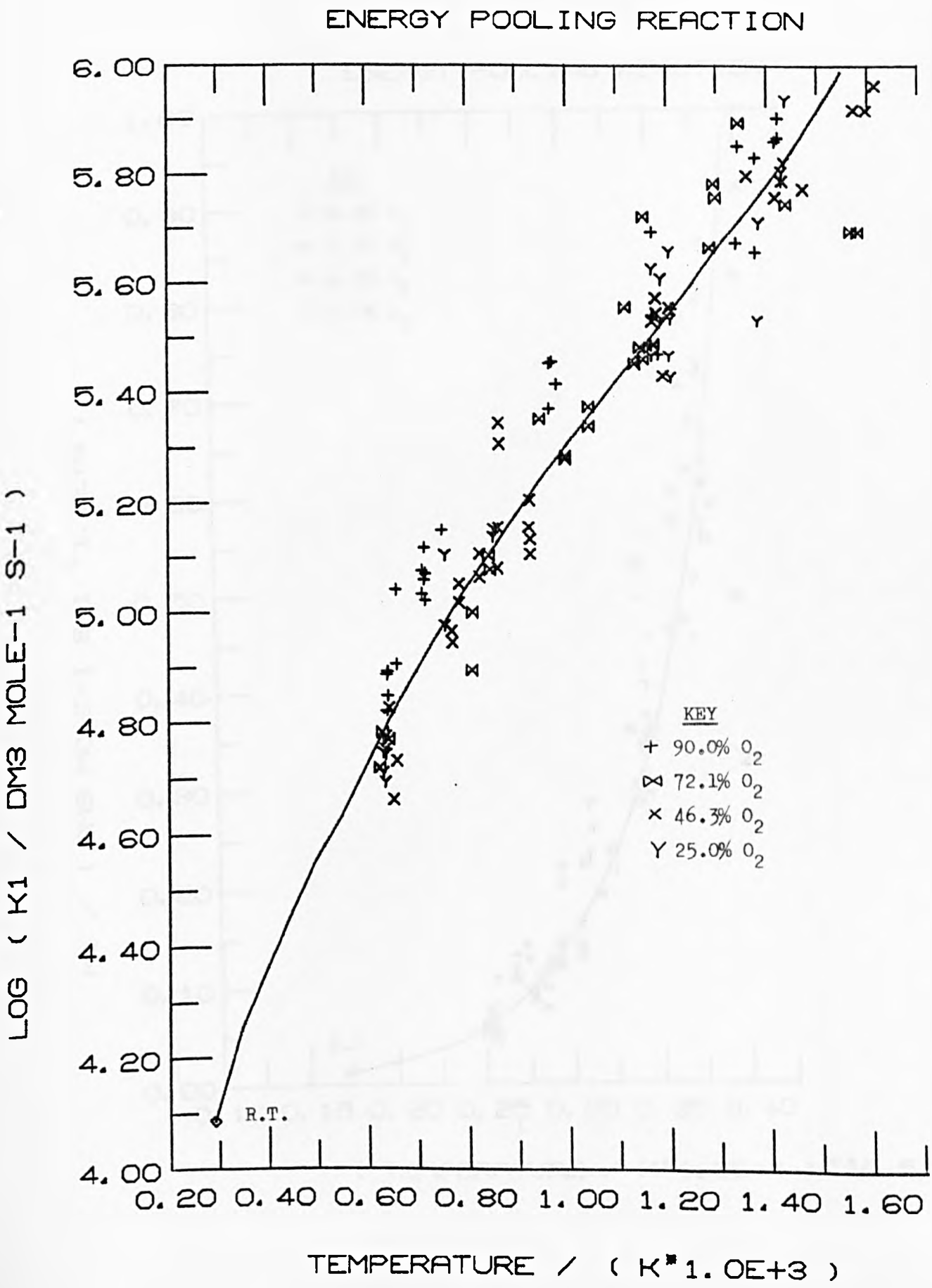
ENERGY POOLING REACTION
LOG (K1 / DM3 MOLE-1 S-1)
6.00
5.80
5.60
5.40
5.20
5.00
4.80
4.60
4.40
4.20
4.00
0.20
0.40
0.60
0.80
1.00
1.20
1.40
1.60
TEMPERATURE / (K*1.0E+3)
R.T.
KEY
+ 90.0% O2
⋈ 72.1% O2
× 46.3% O2
Y 25.0% O2

FIGURE 8.9

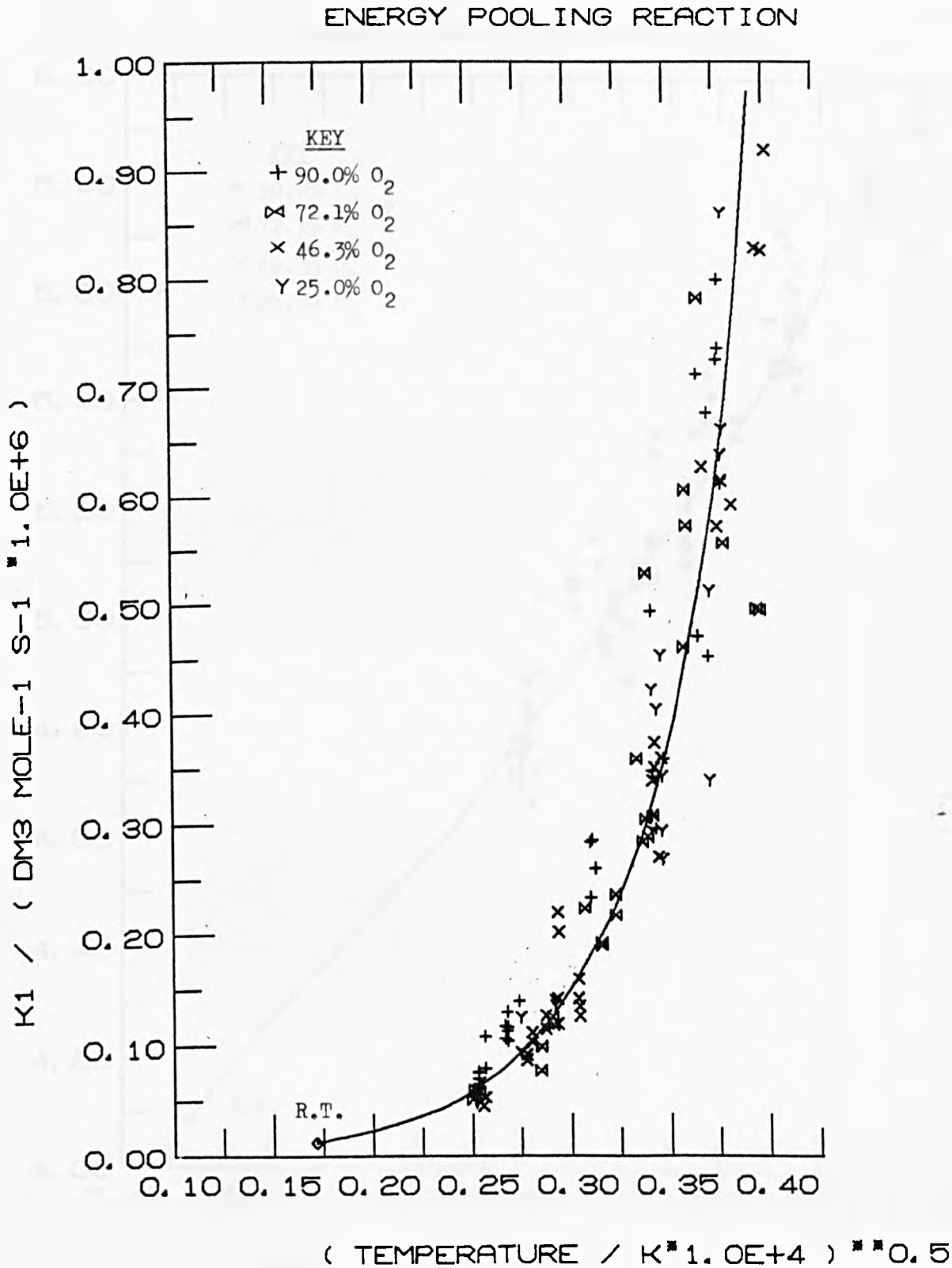
ENERGY POOLING REACTION
KEY
+ 90.0% O2
⋈ 72.1% O2
× 46.3% O2
Y 25.0% O2
R.T.
K1 / (DM3 MOLE-1 S-1 *1.0E+6)
1.00
0.90
0.80
0.70
0.60
0.50
0.40
0.30
0.20
0.10
0.00
0.10 0.15 0.20 0.25 0.30 0.35 0.40
(TEMPERATURE / K*1.0E+4)**0.5

FIGURE 8.10

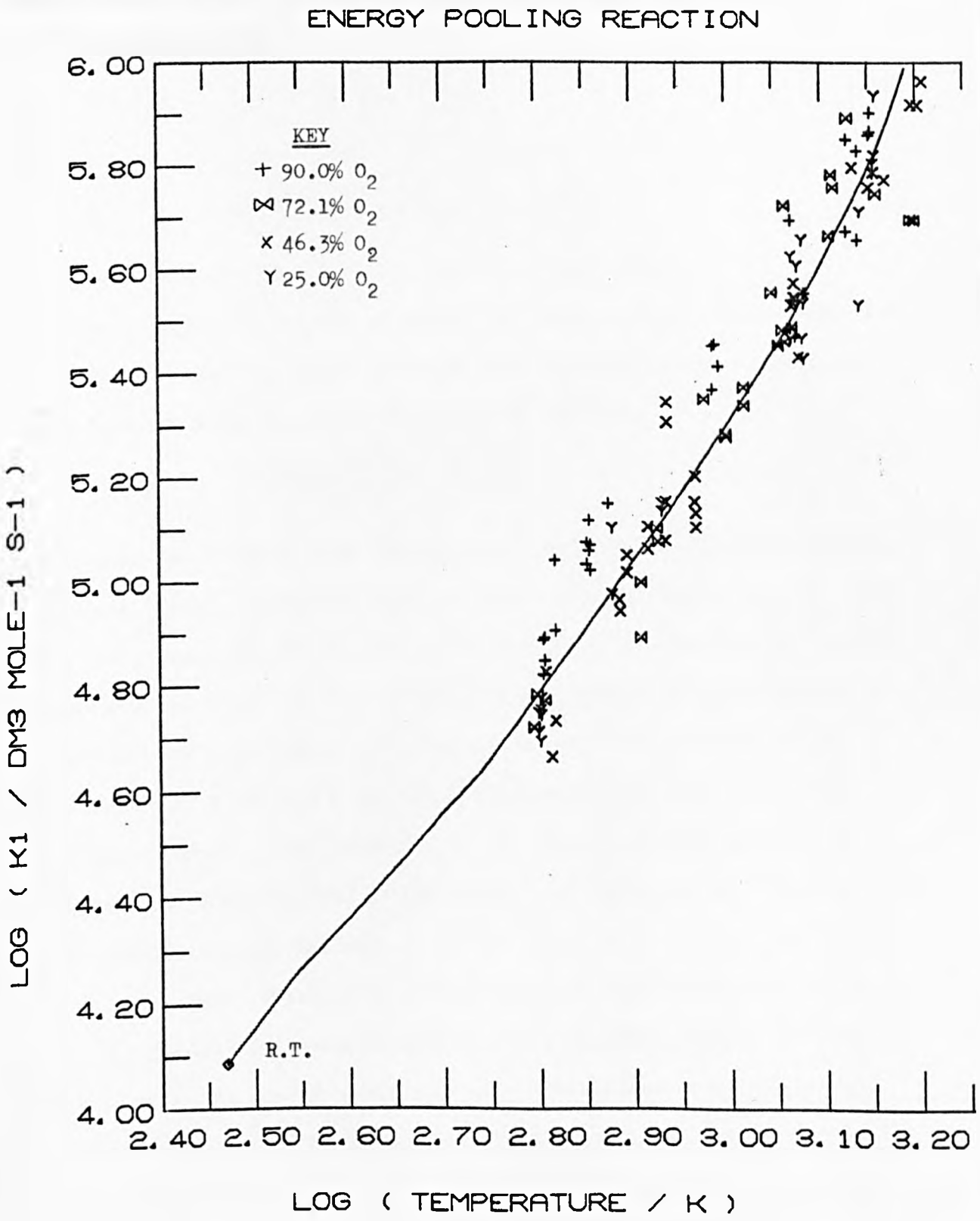
ENERGY POOLING REACTION
KEY
+ 90.0% O_2
⋈ 72.1% O_2
× 46.3% O_2
Y 25.0% O_2
R.T.
6.00
5.80
5.60
5.40
5.20
5.00
4.80
4.60
4.40
4.20
4.00
2.40 2.50 2.60 2.70 2.80 2.90 3.00 3.10 3.20
LOG (K1 / DM3 MOLE-1 S-1)
LOG (TEMPERATURE / K)

log k_1 against T and log k_1 against log T; unfortunately such plots cannot be interpreted in terms of a simple physical model. The temperature dependence of the rate of this reaction is discussed together with those of the rates of other reactions of $O_2(^1\Delta_g)$ and $O_2(^1\Sigma_g^+)$ in section 8.5.

8.4. The Collisional Deactivation of $O_2(^1\Sigma_g^+)$

By analysis of the rate constants obtained at high temperatures for the collisional deactivation of $O_2(^1\Sigma_g^+)$ in oxygen and in oxygen/nitrogen mixtures, the temperature dependences of the rate constants for deactivation in nitrogen

$$O_2(^1\Sigma_g^+) + N_2 \rightarrow O_2(^1\Delta_g) + N_2 \qquad (8.17)$$

and in oxygen

$$O_2(^1\Sigma_g^+) + O_2(^3\Sigma_g^-) \rightarrow O_2(^1\Delta_g) + O_2(^3\Sigma_g^-) \qquad (8.18)$$

which give the best fit to all the results, are obtained.

As a first step in the analysis, the rate constants for collisional deactivation of $O_2(^1\Sigma_g^+)$ in pure oxygen have been recalculated using the energy pooling curve in Figure (8.5) and the relation

$$k_2(T_2) = \frac{k_1(T_2)\ (k_2(T_1) + k_w'/[M])}{k_1(T_1)} \qquad (8.19)$$

The results are compared with the values in Table 7.3, which were obtained by analysis of the relaxation zone, in Table 8.3 and Figure (8.11); with a few exceptions, the recalculated rate constants are greater by a factor between one and two. It is now possible to estimate the rate constants for collisional quenching in pure oxygen for the runs at temperatures below 1000 K in which $K \approx 1$ and the collisional relaxation time, τ_{rel}, cannot be measured. The precision of the rate constants in Table 8.3 is higher than that obtained in the relaxation measurements; they are used in all subsequent calculations.

As the rate constants calculated for the collisional deactivation of $O_2(^1\Sigma_g^+)$ in oxygen/nitrogen mixtures are reasonably precise and the rate constants for energy pooling obtained from these constants do not vary systematically from the curve in Figure (8.5), the data in Tables 7.4, 7.5, 7.6 and 7.7, were not recalculated in this way. In Figures

TABLE 8.3

Rate constants for collisional quenching of $O_2(^1\Sigma_g^+)$ in pure oxygen, calculated using the rate constants for energy pooling in Figure (8.5).

Run No.	Temperature/K	$k_1/10^5$ $dm^3mole^{-1}s^{-1}$ (from curve)	$k_2/10^6$ $dm^3mole^{-1}s^{-1}$ Table 7.3	Recalculated
M110	1140	2.91	2.730	3.13
M124	1498	8.10	6.839	8.38
M125	673	0.70	-	0.94
M127	681	0.72	-	0.94
M129	666	0.68	-	0.93
M146	1220	3.64	-	4.65
M147	1655	13.40	5.026	9.30
M150	1655	13.40	8.135	7.93
M151	1608	11.70	3.370	5.10
770	1475	7.50	3.485	6.07
777	1460	6.93	4.244	7.05
797	1480	7.62	4.129	7.02
799	1429	6.49	2.891	6.09
801	1185	3.29	3.133	3.86
839	1238	3.82	3.382	5.15
842	1184	3.28	2.244	3.54
844	1447	6.83	2.239	5.08
853	961	1.77	-	2.61
854	935	1.66	-	2.40
855	937	1.68	2.002	2.08
856	943	1.70	-	2.28
870	1054	2.31	-	2.96
881A	1179	3.27	3.676	4.06
884A	1438	6.65	4.708	6.46
910	1473	7.45	3.912	4.71
910A	1472	7.45	4.398	4.77
911	1175	3.20	4.600	2.98
882	1181	3.27	2.717	4.06
835	738	0.89	-	1.14

FIGURE 8.11

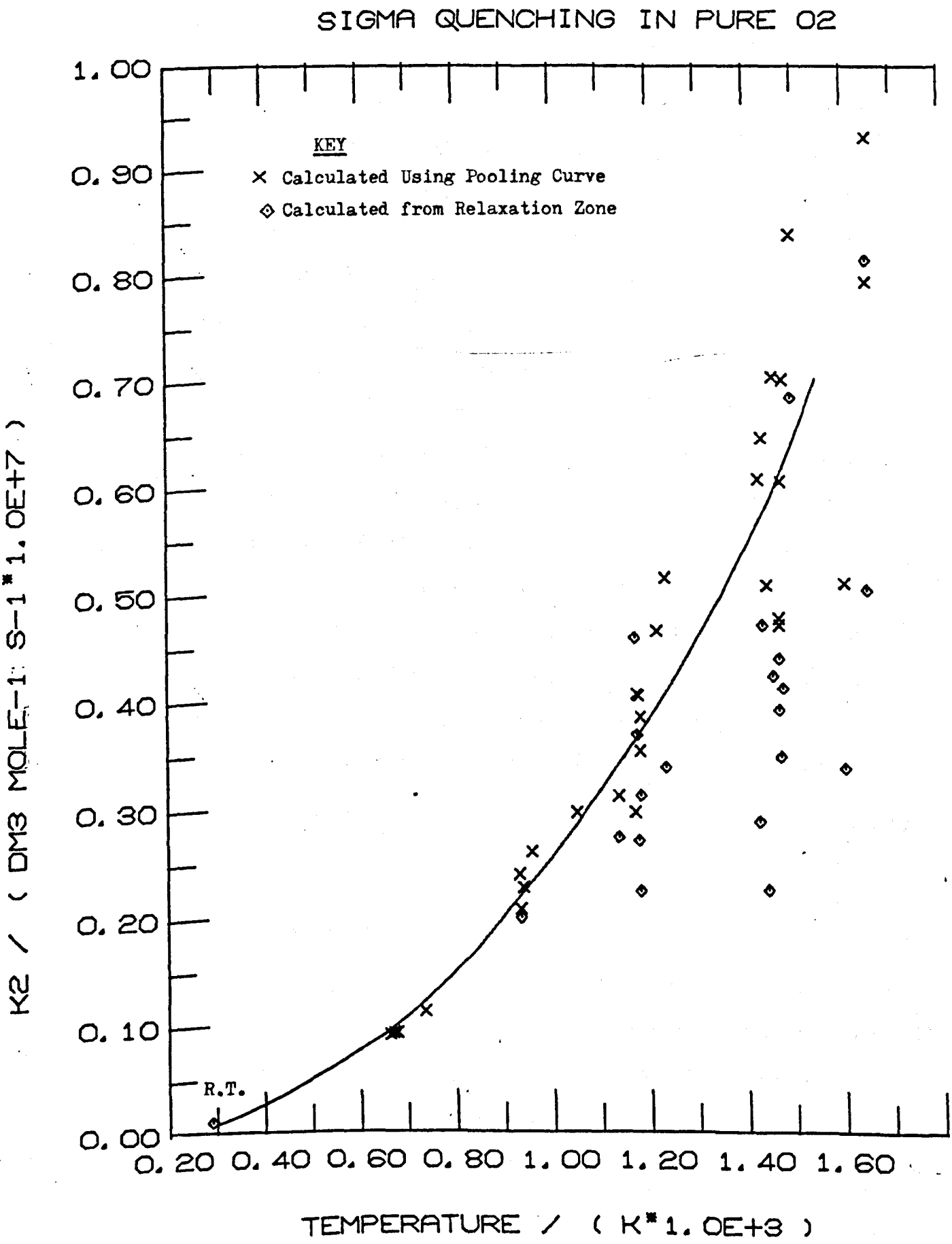
SIGMA QUENCHING IN PURE O2
KEY
× Calculated Using Pooling Curve
◇ Calculated from Relaxation Zone
R.T.
1.00
0.90
0.80
0.70
0.60
0.50
0.40
0.30
0.20
0.10
0.00
0.20 0.40 0.60 0.80 1.00 1.20 1.40 1.60
K2 / (DM3 MOLE-1 S-1 * 1.0E+7)
TEMPERATURE / (K * 1.0E+3)

(8.11), (7.14), (7.16), (7.18) and (7.20), the "best" line through the experimental data on quenching of $O_2(^1\Sigma_g^+)$ in pure oxygen and in the oxygen/nitrogen mixtures has been drawn by eye. The "best" lines are plotted on the same graph in Figure (8.12); the results reveal a definite composition dependence, and the cross over point at $\sim$ 1000 K suggests that the rate constant for deactivation by oxygen is higher than the rate constant for deactivation by nitrogen at high temperatures.
This contrasts with the room temperature rate constants of 1.0×10^5 and 1.3×10^6 dm^3 $mole^{-1}$ s^{-1} for quenching by oxygen and nitrogen respectively.

The results are not perfect; despite our efforts to improve the data for pure oxygen, the curve obtained from Figure (8.11) is still systematically lower than that for mixtures containing 10-75% nitrogen. The low precision of the results at high temperatures is also evident. At temperatures below 1000 K, the rate constants increase systematically with the mole fraction of nitrogen, as is found at room temperature.

The values of the rate constants, k_2, obtained from the curves, are plotted against composition at 100 degree intervals of temperature between 600 and 1500 K in Figures (8.13) and (8.14). In each case the best straight line has been drawn through the data assuming that the composition dependence of the rate constant is linear and of the form

$$k_2(T_2) = k_2(N_2)X_{N_2} + k_2(O_2)X_{O_2} \qquad (8.19)$$

or

$$k_2(T_2) = k_2(N_2) - [k_2(N_2) - k_2(O_2)]X_{O_2} \qquad (8.20)$$

where $k_2(N_2)$ and $k_2(O_2)$ are the rate constants in pure nitrogen and oxygen. In drawing the lines it is assumed that the cross-over point in Figure (8.12) is real and that the gradient of equation (8.20) increases steadily from a negative value at low temperatures to a positive value at high temperatures. Although Figure (8.12) suggests that the rate constants in pure oxygen in

FIGURE 8.12

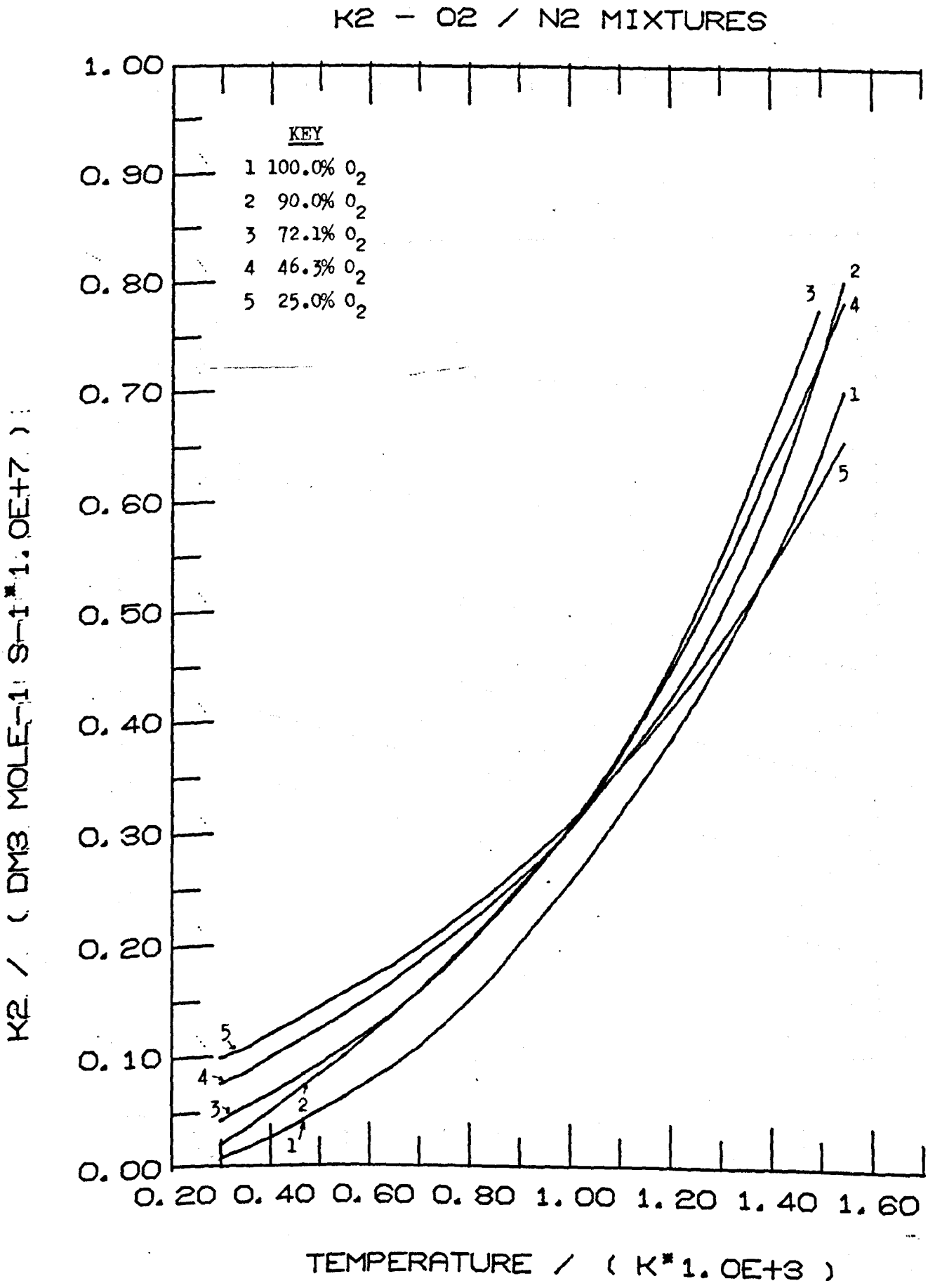
K2 - O2 / N2 MIXTURES
KEY
1 100.0% O2
2 90.0% O2
3 72.1% O2
4 46.3% O2
5 25.0% O2
K2 / (DM3 MOLE-1 S-1 * 1.0E+7)
TEMPERATURE / (K * 1.0E+3)
1.00
0.90
0.80
0.70
0.60
0.50
0.40
0.30
0.20
0.10
0.00
0.20 0.40 0.60 0.80 1.00 1.20 1.40 1.60

FIGURE 8.13

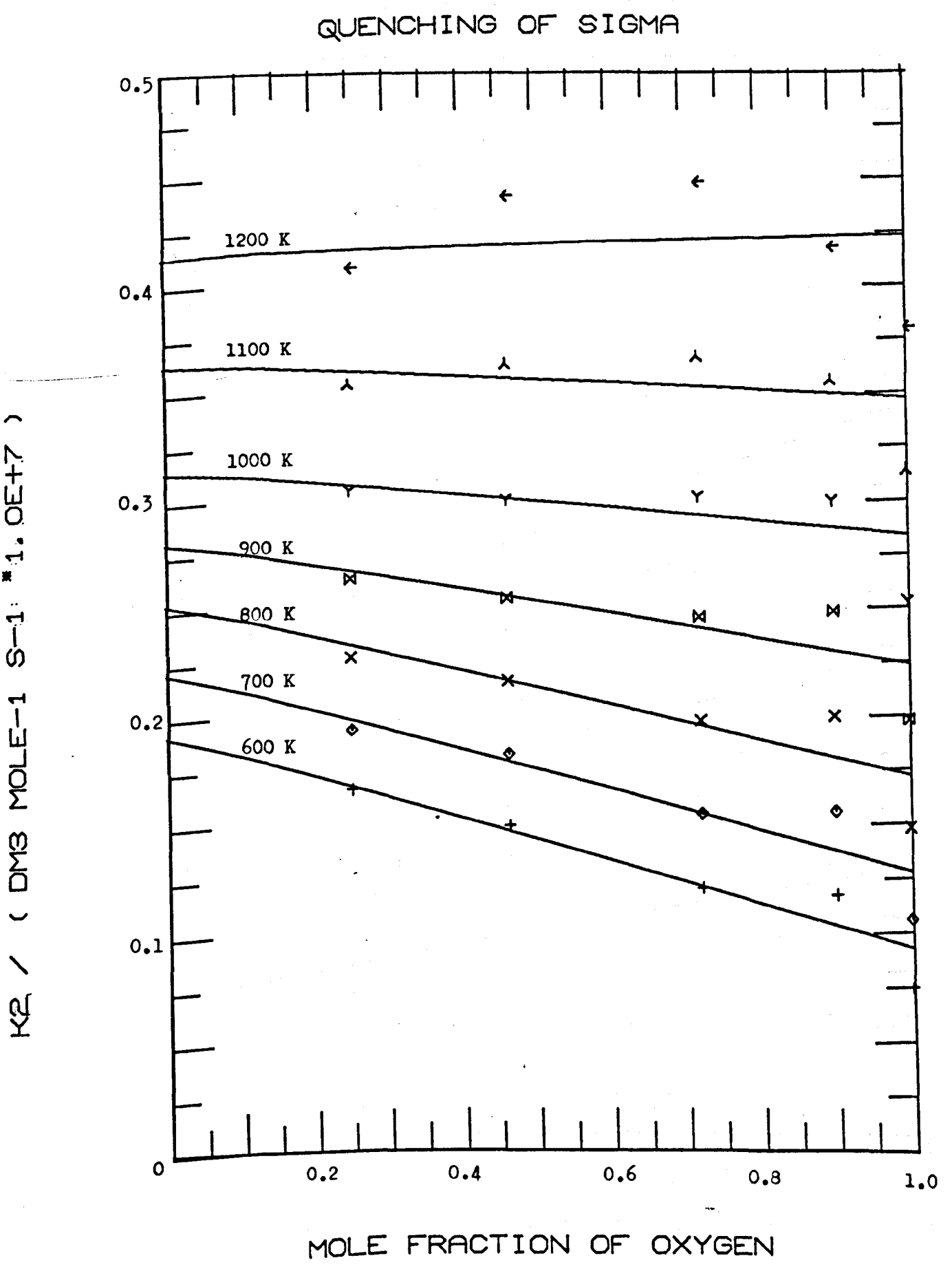
QUENCHING OF SIGMA
1200 K
1100 K
1000 K
900 K
800 K
700 K
600 K
0.5
0.4
0.3
0.2
0.1
0
0.2
0.4
0.6
0.8
1.0
K2 / (DM3 MOLE-1 S-1 * 1.0E+7)
MOLE FRACTION OF OXYGEN

FIGURE 8.14

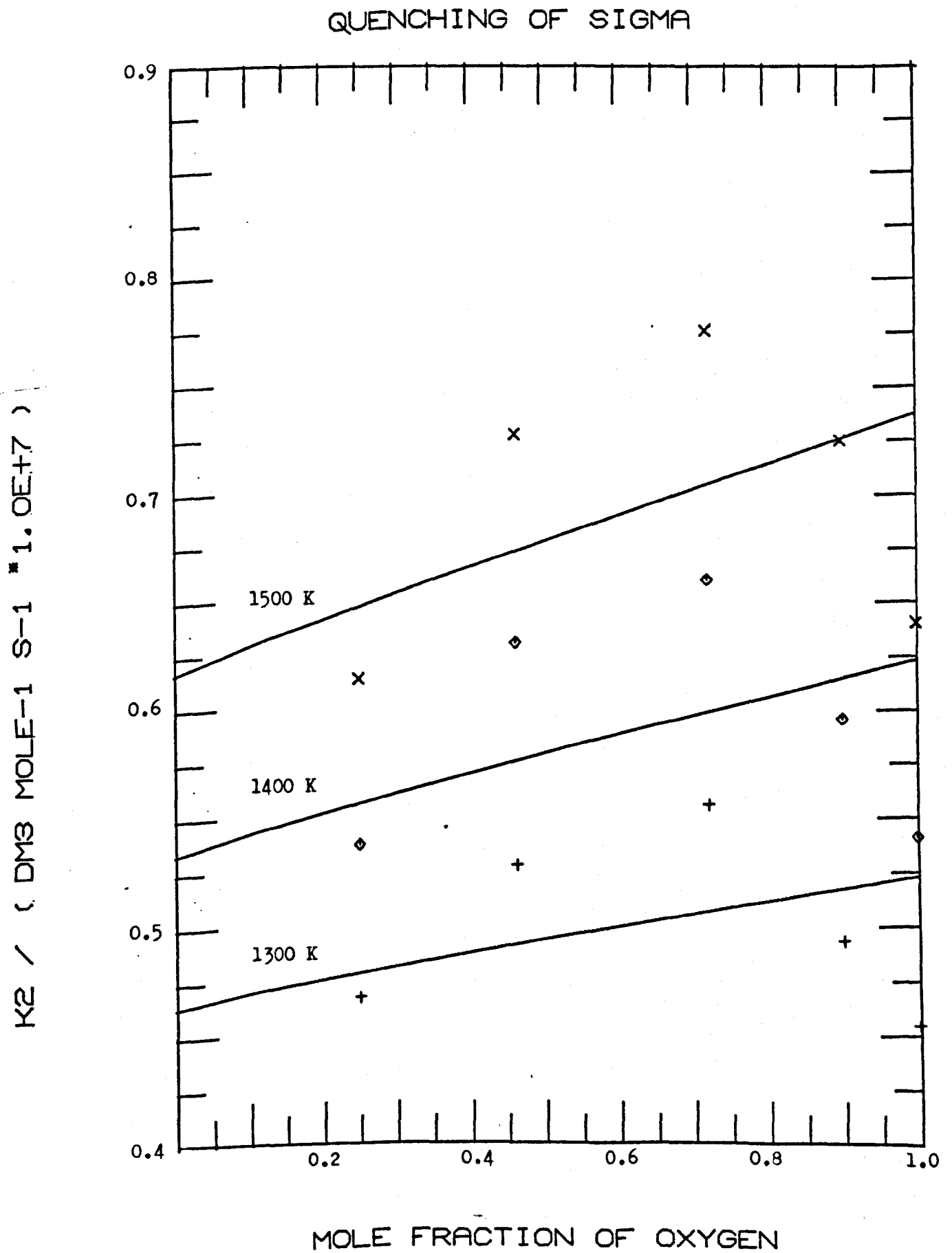
QUENCHING OF SIGMA
0.9
0.8
0.7
0.6
0.5
0.4
1500 K
1400 K
1300 K
0.2
0.4
0.6
0.8
1.0
K2 / (DM3 MOLE-1 S-1 *1.0E+7)
MOLE FRACTION OF OXYGEN

Table 8.3 are still lower than might be expected from the results on the mixtures, they have been calculated with care and are given full weight in Figures (8.13) and (8.14).

At low temperatures the lines obtained in Figure (8.13) from the data at each temperature are of reasonable precision; at temperatures above 1000 K, almost any line could be drawn through the data in Figures (8.13) and (8.14) if the variation in the gradient were not first assumed. The rate constants for deactivation of $O_2(^1\Sigma_g^+)$ by pure oxygen and pure nitrogen are shown in Figure (8.15); the curves drawn for the temperature dependence fit the data points well. It is also satisfying to see that the majority of the rate constants in Table 8.3 for the deactivation of $O_2(^1\Sigma_g^+)$ by pure oxygen are in quite good agreement with the curve in Figure (8.15). Figure (8.16) shows that, with the exception of runs M151, 844, and 910 and 910A, the results in Table 8.3 fit the pure oxygen curve in Figure (8.15) quite well; the four runs which give low results all have an exceptionally high value for the ratio, K, but the reason for this is not known.

As with the energy pooling reaction, it is encouraging to note that the curves shown in Figure (8.15) for the temperature dependence of the collisional deactivation of $O_2(^1\Sigma_g^+)$ by oxygen and nitrogen both extrapolate to the accepted room temperature rate constants. The curves also confirm that the rate constant for deactivation by nitrogen is lower than that for deactivation by oxygen at temperatures greater than 1150 K. Although the high temperature rate constants are of low precision, the precise rate constants at temperatures of 295 - 800 K clearly converge as the temperature increases, confirming that a cross-over point at 1150 K is reasonable.

As for the energy pooling reaction, the nature of the variation of the rate constants with temperature is tested by plotting log k_2

FIGURE 8.15

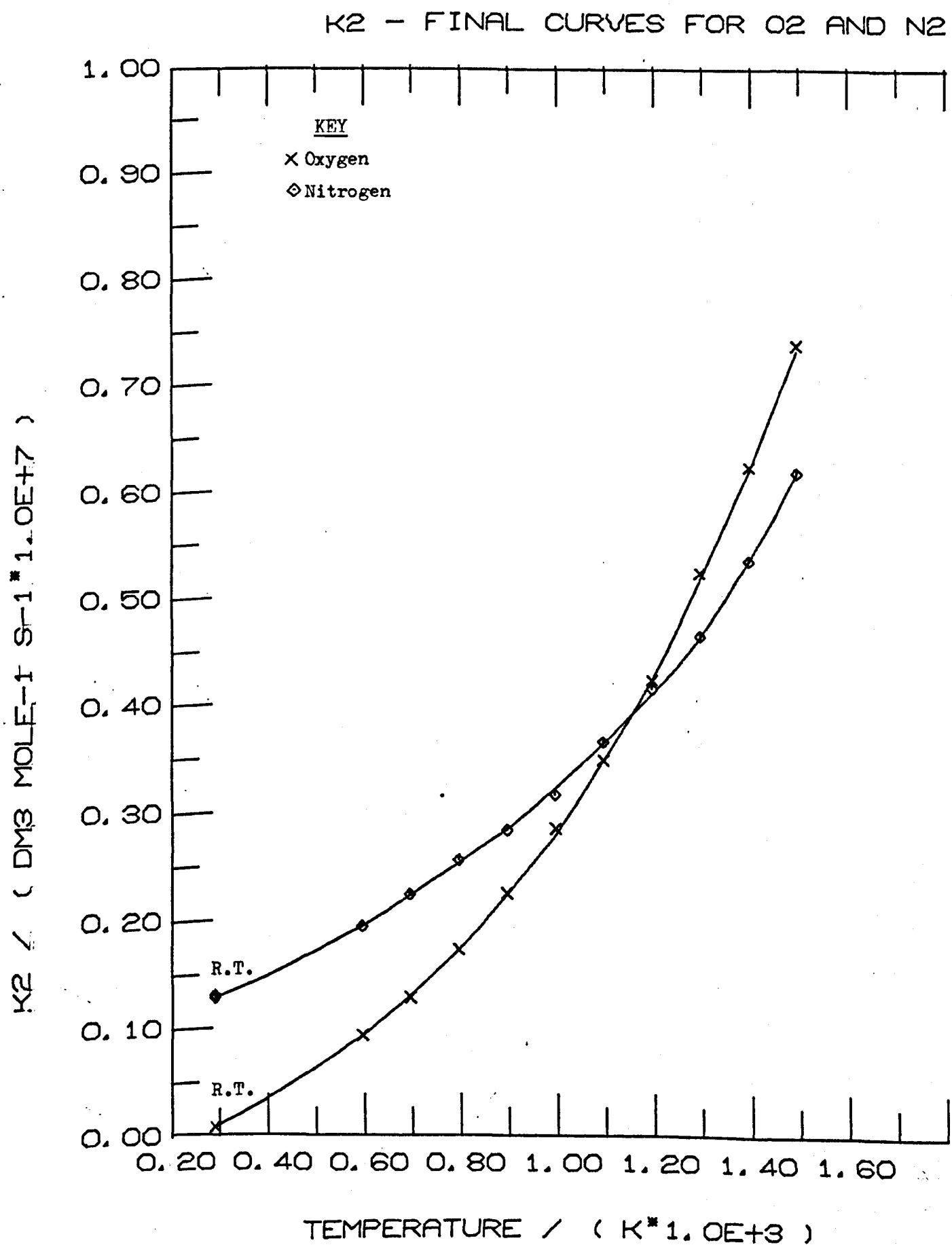
K2 - FINAL CURVES FOR O2 AND N2
KEY
× Oxygen
◇ Nitrogen
R.T.
R.T.
1.00
0.90
0.80
0.70
0.60
0.50
0.40
0.30
0.20
0.10
0.00
0.20 0.40 0.60 0.80 1.00 1.20 1.40 1.60
K2 / (DM3 MOLE-1 S-1 * 1.0E+7)
TEMPERATURE / (K * 1.0E+3)

FIGURE 8.16

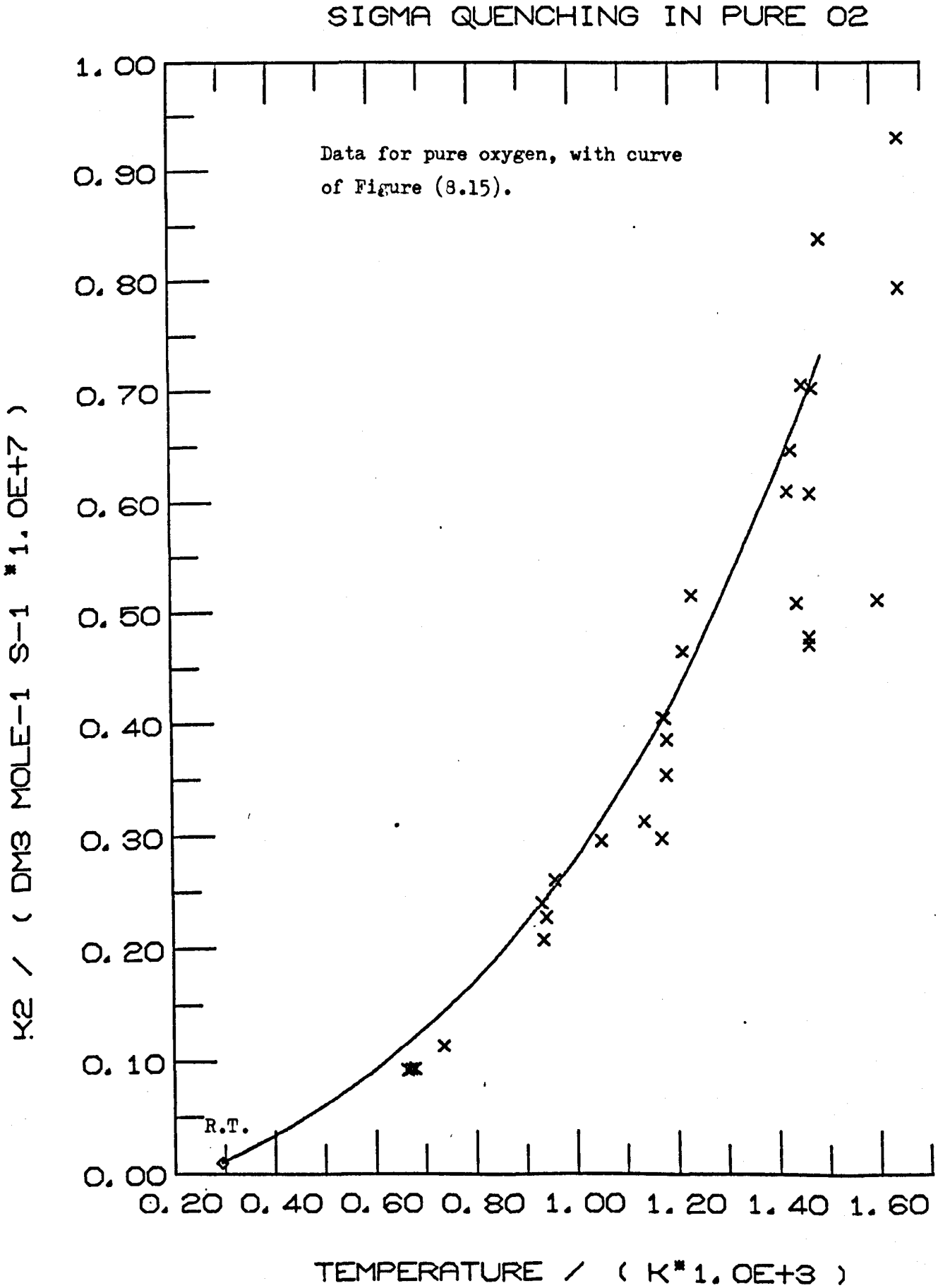
SIGMA QUENCHING IN PURE O2
Data for pure oxygen, with curve of Figure (8.15).
R.T.
K2 / (DM3 MOLE-1 S-1 *1.0E+7)
1.00
0.90
0.80
0.70
0.60
0.50
0.40
0.30
0.20
0.10
0.00
0.20 0.40 0.60 0.80 1.00 1.20 1.40 1.60
TEMPERATURE / (K*1.0E+3)

against $^1/T$, log k_2 against T, k_2 against $T^{\frac{1}{2}}$ and log k_2 against log T in Figures (8.17), (8.18), (8.19) and (8.20) for deactivation of $O_2(^1\Sigma_g^+)$ in oxygen and in nitrogen. The only plot which is reasonably linear is that of log k_2 against T for nitrogen in Figure (8.18); all the plots for oxygen show a marked curvature. The nature of the temperature dependence of these reactions is discussed further in the next section.

FIGURE 8.17

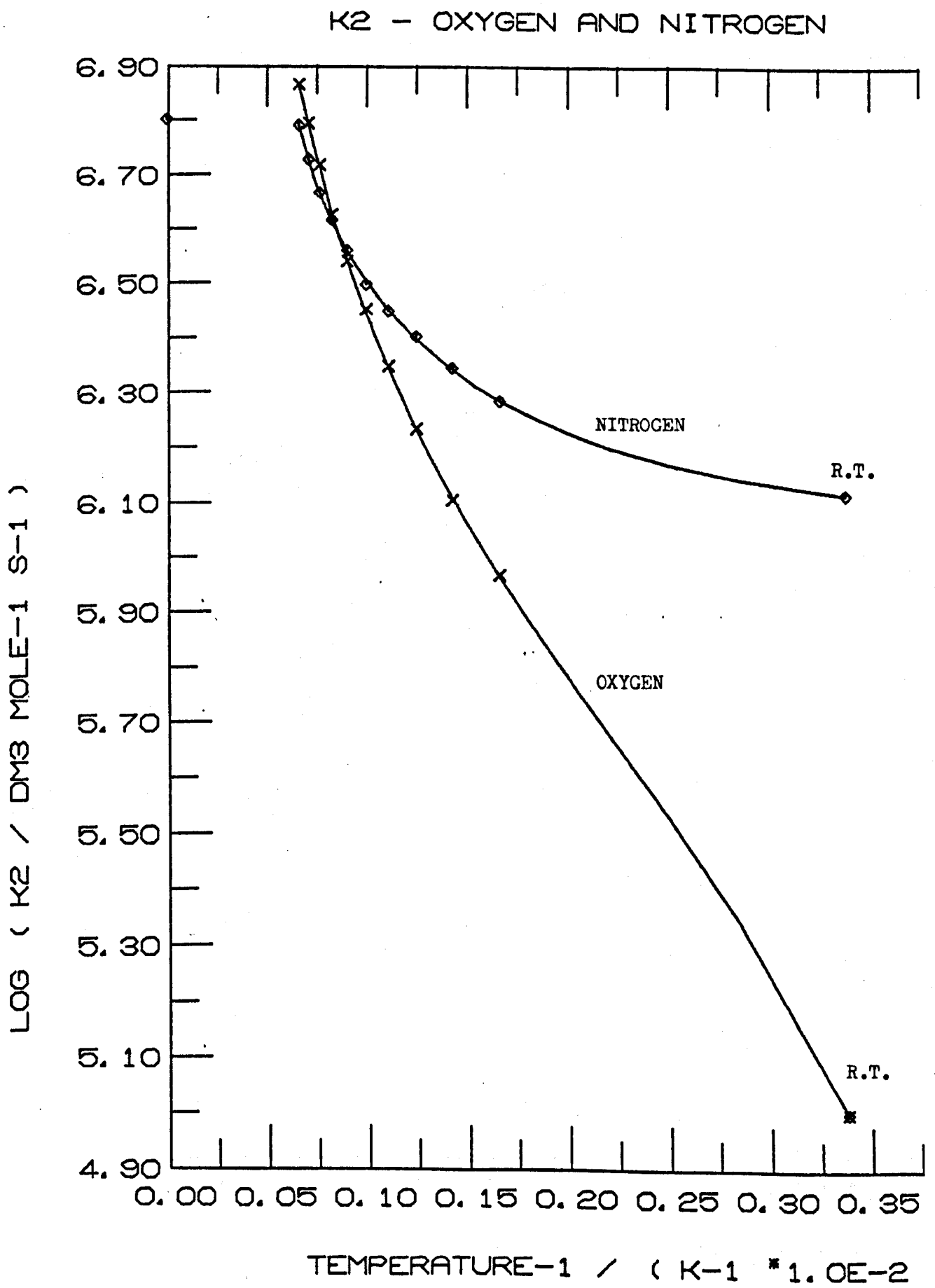
K2 - OXYGEN AND NITROGEN
6.90
6.70
6.50
6.30
6.10
5.90
5.70
5.50
5.30
5.10
4.90
LOG (K2 / DM3 MOLE-1 S-1)
NITROGEN
R.T.
OXYGEN
R.T.
0.00 0.05 0.10 0.15 0.20 0.25 0.30 0.35
TEMPERATURE-1 / (K-1 *1.0E-2

FIGURE 8.18

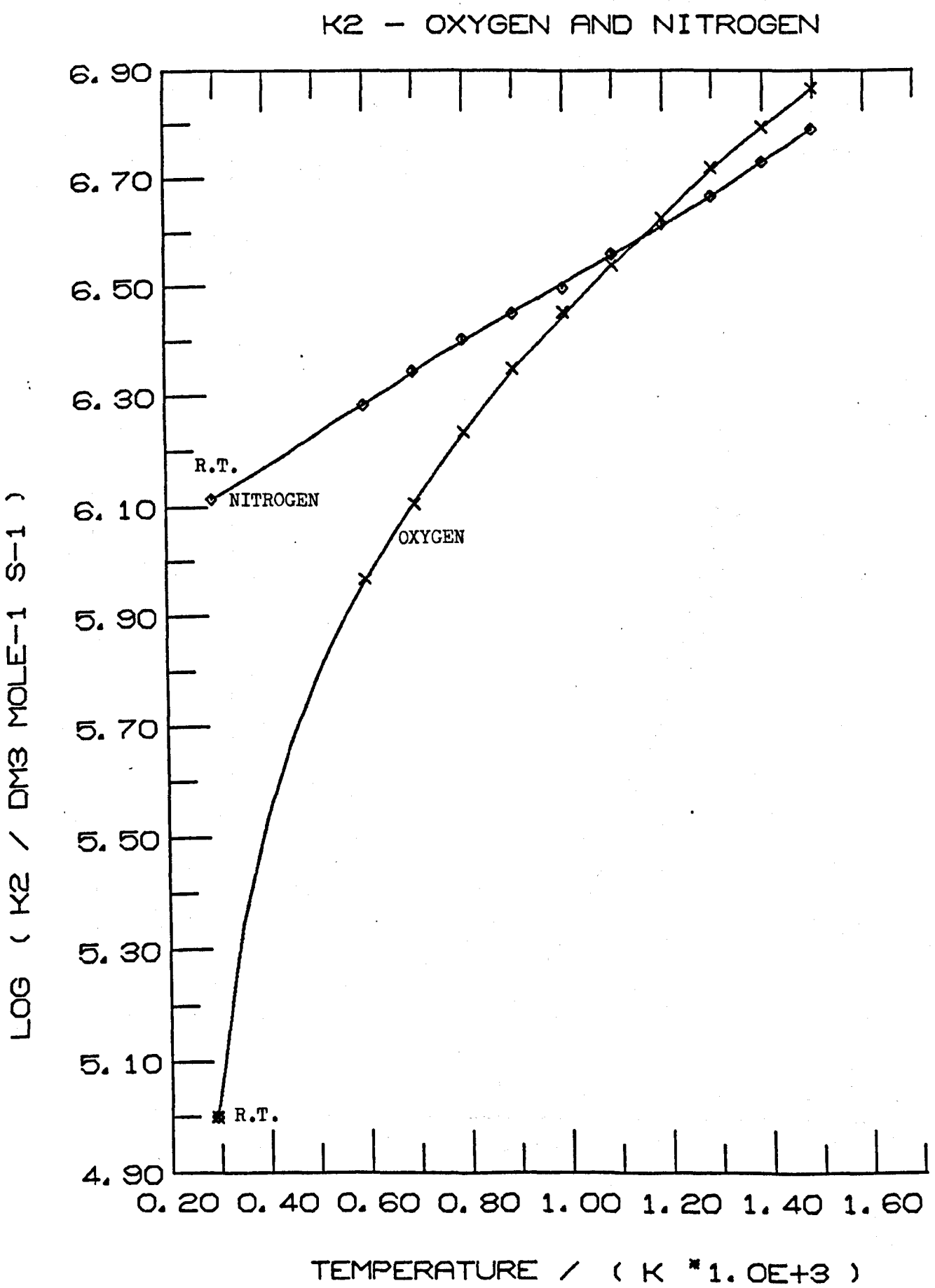
K2 - OXYGEN AND NITROGEN
6.90
6.70
6.50
6.30
6.10
5.90
5.70
5.50
5.30
5.10
4.90
R.T.
NITROGEN
OXYGEN
R.T.
LOG (K2 / DM3 MOLE-1 S-1)
0.20 0.40 0.60 0.80 1.00 1.20 1.40 1.60
TEMPERATURE / (K *1.0E+3)

FIGURE 8.19

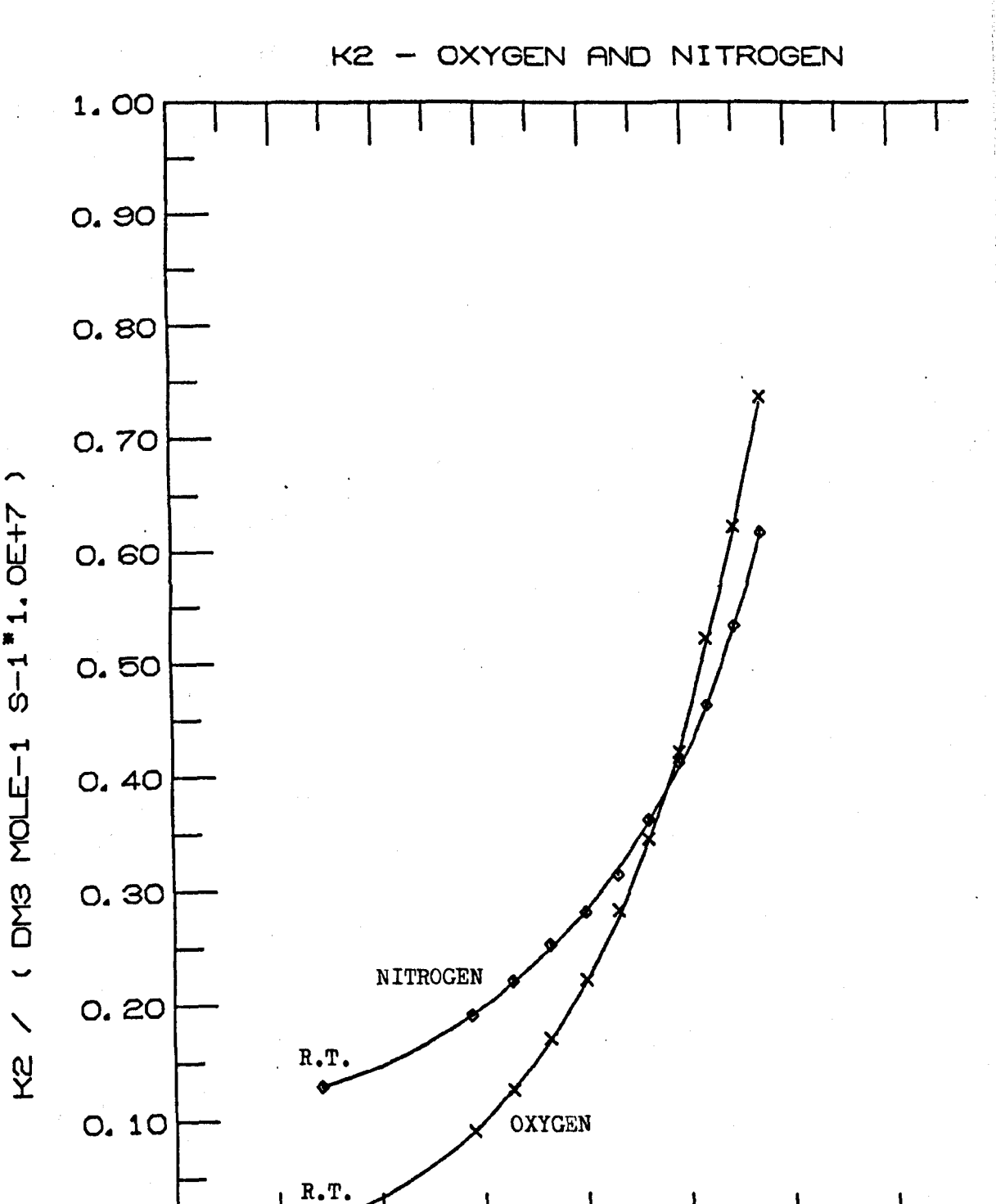
K2 - OXYGEN AND NITROGEN
1.00
0.90
0.80
0.70
0.60
0.50
0.40
0.30
0.20
0.10
0.00
K2 / (DM3 MOLE-1 S-1 * 1.0E+7)
NITROGEN
R.T.
OXYGEN
R.T.
0.10 0.15 0.20 0.25 0.30 0.35 0.40 0.45 0
(TEMPERATURE / K * 1.0E+4) **0.5

FIGURE 8.20

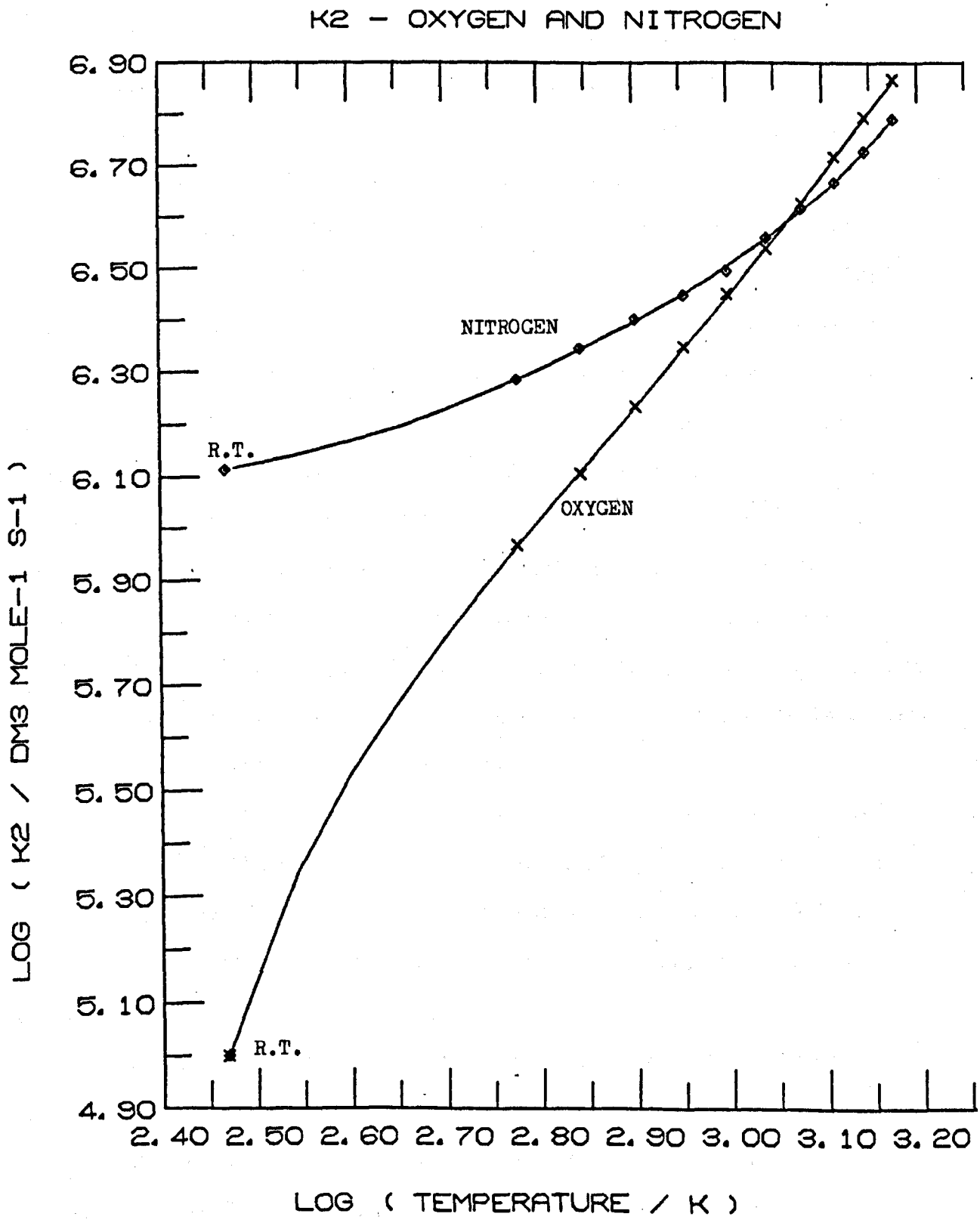
K2 - OXYGEN AND NITROGEN
6.90
6.70
6.50
6.30
6.10
5.90
5.70
5.50
5.30
5.10
4.90
NITROGEN
OXYGEN
R.T.
R.T.
2.40 2.50 2.60 2.70 2.80 2.90 3.00 3.10 3.20
LOG (K2 / DM3 MOLE-1 S-1)
LOG (TEMPERATURE / K)

8.5. The Temperature Dependence of the Reactions of Singlet Molecular Oxygen

At this stage it is worth examining the various temperature dependencies that have been obtained for the rates of reactions of singlet molecular oxygen. Apart from the measurements of the rates of the energy pooling reaction and of collisional deactivation of $O_2(^1\Sigma_g^+)$ by oxygen and nitrogen at temperatures of 600-1500 K described in this work, very little information is available.

Braithwaite, Ogryzlo, Davidson and Schiff have measured the rate constants for deactivation of $O_2(^1\Sigma_g^+)$ by hydrogen[72] and hydrogen bromide[82] at temperatures of 171-393 K; the rate constants were found to increase slowly with temperature, and the Arrhenius plots obtained were curved, as has been observed for quenching by oxygen and nitrogen in the previous section. Recently, Kohse-Höinghaus and Stuhl have studied the collisional deactivation of $O_2(^1\Sigma_g^+)$ by hydrogen and deuterium[149], and by nitrogen[150] over the temperature range 200-350 K; their results for hydrogen are not greatly different from those obtained by Braithwaite et al., but the Arrhenius plot for quenching by both hydrogen and deuterium is reasonably linear. The results for quenching by nitrogen are incomplete but show the temperature dependence to be small.

The only other measurements that have been made are those by Findlay and Snelling[66] on the collisional deactivation of $O_2(^1\Delta_g)$ over the narrow temperature range of 285-324 K, which were discussed in section 8.1, and the measurements of the dimol emission by Arnold et al., discussed in section 8.2.

The high temperature measurements made in this work can be extrapolated to temperatures between 295 and 600 K (Figure (8.15)); the extrapolated rate constants at 400 K are compared with those obtained by other workers in Table 8.4, which gives the ratio of the rate constants at

TABLE 8.4

Temperature dependence of the reactions of singlet molecular oxygen

STATE	QUENCHER	$k_2(T_2)/k_2(298\ K)$			REFERENCE
		400 K	1000 K	1500 K	
$O_2(^1\Sigma_g^+)$	O_2	3.5	25	74	This work
	N_2	1.14	2.46	4.75	This work
	H_2	1.59	-	-	(72)
		1.60	-	-	(149)
	D_2	2.01	-	-	(149)
	HBr	1.09	-	-	(82)
$O_2(^1\Delta_g)$	O_2	-	<50	<50	This work
		(1.25)	(2.56)	(3.51)	(150)
ENERGY POOLING		1.88	16	67	This work
DIMOL EMISSION		1.16	1.83	2.25	This work
COLLISION FREQUENCY		1.16	1.83	2.25	

400 K, 1000 K and 1500 K to the room temperature rate constants.

The results show the ratio $k_2(T_2)/k_2(298)$ to increase far more rapidly for the collisional deactivation of $O_2(^1\Sigma_g^+)$ by oxygen and for the energy pooling reaction than for the collisional deactivation of $O_2(^1\Sigma_g^+)$ by nitrogen and the other reactions in Table 8.4, with the possible exception of quenching of $O_2(^1\Sigma_g^+)$ by hydrogen and deuterium. The similarity of the temperature dependence of the rates of the energy pooling reaction and the collisional deactivation of $O_2(^1\Sigma_g^+)$ by oxygen may be indicative of a common mechanism, but it should be remembered that the rate constants obtained for deactivation of $O_2(^1\Sigma_g^+)$ by "pure oxygen" in Figures (8.13-8.15), are in fact the rate constants in oxygen containing perhaps as much as 30 ppm water (Chapter 3). This would have the effect of increasing the room temperature rate by a factor of four, but it is unlikely that the effect will be the same at high temperatures; if the rate of deactivation by water increases at the same rate as that of most of the reactions in Table 8.4, the presence of 30 ppm would increase the rate constant by only about 5% at 1500 K, and the true ratio $k_2(1500)/k_2(298)$ would then be $\sim$ 250-300, which is considerably greater than that observed for the energy pooling reaction.

The rates of the other reactions in Table 8.4 are seen to increase at a rate little different from the collision frequency. In cases where reactions are collision controlled, the temperature dependence of the pre-exponential factor, z in equation (1.1)

$$k = z\, e^{-E_{act}/RT} \tag{1.1}$$

should be taken into account. As z is proportional to the collision frequency, equation (1.1) may be rewritten

$$k = C\, T^{\frac{1}{2}}\, e^{-E_{act}/RT} \tag{8.21}$$

and a plot of $(k/T^{\frac{1}{2}})$ against $^1/T$ will be linear for simple reactions.

Figures (8.21)-(8.22) show that this is not the case for the energy pooling reaction or for the collisional deactivation of $O_2(^1\Sigma^+)$ by oxygen and nitrogen; it should be noted that for collisional deactivation by nitrogen the ratio $k_2/T_2^{\frac{1}{2}}$ shows little temperature dependence at temperatures below 500 K.

The only other model for chemical reactions which gives rise to a simple temperature dependence is the Landau-Teller model of vibrational energy transfer[115]. This model assumes that energy transfer takes place on the repulsive part of the potential energy curve only, and predicts the rate of vibrational relaxation to vary with temperature as

$$k = c\, e^{-AT^{-1/3}} \tag{8.22}$$

Sophisticated quantum-mechanical treatments of vibrational relaxation lead to much the same result, and it has been confirmed experimentally that in the vast majority of cases the log of the vibrational relaxation time varies linearly with $T^{-1/3}$ [109]. Plots of $\log k_1$ against $T^{-1/3}$ for the energy pooling reaction and of $\log k_2$ against $T^{-1/3}$ for the quenching of $O_2(^1\Sigma_g^+)$ by oxygen and nitrogen are shown in Figures (8.23) and (8.24). The curves for the energy pooling reaction and the quenching of $O_2(^1\Sigma_g^+)$ by nitrogen are not linear, but the results obtained for quenching of $O_2(^1\Sigma_g^+)$ give a reasonable fit to the relation

$$k_2 = 2.327 \times 10^9\, e^{-67.17T^{-1/3}}\ \mathrm{dm^3\ mole^{-1}\ s^{-1}} \tag{8.23}$$

The linear relation for one plot only may well be fortuitous; it is reasonable that electronic and vibrational relaxation should take place by similar processes, but a satisfactory treatment that covers all the electronic energy transfer reactions of singlet molecular oxygen will not be obtained other than by sophisticated calculations. The models for electronic energy transfer processes that are discussed in the next section suggest that the temperature dependence of such reactions is

FIGURE 8.21

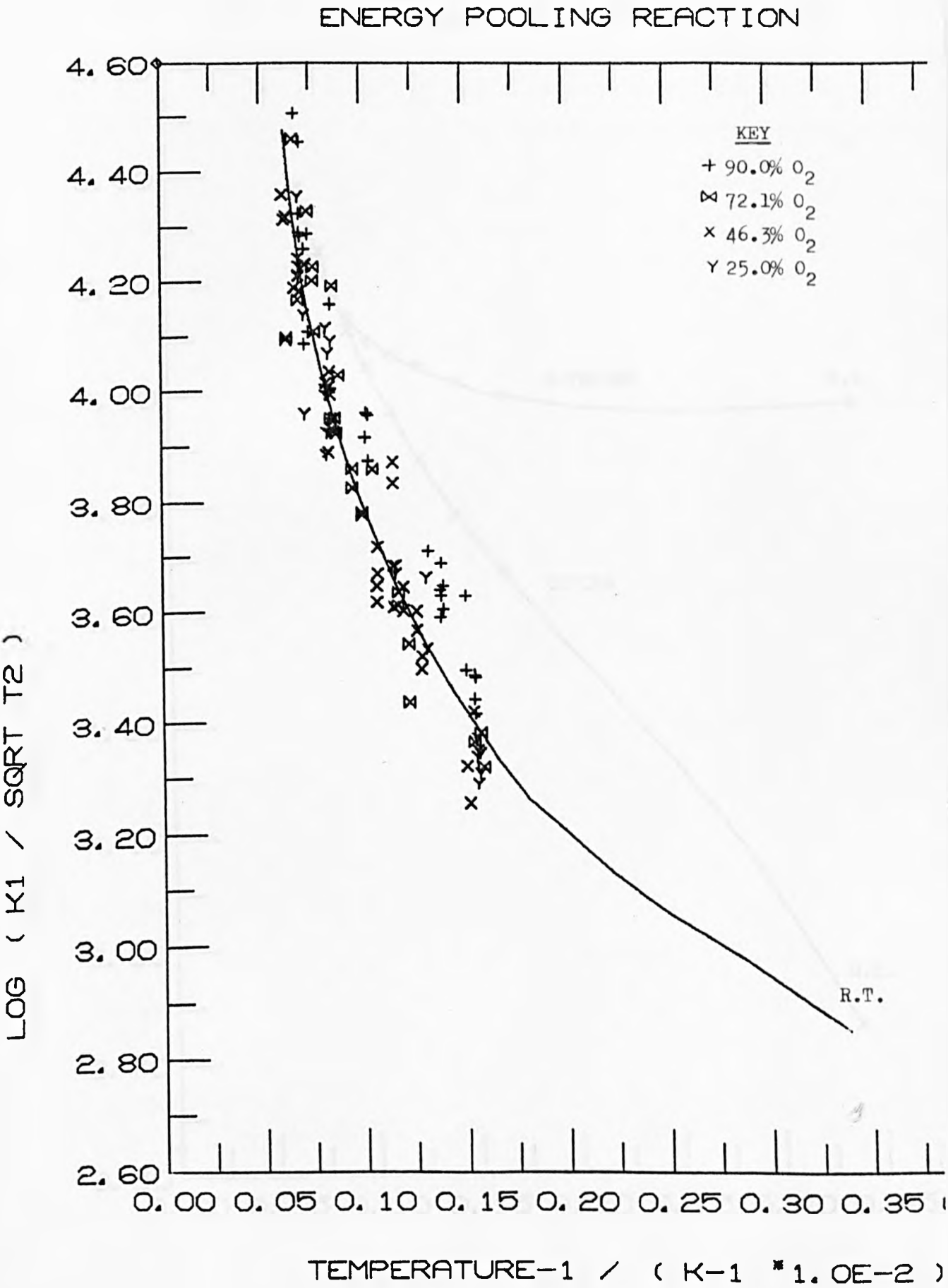
ENERGY POOLING REACTION
KEY
+ 90.0% O_2
⋈ 72.1% O_2
× 46.3% O_2
Y 25.0% O_2
R.T.
LOG (K1 / SQRT T2)
4.60
4.40
4.20
4.00
3.80
3.60
3.40
3.20
3.00
2.80
2.60
0.00 0.05 0.10 0.15 0.20 0.25 0.30 0.35
TEMPERATURE-1 / (K-1 * 1.0E-2)

FIGURE 8.22

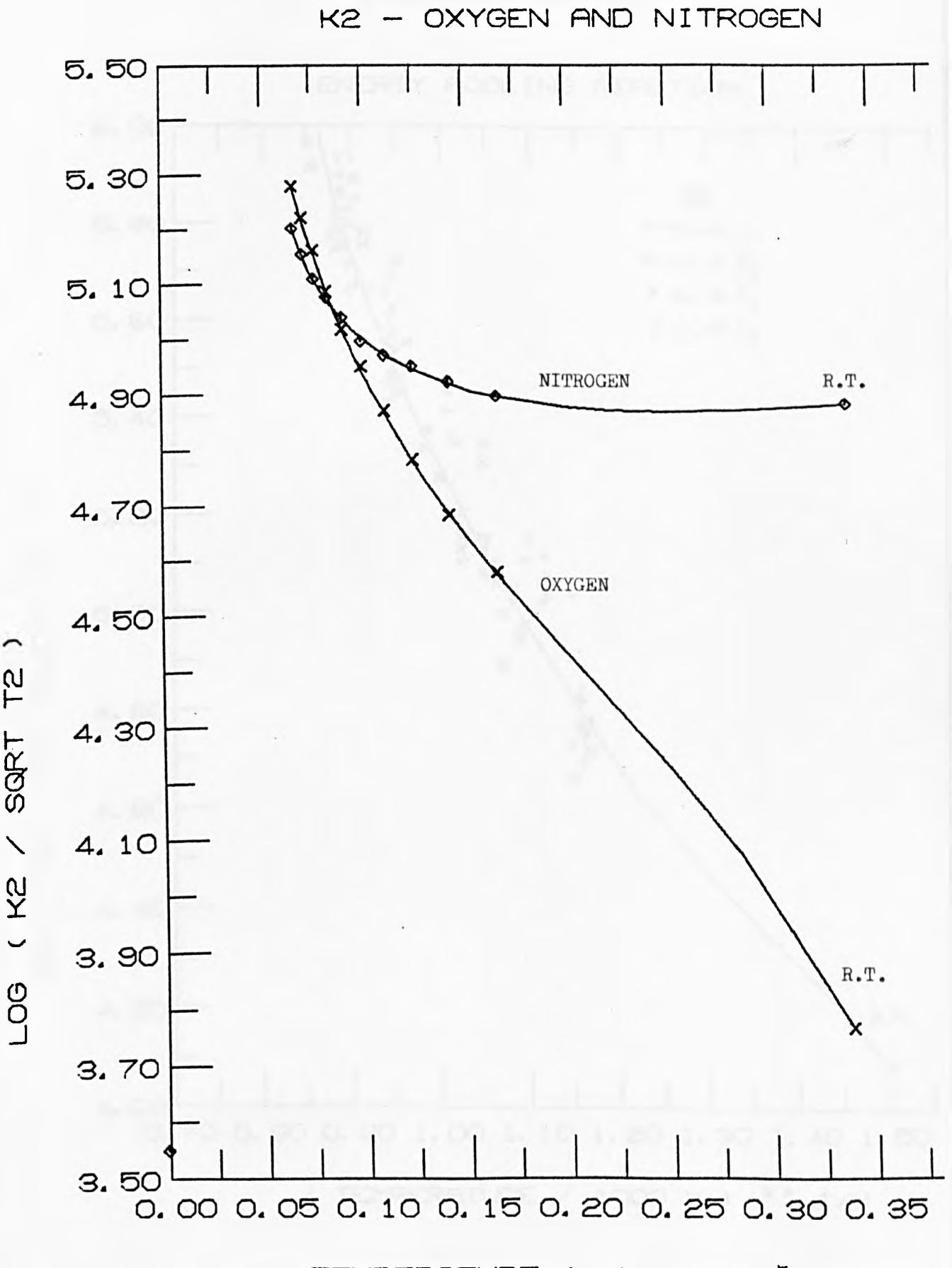
K2 - OXYGEN AND NITROGEN
5.50
5.30
5.10
4.90
4.70
4.50
4.30
4.10
3.90
3.70
3.50
NITROGEN
R.T.
OXYGEN
R.T.
LOG (K2 / SQRT T2)
0.00 0.05 0.10 0.15 0.20 0.25 0.30 0.35
TEMPERATURE-1 / (K-1 *1.0E-2)

FIGURE 8.23

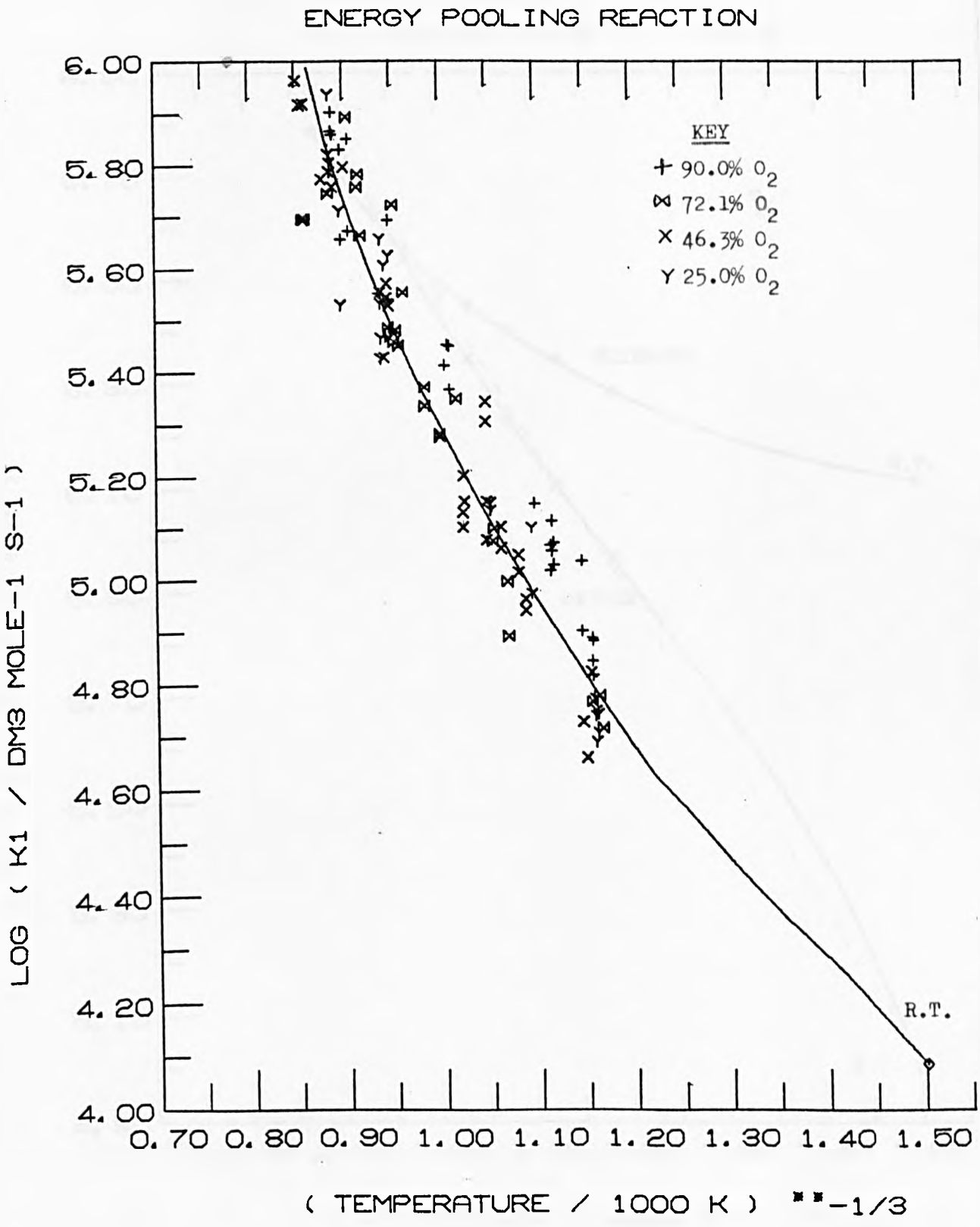
ENERGY POOLING REACTION
KEY
+ 90.0% O2
⋈ 72.1% O2
× 46.3% O2
Y 25.0% O2
R.T.
6.00
5.80
5.60
5.40
5.20
5.00
4.80
4.60
4.40
4.20
4.00
0.70 0.80 0.90 1.00 1.10 1.20 1.30 1.40 1.50
LOG (K1 / DM3 MOLE-1 S-1)
(TEMPERATURE / 1000 K) **-1/3

FIGURE 8.24

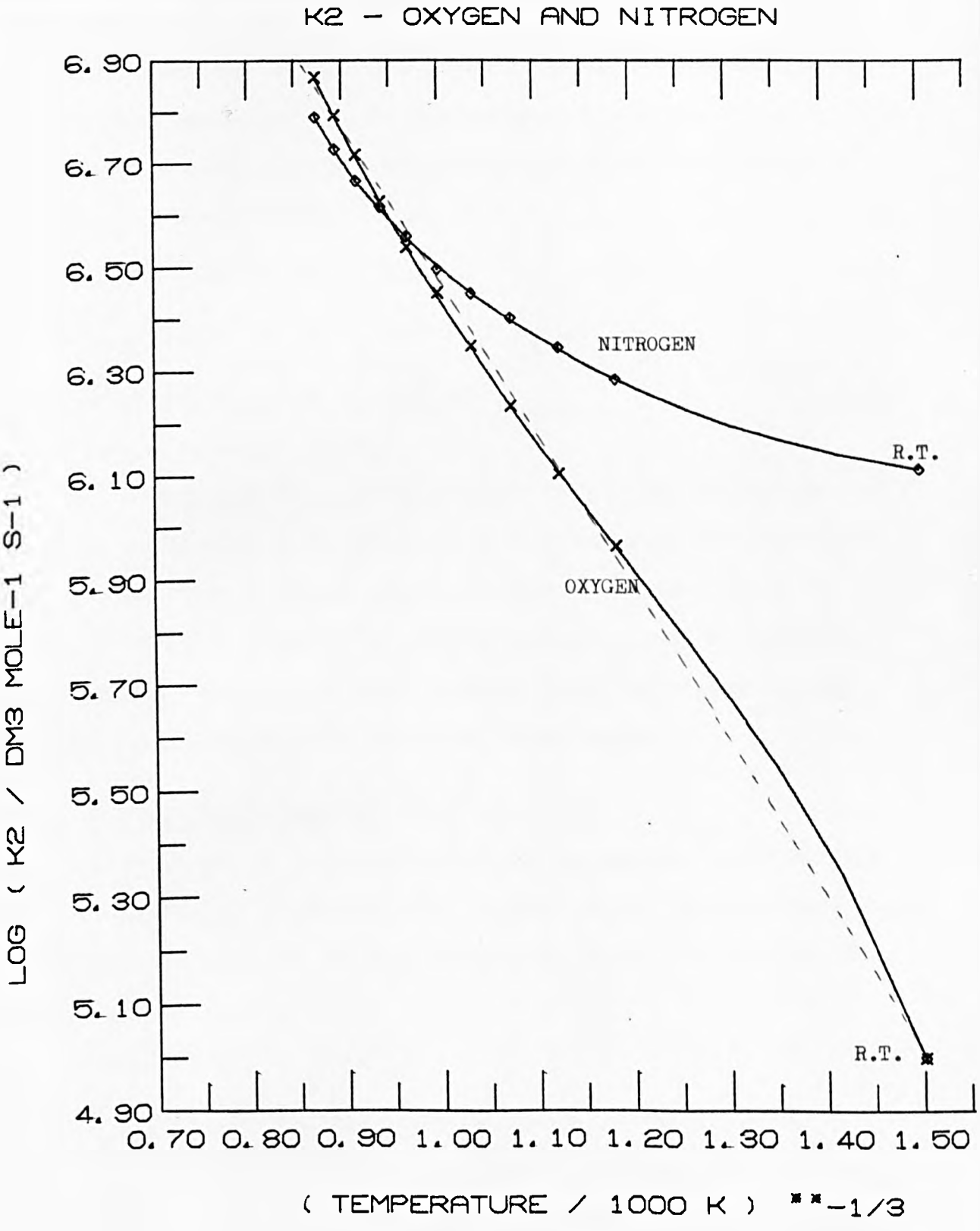
K2 - OXYGEN AND NITROGEN
6.90
6.70
6.50
6.30
6.10
5.90
5.70
5.50
5.30
5.10
4.90
LOG (K2 / DM3 MOLE-1 S-1)
NITROGEN
R.T.
OXYGEN
R.T.
0.70 0.80 0.90 1.00 1.10 1.20 1.30 1.40 1.50
(TEMPERATURE / 1000 K) **-1/3

unlikely to fit any simple relation, and the similarity between the temperature dependence of the rate constants for quenching of $O_2(^1\Sigma_g^+)$ by oxygen and for the energy pooling reaction is probably more significant than the apparent linearity in Figure (8.24).

8.6. Electronic Energy Transfer Mechanisms

In reactions in which electronically excited states are collisionally deactivated, the electronic energy of the excited state must be distributed amongst the product molecules in the form of translational, rotational and vibrational energy. Much interest has been shown in such processes in recent years, and many workers have studied the reactions of excited atoms with quenching molecules[151]; the only reported experiments on the deactivation of electronically excited small molecules have been the reactions of carbon monoxide[152]

$$CO^*(d^3\Delta)(v=7) + CO \rightarrow 2CO^\dagger(v) \qquad (8.24)$$

$$CO^*(d^3\Delta)(v=7) + N_2 \rightarrow CO^\dagger(v) + N_2{}^\dagger(v) \qquad (8.25)$$

$$CO^*(a^3\pi)(v=o) + CO \rightarrow 2CO^\dagger(v) \qquad (8.26)$$

and of singlet molecular oxygen.

As is indicated in equations (8.24) - (8.26), much of the electronic energy is transferred to vibrational energy of the products, and this has been the main focus of energy transfer studies. A recent review by Lemont and Flynn[151] suggests that the two important forms of electronic-to-vibrational energy transfer are resonant energy transfer and energy transfer through a relatively stable collision complex.

8.6.1. Resonant Energy Transfer

In many studies of quenching reactions it has been noted that the rate of deactivation is greatest when the vibrational energy of the quencher is closely matched to the electronic energy of the excited species. Thus in the quenching reaction

$$Hg(6^3P_1) + M \rightarrow Hg(6^3P_o) \qquad (8.27)$$

the energy of the mercury transition is 1770 cm^{-1}. The quenching efficiencies of the three diatomic molecules N_2, CO and NO in reaction (8.27) are in the order NO > CO > N_2; the vibrational energies of their

fundamentals are respectively 1904, 2170 and 2360 cm^{-1}, in agreement with the suggestion that resonant energy transfer is the principal process by which deactivation takes place.

A correlation between the efficiency of quenching of $O_2(^1\Sigma_g^+)$ and the vibrational energies of the fundamental frequencies of the many quenchers that have been studied, was noted some years ago[61] (Table 1.1), and two models have been proposed for collisonal deactivation, in which resonant energy transfer is assumed to be the important process in the quenching reaction: Kear and Abrahamson[68] suggest that energy transfer takes place under the influence of short range interactions on the repulsive part of the intermolecular potential (as for vibrational energy transfer), while Braithwaite, Ogryzlo, Davidson and Schiff[81] consider that resonant energy transfer takes place principally as a result of the long range interactions of the transition quadrupoles of $O_2(^1\Sigma_g^+)$ and the quencher. Both these models underestimate the room temperature rate constants for collisional deactivation, but the relative order of the rate constants for different quenchers is predicted correctly; Ogryzlo et al. have shown[72,82] that the room temperature rate constants are predicted quite well if the calculated effects of short and long range interactions are combined.

The predicted temperature dependence of the rate of collisional deactivation of $O_2(^1\Sigma_g^+)$ is much the same for both models except when the energy transfer process is very near to resonance; the rate constants predicted by the combined models for quenching by HBr[82] (for which the process should be near to resonance) and by H_2[72] (for which it is not) are in quite good agreement with the experimental measurements over the temperature range 171-393 K.

Although at first sight this appears to be a satisfactory model for the quenching of $O_2(^1\Sigma_g^+)$, recent measurements by Thomas and Thrush[90,91]

(Chapter 1) suggest that resonant energy transfer is not important. By following the chemiluminescence from the products of quenching of both $O_2(^1\Sigma_g^+)$ and $O_2(^1\Delta_g)$ they show that although the electronic energy goes principally into vibration of the product molecules, a much broader distribution of vibrational energies than would be expected for resonant energy transfer, is observed. A further failure of the models of Kear and Abrahamson and of Braithwaite, Ogryzlo, Davidson and Schiff is the predicted room temperature rate constant for collisional deactivation of $O_2(^1\Sigma_g^+)$ by oxygen itself; the combined models give a value of 44 dm^3 $mole^{-1}$ s^{-1}, a factor of about twenty below the true rate constant.

Thus it appears that despite the reasonably good predictions of the rate constants for some reactions of $O_2(^1\Sigma_g^+)$, resonant energy transfer is not important in these reactions. The broad, almost statistical distribution of energy amongst the products suggests that the formation of a collision complex of reasonably long lifetime may be the important process.

8.6.2. Energy Transfer through a Collision Complex

A small number of electronic-to-vibrational energy transfer reactions have been shown to take place via a relatively stable collision complex. Thus in reactions (8.28) and (8.29)

$$^{18}O^*(2^1D_2) + {}^{16}O_2 \begin{cases} \nearrow {}^{18}O(2^3P_J) + {}^{16}O_2{}^\dagger \\ \searrow {}^{16}O(2^3P_J) + {}^{16}O{}^{18}O^\dagger \end{cases} \qquad (8.28)$$

$$^{16}O^*(2^1D_2) + C^{18}O \begin{cases} \nearrow 50\%\ C^{16}O^\dagger(v) + {}^{18}O(2^3P_J) \\ \searrow 50\%\ C^{18}O^\dagger(v) + {}^{16}O(2^3P_J) \end{cases} \qquad (8.29)$$

isotope exchange experiments[153,154] show conclusively that a reasonably long-lived collision complex is formed. The intermediates postulated in

these examples are O_3^* and CO_2^*, species for which the existence of the ground states is well established. A further reaction that has attracted several theoretical studies is[155,156,157]

$$O^*(2^1D_2) + N_2 \rightarrow (N_2O^*) \rightarrow O(2^3P_J) + N_2^{\dagger} \qquad (8.30)$$

and again the postulated intermediate is a known species.

The theoretical analyses of reaction (8.30) assume a stable collision complex of lifetime 10^{-11} - 10^{-12}s to be formed and that collisional deactivation results from a crossing of potential energy curves as is shown in Figure (8.25). Figure (8.25) takes no account of the possible relative orientations of the quencher and the excited species, or of the vibrational levels of the complex; a full analysis is possible only if specific information on the nature of the collision complex is available (as is the case for reactions (8.28) - (8.30)). For reaction (8.30), Tully[156] predicts the rate constant to vary with temperature as:

$$k = \left(\frac{8}{\pi\mu}\right)^{\frac{1}{2}} (k_BT)^{3/2} \int_0^{\infty} E\, e^{(-E/k_BT)} \sigma(E)\, d\, E \qquad (8.31)$$

where μ is the reduced mass of the collision complex, k_B is Boltzmann's Constant, E is the initial collision energy and $\sigma(E)$ is the cross-section for quenching at an initial collision energy E.

The parameter $\sigma(E)$ in equation (8.31) is obtained by calculation of the probability of decay of the collision complex to give the reaction products and of the cross-sections for complex formation; Tully's results show that, depending on the variation of $\sigma(E)$ with E, the rate of the reaction may increase or decrease with temperature. The room temperature rate constant for reaction (8.30), obtained from equation (8.31), is in excellent agreement with the experimental data. Zahr, Preston and Miller[157] have criticised Tully's model for determining the cross section for complex formation; using a more realistic model they obtain a similar rate constant

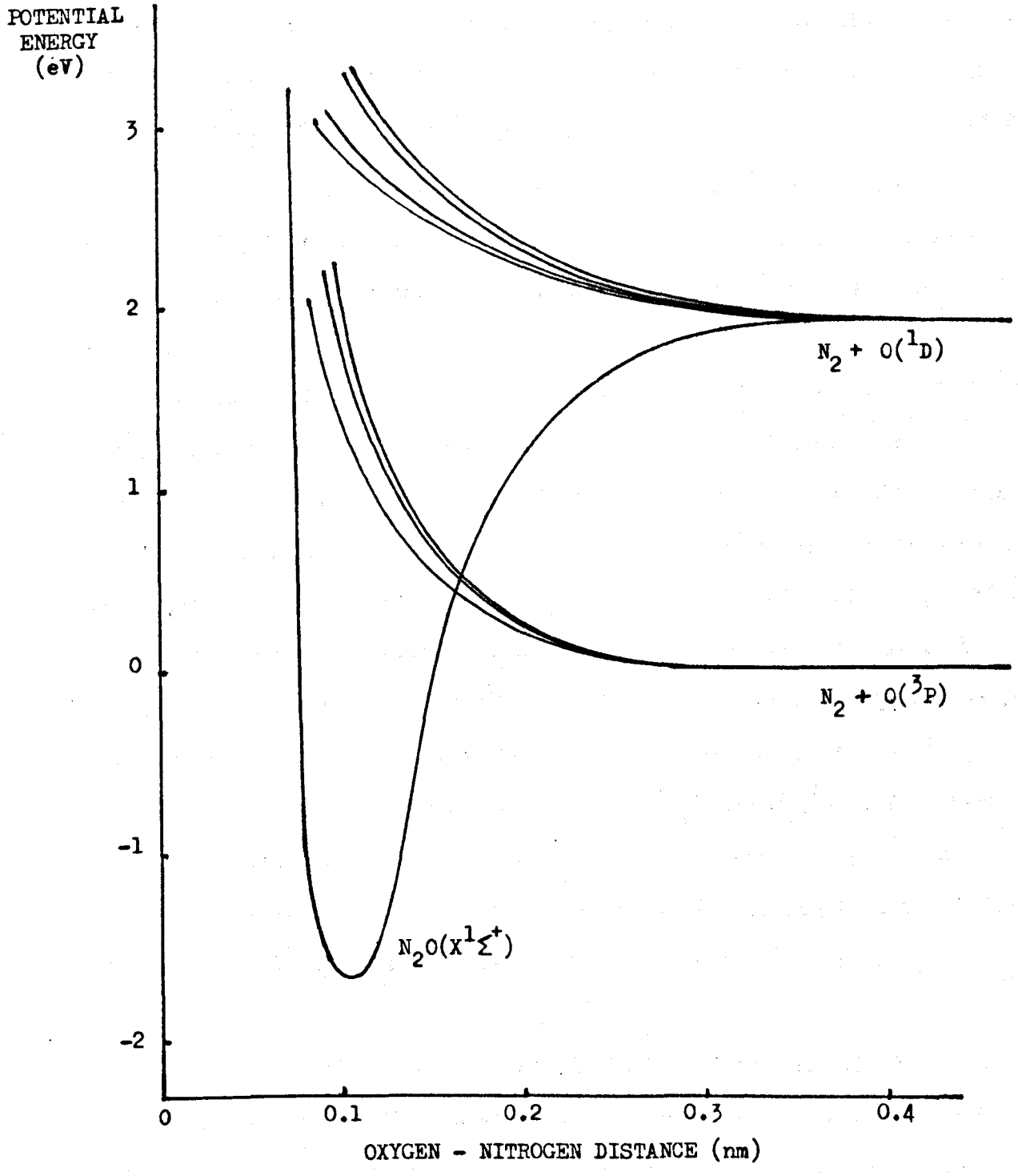

FIGURE 8.25 Schematic Diagram of Ground and Excited Potential Energy Surfaces of N_2O as a Function of O_2-N_2 Separation (after Tully[156]). Curves Are Very Uncertain.

at room temperature and predict that the reaction is less rapid at high temperatures.

Although this model has been shown to explain the observed quenching for a few simple reactions only, it has been postulated on many other occasions. For instance, in the example of the previous section

$$Hg(6^3P_1) + M \rightarrow Hg(6^3P_o) + M^{\dagger} \qquad (8.27)$$

an alternative interpretation of the relative rates of quenching, $NO > CO > N_2$, is that the ease of formation of the collision complex is in this order (which is reasonable as N_2 is considerably less "reactive" than CO).

A quantitative application of this model to the reactions of $O_2(^1\Sigma_g^+)$ and $O_2(^1\Delta_g)$ is not practical as we have no information on the nature of the collision complex. In the analysis of the results on the dimol emission, it was concluded that any collision complex would have a short lifetime ($\sim 10^{-13}$s), but it is probable that a slightly longer lifetime would have little effect on the results. The surprisal plot obtained for reaction (8.29) between $O(2^1D_2)$ and CO, both experimentally and by the theoretical treatment of Tully, has a gradient very close to zero[154]; this is not the case in the quenching of $O_2(^1\Sigma_g^+)$ and $O_2(^1\Delta_g)$, for which there is a definite tendency for the electronic energy to appear as vibrational energy in the products[91], possibly indicating that the lifetime of the collision complex is shorter than in the reactions of $O(^1D)$.

A study of the rate constants in Table 1.1 reveals little information on the conditions which might favour formation of the collision complex. Those quenchers for which hydrogen bonding could contribute to the complex stability (H_2O, NH_3), deactivate $O_2(^1\Sigma_g^+)$ more rapidly than most others; ethylene and ethane react at a similar rate despite the high π electron density, which would be expected to favour

complex formation, in the former. The observed order of the room temperature quenching rates, $O_2 < N_2 \approx CO < HCl < HBr \approx C_2H_6 \approx C_2H_4$, is not easily explained. The reactions of H_2, H_2O and HCl are more rapid than those of the deuterium isomers, and this could be a result of kinetic isotope effects.

The reactions in which the postulated collision complex is of the form $(O_2)_2$

$$O_2(^1\Sigma_g^+) + O_2(^3\Sigma_g^-) \rightarrow O_2(^1\Delta_g) + O_2(^3\Sigma_g^-) \qquad (8.18)$$

$$O_2(^1\Delta_g) + O_2(^3\Sigma_g^-) \rightarrow O_2(^3\Sigma_g^-) + O_2(^3\Sigma_g^-) \qquad (8.1)$$

$$O_2(^1\Delta_g) + O_2(^1\Delta_g) \rightarrow O_2(^1\Sigma_g^+) + (^3\Sigma_g^-) \qquad (1.13)$$

have unexpectedly high rate constants at room temperature, and the rates of reactions (8.18) and (1.13) have been shown to increase more rapidly with temperature than is the case for most reactions of singlet molecular oxygen. Although our studies of the dimol emission suggest that the collision complex is short-lived and cannot really be described as an O_4 molecule, it may be that a collision complex of this form is more stable than most. Certainly, the stability of the O_4 molecule is low because the reactions are still very slow, but it may be sufficient to favour quenching by oxygen, particularly at high temperatures.

It is clear that more information is required before any conclusions as to the mechanisms of the energy transfer reactions of singlet molecular oxygen may be made. It may be possible to test the applicability of the collision complex model by isotope exchange experiments of the form

$$O_2(^1\Sigma_g^+) + C^{18}O \begin{cases} \rightarrow O_2(^1\Delta_g) + C^{18}O^\dagger \\ \overset{?}{\rightarrow} {}^{18}O^{16}O(^1\Delta_g) + CO^\dagger \end{cases} \qquad (8.32)$$

using carbon monoxide or the oxides of nitrogen. Complete isotope exchange is unlikely, but the detection of partial exchange would provide strong support for the collision complex model. At the moment, it can only be said that the expectations of the collision complex model are not inconsistent with the available experimental evidence, and that the temperature dependence of the rate constants obtained from such a model would not be expected to fit any of the simple equations tested in Figures (8.7 - 8.10), (8.17 - 8.20) and (8.21 - 8.24), other than by coincidence. The results obtained by Thomas and Thrush suggest that the quenching reactions of $O_2(^1\Sigma_g^+)$ and $O_2(^1\Delta_g)$ have a common mechanism. A possible reaction pathway that proceeds via the formation of a collision complex is

$$O_2(^1\Sigma_g^+) + M \underset{k_{-1}}{\overset{k_1}{\rightleftharpoons}} [O_2(^1\Sigma_g^+)\text{-}M] \underset{k_{-2}}{\overset{k_2}{\rightleftharpoons}} [O_2(^1\Delta_g)\text{-}M] \underset{k_{-3}}{\overset{k_3}{\rightleftharpoons}} O_2(^1\Delta_g) + M$$

$$k_{-4} \uparrow\downarrow k_4$$

$$O_2(^3\Sigma_g^-) + M \underset{k_{-5}}{\overset{k_5}{\rightleftharpoons}} [O_2(^3\Sigma_g^-)\text{-}M] \qquad (8.33)$$

where $k_{-3} \gg k_4$, k_3, and, as a result, $O_2(^1\Sigma_g^+)$ is quenched almost entirely to $O_2(^1\Delta_g)$, and the quenching of $O_2(^1\Delta_g)$ will be slow. The collision enhanced transition

$$1270\text{ nm: } O_2(^1\Delta_g)(v=o) + O_2(^3\Sigma_g^-)(v=o) \leftarrow O_2(^3\Sigma_g^-)(v=o) + O_2(^3\Sigma_g^-)(v=o) \qquad (1.5)$$

observed in the absorption spectrum of pure oxygen at 1270 nm[16] may be experimental support for the existence of relatively stable collision complexes of the form O_2-M.

It is not easy to fit the energy pooling and dimol reactions into this scheme together; the energy pooling reaction shows a temperature dependence similar to that of quenching of $O_2(^1\Sigma_g^+)$ by oxygen, while the dimol emission shows a smaller $T^{\frac{1}{2}}$ temperature dependence, most easily explained by assuming the reaction to be a simple collisional process.

The lifetime of the O_4 molecule postulated in the reaction scheme is less than 10^{-11}s, but we do not have enough information to say whether it is sufficiently short to explain the dimol result. Similarly, it is not clear whether the scheme would allow an identical intermediate $[O_2(^1\Delta_g)]_2$ for the two reactions or whether it is necessary to postulate the formation of two different intermediates that result from collisions of different orientations. Without further evidence such remarks are purely speculative.

8.7. Conclusions

The analysis of the high temperature results shows that the discharge flow shock tube developed in this work, is suitable for the measurement of the rate constants for the energy pooling reaction and the collisional quenching of $O_2(^1\Sigma_g^+)$. The rate constants obtained for energy pooling and for the collisional deactivation of $O_2(^1\Sigma_g^+)$ by oxygen and nitrogen increase slowly with temperature; the temperature dependence of the rate constants fits none of the simple relations (except possibly the Landau-Teller model for quenching $O_2(^1\Sigma_g^+)$ by oxygen) and the mechanism is not straightforward. In contrast, the temperature dependence of the rate of the dimol emission is in accordance with a simple model that assumes the reaction to be collision controlled.

Of the models proposed for the collisional deactivation of singlet molecular oxygen, those in which the important process is considered to be resonant or near resonant electronic-to-vibrational energy transfer are not acceptable in the light of the recent experimental evidence obtained from studies of the chemiluminescence of the products. As a result the reactions are proposed tentatively to take place by another process of electronic-to-vibrational energy transfer. The model assumes the formation of a relatively stable collision complex (lifetime 10^{-11} - 10^{-12}s) and that quenching takes place on the potential energy surface by a curve crossing mechanism. Using the model, it is possible to devise a reaction pathway for the deactivation of $O_2(^1\Sigma_g^+)$ and $O_2(^1\Delta_g)$ in which the reactions proceed via a common intermediate complex, $[O_2(^1\Delta_g)\text{-}M]$. Further experiments are required for any conclusions on the validity of this model to be made.

9. EVALUATION OF THE DISCHARGE FLOW SHOCK TUBE TECHNIQUE

9.1. Introduction

The discharge flow shock tube studies described in this work are more sophisticated than those of earlier authors, both in the experimental techniques that have been developed and in the analysis of the results. The information gained from our studies allows the evaluation of the technique as an experimental tool for the study of the reactions of short-lived species at high temperatures. In the following sections the experiments that may be made are classified, and the experimental requirements and the limitations of the technique are discussed in detail.

9.2. Classification of Experiments

Singlet molecular oxygen was a particularly suitable choice for testing the discharge-flow shock tube because it allows three different types of measurement to be performed at the same time:

(i) experiments which study the rate of collisional deactivation of $O_2(^1\Delta_g)$;

(ii) studies of the nature of the dimol emission;

(iii) studies of the reactions leading to formation and removal of $O_2(^1\Sigma_g^+)$ as the test gases flow along the shock tube.

The reactions studied by Hartunian et al.[119] and Gross[120,121,122] are all of the same type as category (ii) of this classification, while the vibrational relaxation measurements of Breen, Quy and Glass[3] are a fourth type of experiment (class (iv)). From our knowledge of such experiments we may lay down specific conditions for which each class of measurement may be made:

(i) Direct measurement of the rate of removal of an excited species, by following the change in the decay behind the shock front from that observed prior to the shock requires the rate constant to

increase significantly with temperature. If a 15% change in the decay is significant, the minimum ratio of rate constants, $k_q(T_2)/k_q(T_1)$ is given roughly by

$$\frac{k_q(T_2)}{k_q(T_1)} = \frac{0.15U\ (1-\rho_{21}^{-1})}{v} \qquad (9.1)$$

where v is the flow velocity of the test gas prior to the shock. In our studies of $O_2(^1\Delta_g)$, $v \approx 1 ms^{-1}$, $U \approx 1\ Kms^{-1}$ and $\rho_{21} \approx 5$, indicating that satisfactory measurements could be made only if $k_q(T_2)/k_q(T_1) > \sim 100$. Equation (9.1) shows that high test gas flow velocities are required for accurate calculations of the rate constants at the temperature of the shock. It should be possible to study reactions having an activation energy greater than 15 kJ $mole^{-1}$ by this technique, but our results suggest that at the pressures used in the present work ($\sim$ 9 KN m^{-2}), the post-shock decay will be too rapid for satisfactory analysis in reactions for which the rate constant at the temperature behind the shock front is greater than $\sim 2 \times 10^6$ dm^3 $mole^{-1}$ s^{-1}; a reduction in the overall pressure or the partial pressure of the quenching species will slow the reactions and extend the range of rate constants that may be studied. An accurate estimate of the pre-shock decay is essential and measurements should be made over a long length of tube.

(ii) Measurement of the rate constants of simple collisional reactions such as the dimol reaction, which lead to the emission of electromagnetic radiation, is the easiest form of experiment in the discharge flow shock tube; provided that the intensity of emission prior to the shock is easily measured, it is unlikely that any reactions will be found for which the ratio of the pre- and post-shock levels of emission at the observation station is

outside the suitable range (for the dimol emission, which is a collision controlled reaction, the ratio of levels is typically ~ 50). Our technique for the analysis of the experimental data is superior to that of Hartunian in that allowance is made for the effects of the finite rise time of the system, and the analysis considers the emission along an appreciable length of tube rather than simply the concentration at the observation station. In general terms, the ratio of levels is described by:

$$\frac{I_2}{I_1^o} = \frac{k(T_2)}{k(T_1)} \rho_{21}^2 e^{-\alpha_t t_p} \qquad (9.2)$$

where I_1^o is the pre-shock level of emission at the observation station and I_2 the post-shock emission at the observation station at a time t_p after the arrival of the shock front. The ratio of the high temperature and room temperature rate constants, $k(T_2)/k(T_1)$, is equal to $T_{21}^{\frac{1}{2}}$ for a simple collisonal process such as the dimol emission, but varies exponentially with temperature for reactions that are activation controlled.

(iii) The most interesting results on singlet molecular oxygen have come from the study of the formation and removal of $O_2(^1\Sigma_g^+)$. The results obtained for the quenching of $O_2(^1\Sigma_g^+)$ by oxygen and by nitrogen over the temperature range 600 - 1500 K, suggest that direct measurement of the rate of collisional deactivation, at the pressures of ~ 0.9 KN m^{-2} used in this work, is possible only if the rate constants lie between $\sim 5 \times 10^5$ and $\sim 5 \times 10^7$ dm^3 $mole^{-1}$ s^{-1}; outside this range relaxation will be too rapid for measurement or will not reach completion within the period of hot flow. Again, it should be possible to extend this range by raising or lowering the pressure or by diluting the test gas with an inert carrier gas. The ratio, K, of the high temperature level

of emission to that expected from the shock compression alone should lie between about 1.5 and 20 for an increase in the level or between 0.05-0.65 for a decrease, to allow satisfactory analysis of the relaxation zone. These conditions were fulfilled adequately by most experiments in pure oxygen and very well by the experiments on oxygen/nitrogen mixtures.

As a well-defined curve for the temperature dependence of the rate constant for the energy pooling reaction was obtained from Figure (8.5), the rate of deactivation of $O_2(^1\Sigma_g^+)$ in mixtures that do not fulfill the above conditions, may be calculated from the pooling curve and the ratio K (as has been done for pure oxygen in Table 8.3).

(iv) Measurements of the vibrational relaxation times of test gases in the presence of small concentrations of excited species should indeed be possible, and as vibrational relaxation has a significant effect on the rate constants obtained in the present analysis, such experiments would appear to be most worthwhile.

9.3. Experimental Requirements

In the previous section our primary interest was in the nature of the reactions and the magnitude of the rate constants which should be suitable for study in the discharge flow shock tube. In the evaluation of the suitability of the technique, the experimental requirements such as the rapid pumping rate suggested in the previous section, are of similar importance.

A major requirement in discharge flow shock tube experiments is a reasonably high level of emission; ideally the photomultiplier load resistance should be less than 10kΩ to give a rise time of less than 1μs, but as the intensities of the emission from $O_2(^1\Sigma_g^+)$ and in particular the dimol emission are relatively low, a 51kΩ load resistor was used in this work as a compromise between a high photomultiplier output and a short risetime. At the same time, it is important that the rate of removal of the excited states by radiative decay is not significant in comparison with the rates of the reactions under study. Problems may also arise from the use of narrow band filters to select the wavelength of the emission; if the emission band is significantly broadened at high temperatures and the bandwidth is greater than that of the filter, the post-shock output from the photomultiplier will be low. Complementary spectroscopic studies or studies in which measurements are made at two or three closely spaced wavelengths using narrow band filters, should be made to test the magnitude of these effects; they appear to be unimportant when following the emission from $O_2(^1\Sigma_g^+)$ and the dimol emission.

For a high concentration of the excited species at the observation station, the discharge must, in most cases, be in the shock tube itself. This arrangement is clumsy and is undesirable if gases are to be mixed in after the discharge; it was not necessary in the present experiments because the long lifetime of $O_2(^1\Delta_g)$, together with the fact that large

concentrations are formed in the discharge allows the discharge to be placed before the test gas reaches the shock tube (Chapter 2). $O_2(^1\Sigma_g^+)$ is of course formed continuously by the energy pooling reaction (Chapter 1).

Our experience suggests that the use of a transient recorder to give a record of each shock for computer analysis is essential; hand analysis of photographs is laborious, time consuming and inaccurate, and does not allow corrections to be made for non-uniform conditions behind the shock front and for the finite width of the photomultiplier slit. The interactive graphics system described in Chapter 6 is undoubtedly the most suitable for such experiments, but, if such a system is not readily available, a "blind" computer analysis might suffice.

The non-linear least squares curve fitting programs have proved invaluable for calculating the best fit of the various parameters to the experimental data. They should, however, be treated with caution as the "best" fit is not necessarily the true fit; in consequence, wherever it is possible to provide a satisfactory estimate of one of the parameters for the curve-fitting programs, it is advisable to fix this value and allow the computer to optimise the fit of the function to the data around it.

An important limitation of the discharge flow shock tube is the range of temperature over which measurements can be made. In the present work, the temperatures were restricted to the range 630-1660 K and the scatter of the results was found to increase with temperature. Measurements at higher temperatures will require high diaphragm pressure ratios (the alternative is to use a hydrogen driver, which is not safe for oxygen discharge flow experiments); such experiments are most easily performed using a test gas pressure much lower than was possible in these studies, but other techniques[102] such as electrical heating of the driver gas or the use of a driver section of greater cross sectional area than the test

section, may be useful. Extension of the results to lower temperatures by raising the pressure of the test gas or using argon as the driver may be possible, but 630 K is already a low temperature for shock tube experiments and the practical difficulties (e.g. in the operation of the light screens) may prove to be insuperable.

10. POSSIBILITIES FOR FUTURE WORK

10.1. Further studies of Singlet Molecular Oxygen

The results discussed in Chapter 8 suggest that the rate constants for most reactions of $O_2(^1\Delta_g)$ and $O_2(^1\Sigma_g^+)$ increase slowly with temperature. This gives us some idea of the reactions which are easily studied at high temperatures.

The rate constants for the quenching of $O_2(^1\Delta_g)$ must be greater than the room temperature rate constants by about 2 orders of magnitude, if satisfactory measurements at high temperatures are to be made. This is unlikely as, with the possible exception of the quenching of $O_2(^1\Sigma_g^+)$ by oxygen, the temperature dependences of all the reactions in Table 8.4 are too small. Possibilities are the reactions with amines and sulphides which are unusually fast at room temperature (Table 1.1) and may proceed via a charge transfer complex[86] (Chapter 1).

Our studies of the dimol emission in pure oxygen showed that the collision complex is too short-lived to reach an equilibrium concentration. The scatter of the results does not allow an estimate of the activation energy for the reaction to be made; this is principally a result of the low intensity of the dimol emission and might be improved slightly in the presence of a carrier gas such as nitrogen, which reacts very slowly with $O_2(^1\Delta_g)$.

The reactions of $O_2(^1\Sigma_g^+)$ are much more suitable for study; here it is possible to make the accurate measurements of the temperature dependence of the rate constants for collisional deactivation that are needed to test and compare the models proposed for the quenching of singlet molecular oxygen. Studies should be possible for most of the quenching gases in Table 1.1, although the intensity of emission from $O_2(^1\Sigma_g^+)$ will be severely reduced in the presence of those quenchers for which the room temperature rate constant for collisional deactivation is greater

than $\sim 10^7$ dm^3 $mole^{-1}$ s^{-1}. As the temperature dependence of the rate constant for quenching in pure oxygen has been reasonably well established, experiments in which less than 10% of the test gas is the quencher under study, may prove satisfactory in such circumstances. It is probably inadvisable to study those quenchers, such as the inert gases, which react with $O_2(^1\Sigma_g^+)$ at a rate less than that of pure oxygen; the effects of small concentrations of impurities such as water on the room temperature rate constants is large, and shock tube experiments will probably measure the temperature dependence of the reactions of the impurities rather than of the species under study.

It would be particularly interesting to look at the high temperature quenching of $O_2(^1\Sigma_g^+)$ by some of the gases recently studied by Thomas and Thrush[79,90,91] at room temperature (Chapter 1). All deactivate $O_2(^1\Sigma_g^+)$ extremely rapidly and it is probably best to start with those for which the rate constant is $\sim 10^7$ dm^3 $mole^{-1}$ s^{-1}, CO, N_2O, HCl and DCl. The most interesting results obtained by Thomas and Thrush came from their studies of the chemiluminescence of the quenching agent that results from the transfer of the electronic energy of $O_2(^1\Sigma_g^+)$ and $O_2(^1\Delta_g)$ to vibrational energy of the products of the reaction. Such experiments will be far more difficult to perform in the discharge flow shock tube than in a continuous discharge flow system at room temperature, but if feasible should prove extremely valuable.

A further possible study of singlet molecular oxygen is the vibrational relaxation of the excited states; the weak emission from $O_2(^1\Sigma_g^+)(v=1)$ at 686 nm lies too close to the relatively intense dimol bands at 634 and 703 nm, but the dimol emission from $O_2(^1\Delta_g)(v=1)$ at 580 nm

$$O_2(^1\Delta_g)(v=1) + O_2(^1\Delta_g)(v=o) \rightarrow O_2(^3\Sigma_g^-)(v=o) + O_2(^3\Sigma_g^-)(v=o) + h\nu(580\ nm) \qquad (1.9)$$

is free from such interference.

As the population of the $O_2(^1\Delta_g)(v=1)$ level increases exponentially with temperature, the emission from the shock-heated gas should be considerably greater than that observed prior to the shock; the rate of vibrational relaxation of $O_2(^1\Delta_g)$ dilute in oxygen may be obtained by analysis of the initial relaxation zone, and the ratio of levels, K, should vary exponentially with temperature. The results of such experiments should provide an excellent test of the quality of the discharge flow shock tube system, as the rate of vibrational relaxation of $O_2(^1\Delta_g)$ dilute in oxygen is expected to be very similar to the known rate for $O_2(^3\Sigma_g^-)$, and the spacing of the vibrational levels obtained from the temperature dependence of K may be compared with the values obtained spectroscopically.

10.2. Application to Other Systems

The conditions for which the four classes of discharge flow shock tube experiment are expected to give satisfactory results are described in Chapter 9. The main problems experienced will probably result from the rapid rates of the reactions of most excited species in comparison with $O_2(^1\Sigma_g^+)$ and $O_2(^1\Delta_g)$.

In many discharge flow experiments, such as those described by Hartunian and Gross, the atomic species are generated in the discharge and other excited states are formed by chemical reaction outside the discharge.

e.g. $H\bullet + Cl_2 \rightarrow HCl + Cl\bullet$ (10.1)

$H\bullet + HCl \rightarrow H_2 + Cl\bullet$ (10.2)

$F\bullet + RCHO \rightarrow HF^\dagger + RCO\bullet$ (10.3)

Such reactions are similar in form to the energy pooling reaction, and it may be possible to analyse the results in a similar way to the formation and removal of $O_2(^1\Sigma_g^+)$.

A series of experiments that are suggested by the models of electronic-to-vibrational energy transfer discussed in Chapter 8 are the high temperature studies of reactions (8.29) and (8.30)

$$O^*(2^1D_2) + CO \rightarrow (CO_2^*) \rightarrow O(2^3P_J) + CO^\dagger \quad (8.29)$$

$$O^*(2^1D_2) + N_2 \rightarrow (N_2O^*) \rightarrow O(2^3P_J) + N_2^\dagger \quad (8.30)$$

The observed temperature dependence of the rate constants for these reactions would serve to test the models that have been proposed and might also give information on the shape of the potential energy surface on which the reactions occur.

Kinetic experiments in the discharge flow shock tube are usually of low precision. Chemiluminescence studies have not yet been reported, and are likely to be less accurate than the kinetic studies, but the

information obtained may well be of greater value for determining the nature of the reaction or distinguishing between reaction models. There is plenty of scope for further study in this aspect of the field.

References

1. J.P. Toennies, Ber. Bunsenges. Physik. Chem. 72 927 (1968)
2. M.J. Pilling, "Reaction Kinetics", Clarendon Press (1975).
3. J.E. Breen, R.B. Quy and G.P. Glass in "Recent Developments in Shock Tube Research", Stanford University Press (1973).
4. J. Heicklen, "Atmospheric Chemistry", Academic Press, London and New York, (1976).
5. "Singlet Molecular Oxygen", A.P. Schaap Ed., Dowden, Hutchinson and Ross, distributed by Halstead Press, New York (1976).
6. J. Bland, J. Chem. Ed. 53 274 (1976).
7. K.K. Rohatgi-Mukherjee in "Proceedings of the Symposium on Singlet Molecular Oxygen", Bombay, 1975 (1976).
8. G. Herzberg, "Spectra of Diatomic Molecules", Van Nostrand, New York, N.Y. (1950).
9. P.W. Atkins, "Molecular Quantum Mechanics", Clarendon Press (1970).
10. D.H. Katayama, S. Ogawa, M. Ogawa, and Y. Tanaka, J. Chem. Phys. 67 2132 (1977).
11. R.P. Wayne, Advan. Photochem. 7, 311 (1969).
12. L. Wallace and D.M. Hunten, J. Geophys. Res., 73 4813 (1968).
13. R.M. Badger, A.C. Wright, and R.F. Whitlock, J. Chem. Phys. 43 4345 (1965).
14. R.W. Nicholls, Can. J. Chem. 47 1847 (1969).
15. S. Hayakawa, K. Ito, T. Matsumoto, and T. Nishimura, J. Geomagn. Geoelectr. 25 281 (1973).
16. C. Long and D.R. Kearns, J. Chem. Phys. 59 5729 (1973).
17. K.G. Vohra, J.P.S. Chatha, P.K. Arora, and Nalini Raja in "Proceedings of the Symposium on Singlet Molecular Oxygen", Bombay, 1975 (1976).

18. A.U. Khan and M. Kasha, J. Amer. Chem. Soc. 92 3292 (1970).

19. L. Mallet, C.R. Acad. Sci., 185 352 (1927).

20. P. Groh and K.A. Kirrmann, C.R. Acad. Sci., 215 275 (1942).

21. G. Gattow and A. Schneider, Naturwissenschaften, 41 116 (1954).

22. H.H. Seliger, Anal. Biochem., 1 60 (1960).

23. J. Stauff and H. Schmidkunz, Z. Phys. Chem. (Frankfurt um Main), 35 295 (1962).

24. A.U. Khan and M. Kasha, J. Chem. Phys., 39 2105 (1963); 40 605 (1964).

25. S.J. Arnold, E.A. Ogryzlo, and H. Witke, J. Chem. Phys., 40 1769 (1964).

26. L.W. Bader and E.A. Ogryzlo, Discussions Faraday Soc. 37 46 (1964).

27. Manohar Gopal Bhide in "Proceedings of the Symposium on Singlet Molecular Oxygen", Bombay 1975 (1976).

28. R.A. Young and G. Black, J. Chem. Phys. 42 3740 (1965).

29. J.S. Arnold, R.J. Browne and E.A. Ogryzlo, Photochem. Photobiol. 4 963 (1965).

30. P.H. Krupenie, J. Phys. and Chem. Reference Data, 1 423 (1972).

31. S.E. Novick and H.P. Broida, J. Chem. Phys. 67 5975 (1977).

32. J. Goodman and L.E. Brus, J. Chem. Phys. 67 4398 (1977); 67 4408 (1977).

33. J.W. Peters, P.J. Bekowies, A.M. Winer, and J.N. Pitts Jr., J. Amer. Chem. Soc. 97 3299 (1975).

34. R.W. Murray and M.L. Kaplan, J. Amer. Chem. Soc. 90 537 (1968).

35. A.U. Khan, Science 168 476 (1970).

36. R.A. Young and G. Black, Symposium on Chemiluminescence, Durham, N.C. (1965).

37. L.R. Martin, R.B. Cohen and J.F. Schatz, Chem. Phys. Lett. 41 394 (1976).

38. S.A. Lawton, S.E. Novick, H.P. Broida, and A.V. Phelps, J. Chem. Phys. 66 1381 (1977).

39. J.G. Parker and D.N. Ritke, J. Chem. Phys. 59 3713 (1973); 61 3408 (1974).

40. I.B.C. Matheson, J. Lee, B.S. Yamanashi, and M.L. Wolbarsht, Chem. Phys. Lett. 27 355 (1974).

41. R.J. Collins, D. Husain, and R.J. Donovan, J. Chem. Soc. Faraday II 69 145 (1973).

42. D.R. Snelling, Can. J. Chem. 52 257 (1974).

43. D.R. Kearns, Chemical Reviews, 71 403 (1971).

44. C.K. Duncan and D.R. Kearns, J. Chem. Phys. 55 5822 (1971).

45. P.B. Merkel and D.R. Kearns, J. Amer. Chem. Soc. 94 7244 (1972).

46. D.R. Snelling, Chem. Phys. Lett. 2 346 (1968).

47. L.J. Andrews and E.W. Abrahamson, Chem. Phys. Lett. 10 113 (1971).

48. J.A. Davidson and E.W. Abrahamson, Photochem. Photobiol. 15 403 (1972).

49. J.A. Davidson, K. Kear, and E.W. Abrahamson, J. Photochem. 1 307 (1972/73).

50. T.C. Frankiewicz and R.S. Berry, J. Chem. Phys. 58 1787 (1973).

51. D.J. Giachardi, G.W. Harris and R.P. Wayne, J. Chem. Soc. Faraday II 72 619 (1976).

52. L. Elias, E.A. Ogryzlo, and H.I. Schiff, Can. J. Chem. 37 1680 (1959).

53. I.D. Clark and R.P. Wayne, Chem. Phys. Lett. 3 93 (1969).

54. M. Yaron and A. Von Engel, Chem. Phys. Lett. 33 316 (1975).

55. K. Furukawa and E.A. Ogryzlo, Chem. Phys. Lett. 12 370 (1971).

56. R.D. Ashford and E.A. Ogryzlo, Can. J. Chem. 52 3544 (1974).

57. R.D. Ashford and E.A. Ogryzlo, J.Amer.Chem.Soc. 97 3604 (1975)

58. C.S. Foote and S. Wexler, J. Amer. Chem. Soc. 86 3879 (1964).

59. H. Kautsky, Trans. Faraday Soc. 35 216 (1939).

60. R.H. Kummler and M.H. Bortner, Amer. Chem. Soc. Symp. Petrol. Chem. 16 (1971).

61. J.A. Davidson and E.A. Ogryzlo in "Chemiluminescence and Bioluminescence", M.J. Cornier, D.M. Hercules and J. Lee Ed., Plenum Press, New York (1973).

62. K.H. Becker, W. Groth and U.Schurath, Chem. Phys. Lett. 8 259 (1971).

63. R.J. O'Brien Jr. and G.H. Myers, J. Chem. Phys. 5 3832 (1972).

64. S.V. Filseth, A. Zia and K.H. Welge, J. Chem. Phys. 52 5502 (1970).

65. S.J. Arnold, M. E. Kubo, and E.A. Ogryzlo, Adv. Chem. Ser. 77 133 (1968).

66. F.D. Findlay and D.R. Snelling, J. Chem. Phys. 55 545 (1971).

67. I.D. Clark and R.P. Wayne, Proc. Roy. Soc. (Lond.) A314 111 (1969).

68. K. Kear and E.W. Abrahamson, J. Photochem. 3 409 (1975).

69. F. Stuhl and H. Niki, Chem. Phys. Lett 7 473 (1971).

70. F. Stuhl and K.H. Welge, Can. J. Chem. 47 1870 (1969).

71. R.G.O. Thomas and B.A. Thrush, J. Chem. Soc. Faraday II 71 664 (1975).

72. M.R. Braithwaite, E.A. Ogryzlo, J.A. Davidson, and H.I. Schiff, J. Chem. Soc. Faraday II 72 2075 (1976).

73. J.F. Noxon, J. Chem. Phys. 52 1852 (1970).

74. T.P.J. Izod and R.P. Wayne, Proc. Roy. Soc. (Lond.) A308 81 (1968).

75. P.D. Steer, R.A. Ackerman and J.N. Pitts, J. Chem. Phys. 51 843 (1969).

76. K.G. Vohra, J.P.S. Chatha, P.K. Arova and N. Raja in "Proceedings of the Symposium on Singlet Molecular Oxygen", Bombay, 1975 (1976).

77. P. Borrell, P.M. Borrell and M.D. Pedley, Chem. Phys. Lett. 51 300 (1977).

78. A. Leiss, U. Schurath, K.H. Becker and E.H. Fink, J. Photochem. 8 211 (1978).

79. R.G.O. Thomas and B.A. Thrush, Proc. Roy. Soc. (Lond.) A356 287 (1977).

80. M. Yaron, A. Von Engel, and P.H. Vidaud, Chem. Phys. Lett. 37 159 (1976).

81. M.J.E. Gauthier and D.R. Snelling, J. Photochem. 4 27 (1975).

82. M.R. Braithwaite, E.A. Ogryzlo, J.A. Davidson, and H.I. Schiff, Chem. Phys. Lett. 42, 158 (1976).

83. F. Stuhl and H. Niki, Chem. Phys. Lett. 5 573 (1970).

84. K. Furukawa and E.A. Ogryzlo, J. Photochem. 1 163 (1972).

85. R.A. Ackerman, I. Rosenthal and J.N. Pitts Jr., J. Chem. Phys. 54 4960 (1971).

86. C. Ouannes and T. Wilson, J. Amer. Chem. Soc. 90 6527 (1968).

87. K. Furukawa and E.A. Ogryzlo, Amer. Chem. Soc. Symp. Petrol. Chem. 16 (1971).

88. R.A. Ackerman, J.N. Pitts Jr., and I. Rosenthal, Amer. Chem. Soc. Symp. Petrol. Chem. 16 (1971).

89. M.R. Braithwaite, J.A. Davidson, and E.A. Ogryzlo, J. Chem. Phys. 65 771 (1976).

90. R.G.O. Thomas and B.A. Thrush, Proc. Roy. Soc. (Lond.) A356 295 (1977).

91. R.G.O. Thomas and B.A. Thrush, Proc. Roy. Soc. (Lond.) A356 307 (1977).

92. R.G. Derwent and B.A. Thrush, Trans. Faraday Soc. 67 2036 (1971).

93. U. Schurath, J. Photochem. 4 215 (1975).

94. I.T.N. Jones and K.D. Bayes, J. Chem. Phys. 57 1003 (1972).

95. S.J. Arnold, N. Finlayson, and E.A. Ogryzlo, J. Chem. Phys. 44 2529 (1966).

96. R.G. Derwent and B.A. Thrush, J. Chem. Soc. Faraday II 68 720 (1972).

97. R.G. Derwent and B.A. Thrush, Disc. Faraday Soc. 53 162 (1972).

98. C.K. Duncan and D.R. Kearns, Chem. Phys. Lett. 12 306 (1971).

99. R. Gutteridge, Ph.D. Thesis, University of Keele (1972).

100. A.G. Gaydon and I.R. Hurle, "The Shock Tube in High Temperature Chemical Physics", Chapman and Hall, London (1963).

101. R. Becker, Z. fur Physik. 8 321 (1922).

102. J.N. Bradley, "Shock Waves in Chemistry and Physics", Methuen, London (1962).

103. W.J.M. Rankine, Trans. Roy. Soc. (Lond.) 160 277 (1870).

104. J. Rayleigh, Proc. Roy. Soc. (Lond.) 84 247 (1910).

105. H. Hugoniot, J. de l'ecole Polytechnique 58 1 (1889).

106. I.I. Glass, "Theory and Performance of Simple Shock Tubes, Vols. I and II", Institute of Aerophysics, Report No. 12 (1958).

107. E.F. Greene and J.P. Toennies, "Chemical Reactions in Shock Waves", Arnold Publishers, London (1964).

108. J.K. Wright, "Shock Tubes", Methuen, London (1961).

109. P. Borrell, "Transfer and Storage of Energy by Molecules", (Wiley-Interscience, London) 2 180 (1969).

110. R.C. Millikan, Report 64-RL-3700C, General Electric Co., Schenectady, New York (1964).

111. R.C. Millikan, Report 65-C-106, General Electric Co., Schenectady, New York, (1965).

112. J.A.N.A.F. Thermochemical Tables, The Dow Chemical Company, Midland, Michigan (1965).

113. Programme, 11th International Symposium on Shock-Tubes and -Waves, Seattle (1977).

114. C.F. Hansen in "Recent Developments in Shock Tube Research", Stanford University Press (1973).

115. L.D. Landau and E. Teller, Z. Phys. Sowjetunion 10 34 (1936).

116. K.F. Herzfeld and T.A. Litovitz, "Absorption and Dispersion of Ultrasonic Waves", Academic Press, New York (1959).

117. J.H. Kiefer and R.W. Lutz, Symp. Combust. 11th, 1966, 67 (1967).

118. R.E. Center in "Recent Developments in Shock Tube Research", Stanford University Press (1973).

119. R.A. Hartunian, W.P. Thompson and E.W. Hewitt, J. Chem. Phys. 44 1765 (1966).

120. R.W.F. Gross, J. Chem. Phys. 48 1302 (1968).

121. R.W.F. Gross and N. Cohen, J. Chem. Phys. 48 2582 (1968).

122. N. Cohen and R.W.F. Gross, J. Chem. Phys. 50 3119 (1969).

123. P. Borrell, P.M. Borrell, and A. Brittain, U.S. Clearing-house Fed. Sci. Tech. Inform., AD1969, 702808.

124. R.D.H. Brown, G.P. Glass and I.W.M. Smith, J. Chem. Soc. Faraday II, 71 1963 (1975).

125. R.L. Belford and R.A. Strehlow,Ann. Rev. Phys. Chem. 247 (1969).

126. "QVF Process plant and pipeline", Corning Ltd. (1977).

127. "Union Carbide Molecular Sieves for Selective Adsorption", 3rd Edn.

128. G.E. Millward, Ph.D. Thesis, University of Keele (1970).

129. C.J.S.M. Simpson, Private communication.

130. K.C. Lapworth, L.A. Allnutt, and J.R. Pendlebury, Temp: Its Measu. Control Sci. Ind., 4 665 (1972).

131. C.J. Smith, "The General Properties of Matter", Edward Arnold, London (1953) P.434.

132. R.E. Dodd and P.L. Robinson, "Experimental Inorganic Chemistry", Elsevier Press (1954), p.151.

133. "Handbook of Chemistry and Physics", 45th Ed. Chemical Rubber Publ., Cleveland (1964).

134. "EMI Photomultipliers", EMI Electronics Ltd. (1975).

135. P.M. Borrell, Private communication.

136. P.H. Vidaud, R.P. Wayne, and M. Yaron, Chem. Phys. Lett. 38 306 (1976).

137. H. Mirels in "Shock Tube Research", Chapman and Hall, London, (1971).

138. H. Mirels, Phys. Fluids, 6 1201 (1963).

139. H. Mirels and J.F. Mullen, Phys. Fluids, 7 1208 (1964).

140. H. Mirels, AIAA J., 2 84 (1964)

141. H. Mirels, Phys. Fluids, 9 1907 (1966).

142. R.A. Strehlow and R.L. Belford, A.A.E. Tech. Rept. No.69-1, Univ. Illinois, Urbana (1969).

143. J.N. Fox, T.I. McLaren and R.M. Hobson, Phys. Fluids, 9 2345 (1966).

144. H.B. Dwight, Tables of Integrals and other Mathematical Data, 4th Ed., MacMillan (1961) p.43.

145. J.A. Bander and G. Sanzone, J. Phys. Chem. 81 1 (1977).

146. D.R. White, J. Chem. Phys. 49 5472 (1968).

147. P. Borrell, to be published.

148. NAG Fortran Library Manual Mark 6 (1977).

149. K. Kohse-Höinghaus and F. Stuhl, J. Photochem. 9 102 (1978).

150. K. Kohse-Höinghaus and F. Stuhl, Private communication.

151. S. Lemont and G.W. Flynn, Ann. Rev. Phys. Chem. 28 261 (1977).

152. T.G. Slanger, G. Black, and J. Fournier, J. Photochem. 4 329 (1975).

153. D.W. McCullough and W.D. McGrath, J. Photochem. 1 241 (1972/1973).

154. R.G. Shortridge and M.C. Lin, J. Chem. Phys. 64 4076 (1976).

155. E.R. Fisher and E. Bauer, J. Chem. Phys. 57 1966 (1972).

156. J.C. Tully, J. Chem. Phys. 61 61 (1974).

157. G.E. Zahr, R.K. Preston, and W.H. Miller, J. Chem. Phys. 62 1127 (1975).

158. M.A. Wolfe, "A First Course in Numerical Analysis", Van Nostrand Reinhold Company, London (1972).

APPENDIX A: Ideal Flow Calculations

A.1. Duration of the shock wave

The equations describing the flow duration in the incident shock (as opposed to the reflected shock, which is not observed in the present experiments) are derived in Gaydon and Hurle[100] pp.60-63. The shock wave is assumed to end when the head of the rarefaction fan meets the contact surface; this happens at a time, τ_c, after the diaphragm is burst and a distance X_c from the diaphragm. τ_c is given by the relation

$$\tau_c = \frac{2X_4}{a_4}\left\{1 - \frac{\gamma_4-1}{\gamma_1+1}\,\frac{a_1}{a_4}\left[\frac{M_1^2-1}{M_1^2}\right]\right\}^{-\left[\frac{\gamma_4+1}{2(\gamma_4-1)}\right]} \qquad (A.1)$$

where:

X_4 is the length of the driver section

a_4 is the velocity of sound in the driver gas

γ_4 is the specific heat ratio of the driver gas

a_1 is the velocity of sound in the test gas ahead of the shock front

γ_1 is the specific heat ratio of the test gas

M_1 is the shock Mach number ($M_1 = U/a_1$)

The hot flow duration, $\Delta\tau$, at time τ_c is expressed as

$$\Delta\tau = \tau_c - \tau_s \qquad (A.2)$$

where τ_s is the time at which the shock front was a distance X_c from the diaphragm. In terms of the parameters defined above:

$$\Delta\tau = \tau_c\left\{1 - \frac{2(M_1^2-1)}{(\gamma_1+1)M_1^2}\right\} \qquad (A.3)$$

and

$$X_c = \tau_c\left\{\frac{2a_1(M_1^2-1)}{(\gamma_1+1)\,M_1}\right\} \qquad (A.4)$$

As the shock front and contact surface are assumed to travel at constant

velocities, the hot flow time, $\Delta\tau_i$, at an observation situated at a distance, X_i (which is less than X_c) from the diaphragm is given by simple proportion:

$$\frac{\Delta\tau_i}{\Delta\tau} = \frac{X_i}{X_c} \qquad (A.5)$$

A.2. Shock velocities and diaphragm pressure ratios

The equations relating the shock velocity to the pressure ratio at which the diaphragm bursts are derived in Chapter II of Gaydon and Hurle[100]. The data for Figure (2.6) was generated using the equation:

$$\frac{P_4}{P_1} = \frac{2\gamma_1 M_1^2 - (\gamma_1-1)}{(\gamma_1+1)} \left\{ 1 - \frac{(\gamma_4+1)}{(\gamma_1+1)} \frac{a_4}{a_1} \left[\frac{M_1^2-1}{M_1} \right] \right\}^{-\left[\frac{2\gamma_4}{\gamma_4-1}\right]} \qquad (A.6)$$

where:

P_4 is the diaphragm bursting pressure

P_1 is the initial pressure in the test gas

a_4 is the velocity of sound in the driver gas

γ_4 is the specific heat ratio of the driver gas

a_1 is the velocity of sound in the test gas ahead of the shock front

γ_1 is the specific heat ratio of the test gas

M_1 is the shock Mach number ($M_1 = U/a_1$)

The shock velocity is calculated from Figure (2.6) using the velocity of sound in oxygen (0.328 Km s^{-1} at 298 K).

APPENDIX B: Numerical Integration using Simpson's Rule

There are three common formulae for numerical integration of a set of uniformly spaced data[158]: the rectangle rule, the trapezium rule and Simpson's rule. The simplest and least accurate is the rectangle rule which approximates the area ABCD under the graph of f(x) in Figure (A.1) to the area of the rectangle ABCN. The trapezium rule approximates the area to that of the trapezium ABCD; Figure (A.1) shows this to be a far better fit to the curve. Simpson's rule gives a better fit again; the area under the curve is approximated to that under the parabola which passes through the points (x_o, f_o), (x_1, f_1), and (x_2, f_2).

To apply Simpson's rule, the interval of integration [a, b] is divided into an even number 2n of segments, each of length h, using points labelled (x_i, f_i). The integral is then given by the relation

$$\int_a^b f(x)dx = \frac{h}{3}[f_o + 4f_1 + 2f_2 + 4f_3 + ... + f_{2n}] \qquad (B.1)$$

A minimum number of three data points is required; in this case, n = 1 and

$$\int_a^b f(x)dx = \frac{h}{3}[f_o + 4f_1 + f_2] \qquad (B.2)$$

Obviously the accuracy of the integral increases with the number of segments into which the interval is divided.

In the vibrational relaxation program, VIBREL, the length of each segment, h, is specified by the time increment designated at the start, while the number of segments, n', increases with each cycle of the program. Subroutine NUMINT evaluates the integral using equation (B.1) whenever n' is even; at the end of each calculation, the sum of the data is stored for the next cycle. The numerical integration of the data performed in this way is of the greatest precision possible.

The numerical integration for the rise time of the detection system, described in Chapter 6 and performed in subroutine EQUATA or EQUAT3,

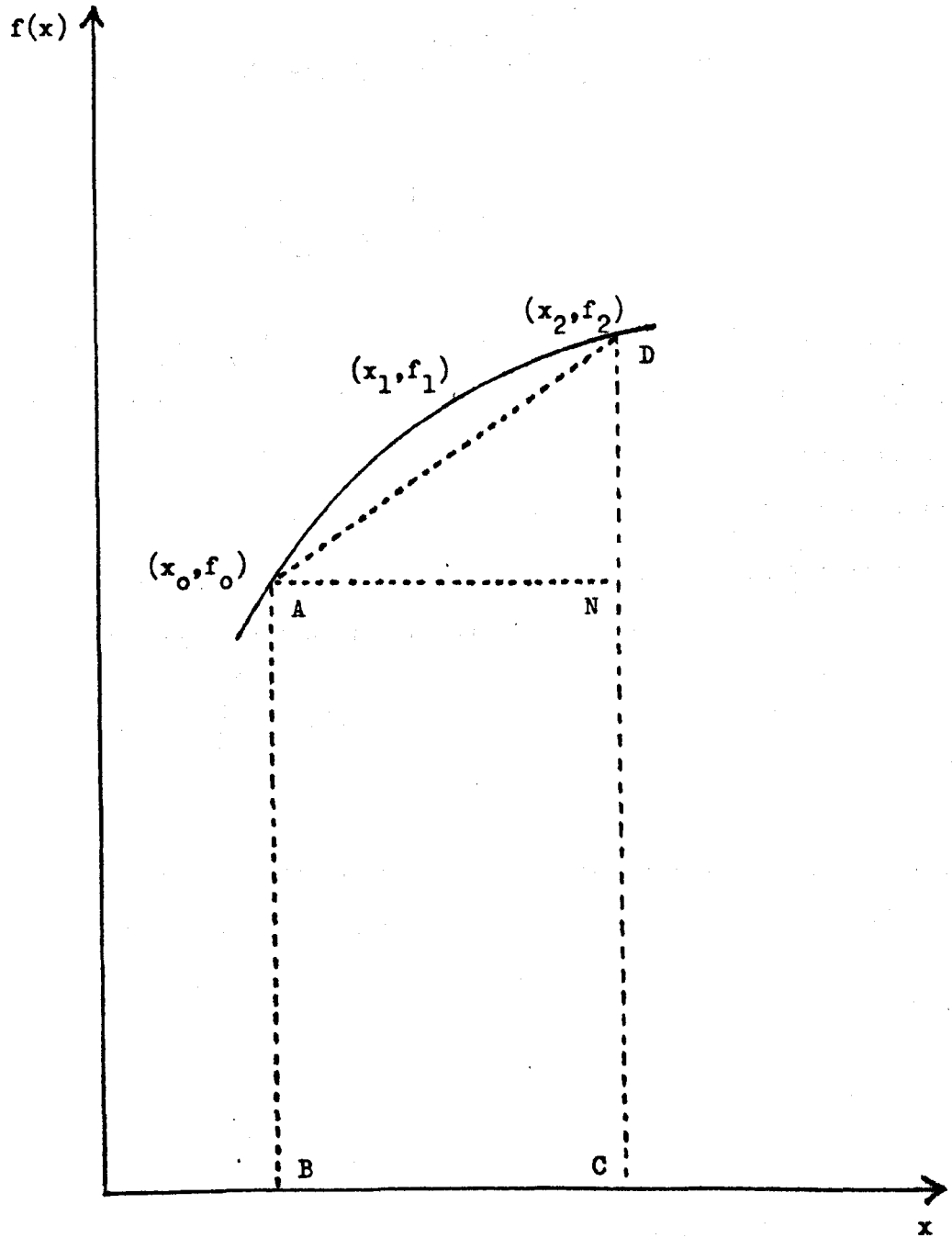

FIGURE A.1 Numerical Integration by Rectangle Rule, Trapezium Rule, and Simpson's Rule.

uses the formula in equation (B.2); the function $Y(t_p)$ is calculated from equations (6.14) and (6.15)-(6.16) or (6.21)-(6.22) by evaluating the relevant relation

$$\frac{I_{\Sigma 2}}{I^o_{\Sigma 1}} = K[1-(1-^1/K)\, e^{-t_p/\tau_{rel}}]\rho_{t1}\, e^{-\alpha_t t_p} \tag{5.5}$$

$$\frac{I_{D2}}{I^o_{D1}} = K\, \rho_{t1}{}^2 \left(\frac{T_t}{T_1}\right)^{\frac{1}{2}} e^{-\alpha_t t_p} \tag{5.6}$$

at times t_p, $(t_p + \frac{1}{2}\tau_{int})$ and $(t_p + \tau_{int})$. It is not necessary to perform the calculations at shorter time intervals in our experiments, because the results agree to five significant figures with those obtained using the exact integrated form of subroutine EQUATA (Chapter 6).

The trapezium and rectangle rules are used in VIBREL to calculate the particle time from the relation

$$t_p = \int_o^{t_\ell} \rho_{t1}\, dt_\ell \tag{5.8}$$

when n is odd or less than 1; the increment calculated by these rules is added to the time calculated by the Simpson's rule integration in the previous cycle.

APPENDIX C: Computer Programs

C.1. Flow Corrections Program, FLOCOR

The calculations performed in the flow corrections program have been described in Chapter 5 and reference 128. The subroutines, DEATH, COFFIN and BLOOD, are essentially unchanged from those written by G.E. Millward[128], but extensive changes to the mainprogram have been made, and subroutines GRAVE and HEARSE have been written to calculate the ratios ($^{\ell}/_{\ell_m}$) and ($^{\ell}/_{\ell_{mt}}$) at each ($^{t_\ell}/_{t_m}$). Table C.1.1. explains the computational symbols used in FLOCOR and relates them to the equations in Chapter 5; the required input data is shown in Table C.1.2. The computer program includes a sample of the output from a typical run.

TABLE C.1.1.

Computational symbols used in the flow corrections program

FORTRAN SYMBOL	INTERPRETATION
XD	length of driver section (mm)
GAMA4	γ_4, specific heat ratio of driver gas
A4	a_4, speed of sound in driver gas
DER	r, radius of shock tube (cm)
YID	velocity decrement (% m^{-1})
IS	number of species in mixture
ZJK(J,K)	name of species J
XNJ (J)	number of atoms in species J
XMWJ(J)	molecular weight of species J
GJ(J), GAJ(J)	specific heat ratio of species J
FJ(J)	mole fraction of species J
NTIMS	number of times flow corrections are to be calculated
NJOBS	number of sets of calculations on each mixture
U	shock velocity (Km s^{-1})
T1	initial temperature (K)
NUM	shock run number
P1	initial pressure (mm Hg)
TL	observation time, laboratory time (s)
RHOS	mean density ratio, ρ_{21}
T2	mean shock temperature, T_2 (K)
XMWAV	mean molecular weight of gas mixture
GMIX, GAMIX	γ, mean specific heat ratio of gas mixture
AAMIX, AT1MIX	a_1, velocity of sound in gas mixture (Km s^{-1})
AY	$(\gamma + 1)$
BY	$(\gamma - 1)$
XM, AM	M_s, shock Mach Number
CY	M_s^2
XMS2	M_{2s} in equation (5.
BA	$(\gamma + 1)/2(\gamma - 1)$
CA	$M_{2s}/[2 + (\gamma - 1)M_{2s}^2](\gamma + 1)/2(\gamma - 1)$

FORTRAN SYMBOL	INTERPRETATION
B	$\frac{2\gamma M_s^2 - (\gamma - 1)}{(\gamma + 1)}$
C	$\frac{(\gamma_4 - 1)}{(\gamma + 1)} \frac{a_4}{a_1}$
D	$(M_s^2 - {}^1/M_s)$
E	$- 2\gamma_4/(\gamma_4 - 1)$
F	$- (\gamma_4 + 1)/[2(\gamma_4 - 1)]$
PRES	diaphragm pressure ratio, P_4/P_1
TC	maximum duration of ideal shock (μs)
TO	hot flow duration of ideal shock at the observation station (μs)
AZ	πr^2
AP	$2\pi r$
TM	t_m, maximum hot flow time for laminar flow (s)
XLT, XLTI	$({}^{\ell}/\ell_m)$
FXLT, FAXLT	$\{1 - \rho_{21}^{-1}[1 - ({}^{\ell}/\ell_m)^{\frac{1}{2}}]\}$
V2	$v_{2\ell}$, velocity of shock-heated gas
TOR	τ_{trans}, time at which transition to turbulent flow occurs.
XLTOR	$({}^{\ell}/\ell_m)$ when $t_\ell = \tau_{trans}$
XLTORT	$({}^{\ell}/\ell_{mt})$ when $t_\ell = \tau_{trans}$
HA	$({}^{\ell}/\ell_m)^{\frac{1}{2}}$ when $t_\ell = \tau_{trans}$
TORLP	particle time, t_p, when $t_p = \tau_{trans}$
TMT	maximum hot flow time for pure turbulent flow (s)
TORLT	apparent value of $t_{\ell t}$ when $t_\ell = \tau_{trans}$ assuming entire flow to be turbulent
HB	$({}^{\ell}/\ell_{mt})^{\frac{1}{2}}$

FORTRAN SYMBOL	INTERPRETATION
TORTP	apparent t_p at $t_\ell = \tau_{trans}$ assuming entire flow to be turbulent
TORAPP	apparent value of τ_{trans} seen when effect of non-linear relation between ℓ and t_ℓ is neglected
TORAPT	as TORAPP, but for turbulent flow at $t_{\ell t}$ = TORLT
TZ	total hot flow time = turbulent hot flow time - TORLT + TOR
DTL	increment in observation time for each cycle of a run
TLT	$t_{\ell t}$ (TLT = TL - TOR + TORLT)
XLTT, XLTTI	(ℓ/ℓ_{mt})
G	$(\ell/\ell_{mt})^{1/5}$
TPT	particle time (apparent) assuming turbulent flow
TP	true particle time; for $t_\ell > \tau_{trans}$ TP = TPT - TORTP + TORLP
DLNMS	$(d \ln M_s/dt)$
DELTD	change in temperature due to shock deceleration = DELTD * DLNMS
EA	turbulent flow $[1 - (\ell/\ell_{mt})^{4/5}]$ laminar flow $[1 - (\ell/\ell_m)^{\frac{1}{2}}]$
TAPPT	apparent time during turbulent flow if (ℓ/ℓ_{mt}) is assumed to equal (t_ℓ/t_{mt}); time origin is origin of turbulent flow
TAPP	apparent time if effect of boundary layer on relation between time and distance is neglected; correct for laminar and turbulent flow.

FORTRAN SYMBOL	INTERPRETATION
TMA	laminar flow: TMA = TM turbulent flow: TMA = TMT
DA	$\frac{[1-(\ell/\ell_m)^{\frac{1}{2}}]M_{2s}}{[2 + (\gamma - 1)M_{2s}^2]^{(\gamma+1)/2(\gamma-1)}}$
XM2I, XM2IT	Mach number, M_2, at station (ℓ/ℓ_m)
DELTB	fraction change in temperature due to boundary layer effects
DTOTAL	fractional change in temperature due to both boundary layer and deceleration effects
TACT	change in temperature (K) due to boundary layer and deceleration effects
DELRO	fractional change in density due to boundary layer and deceleration effects
ROACT	change in density ratio due to boundary layer and deceleration effects
ISSW	Recycle card: if ISSW = 1, the program returns to the start and needs fresh data for a new mixture. A blank card ends the program.

Other symbols, which do not appear in the main program are:

Subroutine BLOOD:

CPJ(J), CPAJ(J)	specific heat of species J at constant pressure
CVJ(J), CVAJ(J)	specific heat of species J at constant volume
JJ	cycle counter
PCM	specific heat of gas mixture at constant pressure
VCM	specific heat of gas mixture at constant volume

Subroutine GRAVE:

TLI	estimate of TL calculated for laminar flow from trial value of (ℓ/ℓ_m)

Subroutine HEARSE:

XI	
XA	
XB	substitutions required for the solution of equation (5.
XC	
XE	

TABLE C.1.2

Input data for FLOCOR; a minimum of eight cards is required

CARD NUMBER	SYMBOL	FORMAT	COMMENT
1	NJOBS	(I5)	
2	XD	(F10.4)	
	GAMA4	(F6.3)	
	A4	(F8.5)	
	DER	(F6.3)	
	YID	(F7.4)	
	IS	(I3)	
3	ZJK(J,K)	(5A3)	a data card is
	XNJ(J)	(F5.2)	required for each
	XMWJ(J)	(F7.3)	species in the
	GJ(J)	(F7.3)	mixture
4	FJ(J)	(5F10.5)	up to five species are allowed
5	NTIMS	(I5)	
6	NUM	(A4)	if NJOBS > 1,
	U	(F6.3)	new cards 6 and 7
	T1	(F8.3)	are required for each job.
7	P1	(F7.3)	
	TL	(E10.4)	TL now unnecessary
	RHOS	(F8.4)	
	T2	(F8.2)	
8	ISSW	(I1)	any value other than unity ends run

```
        AUTOL       JOBTYPE=B   PRIORITY = 5   SIZE= 128  START= 083              DATE  13 07 78

&JOB;CH10;FLOCOR;


&OPTIONS;                                                                          TIME =  03

&FORTRAN;L;                                                                        TIME =  00
   0*
   1* C
   2* C      G MILLWARD(KEELE) CORRECTIONS FOR NON-UNIFORM FLOW IN SHOCK TUBES.
   3* C      THEORY OF H.MIRELS DEVELOPED FOR EXPLICIT USE BY R.A.STREHLOW.
   4* C
   5*        DIMENSION ZJK(5,5),XNJ(5),XMWJ(5),CPJ(5),CVJ(5),CPAJ(5),CVAJ(5),FJ
   6*       1(5),GAJ(5),GJ(5)
   7*        COMMON IS,T1,AY,BY,AT1MIX,AAMIX,GMIX,GAMIX,XMWAV,FJ,ZJK,XMWJ,GJ,PR
   8*       1ES,TO,XM,J,JJ,XNJ
   9*       1 FORMAT(30X,65H**********FLOW NONUNIFORMITY-EFFECT ON SHOCK PARAMET
  10*       1ERS**********)
  11*       2 FORMAT(30X,53H                  ADAPTED BY G.E.MILLWARD 25 AUGUST 196
  12*       18)
  13*         WRITE(2,5)
  14*       5 FORMAT(1H1)
  15*         WRITE(2,1)
  16*         WRITE(2,2)
  17*         WRITE(2,24)
  18*      24 FORMAT(30X,49H                  CORRECTED BY M.D.PEDLEY 8 FEB 1977)
  19*       4 CONTINUE
  20*         JJ=0
  21* C
  22* C      READ IN DATA
  23* C
  24* C
  25* C      CARD 1 START COL 1. NJOBS=NUMBER OF JOBS(I5)FOR ONE MIXTURE
  26* C
  27*         READ(7,21)NJOBS
  28*      21 FORMAT(I5)
  29* C
  30* C      CARD 2
  31* C      XD LENGTH OF DRIVER SECTION (MM)
  32* C      CALCULATION OF HOT FLOW TIME FOR IDEAL SHOCK CONDITIONS
  33* C      IS NOT REALLY NECESSARY
  34* C      GAMMA4  SPECIFIC HEAT RATIO OF DRIVER GAS  (F6.3)
  35* C      A4  SPEED OF SOUND IN DRIVER GAS (KM/S)  (F8.5)
  36* C      DER  RADIUS OF TUBE IN CM   (F6.3)
  37* C      YID  VELOCITY DECREMENT ( %/METRE )  (F7.4)
  38* C       IS  NUMBER OF SPECIES IN MIXTURE  (I3)
  39* C
  40*         READ(7,20)XD,GAMA4,A4,DER,YID,IS
  41*      20 FORMAT(F10.4,F6.3,F8.5,F6.3,F7.4,I3)
  42* C
  43* C      CARD 3 START COL 1. ZJK=SPECIES NAME(5A3),XNJ=NUMBER OF ATOMS IN
  44* C      SPECIES(F5.2),XMWJ=MOLECULAR WEIGHT OF SPECIES(F7.3),GJ=SPECIFIC
  45* C      RATIO OFSPECIES(F7.3)
  46* C      NUMBER OF SPECIES CARDS SIMILAR TO CARD 3 DEPENDS ON THE VALUE
  47* C      OF IS
  48* C
  49*         DO 51 J=1,IS
```

```
      90 FORMAT(5A3,1X,F5.2,F7.3,F7.3)
         READ(7,90)(ZJK(J,K),K=1,5),XNJ(J),XMWJ(J),GJ(J)
      51 CONTINUE
C
C     CARD 4 START COL 1. FJ=MOLE FRACTIONS OF SPECIES A TOTAL OF FIVE
C     SPECIES IS POSSIBLE,READ ACROSS THE CARD(5F10.5)
C
         READ(7,100)(FJ(J),J=1,IS)
    100 FORMAT(5F10.5)
C
C
C     CARD 5 NUMBER OF TIMES FLOW CORRECTIONS ARE TO BE CALCULATED
         READ(7,80)NTIMS
      80 FORMAT(I5)
         DO 2000 M=1,NJOBS
C     CARD 7 RUN NO (A4) U=SHOCK VEL( KM/S ),T1=ROOM TEMP.(F6.3,F8.3)
         READ(7,7)NUM,U,T1
       7 FORMAT(A4,F6.3,F8.3)
C
C     CARD 8 START COL 1. P1=DOWNSTREAM PRESSURE(F7.3),TL=OBSERVATION
C     TIME(E10.4),RHOS=DENSITY RATIO AVERAGE(F8.4),T2=AVERAGE SHOCK
C     TEMPERATURE(F8.2)
C
         READ(7,18)P1,TL,RHOS,T2
      18 FORMAT(F7.3,E10.4,F8.4,F8.2)
         JJ=JJ+1
         WRITE(2,22)NUM
      22 FORMAT(1H0,41X,11HRUN NUMBER=,A4)
      23 FORMAT(42X,16H----------------)
         WRITE(2,23)
C
C     CALCULATIONS ON DIAPHRAGM PRESSURE RATIO,AND THEORETICAL
C     OBSERVATION TIME
C
         CALL BLOOD
         CALL COFFIN
         XM=U/AT1MIX
         AM=U/AAMIX
         CY=AM**2
         XMS2=(((BY*CY)+2.)/((2.*GAMIX*CY)-BY))**0.5
         BA=AY/(BY*2.0)
         CA=XMS2/((2.0+BY*(XMS2**2))**BA)
         B=((2.*GAMIX*CY)-BY)/(AY)
         C=((GAMA4-1.)*AT1MIX)/(AY*A4)
         D=(AM-(1./AM))
         E=(-2.*GAMA4)/(GAMA4-1.)
         F=(1.+GAMA4)/(2.*(1.-GAMA4))
         PRES=((1.-(C*D))**E)*B
         TC=((1.-(C*D/AM))**F)*2.*XD/A4
         TO=TC*(1.-((2.*(CY-1.))/(CY*AY)))
         WRITE(2,11)U,XM,PRES,TO
   11 FORMAT(27X,F11.5,5X,F6.3,6X,F11.4,4X,F15.6)
C
C     CALCULATIONS OF EFFECT OF NON UNIFORM FLOW ON THE EXPERIMENTAL
C     INPUT PARAMETERS PRINT OUT OF TEMPERATURE AND DENSITY INCREASE
C

         AZ=3.142*(DER**2)
         AP=6.284*DER
         TM=5.15*((4.*AZ)**2)*P1/((XM**1.7)*(AP**2)*AT1MIX*10.0**5)
C     TM IS MAX HOT FLOW TIME FOR LAMINAR FLOW
```

```
110*  C
111*  C     CALCULATION OF LAMINAR TO TURBULENT FLOW TRANSITION POINT
112*  C
113*        TL=0.0
114*     30 CALL GRAVE(TL,TM,RHOS,XLT,FXLT,TAPP)
115*        V2=U*FXLT
116*        TOR=4.0*3.14159*DER*(U-V2)/(U*V2*10.0**4)
117*        IF((ABS(TOR-TL)).LT.1.0E-7) GOTO 31
118*        TL=TOR
119*        GOTO 30
120*     31 CONTINUE
121*        WRITE(2,32) TOR
122*     32 FORMAT(1H0,20X,24HLAMINAR FLOW DURATION = ,E10.4,3HSEC)
123*        XLTOR=XLT
124*        HA=XLTOR**0.5
125*        TORLP=-2.0*RHOS*TOR/XLTOR*(HA+ALOG(1.0-HA))
126*        TMT=11.44*((2.0*DER)**1.25)*(P1**0.25)/((XM**1.95)*AT1MIX*10.0**5)
127*  C     TMT IS MAX HOT FLOW TIME FOR TURBULENT FLOW
128*  C
129*        XLTT=XLT**0.625
130*        XLTORT=XLTT
131*        TL=TOR
132*        CALL HEARSE(TLT,TMT,TLTI,RHOS,XLTT,TAPPT,TL,TOR)
133*        TORLT=TLTI
134*        HB=XLTORT**0.2
135*        TORTP=1.25*RHOS*TORLT/XLTORT*(2.0*ATAN(HB)+ALOG((1.0+HB)/(1.0-HB))
136*       1-4.0*HB)
137*        TORAPP=TAPP
138*        TORAPT=TAPPT
139*        TZ=TMT-TORLT+TOR
140*        WRITE(2,37)TZ
141*     37 FORMAT(1H0,20X,16HHOT FLOW TIME = ,E10.4,3HSEC)
142*        DTL=1.0E-4
143*  C     DTL IS INCREMENT OF ORS TIME FOR EACH RUN
144*        IF(TZ.GT.1.0E-3) GOTO 33
145*        DTL=DTL/2.0
146*     33 CONTINUE
147*  C
148*        CALL DEATH(DER,P1,TL,RHOS,YID,T2)
149*        DO 1000 N=1,NTIMS
150*        CALL GRAVE(TL,TM,RHOS,XLT,FXLT,TAPP)
151*        IF (TL.LE.TOR) GOTO34
152*        TLT=TL-TOR+TORLT
153*        IF(TLT.GE.TMT) GOTO 1000
154*  C
155*        XLTT=TLT/TMT
156*        CALL HEARSE(TLT,TMT,TLTI,RHOS,XLTT,TAPPT,TL,TOR)
157*        G=XLTT**0.2
158*        TPT=1.25*RHOS*TLT/XLTT*(2.0*ATAN(G)+ALOG((1.0+G)/(1.0-G))-4.0*G)
159*        TP=TPT-TORTP+TORLP
160*        DLNMS=(10.0*YID*AT1MIX*XM)/((10.0*YID*AT1MIX*TZ*XM)+1.)
161*        DELTD=TPT*((2.*((GY-1.)**2))/((1.+((BY*GY)/2.))*(((2.*GAMIX*GY)/BY
162*       1)-1.)))
163*        EA=(1.0-(XLTT**0.8))
164*        TAPP=TAPPT-TORAPT+TORAPP
165*        TMA=TMT
166*        GOTO 35
167*     34 G=XLT**0.5
168*        TP=-2.0*RHOS*TL/XLT*(G+ALOG(1.0-G))
169*        DLNMS=(10.0*YID*AT1MIX*XM)/((10.0*YID*AT1MIX*TZ*XM)+1.)
```

```
      DELTD=T2*((2.*((CY-1.)**2))/((1.+((BY*CY)/2.))*(((2.*GAMIX*CY)/BY)
     1-1.)))
      EA=(1.0-XLT**0.5)
      TMA=TM
   35 DA=CA*EA
C
      XM2I=XMS2
   40 XM2IT=DA*((2.0+BY*(XM2I**2))**BA)
      IF ((XM2I-XM2IT).LT.0.0001) GOTO 41
      XM2I=XM2IT
      GOTO 40
   41 CONTINUE
      DELTB=((2.0+BY*(XMS2**2))/(2.0+BY*(XM2IT**2)))-1.0
      DTOTAL=DELTB+DELTD+DLNMS
      DELRO=DTOTAL/BY
      TACT=DTOTAL*T2
      ROACT=DELRO*RHOS
      WRITE(2,91)TL,TAPP,TMA,TP,DTOTAL,TACT,DELRO,ROACT
   91 FORMAT(4X,E10.4,3X,E10.4,3X,E10.4,3X,E10.4,4X,F7.5,3X,F10.2,6X,F8.
     1 4,4X,F10.2)
      IF(TL.NE.TOR) GOTO 36
      TL=0.0
   36 TL=TL+DTL
 1000 CONTINUE
 2000 CONTINUE
C     ROUTINE BELOW RECYCLES PROGRAM IF FRESH DATA MUSTBE USED
C     BLANK CARD ENDS RUN; NUMBER 1 ON CARD RECYCLES
      READ(7,3)ISSW
    3 FORMAT(I1)
      IF (ISSW.EQ.1) GO TO 4
      STOP
      END


      SUBROUTINE DEATH(DER,P1,TL,RHOS,YID,T2)
C
C     THIS SUBROUTINE PRINTS OUT HEADINGS FOR THE NON UNIFORM
C     CORRECTION CALCULATIONS
C
      DIMENSION ZJK(5,5),XNJ(5),XMWJ(5),CPJ(5),CVJ(5),CPAJ(5),CVAJ(5),FJ
     1(5),GAJ(5),GJ(5)
      COMMON IS,T1,AY,BY,ATIMIX,AAMIX,GMIX,GAMIX,XMWAV,FJ,ZJK,XMWJ,GJ,PR
     1ES,TO,XM,J,JJ,XNJ
      WRITE(2,700)
  700 FORMAT(1H0,20X,75H**********CORRECTION TO NON UNIFORM FLOW USING M
     1IRELS   EQUATIONS**********)
  750 FORMAT(1H0,10X,10HT2 (DEGK)=,F6.1,5X,14HINITIAL PRES =,F8.3,5X,8HR
     102/RO1=,F8.4)
      WRITE(2,750)T2,P1,RHOS
      WRITE(2,752)YID,DER
  752 FORMAT(10X,19HVELOCITY DECREMENT=,F7.4,5X,7HRADIUS=,F9.5)
      WRITE(2,751)
  751 FORMAT(1H0,4X,8HORS TIME,5X,8HAPP TIME,5X,8HMAX TIME,3X,13HPARTICL
     1E TIME,2X,7HDELT/T2,3X,13HTEMP INCREASE,4X,7HDELR/RO,4X,10HDENSITY
     2 INCREASE)
      RETURN
      END


      SUBROUTINE COFFIN
```

```
C
C     THIS SUBROUTINE PRINTS OUT THE SPECIES CHARACTERISTICS AND
C     THE HEADINGS FOR P4/P1 AND HOT FLOW TIME
C
      DIMENSION ZJK(5,5),XNJ(5),XMWJ(5),CPJ(5),CVJ(5),CPAJ(5),CVAJ(5),FJ
     1(5),GAJ(5),GJ(5)
      COMMON IS,T1,AY,BY,AT1MIX,AAMIX,GMIX,GAMIX,XMWAV,FJ,ZJK,XMWJ,GJ,PR
     1ES,TO,XM,J,JJ,XNJ
  510 FORMAT(1H0,21X,27H                        SPECIES,10X,10HMOLE FRACT,5X
     1,2HMW,5X,6HGAMMA1)
      WRITE(2,510)
      DO 530 J=1,IS
      WRITE(2,540)(ZJK(J,K),K=1,5),FJ(J),XMWJ(J),GJ(J)
  530 CONTINUE
  540 FORMAT(42X,5A3,F10.5,F12.3,F9.3)
      WRITE(2,550)T1,XMWAV,AT1MIX,GMIX
  550 FORMAT(3140                    T1 (DEGK)=,F6.1,5X,7HAV MW =,F8.3,
     15X,17HMIX SOUND SPEED =,F8.5,5X,12HGAMMA(MIX) =,F6.3)
      WRITE(2,10)
   10 FORMAT(//34X,3HVEL,7X,5HMACHN,10X,5HP4/P1,10X,18HTEST TIME(MU-SECS
     1))
      RETURN
      END

      SUBROUTINE BLOOD
C
C     THIS SUBROUTINE CALCULATES THE SPECIFIC HEAT RATIO,THE AVERAGE
C     MOLECULAR WEIGHT AND THE SPEED OF SOUND IN THE MIXTURE.
C
      DIMENSION ZJK(5,5),XNJ(5),XMWJ(5),CPJ(5),CVJ(5),CPAJ(5),CVAJ(5),FJ
     1(5),GAJ(5),GJ(5)
      COMMON IS,T1,AY,BY,AT1MIX,AAMIX,GMIX,GAMIX,XMWAV,FJ,ZJK,XMWJ,GJ,PR
     1ES,TO,XM,J,JJ,XNJ
      XMWAV=0.0
      GMIX=0.0
      CP=0.0
      GAMIX=0.0
      PCM=0.0
      VCM=0.0
      PCAM=0.0
      VCAM=0.0
      DO 50 J=1,IS
      XMWAV=XMWAV+FJ(J)*XMWJ(J)
      CPJ(J)=1.9872*GJ(J)/(GJ(J)-1.)
      CVJ(J)=CPJ(J)-1.9872
      PCM=PCM+FJ(J)*CPJ(J)
      VCM=VCM+FJ(J)*CVJ(J)
   50 CONTINUE
      GMIX=PCM/VCM
      GAMIX=GMIX
      AAMIX=1./10.*SQRT(GAMIX*0.8313*T1/XMWAV)
      AT1MIX=1./10.*SQRT(GMIX*0.8313*T1/XMWAV)
      AY=GAMIX+1.
      BY=GAMIX-1.
      RETURN
      END

C
```

```
282*  C
283*        SUBROUTINE GRAVE(TL,TM,RHOS,XLT,FXLT,TAPP)
284*  C
285*  C
286*  C     THIS SUBROUTINE CALCULATES (L/LM) FROM (TL/TM) FOR LAMINAR FLOW
287*  C
288*        DIMENSION ZJK(5,5),XNJ(5),XMWJ(5),CPJ(5),CVJ(5),CPAJ(5),CVAJ(5),FJ
289*       1(5),GAJ(5),GJ(5)
290*        COMMON IS,T1,AY,BY,AT1MIX,AAMIX,GMIX,GAMIX,YMWAV,FJ,ZJK,XMWJ,GJ,PR
291*       1ES,TO,XM,J,JJ,XNJ
292*  C
293*        XLT=TL/TM
294*    110 TLI=2.0*RHOS*TM*((XLT**0.5)+(RHOS-1.0)*ALOG((RHOS-1.0)/(RHOS-1.0+(
295*       1XLT**0.5))))
296*        XLT=XLT*TL/TLI
297*        IF(ABS(TLI-TL).LT.1.0E-7) GO TO 111
298*        GO TO 110
299*    111 CONTINUE
300*        TAPP=TM*XLT*RHOS/(RHOS-1.0)
301*        FXLT=(1.0-(1.0-(XLT**0.5))/RHOS)
302*        RETURN
303*        END


304*        SUBROUTINE HEARSE(TLT,TMT,TLTI,RHOS,XLTT,TAPPT,TL,TOR)
305*  C
306*  C
307*  C     THIS SUBROUTINE CALCULATES (L/LM) FROM (TL/TM) FOR TURBULENT FLOW
308*  C
309*        DIMENSION ZJK(5,5),XNJ(5),XMWJ(5),CPJ(5),CVJ(5),CPAJ(5),CVAJ(5),FJ
310*       1(5),GAJ(5),GJ(5)
311*        COMMON IS,T1,AY,BY,AT1MIX,AAMIX,GMIX,GAMIX,YMWAV,FJ,ZJK,XMWJ,GJ,PR
312*       1ES,TO,XM,J,JJ,XNJ
313*  C
314*        XI=XLTT**0.2
315*        XA=1.0-(1.0/RHOS)
316*        XB=1.0/RHOS
317*        XC=(XA/XB)**0.25
318*        XE=SQRT(2.0)
319*    120 TLTI=5.0*TMT*(XI-(XA/XB)*((1.0/(4.0*(XC**3)*XE))*ALOG((XI**2+XC*XE
320*       1*XI+XC**2)/(XI**2-XC*XE*XI+XC**2))+(1.0/(2.0*XE*(XC**3)))*ATAN((XC
321*       2*XE*XI)/(XC**2-XI**2))))/XB
322*        IF(TL.EQ.TOR) GO TO 121
323*        XLTT=XLTT*TLT/TLTI
324*        IF(ABS(TLTI-TLT).LT.1.0E-7) GO TO 121
325*        XI=XLTT**0.2
326*        GO TO 120
327*    121 CONTINUE
328*        TAPPT=TMT*XLTT*RHOS/(RHOS-1.0)
329*        RETURN
330*        END



COMMON BLOCKS  START LENGTH
UNNAMED        32768     118


SUBPROGS       CODE          CONSTANT      LOCAL WKSPACE  DYNAMIC
```

```
            START  LENGTH   START  LENGTH   START  LENGTH  ARRAYS
MAINPROG    25351     722    6461     354    7105     139       0
DEATH       25310      41    6815     106    7244       6       0
COFFIN      25276      34    6921     114    7250       2       0
BLOOD       25139     137    7035      26    7252      20      20
GRAVE       25058      81    7061      18    7272      20       0
HEARSE      24881     177    7079      26    7292      60       0

FREE STORE          7352 TO    24880   AND   32886 TO    65536

&RUN;                                                          TIME :
```

```
          **********FLOW NONUNIFORMITY-EFFECT ON SHOCK PARAMETERS**********
                     ADAPTED BY G.F.MILLWARD 25 AUGUST 1968
                     CORRECTED BY M.D.PEDLEY 8 FEB 1977

                    RUN NUMBER=M130
                    ---------------

                    SPECIES          MOLE FRACT      MW      GAMMA1
                    OXYGEN             1.00000      32.000    1.400

          T1 (DEGK)= 293.0     AV MW =  32.000     MIX SOUND SPEED = 0.32644     GAMMA(MIX) = 1.400

                      VEL       MACHN        P4/P1          TEST TIME(MU-SECS)
                    1.40410     4.301       181.0117          587.474173

          LAMINAR FLOW DURATION = 0.3095E-03SEC

          HOT FLOW TIME = 0.4803E-03SEC

          **********CORRECTION TO NON UNIFORM FLOW USING MIRELS  EQUATIONS**********

          T2 (DEG()=1137.1     INITIAL PRES =   6.500     R02/R01= 5.4550
          VELOCITY DECREMENT= 1.0000     RADIUS= 2.54000

     DHS TIME     APP TIME     MAX TIME   PARTICLE TIME  DELT/T2   TEMP INCREASE   DELR/R0   DENSITY INCREASE
    0.3095E-03  0.3255E-03  0.2216E-02  0.2219E-02  0.05399        64.08          0.1350          0.74
    0.6000E-04  0.5102E-04  0.2216E-02  0.3005E-03  0.01501        17.82          0.0375          0.20
    0.1000E-03  0.1229E-03  0.2216E-02  0.6286E-03  0.02340        27.77          0.0595          0.32
    0.1500E-03  0.1353E-03  0.2216E-02  0.9779E-03  0.03096        36.75          0.0774          0.42
    0.2000E-03  0.2082E-03  0.2216E-02  0.1345E-02  0.03823        45.38          0.0956          0.52
    0.2500E-03  0.2516E-03  0.2216E-02  0.1734E-02  0.04542        53.91          0.1135          0.62
    0.3000E-03  0.3152E-03  0.2216E-02  0.2140E-02  0.05261        62.45          0.1315          0.72
    0.3500E-03  0.3597E-03  0.2482E-03  0.2605E-02  0.04130        49.03          0.1033          0.56

  END


 $END;

LINES PRINTED = 20417
REAL TIME =  0001  45
CPU TIME =  0000  36.608
   A
```

C.2. Vibrational Relaxation Program, VIBREL

The calculations performed in this program are described in Chapters 5 and 6. The mainprogram and subroutines TIMDIS and NUMINT are written by M.D. Pedley; subroutine H SHOCK is taken from Millikan's program for calculation of the conditions behind the shock front, and the polynomial curve fitting routine, CURFIT, was written by W.R. Graves.

Two forms of this program are used; the original program reads the required information from cards, while the version incorporated in the interactive graphics program as subroutine VIBREL receives data from and returns the results of the calculations to the mainprogram by means of the argument of the subroutine. The original version is shown here, together with a shortened version of a typical printout; the headings in the table of calculations are explained below:

(i) OBS TIME is the experimental laboratory time, t_ℓ

(ii) TPACT is the true particle time

(iii) TPFA1 is the particle time calculated using the relation

$$t_p = \rho_{A1} t_\ell \qquad (C.1)$$

in which the frozen conditions are assumed.

(iv) TPREL is the particle time calculated using the relation

$$t_p = \rho_{21} t_\ell \qquad (4.9)$$

in which the relaxed conditions are assumed.

(v) TP*FA1 is the hypothetical particle time at which the magnitude of the "frozen" function, $\rho_{A1}\, e^{-u\alpha_\ell (1-1/\rho_{A1})^{(TP*FA1)}}$ is equal to the magnitude of the correct function,

$$\rho_{t1}\, e^{-u\alpha_\ell \int_0^{tp} (1-1/\rho_{t1})\, dt_p}$$

, at the true particle time.

(vi) TP*REL is the hypothetical particle time at which the magnitude of the "relaxed" function $\rho_{21}\, e^{-u\alpha_{\ell}(1-1/\rho_{21})(TP*REL)}$ is equal to the magnitude of the correct function at the true particle time. TP*FAl and TP*REL are calculated in subroutine TIMDIS; the forms described here are those used when following the emission from $O_2(^1\Sigma_g^+)$. The times are estimated at alternate laboratory times; this is a result of the numerical integration using Simpson's Rule in subroutine NUMINT.

(vii) TEMP is the temperature at each observation time t_{ℓ} after the shock front has passed the observation station

(viii) DENSITY RATIO is the ratio ρ_{t1} at time t_{ℓ}.

Table C.2.1 shows the input data required by the program; when used in the graphics program, much of this information is provided by data statements at the start of subroutine VIBREL.

TABLE C.2.1

Input data for VIBREL; a minimum of six cards is required

CARD NUMBER	SYMBOL	FORMAT	COMMENT
1	A	(F6.2)	coefficients in the
	B	(F8.3)	temperature dependence of the relaxation time, τ_{vib}, for pure oxygen
2	IS	(Is)	maximum number of species in mixtures.
	HDEL	(F6.1)	maximum interation error in DISHOCK routine.
3	ZJK(J,K)	(5A3)	name of species J
	ANJ(J)	(F3.0)	number of atoms in species J
	X(J)	(F3.0)	X=0 or X=1 defines species J frozen or relaxed in State B.
	XMWJ(J)	(F6.2)	molecular weight of species J
	SHJ(J)	(F6.2)	specific heat ratio for species J
4	THETJ(J)		coefficients obtained by
	AJ(J)		polynomial curve fitting to
	BJ(J)	(5E11.4)	data in J.A.N.A.F. tables
	CJ(J)		of heat capacities; required
	DJ(J)		for H SHOCK.

Cards 3-4 are repeated for each species defined by IS; cards 1-4 are replaced by data statements in the graphics program.

5	RUNNO	(A6)	shock run number
	IS	(I2)	number of species in shock
	U	(F6.0)	shock velocity (Km s^{-1})
	T1	(F6.0)	initial temperature (K)
	TIMAX	(F6.0)	maximum observation time at which calculations are made (μs)
	DELTIM	(F6.0)	time increment (μs)
	DECAYL	(F6.0)	pre-shock decay (m^{-1})
	PBS	(F5.2)	pre-shock emission (mV)
	XN	(F3.0)	X (J=2)
	FRAC	(F6.0)	mole fraction of second species (J=2)

Table C.2.1 continued:

The program is restricted to mixtures of two species because of the negligible experimental information on vibrational relaxation in mixtures of more than two components. This has not mattered in this work; as it stands calculations can be made in pure oxygen and in oxygen/nitrogen mixtures, but conversion for other species should not be difficult.

CARD NUMBER	SYMBOL	FORMAT	COMMENT
6	IRET	(I1)	any number except IRET=1 ends program.

```
        AUTOL       JOBTYPE=B   PRIORITY = 5   SIZE= 128  START= 083              DATE  21 08 78

&JOB;CH101

&OPTIONS;                                                                          TIME =

&FORTRAN;L;                                                                        TIME =
    0*
    1*  C
    2*        DIMENSION FJ(5),ZJK(5,5),AJ(5),BJ(5),CJ(5),DJ(5),THETJ(5),XMWJ(5),
    3*       1SHJ(5),HJ(5),ANJ(5),X(5)
    4*        COMMON FJ,ZJK,AJ,BJ,CJ,DJ,THETJ,XMWJ,SHJ,HT1,HJ,ANJ,X,T,HT,T1,XMW,
    5*       1VELT1,SH,IS
    6*        COMMON /TIMDIS/ RHOA1,RHO21,RHOT,TIM,TPVA,TPV2,DECAYL,U,TA,T2,AX
    7*        COMMON /NUMINT/ F(10,10),JJ(10),AINT(10),M,K,DELX
    8*        COMMON /CURFIT/ XX(200),YY(200),N
    9*        DIMENSION XTP(1024)
   10*        WRITE(2,110)
   11*    110 FORMAT(1H1,12X,77H**********VIBRATIONAL RELAXATION OF SHOCKED OXYG
   12*       1EN; TIME DEPENDENCE**********)
   13*        WRITE(2,120)
   14*    120 FORMAT(40X,23HM.D.PEDLEY 12 SEPT 1977)
   15*        READ(7,40)A,B
   16*     40 FORMAT(F6.2,F8.3)
   17*  C
   18*  C     CARD 1; A AND B ARE COEFFS IN THE TEMP DEPENDENCE OF THE
   19*  C     RELAXATION TIME TOR
   20*  C
   21*  C
   22*        READ(7,2)IS,HDEL
   23*     2 FORMAT(I2,F6.1)
   24*  C
   25*  C     IS IS MAX NUMBER OF SPECIES IN MIXTURES; HDEL IS MAX ITERATION
   26*  C     ERROR FOR DISHOCK
   27*  C
   28*        DO 12 J=1,IS
   29*        READ(7,5)(ZJK(J,K),K=1,5),ANJ(J),X(J),XMWJ(J),SHJ(J)
   30*     5 FORMAT(5A3,2F3.0,2F6.2)
   31*  C
   32*  C     ZJK IS NAME OF SPECIES (5A3), ANJ(J) IS NUMBER OF ATOMS IN MOL
   33*  C     X(J) =0 ,SPECIES FROZEN IN STATE BI X(J)= 1,SPECIES RELAXED
   34*  C     XMWJ(J) IS MOLECULAR WEIGHT, SHJ(J) IS SPECIFIC HEAT RATIO, GAMMA
   35*  C
   36*        READ(7,4)THETJ(J),AJ(J),BJ(J),CJ(J),DJ(J)
   37*     4 FORMAT(5E11.4)
   38*  C
   39*  C     THE FIVE CONSTANTS IN JANAF TABLES OF HEAT CAPACITY
   40*  C
   41*    12 CONTINUE
   42*   200 CONTINUE
   43*        READ(7,3)RUNNO,IS,U,T1,TIMAX,DELTIM,DECAYL,PBS,XN,FRAC
   44*     3 FORMAT(A6,I2,5F6.0,F5.2,F3.0,F6.0)
   45*  C
   46*  C     RUN NUMBER, NUMBER OF SPECIES FOR THIS SHOCK, SHOCK VELOCITY
   47*  C     INITIAL TEMP., MAX OBSERVATION TIME, INCREMENT IN OBS, TIME
   48*  C     ( BOTH IN US ), DECAY (M-1), INITIAL PRESSURE ( MMHG )
   49*  C     XN= X(J=2); FRAC IS MOLE FRACTION OF THE SECOND SPECIES
   50*  C
   51*        FJ(1)=1.0-FRAC
   52*        FJ(2)=FRAC
   53*        X(2)=XN
   54*  C
```

```
      C=130.49-129.3*(FJ(1))+102.7*((FJ(1))**2)
      D=-4.159+2.118*(FJ(1))-0.7918*((FJ(1))**2)
C
C     C AND D ARE COEFFS IN THE TEMP DEPENDENCE OF THE RELAXATION
C     TIME TOR, FOR THE SECOND SPECIES, NITROGEN
C
      WRITE(2,130) RUNNO
  130 FORMAT(//41X,11HRUN NUMBER=,A6)
      WRITE(2,140)
  140 FORMAT(42X,15H=-=-=-=-=-=-=-=-=-=-=-=-)
      WRITE(2,260)
  260 FORMAT(//14X,7HSPECIES,3X,10HMOLE FRACT,3X,6HGAMMA1,3X,41HVIB. ENE
     1RGY INCL. IN STATE B (1=YES,0=NO))
      DO 290 J=1,IS
      WRITE(2,270)(ZJK(J,K),K=1,5),FJ(J),SHJ(J),X(J)
  270 FORMAT(11X,5A3,1X,F4.2,6X,F6.2,22X,F3.1)
  290 CONTINUE
      WRITE(2,180)T1,PBS,DECAYL
  180 FORMAT(1H0,14X,14HINITIAL TEMP =,F6.1,1HK,5X,19HINITIAL PRESSURE =
     1 ,F5.2,2HMM,5X,6HDECAY = ,F6.3,3HM=1)
      WRITE(2,280)TIMAX,DELTIM
  280 FORMAT(1H0,21X,22HMAX OBSERVATION TIME =,F6.0,2HUS,5X,16HTIME INCR
     1EMENT =,F6.1,2HUS)
      WRITE(2,1500)U
 1500 FORMAT(1H0,40X,16HSHOCK VELOCITY =,F6.3,4HKM/S)
C
C     THIS ROUTINE USES THE OLD DISHOCK PROGRAM BASED ON MILLIKAN TO
C     CALCULATE TEMPS TA,TB,T2, DENSITY RATIOS RHOA1,RHOB1,RHO21, AND
C     PRESSURE RATIOS PA1,PB1,P21
C
      XMW=0.0
      SH=0.0
      DO 13 J=1,IS
      XMW=XMW+FJ(J)*XMWJ(J)
   13 SH=SH+FJ(J)*SHJ(J)
      VELT1=1.0/10.0*SQRT(SH*0.8313*T1/XMW)
  530 XM=U/VELT1
      Y=XM**2
      PA1=(2.0*SH*Y-(SH-1.0))/(SH+1.0)
      RHOA1=((SH+1.0)*Y)/((SH-1.0)*Y+2.0)
      TRA=PA1/RHOA1
      TA=TRA*T1
      P21=PA1
      PB1=PA1
      RHO21=RHOA1
      RHOB1=RHOA1
      T=T1
C
C     THIS LOOP CALCULATES SHOCK CONDITIONS IN OXYGEN/NITROGEN MIXTURES
C     FOR OXYGEN RELAXED AND NITROGEN FROZEN (STATE B)
C
      CALL H SHOCK
      HT1=HT
      T=TA
      IF(IS.EQ.1) GO TO 531
C
      DO 800 J=1,IS
      IF(X(J))631,631,820
  631 CALL H SHOCK
      HDIFT=HT-HT1
      HDIFF=119.503*(U**2)*(1.0-(1.0/RHOB1)**2)*XMW
      ERROR=HDIFT-HDIFF
      ERR=ABS(ERROR)
      IF (HDEL-(ERR))632,632,633
  632 T=T-ERROR/10.0
      RHOB1=PB1*(T1/T)
```

```
      PB1=1.0*(120.274*XMW*(U**2)*(1.0-(1.0/RHOB1)))/T1
      RHOB1=PB1*(T1/T)
      GO TO 631
  633 CONTINUE
C
      TH=T
      X(J)=1.0
      GO TO 830
  820 CONTINUE
  800 CONTINUE
  830 T=T1
C
C     THIS LOOP CALCULATES SHOCK CONDITIONS WHEN OXYGEN AND NITROGEN
C     ARE BOTH RELAXED (STATE 2)
C
      CALL H SHOCK
      HT1=HT
      T=TA
  531 CALL H SHOCK
      HDIFT=HT-HT1
      HDIFF=119.503*(U**2)*(1.0-(1.0/RHO21)**2)*XMW
      ERROR=HDIFT-HDIFF
      ERR=ABS(ERROR)
      IF (HDEL-(ERR))532,532,533
  532 T=T-ERROR/10.0
      RHO21=P21*(T1/T)
      P21=1.0*(120.274*XMW*(U**2)*(1.0-(1.0/RHO21)))/T1
      RHO21=P21*(T1/T)
      GO TO 531
  533 CONTINUE
C
      T2=T
C
C     THIS ITERATIVE LOOP CALCULATES DENSITY, TEMP AND PRESSURE AT ANY
C     GIVEN TIME AFTER THE SHOCK HAS PASSED, LAB AND PARTICLE TIME,
C
C     THE EXACT PARTICLE TIME (TP) IS CALCULATED AT EACH LAB TIME BY
C     NUMERICAL INTEGRATION USING BOTH SIMPSONS RULE AND THE
C     TRAPEZIUM RULE (THE LATTER TO EXTRAPOLATE INTERMEDIATE POINTS )
C
C
      WRITE(2,1000)
 1000 FORMAT(1H0,10X,8HOBS TIME,4X,5HTPACT,7X,5HTPPA1,7X,5HTPREL,5X,6HTP
     1*PA1,4X,6HTP*REL,4X,4HTEMP,3X,13HDENSITY RATIO,6X,4HTIME)
C
      IBACK=0
      T=TA
      RHOT=RHOA1
      PT=PA1
      FLOOR=0.0
      M=1
      TOR2=0.0
      AINT(1)=0.0
      TP=0.0
      RHOTA=RHOT
      RHOTB=RHOT
      DECAYL=DECAYL*1.0E-3
      XX(1)=0.0
      IF(IBACK.NE.2) GO TO 1400
      YY(1)=(RHOA1**2)*((TA/T1)**0.5)
      GO TO 1410
 1400 CONTINUE
      YY(1)=RHOA1
 1410 CONTINUE
      I=2
C
      DO 2000 K=1,10
```

```
187*        JJ(K)=1
186*  2000 CONTINUE
189* C
190* C
191* C
192*        XSENS=220.0
193*        XORIG=119.27
194*        XTB=220.0
195*        IBACK=1
196*        DELX=DELTIM
197* C
198* C
199* C
200*        IXORIG=IFIX(XORIG)
201*        XOR2=FLOAT(IXORIG)
202*        XB=XOR2-XORIG
203*        IF(XB.LE.(0.0)) XB=(1.0+XB)
204* C
205*        II=1
206*        TIME=DELTIM
207*  5010 CONTINUE
208*        IF(TIME.GT.XORIG) GO TO 5020
209*        XTP(II)=TIME*RHOA1
210*        TIME=TIME+DELTIM
211*        II=II+1
212*        GO TO 5010
213*  5020 CONTINUE
214*        TIM=TIME-XORIG
215* C
216* C
217*  3000 CONTINUE
218*        IF(M.EQ.1) GO TO 3005
219*        IF(JJ(1).EQ.1) GO TO 3010
220*        TP=AINT(1)+DELTIM*(RHOTB+4.0*RHOTA+RHOT)/3.0
221*        TP=TP+AX
222*        GO TO 3100
223*  3005 TP=(RHOA1+RHOT)*TIM/2.0
224*        AX=TP
225*        GO TO 3100
226*  3010 TP=AINT(1)+(RHOT+RHOTA)*DELTIM/2.0
227*        TP=TP+AX
228*  3100 CONTINUE
229*        IF(IS.EQ.1) GOTO 50
230* C
231* C     THIS LOOP CALCULATES CONDITIONS FOR OXYGEN/NITROGEN MIXTURES
232* C
233*   330 TORATM=EXP(A*(T**(-0.333333))+B)
234*        TORAT2=EXP(C*(T**(-0.333333))+D)
235*   340 TOR=TORATM*760.0/(PT*PBS)
236*        TOR2=TORAT2*760.0/(PT*PBS)
237*   350 PT1=(P21+(EXP(-TP/TOR))*(PA1-PB1)+(EXP(-TP/TOR2))*(PB1-P21))
238*        PT=PT1+SH*P**FLOCOR/RHOT
239*        TORI=TORATM*760.0/(PT*PBS)
240*        IF((ABS(TOR-TORI)),LT.0.8) GOTO 360
241*        TOR=TORI
242*        GOTO 350
243*   360 CONTINUE
244*        TT=T2+(EXP(-TP/TOR))*(TA-TB)+(EXP(-TP/TOR2))*(TB-T2)
245*        TT=TT+(SH-1.0)**FLOCOR/RHOT
246*        IF((ABS(TT-T)),LT.0.5) GOTO 370
247*        T=TT
248*        GOTO 330
249*   370 CONTINUE
250*        RHOTI=RHO21+(EXP(-TP/TOR))*(RHOA1-RHOR1)+(EXP(-TP/TOR2))*(RHOR1-
251*       1RHO21)
252*        RHOTI=RHOTI+FLOCOR
```

```
      IF((ABS(RHOT-RHOTI)).LT.0.0005) GOTO 85
      RHOT=RHOTI
      GO TO 3000
C
C     THIS LOOP CALCULATES CONDITIONS FOR PURE OXYGEN
C
   50 TORATM=EXP(A*(T**(-0.333333))+B)
   55 TOR=TORATM*760.0/(PT*PBS)
   60 PT1=(P21+(EXP(-TP/TOR))*(PA1-P21))
      PT=PT1+SH*PT*FLOCOR/RHOT
      TORI=TORATM*760.0/(PT*PBS)
      IF((ABS(TOR-TORI)).LT.0.8) GOTO 70
      TOR=TORI
      GOTO 60
   70 CONTINUE
      TT=T2+(EXP(-TP/TOR))*(TA-T2)
      TT=TT+(SH+1.0)*T*FLOCOR/RHOT
      IF((ABS(TT-T)).LT.0.5) GOTO 80
      T=TT
      GOTO 50
   80 CONTINUE
      RHOTI=RHO21+(EXP(-TP/TOR))*(RHOA1-RHO21)
      RHOTI=RHOTI+FLOCOR
      IF((ABS(RHOT-RHOTI)).LT.0.0005) GOTO 85
      RHOT=RHOTI
      GO TO 3000
   85 CONTINUE
      RHOTA=RHOT
C
C
C     TEMPERATURE AND DENSITY AND PRESSURE RATIOS, AND THE VIBRATIONAL
C     RELAXATION RATES, TOR AND TOR2, ARE ALL INTEGRATED NUMERICALLY
C     USING SIMPSONS RULE (SUBROUTINE NUMINT) TO FIND THE MEAN VALUES
C
      IF(M.NE.1) GO TO 86
      F(1,1)=RHOT
      F(1,2)=T
      F(1,3)=TOR
      F(1,4)=TOR2
      F(1,5)=PT
   86 CONTINUE
C
      K=1
      F(4,1)=RHOT
      CALL TIMDIS(IBACK,T)
      WRITE(2,90)TIM,TP,T,RHOT
   90 FORMAT(9X,F7.2,5X,F7.2,50X,F5.0,6X,F5.3)
      WRITE(2,92)TIME
   92 FORMAT(1H+,100X,F7.2)
      IF(M.EQ.1) GO TO 1420
      IF(JJ(1).EQ.2) GO TO 1420
      TPA=TIM*RHOA1
      TP2=TIM*RHO21
      RHOTB=RHOT
      WRITE(2,95)TPA,TP2,TPVA,TPV2
   95 FORMAT(1H+,32X,F7.2,5X,F7.2,4X,F7.2,4X,F7.2)
      IF(TP.GT.TPV2) GO TO 1420
      IF(TIME.GT.XTR) GO TO 1420
      XX(I)=TP
      IF(IBACK.NE.2) GO TO 1418
      YY(I)=(RHOT**2)*((T/T1)**0.5)*EXP(DECAYL*U*(AINT(1)-TIM))
      GO TO 1419
 1418 CONTINUE
      YY(I)=RHOT*EXP(DECAYL*U*(AINT(1)-TIM))
 1419 CONTINUE
      I=I+1
```

```
319*   1420 CONTINUE
320*        IF(TIME.GT.XTB) GO TO 4100
321*        F(4,2)=T
322*        F(4,3)=TOR
323*        F(4,4)=TOR2
324*        F(4,5)=PT
325*        DO 4000 K=2,5
326*        CALL NUMINT
327*   4000 CONTINUE
328*        IF(TIME.NE.XTB) GO TO 4100
329*        AINT(6)=AINT(1)
330*        IF(JJ(1).EQ.2) GO TO 4020
331*        TEND=TIME-XB
332*        GO TO 4100
333*   4020 TEND=TIME-DELTIME-XB
334*   4100 CONTINUE
335* C
336*        XTP(II)=TP
337*        TIME=TIME+DELTIME
338*        II=II+1
339*        M=M+1
340*        IF(II.GT.22) GO TO 210
341*        GO TO 5010
342* C
343*    210 CONTINUE
344*        IF(M.LE.3) GO TO 2003
345* C
346*        RHOAVG=AINT(6)/TEND
347*        TAVG=AINT(2)/TEND
348*        TORAVG=AINT(3)/TEND
349*        TORAV2=AINT(4)/TEND
350*        PAVG=AINT(5)/TEND
351*    420 WRITE(2,150)
352*    150 FORMAT(//33X,4HTEMP,3X,13HDENSITY RATIO,4X,14HPRESSURE RATIO)
353*        WRITE(2,160)TA,RHOA1,PA1
354*    160 FORMAT(25X,6HFROZEN  ,F5.0,6X,F5.3,14X,F5.2)
355*        IF(IS.EQ.1) GOTO 430
356*        WRITE(2,380)TB,RHOB1,PB1
357*    380 FORMAT(25X,6HSTATE B ,F5.0,6X,F5.3,14X,F5.2)
358*    430 WRITE(2,170)T2,RHO21,P21
359*    170 FORMAT(25X,8HRELAXED ,F5.0,6X,F5.3,14X,F5.2)
360*        WRITE(2,220)TAVG,RHOAVG,PAVG
361*    220 FORMAT(25X,6HMEAN    ,F5.0,6X,F5.3,14X,F5.2)
362*        IF(IS.EQ.1) GOTO 440
363*        WRITE(2,390)TORAVG,TORAV2
364*    390 FORMAT(1H0,21X,23HMEAN RELAXATION TIMES =,F7.2,7HUS(O2),,F7.2,6HUS
365*       1(N2))
366*        GOTO 450
367*    440 WRITE(2,230)TORAVG
368*    230 FORMAT(1H0,29X,27HMEAN RELAXATION TIME, TOR =,F7.2,2HUS)
369*        GO TO 450
370*   2003 WRITE(2,2004)
371*   2004 FORMAT(1H0,35X,31HNOT ENOUGH DATA FOR INTEGRATION)
372*    450 N=I-1
373*        CALL CURFIT
374*        READ(7,190)IRET
375*    190 FORMAT(I1)
376*        IF(IRET.EQ.1) GOTO 200
377* C
378* C      CARD 6: IRET (I1) IS A RECYCLE CARD; A BLANK CARD ENDS THE RUN
379* C
380*        STOP
381*        END

382* C
```

```
      SUBROUTINE H SHOCK
      DIMENSION FJ(5),ZJK(5,5),AJ(5),BJ(5),CJ(5),DJ(5),THETJ(5),XMWJ(5),
     1SHJ(5),HJ(5),ANJ(5),X(5)
      COMMON FJ,ZJK,AJ,BJ,CJ,DJ,THETJ,XMWJ,SHJ,HT1,HJ,ANJ,X,T,HT,T1,XMW,
     1VELT1,SH,IS
      Q=T**2
      R=T**3
      Y=T**4
      HT=0.0
      S=1.9872*T
      DO 710 J=1,IS
      IF(X(J))711,711,712
  711 HJ(J)=S*(2.5+(ANJ(J)-1.0))
      GO TO 710
  712 HJ(J)=THETJ(J)+AJ(J)*T+BJ(J)*Q+CJ(J)*R+DJ(J)*Y
  710 HT=HT+FJ(J)*HJ(J)
      RETURN
      END

      SUBROUTINE TIMDIS(IBACK,T)
C
C     THIS ROUTINE CALCULATES AT A PARTICULAR LAB TIME VALUES OF A
C     HYPOTHETICAL PARTICLE TIME WHICH GIVE THE CORRECT VALUE OF
C     DENSITY*DECAY ASSUMING IDEAL SHOCK RELATIONS AND EITHER COMPLETELY
C     FROZEN OR COMPLETELY RELAXED CONDITIONS (TPVA OR TPV2)
C
      COMMON /NUMINT/ F(10,10),J(10),AINT(10),M,K,DELX
      COMMON /TIMDIS/ RHOA1,RHO21,RHOT,TIM,TPVA,TPV2,DECAYL,U,TA,T2,AX
C
      CALL NUMINT
      IF(M.EQ.1) GO TO 60
      IF(J(1).EQ.2) GO TO 60
      RHOINT=AINT(1)*AX
      XINT=RHOINT-TIM
      DECAY3=DECAYL*U*(1.0-(1.0/RHOA1))
      DECAY4=DECAYL*U*(1.0-(1.0/RHO21))
      IF(IBACK.NE.2) GO TO 10
      TPVA=(DECAYL*U*XINT+ALOG(((RHOT/RHOA1)**2)*((T/TA)**0.5)))/DECAY3
      TPV2=(DECAYL*U*XINT+ALOG(((RHOT/RHO21)**2)*((T/T2)**0.5)))/DECAY4
      GO TO 60
   10 CONTINUE
      TPVA=(DECAYL*U*XINT+ALOG(RHOT/RHOA1))/DECAY3
      TPV2=(DECAYL*U*XINT+ALOG(RHOT/RHO21))/DECAY4
   60 CONTINUE
      RETURN
      END

      SUBROUTINE NUMINT
      COMMON /NUMINT/ F(10,10),J(10),AINT(10),M,K,DELX
C
C     THIS GENERAL SUBROUTINE CAN BE USED TO NUMERICALLY INTEGRATE UP TO
C     10 FUNCTIONS SIMULTANEOUSLY
C
C     DATA IS DIRECTED TO THE CORRECT LOCATION BY THE VALUE
C     ASSIGNED TO K
C
C     THE INTEGRATION IS PERFORMED ONLY ONCE FOR EVERY 2 DATA POINTS
C     IF INTEGRATION OF EACH POINT IS ESSENTIAL, THE TRAPEZIUM RULE
C     CAN BE USED TO EXTRAPOLATE BETWEEN THE LAST 2 POINTS
C
C     IT IS NECESSARY TO SPECIFY THE INITIAL VALUE OF THE FUNCTION
C     F(1,K) AND THE LAST VALUE F(4,K), THE X INCREMENT, DELX, MUST
C     BE CONSTANT.
C
```

```
C     NOTE THAT J(10) IS REPLACED BY JJ(10) IN THE MAINPROGRAMME
C
      IF(M.EQ.1) GO TO 100
      IF(J(K).EQ.2) GO TO 20
      F(2,K)=F(2,K)+F(4,K)
      J(K)=2
      GO TO 30
   20 CONTINUE
C
      AINT(K)=DELX*(F(1,K)+4.0*F(2,K)+2.0*F(3,K)+F(4,K))/3.0
      F(3,K)=F(3,K)+F(4,K)
      J(K)=1
      GO TO 30
  100 CONTINUE
      F(2,K)=0.0
      F(3,K)=0.0
   30 CONTINUE
      RETURN
      END


      SUBROUTINE CURFIT
C
C     POLYNOMIAL CURVE FITTING
C
C     DATA TAKEN IN AS X(I), Y(I) = UP TO 100 DATA POINTS (1024 IN
C     GRAPHICS PROGRAM )
C
C     N DEFINES NUMBER OF DATA POINTS
      COMMON /CURFIT/ X(200),Y(200),N
      DIMENSION A(16,16),SUMX(31),SUMY(15)
      DIMENSION AX(6)
      WRITE(2,1)
    1 FORMAT(26H POLOYNOMIAL CURVE FITTING)
   26 CONTINUE
      JSSW=0
      KSSW=0
      LAST=5
      ISSW=0
      SUMX(1)=N
      SUMX(2)=0.0
      SUMX(3)=0.0
      SUMY(1)=0.0
      SUMY(2)=0.0
      DO 10 I=1,N
      SUMX(2)=SUMX(2)+X(I)
      SUMX(3)=SUMX(3)+X(I)*X(I)
      SUMY(1)=SUMY(1)+Y(I)
   10 SUMY(2)=SUMY(2)+Y(I)*X(I)
      NORD=1
   25 L=NORD+1
      KK=L+1
      DO 11 I=1,L
      DO 12 J=1,L
      IK=J-1+I
   12 A(I,J)=SUMX(IK)
   11 A(I,KK)=SUMY(I)
      DO 115 I=1,L
      A(KK,I)=-1.0
      KKK=I+1
      DO 13 J=KKK,KK
   13 A(KK,J)=0.0
      C=1.0/A(1,I)
      DO 14 II=2,KK
      DO 14 J=KKK,KK
   14 A(II,J)=A(II,J)-A(1,J)*A(II,I)*C
```

```
      DO 15 II=1,L
      DO 15 J=KKK,KK
      A(II,J)=A(II+1,J)
   15 CONTINUE
  115 CONTINUE
      S2=0.0
      DO 16 J=1,N
      S1=0.0
      S1=S1+A(1,KK)
      DO 17 I=1, NORD
   17 S1=S1+A(I+1,KK)*X(J)**I
   16 S2=S2+(S1-Y(J))*(S1-Y(J))
      B=N-L
      S2=S2/B
      WRITE (2,5) NORD,S2,N
    5 FORMAT(7H ORDER=,I2,11H   (S2)**2=,F16.8,6H    N=,I3)
      DO 18 I=1,L
      J=I-1
   18 WRITE (2,6) J,A(I,KK)
    6 FORMAT(15H COEFFICIENTS  ,I3,E18.8)
      IF (KSSW.EQ.1) GO TO 50
   51 IF (NORD-LAST)52,50,52
   52 IF(S2)21,50,21
   50 WRITE (2,8)
    8 FORMAT(6H  X(I),6X,4HY(I),10X,8HY(CURVE))
      DO 19 I=1,N
      S1=0.0
      S1=A(1,KK)
      DO 20 J=1,NORD
   20 S1=S1+A(J+1,KK)*X(I)**J
   19 WRITE (2,7) X(I),Y(I),S1
    7 FORMAT(1H ,F7.2,E16.8,E16.8)
      IF(NORD-LAST)39,40,40
   39 IF(S2)21,40,21
   21 NORD=NORD+1
      J=2*NORD
      SUMX(J)=0.0
      SUMX(J+1)=0.0
      SUMY(NORD+1)=0.0
      DO 22 I=1,N
      SUMX(J)=SUMX(J)+X(I)**(J-1)
      SUMX(J+1)=SUMX(J+1)+X(I)**J
   22 SUMY(NORD+1)=SUMY(NORD+1)+Y(I)*X(I)**NORD
      GO TO 25
   40 PAUSE
      IF (ISSW.EQ.1) GO TO 26
      DO 1978 I=1,6
      AX(I)=A(I,7)
 1978 CONTINUE
      RETURN
      END
```

```
COMMON BLOCKS   START LENGTH
UNNAMED         33838    176
TIMDIS          32768     22
NUMINT          32790    246
CURFIT          33036    602

SUBPROGS        CODE            CONSTANT        LOCAL WKSPACE   DYNAMIC
              START  LENGTH   START  LENGTH   START  LENGTH   ARRAYS
MAINPROG      24722    1351    6459     578    7205     116     2048
HSHOCK        24609     113    7037      26    7323      21        0
```

```
TIMDIS      24481      128     7063       26     7344       17        0
NUMINT      24345      136     7089       26     7361        7        0
CURFIT      23703      642     7115       90     7368       28      616

FREE STORE         7396 TO    23702   AND    34014 TO    65536

&RUN;                                                                  TIME
```

**********VIBRATIONAL RELAXATION OF SHOCKED OXYGEN: TIME DEPENDENCE**********
M.P.PERLEY 12 SEPT 1977

RUN NUMBER= M192

SPECIES	MOLE FRACT	GAMMA1	VIB; ENERGY INCL; IN STATE B (1=YES,0=NO)
OXYGEN	0;25	1,40	1,0
NITROGEN	0,75	1,40	0,0

INITIAL TEMP = 291;0K INITIAL PRESSURE = 6;50MM DECAY = -0;380M-1

MAX OBSERVATION TIME = 100;0US TIME INCREMENT = 10,0US

SHOCK VELOCITY = 1;406KM/S

OBS TIME	TRACT	TRFA1	TRREL	TR*FA1	TR*REL	TEMP	DENSITY RATIO	TIME
0;73	3,38					1230;	4,635	120,00
10;73	49,92					1223;	4,672	130,00
20;73	94,79	96;03	104;27	61,28	252,23	1217;	4,702	140,00
30;73	140,95					1212;	4,727	150,00
40;73	191,33	188,68	204;86	133,40	322,82	1208;	4,748	160,00
50;73	238,89					1205;	4,765	170,00
60;73	284,62	281,33	305;46	213,30	401,02	1202;	4,780	180,00
70;73	334,48					1200;	4,792	190,00
80;73	380,47	373,97	406;05	298,26	484,17	1198;	4,803	200,00
90;73	430,55					1196;	4,813	210,00
100,73	479,72	466,62	506;65	386,65	570,68	1194;	4,821	220,00

	TEMP	DENSITY RATIO	PRESSURE RATIO
FROZEN	1231,	4;632	19,59
STATE B	1195,	4;815	19,78
RELAXED	1155,	5;030	19,97
MEAN	1207,	4;753	19,71

MEAN RELAXATION TIMES = 238;41US(02),2827;14US(N2)

POLYNOMIAL CURVE FITTING
ORDER= 1 (S2)**2= 0,22404104E-03 N= 6
COEFFICIENTS 0 0,46523527E+01
COEFFICIENTS 1 -0,14513274E-02
ORDER= 2 (S2)**2= 0,50734178E-04 N= 6
COEFFICIENTS 0 0,46374278E+01
COEFFICIENTS 1 -0,12181085E-02
COEFFICIENTS 2 -0,43432821E-06
ORDER= 3 (S2)**2= 0,43476838E-05 N= 6
COEFFICIENTS 0 0,46330006E+01
COEFFICIENTS 1 -0,10063665E-02
COEFFICIENTS 2 -0,16984009E-05
COEFFICIENTS 3 0,16888323E-08
ORDER= 4 (S2)**2= 0,47409675E-06 N= 6
COEFFICIENTS 0 0,46324363E+01
COEFFICIENTS 1 -0,99585361E-03
COEFFICIENTS 2 -0,98270590E-05
COEFFICIENTS 3 0,65250521E-08
COEFFICIENTS 4 -0,40060493E-11

FROFLO AT 2403R2
ORDER= 5 (S2)**2= 0,57896045E+77 N= 6
COEFFICIENTS 0 0,46323938E+01
COEFFICIENTS 1 -0,95167108E-03

```
 COEFFICIENTS     2    =0,37967934E-05
 COEFFICIENTS     3     0,11268471E-07
 COEFFICIENTS     4    =0,17761661E-10
 COEFFICIENTS     5     0,11485227E-13
  X(I)          Y(I)              Y(CURVE)
    0,00   0,46323938E+01   0,46323938E+01
   96,79   0,45231453E+01   0,45231454E+01
  191,33   0,43885277E+01   0,43885276E+01
  286,62   0,42440596E+01   0,42440599E+01
  382,47   0,40956488E+01   0,40956488E+01
  478,72   0,39467572E+01   0,39467573E+01

   END


 &END)

LINES PRINTED = 00701
REAL TIME = 0001  33
CPU TIME =  0000  57,962
   A
```

C.3. Results Plotting Program, PLTRES

Almost all the results in Chapters 7 and 8 have been plotted using the graphics facilities available on the ICL 4130 computer. The mainprogram PLTRES reads the data to be plotted, the labels of the headings and axes, and allows a choice of sizes for the axes. The plotting is performed by calling the University of Keele Computer Centre Library subprogram, ISEASY, written by Dr. Peter Borrell (a full description is in the library manual). The principal function of the mainprogram is to allow plots of f(y) against f(x) to be made for data received in the form y(I), x(I); the scale of the axes may be fixed in the mainprogram to allow plots in which the fraction of the scale used is a suitable size for A4 paper.

The data cards required are listed in Table C.3.1 and the options available are described in the listing of the program and in the library manual.

TABLE C.3.1

Data required for PLTRES plotting program

CARD NUMBER	REQUIRED DATA	FORMAT
1	IGO, ISHEET, ILINE, IPOINT, NSH	5I4
2	SHEAD(J)	8A8
3	IOR, IPRINT, ISIZE	3I4
4	XSIZE, YSIZE	2F10.0
5	NH, NX, NY	3I4
6	HEAD(J)	5A8
7	XLABEL(J)	8A8
8	YLABEL(J)	8A8
9	*M*	I4
10	FRAC	F5.0
11	N	I4
12 etc.	X(I), Y(I)	2F10.0

```
          AUTOL       JOBTYPE=B    PRIORITY = 5    SIZE= 128  START= 083                    DATE  15 (

 &JOB;CH10:PLTRES:
SWOP

 &OPTIONS;                                                                                    TI

 &FORTRAN;L;                                                                                  TI
    0*
    1*        DIMENSION HEAD(5),SHEAD(8),XLABEL(8),YLABEL(8)
    2*        DIMENSION X(200),Y(200),AX(200),AY(200)
    3*        DIMENSION A(7)
    4*  1500 CONTINUE
    5*        READ(7,20)IGO,ISHEET,ILINE,IPOINT,NSH
    6* C                                 IGO=0 - FINISH
    7* C                                 IGO=1 - FIRST RUN
    8* C                                 IGO=2 - NEW RUN, SAME AXES AND LABELS
    9* C                                 IGO=3 - NEW RUN, SAME SIZE AXES, NEW LABELS
   10* C                                 IGO=4 - AXES NOT PRESET
   11* C                                 IGO=5 - READS NEW DATA ONLY
   12* C                                 ISHEET=0 (ONLY IF IGO=0 ) - SINGLE PLOT
   13* C                                 ISHEET=1 ( ONLY IF IGO=4 ) - FIRST PLOT OF
   14* C                                 SERIES ON SAME AXES
   15* C                                 ISHEET=2 - STANDARD - ONE OF SERIES OF
   16* C                                 PLOTS ON SAME AXES
   17* C                                 ISHEET=3 - LAST OF SERIES ON SAME AXES
   18* C                                 ILINE=0 - DRAWS LINE THROUGH DATA
   19* C                                 ILINE=1 - PLOTS DATA POINTS
   20* C                                           ( OTHER OPTIONS AVAILABLE )
   21* C                                 IPOINT DEFINES SYMBOL PLOTTED IF ILINE=1
   22* C                                 IPOINT=1 - 10 :PLOTS X IF IPOINT=3
   23* C                                 NSH - DIMENSIONS SUBHEADING -NA8
   24*        IF(IGO.EQ.0) GOTO 2000
   25*        IF(IGO.EQ.5) GOTO 200
   26*        IF(NSH.EQ.0) GOTO 90
   27*        READ(7,60)(SHEAD(J),J=1,8)
   28* C                                 SHEAD - SUBHEADING
   29*        WRITE(2,60)(SHEAD(J),J=1,8)
   30*    90 CONTINUE
   31*        IF((IGO.EQ.2).OR.(IGO.EQ.3)) GOTO 105
   32*        READ(7,40)IOR,IPRINT,ISIZE
   33* C                                 IOR=0 - ORIGIN NOT SPECIFICALLY INCLUDED
   34* C                                 IOR=1 - ORIGIN SPECIFICALLY INCLUDED
   35* C                                 IPRINT=1 - SUPPRESSES PRINTING OF NUMBERS
   36* C                                           ON AXES
   37* C                                 ISIZE=1 - NON STANDARD SIZE REQUIRED
   38* C                                           STANDARD SIZE 10 X 8 INCHES
   39*        IF(ISIZE.NE.1) GO TO 100
   40*        READ(7,50)XSIZE,YSIZE
   41* C                                 XSIZE, YSIZE - DEFINE SIZE OF GRAPH-INCHES
   42*   100 CONTINUE
   43*        READ(7,40)NH,NX,NY
   44* C                                 NH,NX,NY - DIMENSION LABELS FOR HEADING
   45* C                                           AND X,Y AXES
   46*   105 CONTINUE
   47*        IF(NH.EQ.0) GOTO 110
   48*        READ(7,60)(HEAD(J),J=1,5)
```

```
C                                   HEAD - HEADING
  110 CONTINUE
      IF(IGO.EQ.2) GOTO 130
      IF(NX.EQ.0) GOTO 120
      READ(7,60)(XLABEL(J),J=1,8)
C                                   XLABEL, YLABEL - LABELS FOR AXES
  120 CONTINUE
      IF(NY.EQ.0) GOTO 130
      READ(7,60)(YLABEL(J),J=1,8)
  130 CONTINUE
      READ(7,10)M
C                                   M=0- PLOTS K AGAINST TEMP
C                                   M=1- PLOTS LOG10K AGAINST TEMP
C                                   M=2- PLOTS LOG10K AGAINST 1/TEMP
C                                   M=3- PLOTS K AGAINST 1/TEMP
C                                   M=4- PLOTS LOG10K AGAINST LOG10 TEMP
C                                   M=5 - PLOTS K AGAINST SQRT TEMP
C                                   M=6 - PLOTS LOG(K/SQRT T2 ) AGAINST 1/TEMP
      READ(7,70)FRAC
C                                   FRAC - MOLE FRACTION OF N2 IN O2/N2
C                                          MIXTURE - IF FRAC >1.0 POOLING
C                                          REACTION STUDIED INSTEAD
      IF(IGO.EQ.4) GOTO 200
C                                   SETS UP AXES IF IGO NE 4, BEFORE
C                                          PLOTTING POINTS
      JSHEET=1
      JLINE=1
      JPOINT=2
      N=2
      X(1)=295.0
      Y(1)=0.1*(1.0-FRAC)+1.3*FRAC
      IF(FRAC.GT.1.0) Y(1)=0.122
      X(2)=2100
      Y(2)=10.0
      CONST=6.0
      ACONST=5.8
      IF(FRAC.GT.1.0) CONST=5.0
      IF(FRAC.GT.1.0) ACONST=5.0
      IF((M.EQ.1).OR.(M.EQ.2)) Y(1)=ALOG10(Y(1))+CONST
      IF((M.EQ.1).OR.(M.EQ.2)) Y(2)=1.0+ACONST
      IF((M.EQ.2).OR.(M.EQ.3)) X(1)=1.0/X(1)
      IF((M.EQ.2).OR.(M.EQ.3)) X(2)=0.0
      IF(M.EQ.4) X(1)=ALOG10(X(1))
      IF(M.EQ.4) X(2)=ALOG10(X(2))
      IF(M.EQ.4) Y(1)=ALOG10(Y(1))+CONST
      IF(M.EQ.4) Y(2)=1.0+ACONST
      IF(M.EQ.5) X(1)=SQRT(X(1))
      IF(M.EQ.5) X(2)=60.0
      IF(M.EQ.6) Y(1)=2.7
      IF(M.EQ.6) Y(2)=4.6
      IF((FRAC.LE.1.0).AND.(M.EQ.6)) Y(1)=5.35
      IF((FRAC.LE.1.0).AND.(M.EQ.6)) Y(2)=3.55
      IF(M.EQ.6) X(1)=1.0/X(1)
      IF(M.EQ.6) X(2)=0.0
      CALL ISEASY(N,X,Y,IOR,JLINE,JPOINT,JSHEET,IPRINT,ISIZE,XSIZE,
     1YSIZE,NH,HEAD,NSH,SHEAD,NX,XLABEL,NY,YLABEL)
  200 CONTINUE
      WRITE(2,300)
  300 FORMAT(1H1,30X,6H X(I) ,10X,6H Y(I) )
      READ(7,10)N
```

```
109*C                                   N - NUMBER OF DATA POINTS
110*      DO 1000 I=1,N
111*      READ(7,30)X(I),Y(I)
112*C                                       X(I),Y(I) - EXPERIMENTAL DATA
113*      IF((M.EQ.1).OR.(M.EQ.2)) Y(I)=ALOG10(Y(I))+CONST
114*      IF((M.EQ.2).OR.(M.EQ.3)) X(I)=(1.0/X(I))
115*      IF(M.EQ.4) X(I)=ALOG10(X(I))
116*      IF(M.EQ.4) Y(I)=ALOG10(Y(I))+CONST
117*      IF(M.EQ.5) X(I)=SQRT(X(I))
118*      IF(M.EQ.6) Y(I)=ALOG10(Y(I)/SQRT(X(I)))+CONST
119*      IF(M.EQ.6) X(I)=(1.0/X(I))
120*      WRITE(2,210)X(I),Y(I)
121*  210 FORMAT(29X,E10.4,6X,E10.4)
122* 1000 CONTINUE
123*      CALL ISEASY(N,X,Y,IOR,ILINE,IPOINT,ISHEET,IPRINT,ISIZE,XSIZE,
124*     1YSIZE,NH,HEAD,NSH,SHEAD,NX,XLABEL,NY,YLABEL)
125*      GO TO 1500
126* 2000 CONTINUE
127*   10 FORMAT(I4)
128*   20 FORMAT(5I4)
129*   30 FORMAT(2F10.0)
130*   40 FORMAT(3I4)
131*   50 FORMAT(2F10.0)
132*   60 FORMAT(9A5)
133*   70 FORMAT(F5.0)
134*      STOP
135*      END

&ENDRUN;                                                              TIME =

&END;

LINES PRINTED = 00158
REAL TIME =  0000  41
CPU TIME =   0000  13.903
   A
```